



LATE ACCRETION
ONTO TERRESTRIAL PLANETS



Early Bombardment History of the Inner
Solar System and Links to Future Human and
Robotic Exploration Missions to the Moon

Dissertation

Submission for the Academic Title
Doktor der Naturwissenschaften
(Dr. rer. nat.)

Submitted by
Csilla Orgel

Freie Universität Berlin
Fachbereich Geowissenschaften

Berlin, April 2020

Rewier 1: Prof. Dr. Kai Wünnemann
Museum für Naturkunde, Berlin, Germany

Rewier 2: Prof. Dr. Harald Hiesinger
Westfälische Wilhelms-Universität, Münster, Germany

Date of defense: 18. August 2020

Summary

The lunar and mercurian cratering records provide valuable information about the late accretion history of the inner Solar System. However, our understanding of the origin, rate, and timing of the impacting projectiles is far from complete. Different late accretion models including single and multiple impactor populations may explain the early lunar bombardment history. The single impactor population model explains the exponential decay of impactors over time (e.g., Neukum, 1983; Neukum & Ivanov, 1994; Hartmann, 1995), and the Late Heavy Bombardment (LHB) or lunar cataclysm model suggests different impactor populations with a rapidly increasing impact flux at 3.9 Gyr (Ryder, 1990, 2002). The primary aim of this work is to test various accretion models and improve the lunar production function (PF) by re-evaluating its shape to infer potential impactor populations. To learn more about these projectiles, we can examine crater size-frequency distributions (CSFDs) on the Moon and Mercury. This PhD thesis re-investigates the crater populations of large ($D \geq 300$ km) lunar and mercurian basins using the buffered crater counting (BCC) and buffered non-sparseness correction (BNSC) techniques. BNSC is a novel CSFD technique, which takes crater obliteration on highly cratered surfaces into account, thus providing more accurate measurements for the frequencies of smaller crater sizes. The BNSC-corrected CSFDs of individual basins, particularly at smaller crater diameters increase compared to the crater frequencies derived from the BCC technique alone. Furthermore, a new basin catalogue of 94 basins has been produced on Mercury, 80 of which have been classified as certain or probable, 1.7× times more than previously recognized. However, this number of basins has been estimated to represent roughly half of the expected basin record, where basins older than Borealis have been obscured by different processes (e.g., higher impact melt production, volcanism, subsequent impacts, and viscoelastic relaxation of basins). Consequently, if the Neukum (1983) and Neukum et al. (2001a) theories are correct that the impactor population in the inner Solar System did not change over time, one could expect that the summed CSFDs of basins in different time periods maintain a single shape following the lunar PF. Contrary to previous studies, the shape of summed CSFDs of Pre-Nectarian (excluding South Pole-Aitken Basin), Nectarian (including Nectaris) and Imbrian (including Imbrium) basins show no statistically significant differences, and thus provide no evidence for a change of impactor population bombarded the lunar surface. Similarly, the results on the shape of summed CSFDs of Pre-Tolstojan and Tolstojan basins on Mercury are consistent with the lunar study. The secondary aim is to find potential key landing sites for future human and robotic exploration missions with sample return capability on the lunar surface, which could target key sampling locations in order to verify the preferred late accretion model and refine the lunar chronology model, and thus, the absolute model ages (AMA) of different geologic units on the Moon and other terrestrial planets. In order to do so, this dissertation focus on the exploration of the South Pole-Aitken basin with the main focus on the south polar

region of the Moon, a region that has not been visited by any human missions, yet exhibits a multitude of scientifically important locations – the investigation of which address long-standing questions in lunar research. The findings show that a human-assisted robotic mission to the South Pole-Aitken basin, can address all seven US National Research Council (2007) lunar science concepts, and would be a valuable resource to reveal the early history and evolution of the Solar System.

Kurzfassung

Die Krater auf dem Mond und Merkur liefern wertvolle Informationen über die späte Akkretionsgeschichte des inneren Sonnensystems. Unser Verständnis von Ursprung, Geschwindigkeit und Zeit der impaktierten Projektile ist nicht jedoch vollständig. Verschiedene Modelle der späten Akkretion, einschließlich einzelner und mehrerer Impaktorpopulationen, können die frühe Impaktgeschichte des Mondes erklären. Das Einzelimpaktor-Populationsmodell erklärt die exponentielle Verringerung der Impaktoren im Laufe der Zeit (z. B. Neukum, 1983; Neukum & Ivanov, 1994; Hartmann, 1995), und das "Late Heavy Bombardment" (LHB) - oder "lunar cataclysm"-Szenario schlägt unterschiedliche Impaktorpopulationen vor, wobei eine signifikante Erhöhung der Impaktoreinschläge vor 3,9 Milliarden Jahren auftritt (Ryder, 1990, 2002). Das Hauptziel dieser Arbeit ist die verschiedenen Akkretionsmodelle zu testen und die Produktionsfunktion (PF) für den Mond zu verbessern, indem ihre Form neu bewertet wird, um auf potenzielle Impaktorpopulationen zu schlussfolgern. Um mehr über diese Projektile zu erfahren, können wir Kratergrößen-Häufigkeitsverteilungen (CSFDs) auf dem Mond und Merkur untersuchen. In dieser Doktorarbeit werden die Kraterpopulationen der großen ($D \geq 300$ km) Mond- und Merkurbecken mithilfe der Techniken "Buffered Crater Counting" (BCC) und "Buffered Non-Sparseness Correction" (BNSC) erneut untersucht. BNSC ist eine neuartige CSFD-Technik, die die Auslöschung von Kratern auf stark verkraterten Oberflächen berücksichtigt und somit eine genauere Messung für das Auftreten kleinerer Krater ermöglicht. Die BNSC-korrigierten CSFDs einzelner Becken, insbesondere der mit kleineren Kraterdurchmessern, nehmen im Vergleich zu den Kraterhäufigkeiten zu, die allein von der BCC-Technik abgeleitet wurden. Darüber hinaus wurde ein neuer Becken-Katalog mit 94 Becken auf Merkur erstellt, von denen 80 als sicher oder wahrscheinlich eingestuft wurden, 1,7-mal mehr als bisher bekannt. Diese Anzahl an Becken stellt schätzungsweise ungefähr die Hälfte aller erwarteten Becken dar. Becken, die älter als Borealis sind, wurden durch verschiedene Prozesse (z. B. hohe Schmelzproduktion, Vulkanismus, Viskoelastische Relaxation von Becken) überprägt. Wenn die Modelle von Neukum (1983) und Neukum et al. (2001a) richtig sind und sich die Impaktorpopulation im inneren Sonnensystem im Laufe der Zeit nicht verändert hat, könnte man erwarten, dass die aufsummierten CSFDs von Becken verschiedener Zeiträume Neukum's PF folgen. Im Gegensatz zu früheren Studien zeigt die Form der summierten CSFDs der Becken von Pre-Nectarian (ohne South Pole-Aitken Becken), Nectarian (einschließlich Nectaris) und Imbrian (einschließlich Imbrium) keine statistisch signifikanten Unterschiede und liefert daher keine Hinweise auf eine Änderung der Impaktorpopulation, die die Mondoberfläche bombardierte. Die Ergebnisse der Pre-Tolstojan- und Tolstojan-Becken auf Merkur stimmen mit denen der Mondstudie überein.

Das zweite Ziel dieser Arbeit besteht darin, potenzielle Landestellen für zukünftige bemannten und robotischen Missionen auf der Mondoberfläche zu finden, von denen Proben zur Erde zurück gebracht werden können. Die untersuchten Landestellen zielen darauf ab, Proben zu sammeln, um das bevorzugte Modell der späten Akkretion

zu verifizieren und das Modell der Mondchronologie zu verfeinern. Dies wird schließlich das absolute Modellalter (AMA) verschiedener geologischer Einheiten auf dem Mond und anderer terrestrischer Planeten verbessern. Diese Dissertation fokussiert sich deshalb auf die Erforschung des South Pole-Aitken Beckens und legt einen Schwerpunkt auf die Südpole des Mondes, einer Region, die bisher von keiner bemannten Mission besucht wurde, jedoch eine Vielzahl von wissenschaftlich relevanten Orten aufweist. Das Untersuchen dieser Orte wird langjährige Fragen der Mondforschung beantworten können. Die Ergebnisse zeigen, dass alle sieben Mondforschungskonzepte des US National Research Council (2007) mit einer von Menschen unterstützten Robotermissionen zum South Pole-Aitken Becken untersucht werden können. Dies ist von großer Wichtigkeit, um die frühere Impaktgeschichte des Mondes und die Entstehung des Sonnensystems besser zu verstehen.

Acknowledgment

I own a BIG THANK YOU to many people who helped me to present this work. First of all, I am thankful for the continuous support and guidance of *Dr. Greg Michael*. He introduced me to crater statistics and crater counting and many more skills I can use as a scientist. Also, I am grateful for my supervisor, *Prof. Dr. Kai Wünnemann* for the discussions and support to finish this thesis. I would like to thank to my co-supervisor, *Prof. Dr. Harald Hiesinger* for his support, and invitation to work with him and *Mikhail Ivanov* on the landing site analysis in the Apollo basin at Westfälische Wilhelms-Universität in Münster. Moreover, I am thankful for the interesting discussions and joint work to *Dr. Carolyn van der Bogert*, *Wajiha Iqbal* and the whole Planetary Science Group in Münster. I am also very grateful for *Dr. Caleb I. Fassett* who introduced me to Mercury research and invited me to NASA Marshall Space Flight Center where I spent two fruitful months working on large Mercurian basins. Moreover, I am thankful for *Dr. David Kring* who selected me to participate in the 2016 Exploration Science Summer Intern Program hosted by the Lunar and Planetary Institute (LPI). There, I got the opportunity to work on future lunar landing sites and most importantly drove my attention to the Moon.

I am very thankful for SFB/TRR-170 project and *Prof. Dr. Harry Becker* for the financial support to carry out this PhD thesis and let me attend several international/national conferences, meetings, summer/winter schools and research visits. I also greatly appreciate the support of all TRR students and scientists, I learned a lot from you all. Especially, I enjoyed very much the discussions and travels with *Christian Riedel* with whom I shared the best office of all times.

I cannot be enough grateful for my colleagues, and friends in the Planetary Science & Remote Sensing Group at Freie Universität Berlin, all of you who truly supported me all those years. I will never forget the discussions, social gatherings, and events! THANK YOU!

Finally, I am very grateful for my friends, family and my “Drágám” for their continuous support and for keeping me motivated until finishing this work.

CONTENTS

| | |
|------------------------|-----|
| Summary | i |
| Kurzfassung | ii |
| Acknowledgments | iii |
| Contents | v |
| List of Figures | xi |
| List of Tables | xv |

I. INTRODUCTION

| | |
|---|----|
| 1. The basics of impact cratering and late accretion models | 1 |
| 1.1. Significance of Impact Cratering | 1 |
| 1.1.1. Impact Crater Formation | 1 |
| 1.1.2. Simple to Complex Crater | 3 |
| 1.1.3. Impact Generated Lithologies | 5 |
| 1.1.4. Radioisotopic Dating of Impact Melt Rocks | 6 |
| 1.2. Late Accretion Models | 7 |
| 1.3. Science Enabled by Future Human and Robotic Exploration Missions to the Moon | 10 |
| 2. Research aims | 15 |
| 2.1. Research Framework of This Thesis | 15 |
| 2.2. Scientific Objectives and Motivation | 16 |
| 3. Personal contribution and structure of this thesis | 19 |
| 3.1. Personal Contribution | 19 |
| 3.2. Structure | 25 |
| 4. Methods | 27 |
| 4.1. Measuring Crater Populations | 28 |
| 4.2. Crater Size-Frequency Distribution Techniques | 28 |
| 4.3. Interpreting Crater Size-Frequency Distributions | 30 |

| | |
|---|----|
| 4.3.1. Cumulative Size-Frequency Plot | 30 |
| 4.3.2. Differential Size-Frequency Plot | 31 |
| 4.3.3. Relative Size-Frequency Plot | 32 |
| 4.4. Deriving Absolute Model Age on the Lunar Surface | 32 |
| 4.4.1. Production Function | 33 |
| 4.4.2. Chronology Function | 33 |
| 4.5. Chronostratigraphy | 37 |

II. EARLY BOMBARDMENT HISTORY OF THE INNER SOLAR SYSTEM

| | |
|--|-----------|
| 5. Ancient bombardment of the inner Solar System – Reinvestigation of the "fingerprints" of different impactor populations on the lunar surface | 39 |
| Abstract | 39 |
| 5.1. Introduction | 39 |
| 5.2. Data and Methods | 42 |
| 5.3. Results and Interpretation | 45 |
| 5.3.1. Crater Frequencies with BNSC | 45 |
| 5.3.2. Refined Basin Sequence | 46 |
| 5.3.3. Impactor Population | 48 |
| 5.4. Discussion | 48 |
| 5.4.1. Impactor Populations and the LHB | 48 |
| 5.4.2. Basin Sequence and Sample Ages | 51 |
| 5.4.2.1. Serenitatis Basin | 51 |
| 5.4.2.2. Nectaris Basin | 53 |
| 5.4.2.3. Crisium Basin | 53 |
| 5.4.2.4. Imbrium Basin | 54 |
| 5.4.3. Saturation Equilibrium | 55 |
| 5.5. Conclusion | 56 |

| | |
|--|-----------|
| 6. Re-examination of the population, stratigraphy, and sequence of mercurian basins: Implications for Mercury's early impact history and comparison with the Moon | 59 |
| Abstract | 59 |
| 6.1. Introduction | 59 |
| 6.2. Background | 62 |
| 6.3. Data and Methods | 63 |
| 6.3.1. Data | 63 |
| 6.3.2. Crater Size-Frequency Distribution Measurements | 65 |
| 6.3.3. Determination of Absolute Model Ages | 67 |
| 6.3.4. Comparison with Lunar Basins | 67 |
| 6.4. Results | 69 |
| 6.4.1. Updated Basin Inventory on Mercury | 69 |
| 6.4.1.1. Examples of Newly Discovered Basins | 69 |
| 6.4.1.1.1. The 375-Km-Diameter Basin (b102) at -11.7°S, -75.4°W | 69 |
| 6.4.1.1.2. The 645-Km-Diameter Basin (b79) at 53.7°N, 164.8°E | 71 |
| 6.4.1.2. Examples of Newly Identified Tentative Basins | 71 |
| 6.4.1.2.1. The 2081-km-Diameter Basin (b100) at -60.9°S, 75.7°E | 71 |
| 6.4.1.2.2. The 2032-Km-Diameter Basin (b69) at 3.9°N, -112.7°W | 76 |
| 6.4.2. Crater Frequencies with Buffered Non-Sparseness Correction | 76 |
| 6.4.3. Spatial Densities of Basins on Mercury and the Moon | 79 |
| 6.4.4. Impactor Population | 81 |
| 6.5. Discussion | 82 |
| 6.5.1. Geographic Distribution of Basins | 82 |
| 6.5.2. Basin Formation and Subsequent Geologic Activities | 84 |
| 6.5.3. Saturation Equilibrium | 88 |
| 6.5.4. Impactor Population(s) and the Late Heavy Bombardment | 91 |
| 6.6. Conclusion | 92 |

III. HUMAN AND ROBOTIC EXPLORATION MISSIONS TO THE MOON

| | |
|--|-----------|
| 7. Traverses for the ISECG-GER Design Reference Mission for humans on the lunar surface | 95 |
| Abstract | 95 |
| 7.1. Introduction | 95 |
| 7.2. SPA Geology and Landing Sites | 99 |
| 7.2.1. Malapert Massif | 100 |
| 7.2.2. Shackleton Crater | 101 |
| 7.2.3. Schrödinger Basin | 101 |
| 7.2.4. Antoniadi Crater | 102 |
| 7.2.5. SPA Basin Center | 102 |
| 7.3. Concept of Operations | 102 |
| 7.3.1. Mission Architecture | 103 |
| 7.3.2. Small Pressurized Rovers (SPR) | 104 |
| 7.3.3. Sampling Requirements | 106 |
| 7.3.4. Communications | 107 |
| 7.4. Methodology | 109 |
| 7.5. Results | 110 |
| 7.5.1. Tele-Robotic Traverses Between Landing Sites | 110 |
| 7.5.1.1. Malapert Massif to Shackleton Crater | 114 |
| 7.5.1.2. Shackleton Crater to Schrödinger Basin | 116 |
| 7.5.1.3. Schrödinger Basin to Antoniadi Crater | 119 |
| 7.5.1.4. Antoniadi Crater to South Pole–Aitken Basin Center | 121 |
| 7.5.2. Crew Traverses At and Around Landing Sites | 123 |
| 7.5.2.1. Malapert Massif Traverse | 124 |
| 7.5.2.2. South Pole (Shackleton Crater) Traverse | 130 |
| 7.5.2.3. Schrödinger Basin Traverse | 132 |
| 7.5.2.4. Antoniadi Crater Traverse | 137 |
| 7.5.2.5. South Pole-Aitken Basin Center Traverse | 141 |

| | |
|--|------------|
| 7.6. Implied Trade Studies | 144 |
| 7.7. Conclusion | 147 |
| 8. Characterization of high-priority landing sites for robotic exploration missions in the Apollo basin, Moon | 149 |
| Abstract | 149 |
| 8.1. Introduction | 149 |
| 8.2. Science Rationale | 151 |
| 8.2.1. South Pole-Aitken Basin | 151 |
| 8.2.2. Apollo Basin | 151 |
| 8.3. Selection Criteria for Regions of Interest (ROI) | 155 |
| 8.4. Data and Methods | 157 |
| 8.4.1. Data | 157 |
| 8.4.2. Methods | 157 |
| 8.4.2.1. Absolute Model Age (AMA) | 157 |
| 8.4.2.2. Regolith Thickness and Stratigraphy | 158 |
| 8.5. Results | 159 |
| 8.5.1. Terrain Hazards: DEM, Slopes, Craters and Rock Abundance | 159 |
| 8.5.2. Science Potential | 163 |
| 8.5.2.1. Geologic Mapping and Absolute Model Ages | 163 |
| 8.5.2.2. Regolith Thickness and Subsurface Stratigraphy | 169 |
| 8.5.2.3. In Situ Resource Utilization (ISRU) Potential | 172 |
| 8.6. Discussion | 175 |
| 8.7. Conclusions | 177 |
| | |
| IV. CONCLUSIONS | |
| | |
| 9. Conclusions | 179 |
| | |
| BIBLIOGRAPHY | 187 |

| | |
|--|------------|
| Eidesstattliche Erklärung | 223 |
| Curriculum Vitae | 225 |
| V. APPENDICES | 231 |
| A Supplementary Information, Chapter 5 | |
| B Supplementary Information, Chapter 6 | |
| C Supplementary Information, Chapter 7 | |
| D Supplementary Information, Chapter 8 | |
| E Supplementary Information | |

LIST OF FIGURES

| | | |
|------|---|-----|
| 1.1 | Schematic illustration of the different stages of crater formation | 2 |
| 1.2 | Transition from simple to complex impact craters on the Moon | 4 |
| 1.3 | Variety of impact rocks from the proximal and distal impactites | 6 |
| 1.4 | Different late accretion models | 8 |
| 4.1 | Analysis of crater size-frequency distributions using different techniques | 29 |
| 4.2 | Functions used for CSFD-based absolute model age determinations | 34 |
| 4.3 | Lunar cratering chronology curve after Neukum (1983) | 36 |
| 5.1 | Schematic of buffered non-sparseness correction | 41 |
| 5.2 | Effect of different exclusion radius | 43 |
| 5.3 | Crater measurement map and derived CSFD | 46 |
| 5.4 | Summed CSFDs of the Pre-Nectarian-aged basins, Nectarian-aged basins and Imbrian-aged basins | 52 |
| 5.5 | Saturation of lunar basins | 56 |
| 6.1 | Different mapping approaches for the crater measurements | 64 |
| 6.2 | Schematic of non-sparseness correction | 65 |
| 6.3 | Schematic of buffered non-sparseness correction | 66 |
| 6.4 | Global distribution of basins on Mercury | 70 |
| 6.5 | Examples of newly discovered basins | 75 |
| 6.6 | Crater measurement maps and derived CSFD with AMA of Sobkou | 77 |
| 6.7 | Difference between the BNSC and the BCC1 results | 78 |
| 6.8 | Relative plot of the spatial density of (a) large basins ($D \geq 300$ km) and (b) craters superposing large basins on Mercury | 79 |
| 6.9 | Summed CSFDs to study the impactor population(s) | 80 |
| 6.10 | Basin asymmetry on Mercury | 82 |
| 6.11 | Sequence of basin formation on the Moon (a) and Mercury (b) | 87 |
| 6.12 | Saturation of lunar and mercurian basins | 89 |
| 7.1 | An overview of all landing sites considered in this study | 96 |
| 7.2 | Percentage communication coverage for landing sites | 109 |
| 7.3 | Colorized DEM of between landing site traverses from Malapert massif to South Pole-Aitken basin | 111 |

| | | |
|------|---|-----|
| 7.4 | Colorized slope profile between landing site traverses from Malapert massif to South Pole-Aitken basin center | 112 |
| 7.5 | Direct and science traverses from Malapert massif to South Pole/ Shackleton crater | 115 |
| 7.6 | Direct and science traverses from South Pole/Shackleton crater to Schrödinger basin | 117 |
| 7.7 | The science traverse descending to the interior of Amundsen crater | 118 |
| 7.8 | 3D image of Schrödinger basin wall | 119 |
| 7.9 | Direct and science traverses from Schrödinger basin to Antoniadi crater | 120 |
| 7.10 | 3D image of Antoniadi crater wall | 121 |
| 7.11 | Direct and science traverses from Antoniadi crater to South Pole-Aitken basin center | 122 |
| 7.12 | Colorized LOLA DEM of Malapert massif | 125 |
| 7.13 | Spudis et al. (2008) map of geologic units | 126 |
| 7.14 | Slope profile for Traverse Loop 1 of Malapert massif | 128 |
| 7.15 | Colorized DEM of the South Pole region | 131 |
| 7.16 | Colorized DEM of Schrödinger basin | 133 |
| 7.17 | Oblique view of Schrödinger basin exploration zone from 100 m/pix LROC WAC mosaic | 135 |
| 7.18 | Proposed internal and external landing sites and exploration zones for Schrödinger basin | 136 |
| 7.19 | Colorized DEM of Antoniadi crater | 138 |
| 7.20 | Proposed external and internal landing sites and exploration zones for Antoniadi crater | 140 |
| 7.21 | Colorized DEM of SPA basin center | 143 |
| 8.1 | South Pole-Aitken basin overview | 150 |
| 8.2 | Oblique view of Apollo basin | 152 |
| 8.3 | Maps of the Apollo basin | 154 |
| 8.4 | Digital elevation models and slopes for ROI 1, 2, and 3 | 160 |
| 8.5 | Maps of craters ≥ 70 m and derived crater densities for ROI 1, 2, and 3 | 161 |
| 8.6 | Rock abundance for ROI 1, 2, and 3 | 162 |
| 8.7 | Geologic map of the central mare province of the Apollo basin | 165 |
| 8.8 | Geologic map of the southern mare province of the Apollo basin | 166 |
| 8.9 | Geologic maps of ROIs with a correlation chart of the geologic units | 167 |

| | | |
|------|--|-----|
| 8.10 | Crater size-frequency distribution and absolute model age of ROIs | 168 |
| 8.11 | Map of regolith thickness estimation | 170 |
| 8.12 | Chandrayaan M ³ pyroxene and Kaguya MI plagioclase spectral maps | 171 |
| 8.13 | Simplified subsurface stratigraphy at ROI 1 | 172 |
| 8.14 | FeO and TiO ₂ contents derived from Clementine 400 m/pix data | 173 |
| 8.15 | FeO abundances of mare deposits derived from Kaguya MI 60 m/pix data | 174 |
| 8.16 | NRC (2007) science concepts and goals in case of robotic exploration mission with rover and lander assets to the lunar surface | 175 |
| 8.17 | NRC (2007) science concepts and goals in case of robotic exploration mission to the lunar surface with a rover, lander, and sample return capability | 176 |

LIST OF TABLES

| | | |
|-----|---|-----|
| 1.1 | List of National Research Council (NRC, 2007) science concepts and goals of lunar exploration | 12 |
| 4.1 | List of instruments | 27 |
| 4.2 | The production function coefficients for different chronology models on the Moon and Mercury | 35 |
| 4.3 | Lunar chronostratigraphic system with relative and absolute ages (Neukum, 1983) | 38 |
| 4.4 | Mercurian chronostratigraphic system with relative and absolute ages (Spudis & Guest, 1988) | 38 |
| 5.1 | Derived absolute model ages of lunar basins using the buffered non-sparseness correction, ranked by $N(20)$ frequency | 49 |
| 5.2 | Derived absolute model ages of lunar basins using the buffered non-sparseness correction, ranked by model age | 50 |
| 6.1 | Parameters used for equations (1) and (2) on the Moon and Mercury | 68 |
| 6.2 | Certain and probable impact basins on Mercury, $D \geq 300$ km | 72 |
| 6.3 | Tentative impact basins on Mercury, $D \geq 300$ km | 74 |
| 6.4 | AMA intervals for Pre-Tolstojan and Tolstojan basins | 85 |
| 7.1 | Summary table of concept of operations | 103 |
| 7.2 | NRC (2007) goals addressed with the addition of notional instrumentation to the LER | 105 |
| 7.3 | Summary of minimum sample masses collected for traverses at each site in this study | 107 |
| 7.4 | Sample masses per landing site calculated using a sampling rate of 2.3 kg per crew member per EVA hour (Kring, 2007) | 107 |
| 7.5 | Communication coverage at landing sites utilizing a relay in a halo EM-L2 configuration | 108 |
| 7.6 | Direct and science traverse lengths with respect to 'safe' driving distance with the LER tele-operated from EM-L2 | 113 |
| 8.1 | Crater statistics of craters ≥ 70 m in diameter at within the three ROIs | 159 |
| 8.2 | Rock abundance (in areal %) based on LRO Diviner 236 m/pix data | 162 |
| 8.3 | Regolith thickness (m) estimated using concentric craters (CC) | 169 |

| | | |
|-----|---|-----|
| 8.4 | FeO and TiO ₂ weight percent (wt%) of mare deposits based on 400 m/pix Clementine data | 174 |
| 8.5 | FeO weight percent (wt%) of mare deposits based on Kaguya MI 60 m/pix global dataset | 174 |

CHAPTER 1

THE BASICS OF IMPACT CRATERING AND LATE ACCRETION MODELS

1.1. Significance of Impact Cratering

Impact craters are the most common landforms on planetary surfaces throughout the Solar System. However, the completeness of the cratering record is greatly affected by the rate of geologic activity and the presence of the atmosphere on the planetary body. Earth, Venus and Mars are geologically active planets at different time-scales and have significant atmospheres which modify their surface. Therefore, these planets are not suitable candidates to evaluate the early bombardment history of the inner Solar System. Nonetheless, airless bodies with low or moderate rate of surface modification are providing the best cratering records. Consequently, the lunar and mercurian cratering record may provide valuable information about the origin, rate and timing of the impacting projectiles and the late accretion history of the inner Solar System.

1.1.1. Impact Crater Formation

Hypervelocity impacts tend to occur in various sizes from micrometeoritic bombardment to giant, planet-sized impacts. The velocity of such impacts vary depending on the location in the Solar System: In the asteroid belt impacts occur on average with 5 kms^{-1} (Bottke et al., 1994), in the Earth-Moon system the impactor velocities increase between $15\text{-}25 \text{ kms}^{-1}$ (Le Feuvre & Wieczorek, 2011; Oberst et al., 2012), and reaches up to 42.5 kms^{-1} on Mercury (Le Feuvre & Wieczorek, 2011). The physics of impact cratering has been described with three stages: (1) contact and compression, (2) excavation, and (3) modification, however, in reality these processes continuously grade into another (e.g., Ahrens & O'Keefe, 1972, 1977; Melosh, 1989; Pierazzo et al., 1997; French, 1998; Wünnemann et al., 2016).

First, during the *contact and compression stage* (Figure 1.1/a-b) the projectile contacts the target's surface, and penetrates it to a depth about one or two projectile diameters. In this stage kinetic energy from the projectile to the target is transferred, while shock waves are generated through the projectile and the target with several tens (5-50 GPa) or even hundreds of gigapascals that drops rapidly with increasing distance in the target. While the shock waves travel in the materials irreversible mechanical and physical effects occur, such as deformation, solid-state phase transformation, melting or vaporization. When the shock wave reaches the free surface, the energy is released in the form of a rarefaction wave, which unloads the material from high shock pressures. However, certain fraction of energy remains as internal energy and induces melting or even vaporization of both the projectile and target materials. The duration

of this stage depends on the size, composition and the velocity of the projectile, but lasts typically between 10^{-3} s and 1-2 s.

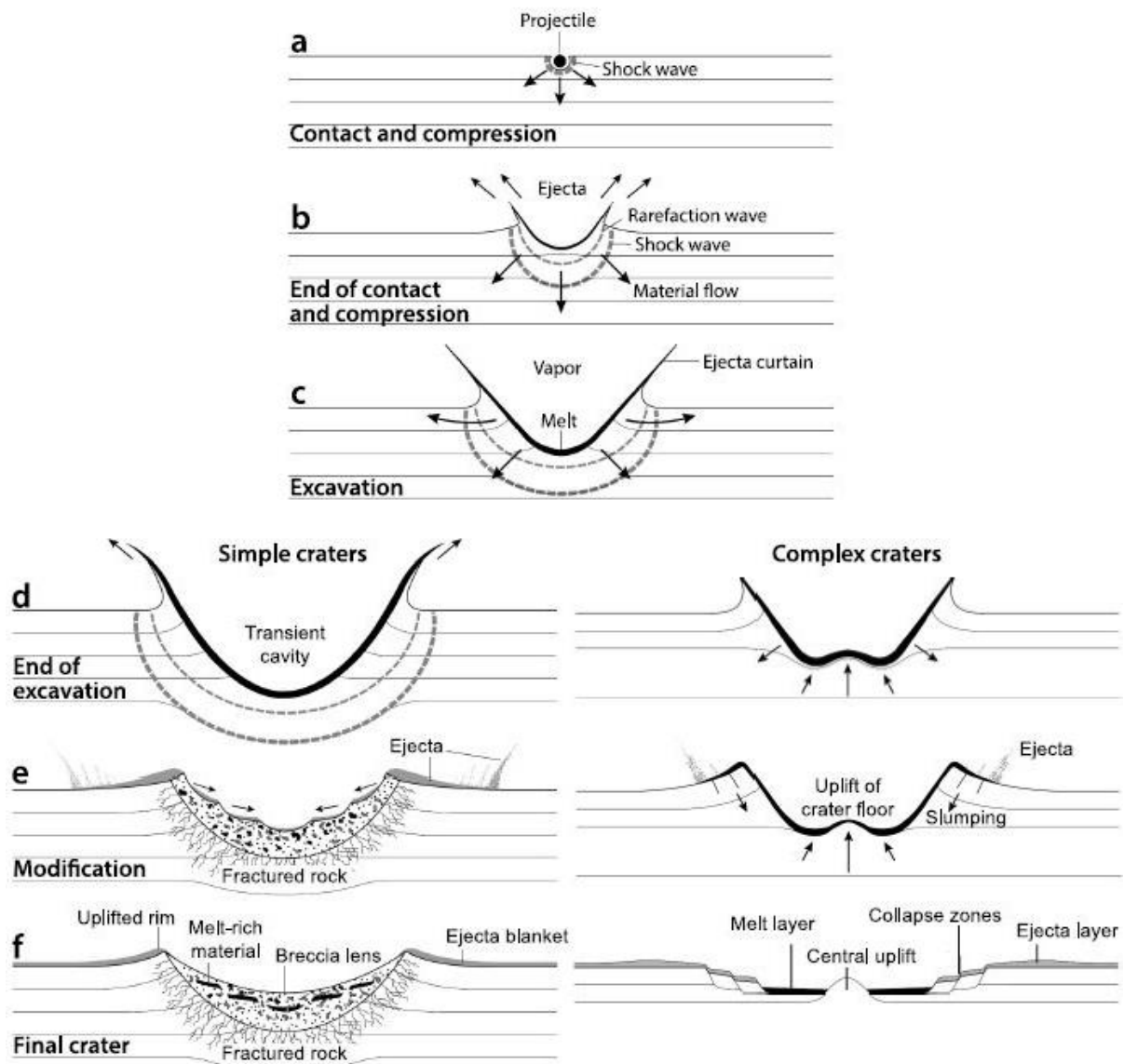


Figure 1.1: Schematic illustration of the different stages of simple and complex crater formation (modified after French, 1998 in Hamann, 2017). a-b) contact and compression, c-d) excavation, and e-f) modification stage of impact crater formation process. Depending on the gravity of the target body, and the size of the transient crater, a simple or a complex crater will form. See the complexity of craters in Figure 1.2.

The subsequent *excavation* stage (Figure 1.1/c-d) begins with the opening of a transient crater cavity and ejection of material upward and outward in ballistic trajectories. As more and more material is excavated, an ejecta curtain forms and

deposits material onto the target's surface. Depending on the projectile size, gravity and the target's strength, the duration of this stage requires between seconds and minutes until completion. The following step is the *modification stage* (Figure 1.1/e-f) which begins after the transient crater reaches its maximum size and finally collapses under the effect of the target's gravity. There are two main competing processes: (1) gravitational collapse of the inner rim, and (2) uplift of the transient crater floor. The modification stage might take from several minutes (simple crater) to millions of years (complex crater) to be completed, where isostatic rebound and/or post-impact volcanism might slowly effect the large craters and basins.

1.1.2. Simple to Complex Crater

Depending on the gravity and the rheological properties of the target, as well as the size of the transient crater, a simple or a complex crater with a central peak, peak-ring or multi-ring basin will form (Figure 1.2) (e.g., Pike, 1988; Melosh, 1989; French, 1998; Osinski & Pierazzo, 2012). Additionally, basins between complex craters with central and peak-ring are called as proto-basins (Pike, 1988). Simple craters are circular, bowl-shaped depressions with raised rims, which show loose debris formed by the avalanche of fragmented material from the transient crater walls (Figure 1.2, Lichtenberg B crater). Complex craters with central peak (Figure 1.2, Tycho crater) exhibit central structural uplifts from the depth of the crust and have slumped terraces. Complex craters with one (Figure 1.2, Apollo basin) or multiple inner rings (Figure 1.2, Orientale basin) show uplifted, central ring structures, which originate from the depth of the crust/mantle boundary. Complex crater with one or multiple inner ring structures are commonly filled with post-impact volcanic material. However, the transition from simple to complex crater is inversely proportional to the gravity of the target body (Melosh, 1989). On Earth, complex craters form from 2 – 4 km diameter (2 km for sedimentary target rocks, 4 km for crystalline target rocks, Pike, 1980), on the Moon from 15 – 20 km diameter (Pike, 1980; Osinski & Pierazzo, 2012), on Mars around 7 km diameter (Pike, 1980; Werner & Ivanov, 2015), while on Mercury around 11 km diameter (Pike, 1980, Werner & Ivanov, 2015). The main focus of this PhD thesis is on large impact basins ($D \geq 300$ km) with peak-ring and multi-ring impact structures on the Moon and Mercury.

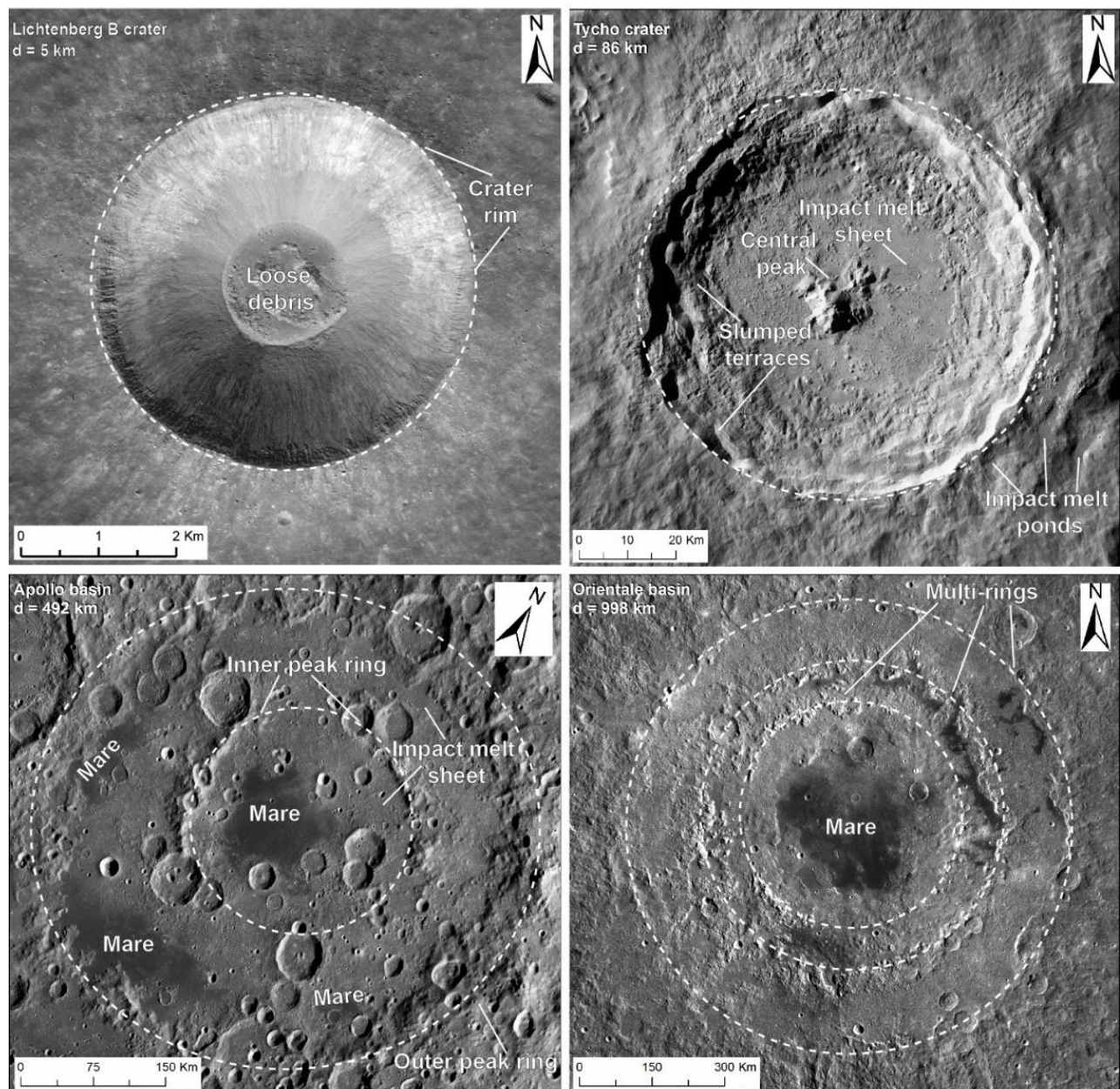


Figure 1.2: Transition from simple to complex impact craters on the Moon. Lichtenberg B crater is a simple crater with 5 km in diameter. Image from Lunar Reconnaissance Orbiter Camera Narrow Angle Camera (LROC NAC, 1 m/pix). Tycho crater is an 86 km diameter complex crater with a central peak. Apollo basin is a 492 km diameter inner peak-ring basin. Orientale basin with 998 km in diameter is the youngest multi-ring basin. Images from Lunar Reconnaissance Orbiter Camera Wide Angle Camera (LROC WAC, 100 m/pix).

1.1.3. Impact Generated Lithologies

The impact cratering process generates a wide variety of distinctive impact rocks, minerals, and glass by vaporizing, melting and shock metamorphosing the target material with high pressure and temperature (Osinski & Pierazzo, 2012). The impact rocks can be distinguished resulting from a single impact (terrestrial impact-related rocks) and those from multiple impact (lunar impact-related rocks) events (Figure 1.3). These impact rocks can be sub-divided and classified into groups recommended by International Union of Geological Sciences (IUGS; Stöffler and Grieve 2007):

I. CLASSIFICATION OF IMPACTITES FROM SINGLE IMPACTS

- 1.1. Proximal impactites: form at or within few crater radii from the crater rim
 - 1.1.1. Shocked rocks: are non-brecciated rocks with various stages of shock metamorphic effects
 - 1.1.2. Impact melt rocks: are sub-divided according to the amount of clasts within impact melt
 - 1.1.2.1. clast-rich
 - 1.1.2.2. clast-poor
 - 1.1.2.3. clast-free
 - 1.1.3. Impact breccias: are mixed with various target lithologies
 - 1.1.3.1. Monomict breccia: is brecciated single lithology target
 - 1.1.3.2. Lithic breccia: is polymict breccia without melt inclusions
 - 1.1.3.3. Suevite: is polymict breccia with melt inclusions
- 1.2. Distal impactites: form far from the crater rim
 - 1.2.1. Consolidated
 - 1.2.1.1. Tektites: are centimeter-sized, splash-formed molten glasses in black, green, brown or gray colors and contain very low amount of water and volatiles
 - 1.2.1.2. Microtektites: are millimeter-sized tektites
 - 1.2.2. Unconsolidated
 - 1.2.2.1. Air fall bed deposits

II. CLASSIFICATION OF IMPACTITES FROM MULTIPLE IMPACTS

- 2.1. Unconsolidated clastic impact debris
 - 2.1.1. Impact regolith
- 2.2. Consolidated clastic impact debris
 - 2.2.1. Shock lithified impact regolith
 - 2.2.1.1. Regolith breccias: form *in situ* formed matrix melt and melt particles
 - 2.2.1.2. Lithic breccias: are without matrix melt and melt particles

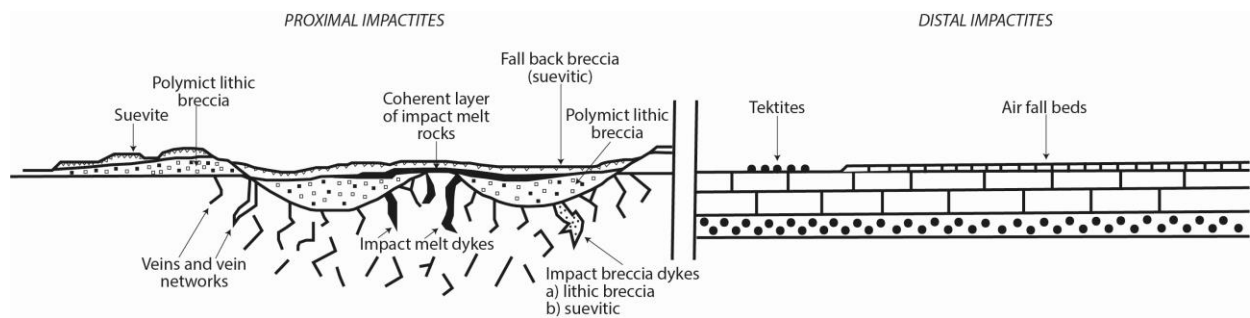


Figure 1.3: Variety of impact rocks form the proximal and distal impactites. Figure modified from Stöffler and Grieve (2007).

Impact melt-bearing rocks on the lunar surface record the history of multiple impact events. They generally form melt pool and impact melt dykes inside the crater (Figure 1.3) or melt ponds close to the crater rim in a wide range of crater sizes. The hot impact melt may mix with colder rocks and mineral fragments in different volumes, which cause the rapid cooling and solidification of the melt. The resulting product is called impact melt breccia, which can be clast-rich and clast-poor.

1.1.4. Radioisotopic Dating of Impact Melt Rocks

Impact melt rocks are used to date the absolute age of lunar samples and meteorites. The impact history is recorded in the radiogenic clocks of impact melts. The method uses the naturally occurring isotope of an element and compares the abundances of its decaying nucleus (“parent nuclide”) and the corresponding decay product (“daughter nuclide”), which forms at a constant decay rate. A radioactive nuclide decays exponentially at a given rate, with the decay rate being described by the half-life of the isotope, means the time to reduce the isotope’s initial quantity to half. Radiometric dating methods for impact melt rocks include U-Pb, Rb-Sr, Sm-Nd, and K-Ar, (e.g., McDougall & Harrison 1999; Flude et al. 2014; Jourdan et al. 2014; Wartho et al. 2014). The results derived from the K-Ar method were used to initially date the lunar rock samples and derive the chronology of the Moon (Neukum, 1983 and references therein). The parent nuclide (^{40}K) of the K-Ar radioisotopic technique has a half-life of 1.25 Ga, and thus capable to determine the age of impact events happened billions of years ago. The radioactive isotope of potassium, ^{40}K , decays to the isotope of argon, ^{40}Ar . Another widely used dating method is the ^{39}Ar - ^{40}Ar technique, which is related to the K-Ar technique. Ar is a noble gas, which builds up inside mineral crystals over time. However, the crystal’s structure is sensitive to high temperatures and argon can easily escape by subsequent re-melting events, such as impacts. Consequently, primary impact melts are exposed to a long-term impact gardening process (i.e. excavation, re-melting, burial, and re-excavation) by subsequent impacts resulting in a mixture of materials with various ages and origin of spatially distributed impact events (Liu et al., 2019). Thus, absolute age of most of the samples is difficult to assign to only one impact event.

1.2. Late Accretion Models

In order to reconstruct the early geologic history of planetary bodies, it is crucial to understand the impact processes modifying their surface. However, our understanding on the origin, rate and timing of the impacting projectiles is far from complete. The formation time of large impact basins ($D \geq 300$ km) are important to determine the early bombardment history after planetary accretion. This early history of the Solar System consists of the time period from the last giant collision events between planetary embryos to the late bombardment with smaller-sized projectiles between 4.5 to 3.8 Gyr. The main assumption is that potential projectiles could be asteroids from the Main Asteroid Belt (MAB), the hypothesized E-belt, – a largely extinct portion of the asteroid belt between 1.7 and 2.1 Astronomical Units (AU) –, comets, or even remnant ejecta fragments from the giant impact that formed the Moon (Kring & Cohen, 2002; Gomes et al., 2005; Strom et al., 2005; Morbidelli et al., 2010; Bottke et al., 2012; Bottke et al., 2015). These projectiles strike the planetary bodies and form impact craters that accumulate on the respective planetary surface. Consequently, older geologic terrains have higher crater densities in a given crater size range than younger surfaces. Thus, the population of impact craters can be used as chronometers and has long been used by the planetary community to estimate relative and absolute surface ages (Öpik, 1960; Baldwin, 1964; Neukum, 1983). There are two functions – “production function” (PF) and “chronology function” (CF) (Neukum, 1983) –, which were originally established for the Moon and used to describe the population of craters forming through time on a planetary surface. The PF is a polynomial of degree eleven created by measuring the impact crater size-frequency distributions (CSFD) on various, geologically undisturbed areas. However, the behavior of the shape of the PF over time is heavily debated.

There are two major hypotheses regarding the shape of the PF. First, the radiometric age results of K-Ar dating of the returned samples from the Apollo and Luna missions revealed the presence of a peak age centered at ~ 3.87 Gyr (Stöffler et al., 2006). This result led to the hypothesis of one or multiple lunar cataclysmic events with a larger peak around 3.9 Gyr when the impact flux rapidly increased and lasted for less than 200 Myr (Tera et al., 1974) (Figure 1.4). However, the peak age in the distribution of collected samples was well-known to be related to the formation age of the Imbrium basin around 3.9 Gyr (Tera et al., 1974). At the same time, the analysis of the lunar meteorites, which represent random samples from the lunar surface, does not show any peak in the distribution of K-Ar ages, thus, the lunar meteorites do not support the lunar terminal cataclysm hypothesis (Hartmann, 2003; Stöffler et al., 2006; Michael et al., 2018). Another similar hypothesis from Ryder (1990) and Ryder (2002) suggested that the cataclysm also termed as Late Heavy Bombardment (LHB) was short, unimodal with a rapidly increasing impact flux at ~ 3.9 Gyr (Figure 1.4). They suggest that all the large impact basins were formed during the LHB. These early results argued that different impactor populations bombarded the lunar surface and the shape of the PF changed over time.

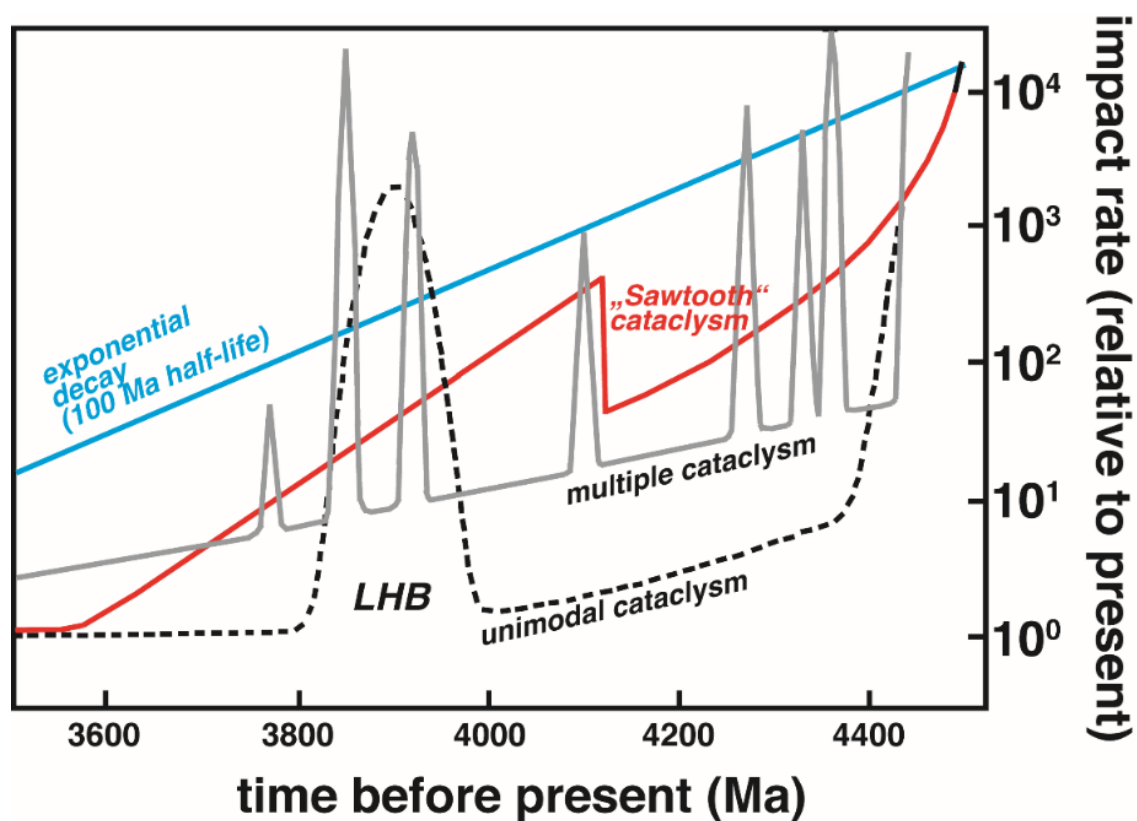


Figure 1.4: Different late accretion models including one and multiple impactor populations to explain the early lunar bombardment history. The one impactor population model (blue solid line) explains the exponential decay of impactors over time (e.g., Neukum, 1983; Neukum & Ivanov, 1994; Hartmann, 1995). Tera et al. (1974) suggested multiple cataclysm scenarios with several increased bombardment episodes. The Late Heavy Bombardment (LHB) or lunar cataclysm model (black dashed line) is the „classical“ view of the unimodal cataclysm, which represents a rapidly increasing impact flux at 3.9 Gyr (Ryder, 1990, 2002). Morbidelli et al. (2012) proposed the “sawtooth” cataclysm (red solid line), which is a relatively weaker cataclysm with an uptick in the impact flux at 4.1 Gyr. Figure modified after Hopkins & Mojzsis (2015).

Second, a number of publications suggested that the impact rate using crater density analysis can be described by a smoothly decaying impact flux (Figure 1.4) (Baldwin, 1974; Hartmann, 1975; Neukum, 1983; Neukum & Ivanov, 1994; Hartmann, 1995). They proposed that the Moon and other planetary bodies in the Solar System were bombarded with only one impactor population and argued that the PF did not change over time. However, the same size-frequency distribution of impactors could also be explained by collisionally evolving different impactor populations (Bottke et al., 2005). Later, Bottke et al. (2007) argued that the late timing of basin formation (~ 3.9 Gyr) with the decay of accretion leftovers are hard to reconcile.

In the early 2000's, after the discovery of the first extrasolar gas giant around a main-sequence star well inside the orbit of Mercury (Mayor & Queloz, 1995), dynamical models attempted to describe exoplanets with high eccentricities and few days of orbital periods (e.g. Zakamska & Tremaine, 2004). Numerical simulations of orbital mechanics were adapted to our Solar System called as the Nice model, which gave additional support to the LHB (Gomes et al., 2005; Tsiganis et al., 2005; Morbidelli et al., 2005). The initial Nice model is a dynamical simulation where Jupiter and Saturn crossed their mutual 1:2 mean motion resonance and their orbits became eccentric. This change in the resonance between the two planets led to the destabilization of the cometary projectiles in the Kuiper Belt beyond the orbit of Neptune and effected the asteroids in the MAB between Jupiter and Mars. The migration of the giant planets in the numerical simulations occurred around 3.9 Gyr and lasted over few tens of millions of years. An updated version of the Nice model predicts that the migration of the giant planets destabilized the MAB and the hypothesized E-belt, and injected projectiles into the inner Solar System around 4.1 Gyr (e.g., Bottke et al., 2012, Morbidelli et al., 2012). Morbidelli et al. (2012) suggested an exponentially decaying impact flux with a weaker uptick in the impact flux around 4.1 Gyr (Figure 1.4), which is nearly identical to the proposed model by Neukum (1983) and Neukum & Ivanov (1994) from 4.1 Gyr until today.

Strom et al. (2005, 2011, 2015) investigated the crater populations on the terrestrial bodies and proposed two different impactor populations: Population 1 and Population 2. They suggested that Population 1 impactors from the MAB formed the oldest, heavily cratered surfaces on Mercury, Moon and Mars during the LHB. They predicted that LHB began sometime before ~ 3.9 Gyr and lasted ~100 to 300 Myr. Subsequently, near-Earth objects (NEOs) dominated the Population 2 impactors that cratered younger lightly cratered terrains after 3.8 – 3.7 Gyr. Based on the CSFDs, they argued that a transition in impactor populations occurred between 3.9 – 3.8 Gyr. These results were supported by a later CSFD study by Head et al. (2010). Head et al. (2010) determined two different populations of impactors with a transition during the Imbrian period at less than 3.9 Gyr, close to the formation time of the Orientale basin. Their conclusions were mainly based on the pre- and post-mare crater populations. In contrast to the study conducted by Head et al. (2010), Fassett et al. (2012b) normalized and summed the CSFDs of 30 key lunar basins assigned to the same chronostratigraphic period. Their results showed a change in impactor population prior mid-Nectarian period, which could be consistent with Morbidelli et al. (2012).

However, since Tera et al. (1974) proposed the lunar cataclysm hypothesis, it has become evident that the peak sample age around 3.9 Gyr could be the result of sampling bias. The reason for sampling bias is that the human and robotic missions collected Imbrium ejecta material from the upper layer of the lunar surface at different landing sites (e.g., Stöffler et al., 2006). Based on numerical modeling, the Imbrium basin ejecta could be hundreds of meters thick at the Apollo landing sites, which landing sites are spatially relatively close to one another (Haskin et al., 1998). Moreover, the peak sample age of Apollo 14 and 15 landing sites shows the prominent

domination of Imbrium basin ejecta. Furthermore, Apollo 16 and 17 sites have a much more complex geologic history, which were not only effected by the Imbrium ejecta, but Nectaris and Serenitatis basin materials, respectively. These older basin materials could have been excavated by subsequent impacts and mixed up with overlying Imbrium basin ejecta (Haskin et al., 1998, Michael et al., 2018, Liu et al., 2019). Michael et al. (2018) summarized the radiometric ages of 269 Luna and Apollo impact melt rocks and analyzed the data on histograms and relative probability plots, and concluded that the distribution of ages not only show a peak at 3.87 Gyr, but also several secondary peaks between 3.87 and 4.25 Gyr. Consequently, the distribution of K-Ar ages are inconsistent with the lunar cataclysm hypothesis (Tera et al., 1974; Ryder, 1990, 2002). Additionally, Liu et al. (2019) used numerical modelling to predict the survival probability and relative abundance of basin melt occurrence at the Apollo and Luna landing sites. They found that Imbrium and Crisium impact melt is dominant at historical landing sites, consistent with the K-Ar radiometric dates. Whereas, due to the long-term impact gardening, Serenitatis basin melt at Apollo 17 landing site is less abundant and may not be collected by the astronauts (Spudis et al., 2011). Consequently, the lunar cataclysm hypothesis is still a strongly debated topic in lunar science and discussed in chapter 5 and 6.

1.3. Science Enabled by Future Human and Robotic Exploration Missions to the Moon

After a long break in lunar exploration, the release of the Vision for Space Exploration (VSE) (2004) brought back the focus for lunar science. The VSE originally envisioned a step-by-step plan for the United States (US), which planned to develop the capabilities to ultimately establish a human outpost by 2020 on the lunar surface and enable technologies to move forward to explore the Solar System in a sustainable fashion. Later, the Global Exploration Roadmap (GER) developed by the International Space Exploration Coordination Group (ISECG, 2013, 2018) communicates the effort of the international community to explore the Solar System, which begins with the activities in the International Space Station (ISS), continuing to the lunar vicinity and, eventually, leading to human missions to Mars. Additionally, GER generates a framework for inter-agency discussion and collaboration to address high-priority scientific questions in the overall strategic vision. Several documents including the Lunar Exploration Roadmap developed by the Lunar Exploration Analysis Group (LEAG, 2016), the Advancing Science of the Moon: Report of the Specific Action Team released by the LEAG (2017), and the Lunar Science for Landed Missions Workshop Findings Report (Jawin et al., 2019) build upon the US National Research Council (NRC, 2007) report, which provides guideline on the scientific challenges and opportunities enabled by sustainable robotic and human exploration of the Moon. These missions will include extensive field studies and sample-return capability, which will address broad areas of scientific research. The NRC (2007) report prioritizes eight science concepts (Table 1.1) and goals of lunar exploration. The overarching themes

cover various aspects of the early Earth-Moon evolution, planetary accretion and differentiation, impact history, and lunar environment. The eight prioritized science concepts are:

1. The bombardment history of the inner Solar System is uniquely revealed on the Moon.
2. The structure and composition of the lunar interior provide fundamental information on the evolution of a differentiated planetary body.
3. Key planetary processes are manifested in the diversity of lunar crustal rocks.
4. Lunar volatiles increase our understanding of the composition state and distribution of volatiles in the lunar polar regions.
5. Lunar volcanism provides a window into the thermal and compositional evolution of the Moon.
6. The Moon is an accessible laboratory for studying the impact process on planetary scales.
7. The Moon is a natural laboratory for regolith processes and weathering on anhydrous airless bodies.
8. Processes involved with the atmosphere and dust environment of the Moon are accessible for scientific study while the environment remains in a pristine state.

Additionally, the NRC committee has identified and ranked 35 specific science goals (a-e) within respective science concepts (Figure 1.5). This committee ranked and evaluated the scientific merit of these science goals, as well as possibilities to achieve these with near-term technological readiness (see also LEAG, 2016).

The main science questions of this PhD thesis focus on the highest ranked science Concept 1 of the NRC (2007). The overarching science objective of Concept 1 is to characterize and determine the early and recent impact flux of the inner Solar System. Concept 1 addresses questions on the importance of large impact events in the evolution of terrestrial planets and satellites, and the role of these early impacts on the habitability of Earth. The correlation between radiometric ages of lunar impact melt rocks and crater densities served as the basis for estimating surface ages on the Moon and other planetary bodies. Concept 1 includes five specific science goals from which the first three (1a, 1b, 1c) are listed as the highest-ranking lunar science goals among all 35 specific science goals together. The five science goals of Concept 1 are:

Table 1.1. List of National Research Council (NRC, 2007) science concepts and goals of lunar exploration.

| NRC Concept/Goal | a | b | c | d | e |
|---|--|---|---|---|--|
| 1. Bombardment history of the inner Solar System | Test cataclysm hypothesis | Age of South Pole-Aitken basin | Establish absolute chronology | Recent impact flux | Secondary craters |
| 2. Structure and composition of lunar interior | Thickness/variability of lunar crust | Stratification of mantle | Size, composition, state of core | Thermal state of interior | N/A |
| 3. Diversity of lunar crustal rocks | Differentiation products | Age, distribution, origin of rocks | Composition of lower crust | Complexity of lunar crust | Extent/structure of megaregolith |
| 4. Lunar poles and volatiles | State and distribution of volatiles | Source of volatiles | Transport, alteration, loss, processes | Properties of polar regolith | Polar regolith and ancient solar environment |
| 5. Lunar volcanism | Origin/variability of basalts | Age of mare basalts | Range/extent of pyroclastic deposits | Lunar volcanic flux | N/A |
| 6. Impact processes | Melt sheet differentiation | Structure of multi-ring impact basins | Crater formation | Mixing of local and ejecta material | N/A |
| 7. Regolith processes | Ancient regolith | Physical properties of regolith | Regolith modification processes | Rare minerals in regolith | N/A |
| 8. Atmosphere and dust environment | Density, composition, and time-variability of atmosphere | Size, charge, and spatial distribution of electrostatically transported dust grains | Time-variable release of ^{40}Ar and radon | Release of water vapour and other volatiles | N/A |

1a. Test the cataclysm hypothesis by determining the spacing in time of the creation of lunar basins. The impact history before 3.0 Gyr has large uncertainties, when the impactor flux was much higher and rapidly decreasing. During that time the large lunar basins were formed with unknown spacing in time. Using the currently available datasets, it is challenging to decide whether a cataclysm occurred and how rapidly the cratering rate declined. In order to verify this question, exploration missions with sample return capability to key impact basins (e.g., South Pole-Aitken Basin (SPA) and subsequent major impact basins within SPA, Nectaris, Crisium, Orientale, Moscoviense, Birkhoff, Humboldtianum) in combination with high-resolution images, topography and gravity datasets are required to resolve this issue.

1b. Anchor the early Earth-Moon impact flux curve by determining the age of the oldest lunar basin (South Pole-Aitken Basin). SPA Basin is the largest and deepest impact structure on the Moon, however, its absolute age is not well constrained due to the absence of samples. The oldest multi-ring basins are important calibration points for the lunar chronology curve and also other planetary surfaces. High-resolution images and topography datasets are essential to provide absolute model age using crater statistics and returned samples from various locations in the SPA to provide anchor points for the chronology curve.

1c. Establish a precise absolute chronology. An absolute lunar chronology is constrained from the combination of lunar crater counts using high-resolution images, and radiometric ages of returned samples from several key benchmark craters, old basins, and volcanic features from the lunar surface. A well-calibrated lunar chronology can be applied to constrain models to date other planetary surfaces.

1d. Asses the recent impact flux. The Moon has the best impact record, which includes the imprints of recent projectile flux in the Earth-Moon system over the past ~ 3.5 Gyr. The questions are whether this flux has been constant, or exhibit shorter-term fluctuations. The variability in the recent lunar and terrestrial impact flux may be related to asteroid breakups and changes in dynamics in the asteroid belt. In order to derive precise estimates of the recent impact flux, determining crater populations on known young surfaces using high-resolution images, constant imaging the lunar surface and radiometric ages of lunar soil spherules are important.

1e. Study the role of secondary impact craters on crater counts. New studies on young impact craters revealed surprisingly large number of secondary impact craters around Zunil crater on Mars, and argued that large number of small impact craters on the Moon could be secondaries as well. If true, the flux of small primary impact craters might have been overestimated. Detailed studies of young lunar impact craters and the distribution of their secondary impact craters using high-resolution images could help to better constrain the effects on crater statistics, thus, understand the process of secondary impact cratering.

This Ph.D. work addresses mainly science goals 1a and 1b. To achieve these goals, the NRC committee identified possible means of implementation including *remote sensing observations* (e.g., crater counts of benchmark terrain using high-resolution images, geologic mapping), *targeted orbital measurements* (e.g., high-resolution images of specific terrains), *in-situ analyses on the lunar surface with specific instruments* (e.g., development of in-situ instrumentation for dating planetary surfaces), *sample-return mission with robotic assets* (e.g., sample return from the

impact-melt sheet of SPA, and subsequent basins, from young basalt flows, and from benchmark craters (e.g., Copernicus and Tycho)), and *human field work* (e.g., field observations provide critical geologic context, and human interaction improves chances of obtaining best/most appropriate samples). However, the minimum requirement to solve the impact bombardment history of the Earth-Moon system and re-calibrate the lunar chronology curve might be only possible by returned samples from several key geologic features enabled by exploration missions. Thus, this dissertation is investigating possible landings sites in chapter 7 and 8, where most of the science goals could be addressed for early decisions in system design and operations planning for human and robotic activities on the lunar surface.

2.1. Research Framework of This Thesis

This Ph.D. thesis focuses on the early bombardment history of the inner Solar System and how future human and robotic exploration missions with sample return capability to the lunar surface could enhance our understanding about the origin, nature and timing of impacting projectiles. This work was carried out within the framework of the Transregional Collaborative Research Center TRR 170 Berlin-Münster: Late Accretion onto Terrestrial Planets (LATP) (SFB/TRR-170, A3) project in the Planetary Sciences and Remote Sensing Group at the Freie Universität Berlin.

The goal of this research program is to use a multidisciplinary approach to constrain the timing and rates (Project A, A1-A4), chemical budget (Project B, B1-B5), and geodynamic processes (Project C, C1-C6) of the late accretion history of the terrestrial planets (Earth, its Moon, and other terrestrial planets). The project utilizes various expertise in planetary remote sensing, planetary physics, geodynamic modelling, cosmochemistry and geomaterial sciences.

Project area A provides novel understanding about the timing and rate of late accretion of the terrestrial planets. The Moon and its cratering record is in the focus, because it has been used to calibrate the absolute age of planetary surfaces. The main goal is to test different late accretion models describing the impact flux from 4.5 to 3.5 Gyr and test the lunar chronology model. The interdisciplinary approach combines the obtained results from isotopic ages of lunar impact rocks derived with multiple geochronometers (relation to Project area B), newly calculated crater size-frequency distributions (CSFDs) to obtain absolute model ages (AMA) of large lunar basins (e.g. Nectaris, Imbrium, Serenitatis) including South Pole-Aitken basin using remote sensing data, as well as the numerical simulations of basin formation and ejecta distribution (relation to Project area C). **Project area B** contributes to better constrain the genetic link of late-accreted material (the 'late veneer') to meteorites, its chemical composition, and the extent of volatile delivery to the Earth and Moon system (relation to Project area C), if a late veneer played a role after planetary accretion. **Project area C** investigates the significance and the effect of 'late veneer' delivery to the thermodynamic evolution, and differentiation of the Earth, Moon and other terrestrial planets. The main objectives are to investigate the boundary conditions of the giant impact and subsequent impacts on the magma ocean and the segregation of metal-sulfide-silicate melt during late accretion and core formation (relation to Project area B).

2.2. Scientific Objectives and Motivation

The SFB/TRR-170 A3 subproject *primarily aims* to test various accretion models and improve the lunar production function (PF) by re-evaluating its shape to infer potential impactor populations. Our understanding on the origin, rate and timing of the impacting projectiles is far from complete. Since the Apollo and Luna missions brought lunar samples back to Earth, there is an ongoing discussion about whether the shape of the PF has changed over time, and if so, at what time it has transitioned. If the PF remained unchanged, that the obtained AMAs of large lunar basins ($D \geq 300$ km) are accurate and confirm one impactor population. However, if the PF has changed over time, that would affect the AMA of impact basins and imply for different impactor populations. Moreover, the potential existence of multiple impactor populations supports the theory about the Late Heavy Bombardment (LHB) around 3.9 – 4.1 Gyr, which would have a significant influence on the surface development and the distribution of volatiles in the inner Solar System. Still, geologic processes could greatly modify the cratering record, thus can subsequently influence the CSFD results, which are the key features to understand the behavior of the PF and the nature of impactor populations.

The second aim of the project is to investigate the crater and impactor populations on other terrestrial planets, such as Mercury, because it has one of the best-preserved impact records in the inner Solar System due to the absence of an atmosphere and relatively unmodified ancient surface. If the one impactor population model was correct, and the planetary bodies were bombarded with the same impactor population, then, comparing the crater and impactor population of the Moon with Mercury is crucial to understand the early bombardment history of the inner Solar System.

The third aim is to find potential key landing sites for future human and robotic exploration missions with sample return capability to the lunar surface, which could target key sampling locations in order to refine the lunar chronology model, and thus, the AMAs of different geologic units on the Moon and other terrestrial planets. The National Research Council (NRC, 2007) Concept 1 addresses the highest ranked science goals about the bombardment history of the Solar System, thus it will remain in focus for future exploration activities.

The main research questions (Q) of this thesis are:

Q1. What is the timing, and nature of basin-forming impacts on the Moon and other terrestrial planets?

Q2. What is the origin of late-accreted materials?

Q3. Where are the key landing sites for future human and robotic exploration missions and how many NRC (2007) objectives could be addressed there?

The following scientific objectives (O) and steps are necessary to address these questions:

O1. Understanding the history of cratering populations on the lunar and mercurian surface,

- Re-examine the population of large impact basins ($D \geq 300$ km) on the Moon and Mercury using Geographic Information System (GIS).
- Map the crater populations related to respective basins on the Moon and Mercury.

O2. Investigating the origin of impactors and whether the impactor population size-frequency distribution changed over time and if so, when,

- Analyze the shape of the summed CSFDs of basins from the same chronostratigraphic period on the Moon and Mercury using a relative plot.

O3. Analyzing the influence of non-sparseness correction measurement technique on the CSFDs on the Moon and Mercury,

- Derive the CSFDs using 2 different approaches: (1) Buffered Crater Counting (BCC) – as done by previous studies, and the new approach (2) Buffered Non-Sparseness Correction (BNSC). Derive the $N(20)$, i.e., the frequency of craters ≥ 20 km on the Moon, and $N(25)$ on Mercury and normalize these to an area of 10^6 km².
- Compare the results of different techniques applied systematically to different key regions on the Moon and Mercury.
- Derive the spatial densities of basins and craters on the Moon and Mercury.

O4. Studying how large-scale resurfacing events affect the shape of ancient CSFDs,

- Measure the effect of crater obliteration on ancient CSFDs.
- Study the effect of volcanism and other possible processes on the CSFDs and the spatial distribution of basins.

O5. Analyzing the saturation state of the lunar and mercurian basins,

- Compared the fraction of the original and the BNSC modified count area sizes for each basin to its $N(20)$ and $N(25)$ crater frequencies on the Moon and Mercury, respectively.

O6. Refining the lunar and mercurian basin stratigraphy and their AMAs,

- To compare the crater densities of mercurian basins with the lunar basins, rescale the values of $N(20)$ Moon, to $N(X)$ Mercury.
- Derive AMAs of large basins on the Moon and Mercury using different chronology models.

- Study the relationships of the crater densities and AMAs to stratigraphic observations and compare with previous studies.

O7. Characterizing potential landing sites for future human and robotic exploration missions with sample return capability and investigating how these missions could test the cataclysm hypothesis.

- Study the potential exploration of the South Pole-Aitken basin including the south polar region of the Moon, a region that has not been visited by any human missions, yet exhibits a multitude of scientifically important locations.
- Explore the feasibility of tele-robotic operation of two Lunar Electric Rovers (LER) between five human lunar landing sites, and identify potential high interest sampling locations en-route using various datasets (e.g. optical, topographical and spectral).
- Plan sample collection activities and return traverses for each individual human landing site across key geologic terrains.
- Design exploration at and between human landing sites to address a suite of National Research Council (NRC, 2007) scientific concepts and goals.

CHAPTER 3

PERSONAL CONTRIBUTION AND STRUCTURE OF THIS THESIS

This Ph.D. thesis was written within the framework of the SFB/TRR-170, A3 subproject and was funded by the Deutsche Forschungsgemeinschaft (DFG). The scientific programme was carried out within the Interdisciplinary Graduate Programme of the Integrated Research Training Group in Planetary Sciences. This Ph.D. thesis represents a cumulative dissertation and comprises three published, peer-reviewed articles, one manuscript under preparation to a peer-reviewed journal, and one conference abstract. This dissertation was carried out with several colleagues and collaborators from Germany, United States of America, United Kingdom, Finland, The Netherlands, and Russia. The results were presented in oral and poster contributions at several international conferences, team meetings and workshops.

3.1. Personal Contribution

The three published, peer-reviewed articles, one manuscript under preparation, and one conference abstract form Parts II and III are:

1. **Orgel, C.**, Michael, G., Fassett, C. I., van der Bogert, C. H., Riedel, C., Kneissl, T., & Hiesinger, H. (2018). Ancient bombardment of the inner Solar System – Reinvestigation of the "fingerprints" of different impactor populations on the lunar surface. *Journal of Geophysical Research*, 123, 748–762, <https://doi.org/10.1002/2017JE005451>
2. **Orgel, C.**, Fassett, C. I., Michael, G., Riedel, C., van der Bogert, C. H., & Hiesinger, H. (2020). Re-examination of the population, stratigraphy, and sequence of mercurian basins: Implications for Mercury's early impact history and comparison with the Moon. *Journal of Geophysical Research*, 125, e2019JE006212. <https://doi.org/10.1029/2019JE006212>
3. Allender, E. J., **Orgel, C.**, Almeida, N. V., Cook, J., Ende, J. J., Kamps, O., Mazrouei, S., Slezak, T. J., Soini, A.-J., & Kring, D. A. (2018). Traverses for the ISECG-GER Design Reference Mission for humans on the lunar surface. *Advances in Space Research*, 63,(1), 692–727, <https://doi.org/10.1016/j.asr.2018.08.032>
4. **Orgel, C.**, Ivanov, M. A., Hiesinger, H., Prissang, R., Michael, G., van der Bogert, C. H., Pasckert, J. H., & Walter, S. H. G. Characterization of high-priority

landing sites for robotic exploration missions in the Apollo basin, Moon. Manuscript in preparation to *Planetary Science Journal*.

5. **Orgel, C.**, Ivanov, M. A., Hiesinger, H., Pasckert, J. H., van der Bogert, C. H., & Michael, G. (2018). Potential landing sites for the Chang'e-4 exploration mission to the Apollo basin, Moon. *6th European Lunar Symposium*, 14–16 May, Toulouse, France,
https://els2018.arc.nasa.gov/downloads/ELS_2018_Abstract_Booklet_08052018.pdf

Article 1 forms Chapter 5 and was conducted within the framework of SFB/TRR-170 project at the Freie Universität Berlin. The PhD candidate carried out the literature review, performed all data collection and analysis, interpreted and discussed the results, wrote the entire manuscript, prepared the figures and Appendix A, as well as managed the manuscript through the peer-review process under the supervision of Dr. Gregory G. Michael. Caleb I. Fassett provided his original dataset to perform the analysis for this manuscript. Thomas Kneissl provided his code to perform the data analysis in ArcGIS. All co-authors contributed to discussions and improved the language of the manuscript.

Article 2 forms Chapter 6 and was conducted within the framework of SFB/TRR-170 project at the Freie Universität Berlin and NASA Marshall Space Flight Center in Huntsville, Alabama, USA. The PhD candidate carried out the literature review, performed all data collection and analysis, interpreted and discussed the results, wrote the entire manuscript, prepared the figures and Appendix B, as well as managed the manuscript through the peer-review process under the supervision of Dr. Caleb I. Fassett and Dr. Gregory G. Michael. For the discussion Christian Riedel investigated the spatial basin asymmetry and Caleb I. Fassett performed Monte Carlo simulation (chapter 6.5.1). All co-authors contributed to discussions and improved the language of the manuscript.

Article 3 forms Chapter 7 and was carried out through the Center for Lunar Science and Exploration (CLSE) 2016 Exploration Science Summer Intern Program hosted by the Lunar and Planetary Institute (LPI) and Johnson Space Center (JSC). Elyse J. Allender, Csilla Orgel, Natasha V. Almeida, Jessica J. Ende, Oscar Kamps, and Sara Mazrouei carried out the literature review, performed all data collection and analysis, interpreted and discussed the results under the supervision of David A. Kring. Specifically, the PhD candidate worked on the content of SPA geology and landing sites (section 7.2), Small Pressurized Rovers (SPR) (section 7.3.2 and Table 7.2), Sampling requirements (section 7.3.3), Tele-robotic traverses between landing sites (section 7.5.1.1., 7.5.1.2., and 7.5.1.4), crew traverses at and around landing sites

(section 7.5.2.2, 7.5.2.3, and 7.5.2.5), and implied trade studies (section 7.6), as well as tables and figures in Appendices C1-C2, C4-C5. Josh Hopkins and Chelsea Welch at Lockheed Martin calculated the orbital coverage for the given landing sites. Elyse J. Allender and the PhD candidate wrote the entire manuscript based on the final report of the internship and managed the manuscript through the peer-review process under the supervision of Dr. David A. Kring.

Article 4 forms Chapter 8 and was conducted within the framework of SFB/TRR-170 project at the Freie Universität Berlin and Westfälische Wilhelms-Universität in Münster. The PhD candidate carried out the literature review, performed most of the data collection and analysis, interpreted and discussed the results, worked on the manuscript, prepared the figures and compiled Appendix D. Jan Hendrik Pasckert and Sebastian H. G. Walter provided Kaguya TC data and LROC NAC image data, respectively. All co-authors contributed to discussions.

Other conference abstracts related to Article from 1 to 4 are:

1. **Orgel, C.**, Michael, G., & Kneissl, T. (2017). Ancient bombardment of the inner Solar System – Reinvestigation of the “fingerprints” of different impactor populations on the lunar surface. *48th Lunar and Planetary Science Conference*, 20– 25 March, The Woodlands, TX, USA, Abstract #1033, <https://www.hou.usra.edu/meetings/lpsc2017/pdf/1033.pdf>
2. Kamps, O., Allender, E. J., Almeida, N. V., Cook, J., Ende, J. J., Mazrouei, S., **Orgel, C.**, Slezak, T. J., Soini, A. J., & Kring, D. A. (2017). Exploration of South Polar region of the Moon: Tele-operated traverses. *48th Lunar and Planetary Science Conference*, 20– 25 March, The Woodlands, TX, USA, Abstract #1909, <https://www.hou.usra.edu/meetings/lpsc2017/pdf/1909.pdf>
3. Ende, J. J., Allender, E. J., Almeida, N. V., Cook, J., Kamps, O., Mazrouei, S., **Orgel, C.**, Slezak, T. J., Soini, A. J., & Kring, D. A. (2017). Landing site assessment for phase 2 of eDSH-enabled lunar missions being examined as an ISECG-GER mission scenario. *48th Lunar and Planetary Science Conference*, 20– 25 March, The Woodlands, TX, USA, Abstract #1880, <https://www.hou.usra.edu/meetings/lpsc2017/pdf/1880.pdf>
4. **Orgel, C.**, Allender, E. J., Almeida, N. V., Cook, J., Ende, J. J., Kamps, O., Mazrouei, S., Slezak, T. J., Soini, A. J., & Kring, D. A. (2017). Landing site assessment for phase 2 of eDSH-enabled lunar missions being examined as an ISECG-GER mission scenario. *5th European Lunar Symposium*, Münster, Germany, https://els2017.arc.nasa.gov/downloads/ELS_2017_Program_Abstract_Booklet.pdf

5. **Orgel, C.**, Michael, G., & Kneissl, T. (2017). Ancient bombardment of the inner Solar System – Reinvestigation of the key lunar basins with a new crater counting approach, the buffered non-sparseness correction. *5th European Lunar Symposium*, Münster, Germany,

https://els2017.arc.nasa.gov/downloads/ELS_2017_Program_Abstract_Booklet.pdf

6. **Orgel, C.**, Michael, G., Fassett, C. I., van der Bogert, C. H., Riedel, C., Kneissl, T., & Hiesinger, H. (2017). Ancient bombardment of the inner Solar System – Reinvestigation of the “fingerprints” of different impactor populations on the lunar surface. *Paneth Kolloquium*, Nördlingen, Germany, Abstract #0033,

<https://www.paneth.eu/PanethKolloquium/2017/0033.pdf>

7. **Orgel, C.**, Ivanov, M. A., Hiesinger, H., Pasckert, J. H., van der Bogert, C. H., & Michael, G. (2018). Characterization of high priority landing sites for the Chang’e-4 exploration mission to the Apollo Basin, Moon. *49th Lunar and Planetary Science Conference*, 19–23 March, Houston, TX, USA, Abstract #1969,

<https://www.hou.usra.edu/meetings/lpsc2018/pdf/1969.pdf>

8. **Orgel, C.**, Michael, G., Fassett, C. I., van der Bogert, C. H., Riedel, C., Kneissl, T., & Hiesinger, H. (2018). The lunar basin sequence based on absolute model ages derived via Buffered Non-Sparseness Correction: Implications for impactor population(s). *49th Lunar and Planetary Science Conference*, 19–23 March, The Woodlands, TX, USA, Abstract #1395,

<https://www.hou.usra.edu/meetings/lpsc2018/pdf/1395.pdf>

9. **Orgel, C.**, Ivanov, M. A., Hiesinger, H., Pasckert, J. H., van der Bogert, C. H., & Michael, G. (2018). Potential landing sites for the Chang’e-4 exploration mission to the Apollo basin, Moon. *6th European Lunar Symposium*, 14–16 May, Toulouse, France,

https://els2018.arc.nasa.gov/downloads/ELS_2018_Abstract_Booklet_08052018.pdf

10. **Orgel, C.**, Fassett, C. I., Michael, G., van der Bogert, C. H., & Hiesinger, H. (2018). Re-examination of the population, stratigraphy, and sequence of Mercurian basins: Implications for Mercury’s early impact history and comparison with the Moon. EPSC Abstracts Vol. 12, European Planetary Science Congress, 17–21 September, Berlin, Germany, Abstract #EPSC-2018-533, https://www.epsc2018.eu/programme/abstract_download.html

11. **Orgel, C.**, Fassett, C. I., Michael, G., van der Bogert, C. H., Manske, L., & Hiesinger, H. (2018). Re-examination of the population, stratigraphy, and

sequence of Mercurian basins: Implications for Mercury's early impact history and comparison with the Moon. AGU Fall Meeting, 10–14 December, Washington, D.C., Abstract # 352733,

<https://agu.confex.com/agu/fm18/meetingapp.cgi/Paper/352733>

12. **Orgel, C.**, Fassett, C. I., Michael, G., van der Bogert, C. H., Manske, L., Hiesinger, H. (2019). Re-examination of the population, stratigraphy, and sequence of Mercurian basins: Implications for Mercury's early impact history and comparison with the Moon. *50th Lunar and Planetary Science Conference*, 18–22 March, The Woodlands, TX, USA, Abstract #2059, <https://www.hou.usra.edu/meetings/lpsc2019/pdf/2059.pdf>

13. **Orgel, C.**, Fassett, C. I., Michael, G., van der Bogert, C. H., Manske, L., Hiesinger, H. (2020). Mercury's early impact history and its comparison with the Moon. *51st Lunar and Planetary Science Conference*, 16–20 March, The Woodlands, TX, USA, Abstract #1877, <https://www.hou.usra.edu/meetings/lpsc2020/pdf/1877.pdf>

Other peer-reviewed publications where C. Orgel has participated as a co-author and related to respective chapters of this thesis can be found in Appendices A and D, respectively.

1. Riedel, C., Michael, G., Kneissl, T., **Orgel, C.**, Hiesinger, H., & van der Bogert, C. H. (2018). A New Tool to Account for Crater Obliteration Effects in Crater Size-Frequency Distribution Measurements. *Earth and Space Science*, 5, 258–267, <https://doi.org/10.1002/2018EA000383>
2. Ivanov, M. A., Hiesinger, H., van der Bogert, C. H., **Orgel, C.**, Paskert, J. H., & Head, J. W. (2018). Geologic history of the northern portion of the South Pole-Aitken basin on the Moon. *Journal of Geophysical Research Planets*, 123, Issue 10, 2585–2612, <https://doi.org/10.1029/2018JE005590>
3. Riedel, C., Minton, D. A., Michael, G., **Orgel, C.**, van der Bogert, C. H., & Hiesinger, H. (2020). Degradation of Small Simple and Large Complex Lunar Craters: Not a Simple Scale Dependence. *Journal of Geophysical Research*, <https://doi.org/10.1029/2019JE006273>,

Other peer-reviewed publications where C. Orgel has contributed as first- or co-author during the graduate program (2016-), but unrelated to this PhD thesis are:

1. Cross, M., Battler, M., Maiwald, V., van't Woud, H., Ono, A., Schlacht, I., L., **Orgel, C.**, Foing, B., & Mclsaac, K. (2016). Operational Lessons Learnt from

- the 2013 ILEWG EuroMoonMars-B Analogue Campaign for Future Habitat Operations on Moon and Mars. *Acta Futura*, 10, 61–73, <https://zenodo.org/record/202179#.XhSbOfIKg2w>
2. Ramsdale, J. D., Balme, M. R., Conway, S. J., Gallagher, C., van Gasselt, S., Hauber, E., **Orgel, C.**, Sejourne, A., Skinner, J. A., Jr., Costard, F., Johnsson, A., Losiak, A., Reiss, D., Swirad, Z., Kereszturi, A., Smith, I., & Platz, T. (2017). Grid-based mapping: a method for rapidly determining the spatial distributions of small features over very large areas. *Planetary and Space Science*, 140, 49–61, <https://doi.org/10.1016/j.pss.2017.04.002>
 3. De Toffoli, B., Pozzobon, R., Mazzarini, F., **Orgel, C.**, Massironi, M., Giacomini, L., Mangold, N., & Cremonese, G. (2018). Estimate of depths of source fluids related to mound fields on Mars. *Planetary and Space Science*, 164, 164–173, <https://doi.org/10.1016/j.pss.2018.07.005>
 4. Ramsdale, J. D., Balme, M. R., Gallagher, C., Conway, S. J., Smith, I., Hauber, E., **Orgel, C.**, Séjourné, A., Costard, F., Eke, V. R., van Gasselt, S., Johnsson, A., Kereszturi, A., Łosiak, A., Massey, R. J., Platz, T., Reiss, D., Skinner, J. A., Swirad, Z. M., Teodoros, L. F. A., & Wilson, J. T. (2019). Gridmapping the northern plains of Mars: Geomorphological, Radar and Water-Equivalent Hydrogen results from Arcadia Planitia suggest possible fluvial and volcanic systems overlain by a ubiquitous and heavily degraded ice-rich latitude-dependent mantle. *Journal of Geophysical Research Planets*, Volume 124, Issue 2, 504–527, <http://doi:10.1029/2018JE005663>
 5. **Orgel, C.**, Hauber, E., van Gasselt, S., Reiss, D., Johnsson, A., Ramsdale, J. D., Smith, I., Swirad, Z. M., Wilson, J. T., Séjourné, A., Balme, M. R., Conway, S. J., Costard, F., Eke, V. R., Gallagher, C., Kereszturi, A., Łosiak, A., Massey, R. J., Platz, T., Skinner, J. A., & Teodoro, L. F. A. (2019). Gridmapping the Northern Plains of Mars: A New Overview of Recent Water- and Ice-Related Landforms in Acidalia Planitia. *Journal of Geophysical Research Planets*, Volume 124, Issue 2, 454–482, <http://doi:10.1029/2018JE005664>
 6. Séjourné, A., Costard, F., Swirad, Z. M., Łosiak, A., Bouley, S., Smith, I., Balme, M. R., **Orgel, C.**, Ramsdale, J. D., Hauber, E., Conway, S. J., van Gasselt, S., Reiss, D., Johnsson, A., Gallagher, C., Skinner, J. A., Kereszturi, A., & Platz T. (2019). Mapping the northern plains of Mars: using morphotype and distribution of ice-related landforms to understand multiple ice-rich deposits in Utopia Planitia. *Journal of Geophysical Research Planets*, Volume 124, Issue 2, 483–503, <http://doi:10.1029/2018JE005665>
 7. Poulet, F., Gross, C., Horgan, B., Loizeau, D., Bishop, J. L., Carter, J., & **Orgel, C.** (2020). Mawrth Vallis, Mars: a fascinating place for in situ exploration. *Astrobiology*, 20, 2, <http://doi:10.1089/ast.2019.2074>

8. **Orgel, C., & Neesemann, A.:** Ice-related geomorphology in Promethei Terra, Mars: Complex landscape evolution history of the Hourglass-shaped lobate debris apron and implications for climate models. Manuscript under revision in *Icarus*.

3.2. Structure

This thesis is divided into five consecutive parts. Part I gives the general introduction of the thesis and consists chapters 1 – 4. Part II contains two first author peer-reviewed publications related to the early bombardment history of the inner Solar System and includes chapter 5 and 6. Part III consists of one second author peer-reviewed publication and one first author manuscript under preparation, and explains how human and robotic exploration missions with sample return capacity could broaden our knowledge about the early impact history of the inner Solar System. The text of chapter 5, 6 and 7 is given as published. The first and co-authored publications where C. Orgel has contributed are marked with bold in the text. Part IV provides major conclusions drawn from Part II and Part III. Part V presents the Appendices published along with the peer-reviewed publications and related to specific chapters. Due to the extensive nature of the Appendices, they can be found electronically on the attached CD to this thesis. All articles cited are in the Bibliography.

Part I: Introduction

Chapter 1 (The basics of impact cratering), Chapter 2 (Research aims), Chapter 3 (Personal contribution and structure of this thesis), Chapter 4 (Methods) have been written to explain the link between each published papers and to provide additional information to understand the topic of this thesis.

Part II: Early bombardment history of the inner Solar System

Chapter 5 and 6 re-investigate the crater populations and stratigraphic relationships of the large lunar and mercurian basins, which were previously investigated by Fassett et al. (2012a, 2012b). To derive the crater populations, a novel crater size-frequency distribution (CSFD) technique, the buffered non-sparseness correction (Kneissl et al., 2016; **Orgel et al., 2018; Riedel et al., 2018, Orgel et al., 2020**) has been applied, which more precisely accounts for crater obliteration on densely cratered surfaces. The nature of the impactor population(s) is one of the major questions, where the shape of the summed CSFDs of basins from the same chronostratigraphic period has been analyzed using a relative crater size-frequency plot. If the Neukum's model (1983, 2001a) about an unchanging population of impactors is correct, the CSFDs

must fit with the isochrones of the production function (PF) on the R-plot. If that is not the case, the CSFDs should deviate from that PF.

Part III: Human and robotic exploration missions to the Moon

Chapter 7 explores the feasibility of tele-robotic operation of the Lunar Electric Rovers (LERs) between five lunar landing sites (Malapert massif, South Pole /Shackleton crater, Schrödinger basin, Antoniadi crater, and the South Pole-Aitken basin center) in the South Pole-Aitken (SPA) basin and identify potential high interest sampling locations en-route. In order to revise the lunar chronology, samples containing impact melt are in the focus. Sample collection and traverses are identified for each individual landing site across key geologic terrains, which also details crew Extra-Vehicular Activity (EVA). Additionally, exploration at and between landing sites is designed to address a suite of NRC (2007) scientific concepts. Chapter 8 discusses the science potential of three candidate landing sites in the Apollo basin by addressing the NRC (2007) objectives using various remote sensing datasets.

Part IV: Conclusions

Chapter 9 discusses the major findings of Part II and Part III and answers the questions addressed in Chapter 2.

Part V: Appendices

Appendix A gives Supplementary Information to Chapter 5

CD directory\Csilla_Orgel_PhD\APPENDIX\APPENDIX_A

Appendix B gives Supplementary Information to Chapter 6

CD directory\Csilla_Orgel_PhD\APPENDIX\APPENDIX_B

Appendix C gives Supplementary Information to Chapter 7

CD directory\Csilla_Orgel_PhD\APPENDIX\APPENDIX_C

Appendix D gives Supplementary Information to Chapter 8

CD directory\Csilla_Orgel_PhD\APPENDIX\APPENDIX_D

CHAPTER 4

METHODS

This chapter focuses on the details on methodology not included or discussed in detail in the presented publications. First, the measurement of crater populations on planetary surfaces is discussed. Then, the techniques to derive crater size-frequency distributions (CSFD) and the representation of the data on various plots are shown. Finally, the determination of absolute model age (AMA) of planetary surfaces and the related functions are presented.

This PhD thesis investigates the addressed scientific objectives using available planetary remote sensing datasets that are freely hosted on NASA's Planetary Data System (PDS).

Table 4.1. List of instruments. Ref. (1) Robinson et al., 2010, (2) Mahanti et al., 2016, (3) Humm et al., 2016, (4) Haruyama et al., 2008, (5) Hawkins et al., 2007, (6) Chabot et al., 2016, (7) Denevi et al., 2016, (8) Denevi et al., 2018b, (9) Smith et al., 2010, (10) Smith et al., 2017, (11) Becker et al., 2016, (12) Cavanaugh et al., 2007, (13) Bandfield et al., 2011, (14) Lucey et al., 1998b, (15) Lucey et al., 2000, (16) Lemelin et al., 2016, (17) Pieters et al., (2009), (18) Green et al., (2011).

| Camera | Sensor Type | Spatial Resolution (m/pix) | Ref. | |
|---|--|----------------------------|------------|------|
| Lunar Reconnaissance Orbiter Camera (LROC) | Wide-Angle Camera (WAC) Narrow Angle Camera (NAC) | Optical | 100 | 1, 2 |
| Kaguya Terrain Camera (TC) | Optical | 7-10 | 4 | |
| Mercury Dual Imaging System (MDIS) | Optical | 166-665 | 5, 6, 7, 8 | |
| Lunar Reconnaissance Orbiter Laser Altimeter (LOLA) | Topographical | 10-100 | 9, 10 | |
| MDIS Digital Elevation Model | Topographical | 665 | 11 | |
| Mercury Laser Altimeter | Topographical | 250 | 12 | |
| Diviner Lunar Radiometer Experiment (DLRE) | Multispectral | 236 | 13 | |
| Clementine UV/VIS Multiband Imager (MI) | Multispectral | 400 | 14, 15 | |
| Chandrayaan-1/M ³ | Multispectral | 60 | 16 | |
| | Hyperspectral | 140 (global) | 17, 18 | |

Primarily, Chapter 5 – 8 are using visible camera and topographic datasets (Table 2.1), such as Lunar Reconnaissance Orbiter Camera (LROC, Robinson et al., 2010)

Wide-Angle Camera (LROC WAC, 100 m/pix mosaic base map, Mahanti et al., 2016), LROC Narrow Angle Camera (LROC NAC, 1m/pix, Humm et al., 2016), Kaguya Terrain Camera (TC) images of 7 m/pix (Haruyama et al., 2008) and MESSENGER's Mercury Dual Imaging System (MDIS, 166 m/pix with a variety of solar incidence and illumination azimuths, and 665 m/pix colour and enhanced data products, Hawkins et al., 2007; Chabot et al., 2016; Denevi et al., 2016; Denevi et al., 2018b). Additionally, Lunar Reconnaissance Orbiter Lunar Orbiter Laser Altimeter (LRO LOLA, from 10 to 100 m/pix global map, Smith et al., 2010; Smith et al., 2017), MDIS DEM (665 m/pixel, Becker et al., 2016), and Mercury Laser Altimeter (MLA, 250 m/pixel, Cavanaugh et al., 2007) have been obtained to create digital elevation models. Moreover, Chapter 8 applies various spectral datasets (Table 2.1), such as LRO Diviner Lunar Radiometer Experiment (DLRE, 236 m/pix, Bandfield et al., 2011), Clementine's UV/VIS 400 m/pix global maps (Lucey et al., 1998b, 2000), as well as Kaguya Multiband Imager (MI) ~60 m/pix global data (Lemelin et al., 2016) and M³ (Green et al., 2011). Summary of the used instruments is presented in Table 4.1.

4.1. Measuring Crater Populations

The first step to investigate the crater populations on a planetary surface is to map and measure the size of all impact craters superposed on a homogenous geologic unit with a well-defined count area using optical and topographic datasets (Wilhelms, 1987). In order to carefully determine the size of the count area and the craters, the appropriate selection of the map projection for all vector and raster data sets as well as the suitable mapping scale are crucial. One solution is to map the region of interest and the craters in Geographic Information System (GIS) applying an equal-area map projection (e.g., Sinusoidal Equal Area, Lambert Azimuthal Equal Area). Alternatively, CraterTools (Kneissl et al., 2011), an extension for Esri's ArcMap, can calculate true area sizes in arbitrary map projections. Defining the count area demands care with respect to at least six factors (Platz et al., 2013): (1) geologically homogenous count area, (2) appropriate size of the count area, (3) artefacts-free images, (4) same image resolution all over the count area, (5) avoid inclined and rough surfaces, and (6) exclude secondary crater clusters. Mapping of craters commonly requires to measure all craters intersecting the count area irrespective of erosional state and crater classes. Moreover, it is necessary to differ between impact craters and other near-circular features (e.g., volcanic craters, volcanic edifices, calderas, collapsed lava tubes, pseudo craters, pit craters, and thermokarst) while counting craters (Platz et al., 2013).

4.2. Crater Size-Frequency Distribution (CSFD) Techniques

Analysis of the measured CSFDs can be performed by applying different approaches using a newly available standalone tool, the so-called CSFD_Tools (Riedel et al., 2018). There are four techniques to derive the CSFDs of the measured craters in a given count area: (1) Traditional crater counting (TCC) (Arvidson et al., 1978), (2)

Buffered crater counting (BCC) (Tanaka, 1982; Wichman & Schultz, 1989; Fassett & Head, 2008; Fassett et al., 2012b; Kneissl et al., 2015), (3) Non-sparseness correction (NSC) (Kneissl et al., 2016; **Riedel et al., 2018**), and (4) Buffered non-sparseness correction (BNSC) (Kneissl et al., 2016; **Orgel et al., 2018; Riedel et al., 2018, Orgel et al., 2020**) (Figure 4.1).

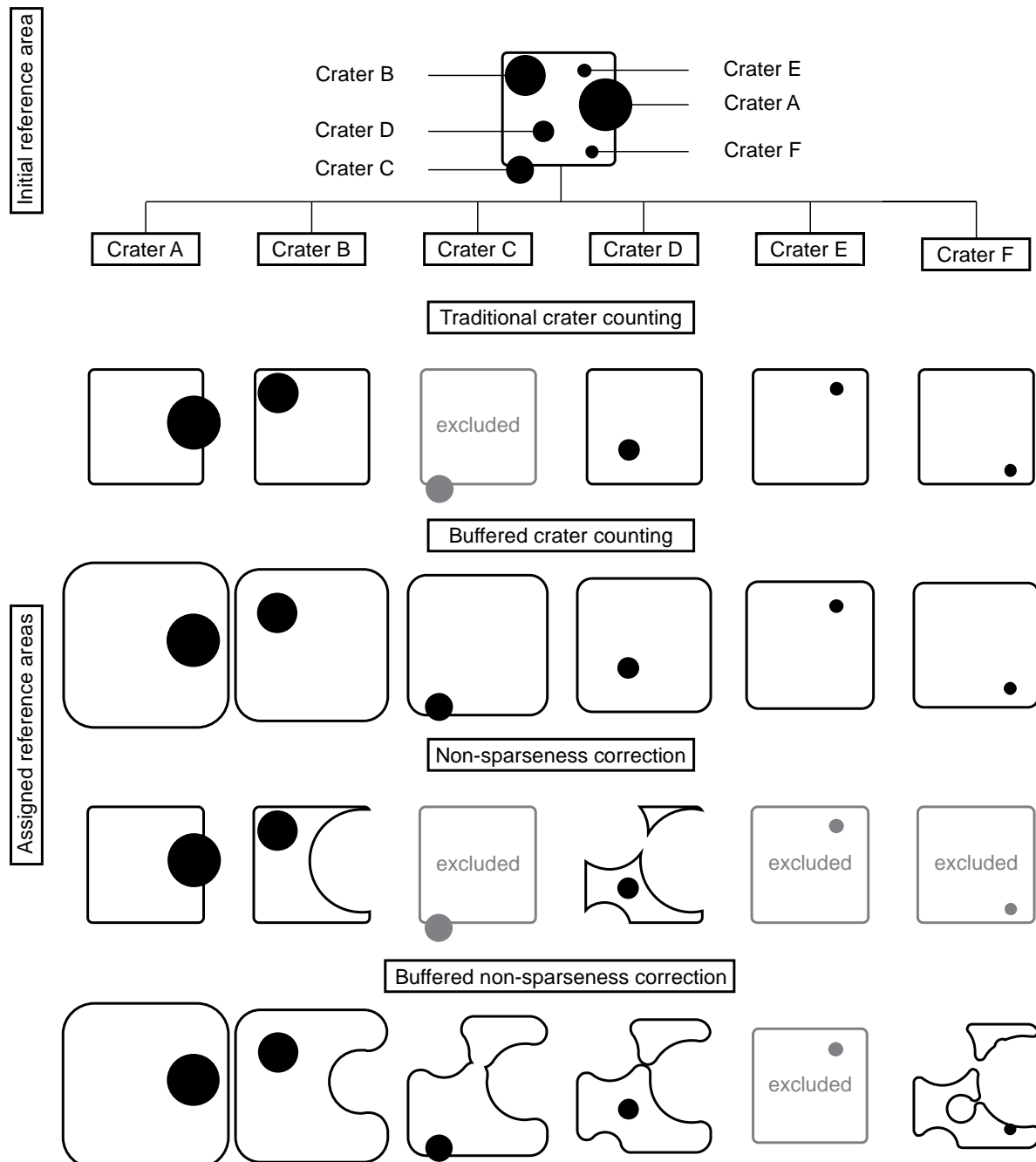


Figure 4.1: Analysis of crater size-frequency distributions using different techniques: (1) Traditional crater counting, (2) Buffered crater counting, (3) Non-sparseness correction, and (4) Buffered non-sparseness correction. Figure from **Riedel et al. (2018)**.

The TCC and BCC are well-established techniques in the planetary community. The TCC approach includes all impact craters whose centers fall inside the count area and the area assigned to each crater is the same. The BCC technique includes all craters crosscutting the region of interest within a buffer, increasing the number of craters included in the measurements and improve statistics. In contrast to TCC approach, the BCC, NSC and BNSC techniques designate an individual reference area to each crater, which reference area becomes smaller for correspondingly smaller crater sizes. The new CSFD techniques, both NSC and BNSC consider crater obliteration of smaller diameter craters by subsequent larger craters and their ejecta deposits by excluding regions that have been modified by these impacts. Additionally, to take the non-sparseness into account, BNSC approach utilizes the buffer used in BCC technique. More details about NSC and BNSC is in chapter 5 and 6.

4.3. Interpreting Crater Size-Frequency Distributions

If the cratering rate is the same across the measured units, the relative age between different geologic units can be compared by analyzing the CSFDs. The frequency of crater population can be described by

$$n[Da, Db] = \frac{c}{A}$$

where, c is the number of craters per count area A in a diameter range from D_a to D_b ($D_b > D_a$). The error is approximated as

$$\sigma = \sqrt{c}$$

After deriving CSFDs of different terrains using the CSFD_Tools (Riedel et al., 2018), size-frequency plots can facilitate for displaying crater populations in CraterStats software (Michael & Neukum, 2010; Michael, 2013). There are three most commonly used techniques to represent the data: cumulative plots, differential plots, and relative (R) plots (Arvidson et al., 1978; Neukum, 1983; Michael, 2013; Fassett, 2016). The data are plotted on a log-log scale with equal decadal length (the interval for example between 1 km and 10 km), showing crater diameter in kilometer on the x-axis and crater density given per square kilometer on the y-axis. The CSFD data can be binned or unbinned before plotting.

4.3.1. Cumulative Size-Frequency Plot

The *cumulative* plot (Figure 4.2/A) represents the number of craters equal to or larger than a given diameter D on a planetary surface after time t (Öpik, 1960; Arvidson et

al., 1978; Neukum, 1983; Michael, 2013; Fassett, 2016). The cumulative method is the suitable method to compare crater densities with each other.

$$N(D, t) = \int_0^t \phi(D, t) dt$$

Cumulative and differential plots in this thesis, use pseudo-log crater binning, the sum of discrete numbers per bin, where bin-sizes can be previously defined (Arvidson et al., 1978). The data in each bin has a diameter limit from D_a to D_b ($D_b > D_a$) containing the measured craters. The pseudo-log crater binning uses 18 bins per decade with the boundaries approximately evenly spaced.

$$D_i(a, n) = a * 10^n$$

where, D_i is the bin-size, $a = (1.0, 1.1, 1.2, 1.3, 1.4, 1.5, 1.7, 2.0, 2.5, 3.0, 3.5, 4.0, 4.5, 5.0, 6.0, 7.0, 8.0, 9.0)$ is the bin's lower boundary, and $n = (-3, \dots, 3)$ is the decade number. All measured crater bin-sizes of an interval (decade) are described as:

$$D_i = D_a$$

CSFDs derived from different count area sizes A are scaled for each bin and plotted as $\log(N)$ versus $\log(D_a)$:

$$N = \sum_{k=1}^i \frac{n_k}{A_k}$$

This equation allows to measure the population in each bin on a different surface area. The uncertainty $\sigma(N)$ of the cumulative number N per bin for each bin is given by:

$$\sigma(N) = \log\left[\frac{N \pm N^{1/2}}{A}\right]$$

4.3.2. Differential Size-Frequency Plot

The *differential* plot (Figure 4.3) can be described as a number of craters for a specific crater diameter D per unit area (Arvidson et al., 1978; Neukum, 1983; Michael, 2013; Fassett, 2016). The differential representation of CSFDs allows to identify discrete short and long-lived resurfacing events (Michael, 2013). The series of chosen bin-widths is a trade-off between losing information by over-binning or losing information

by over-smoothing. The density of craters $n[D_a, D_b]$ per unit area A is calculated in the given size range of each bin. Consequently, the differential plot is independent of the binning. The differential crater size-frequency $F(D_c)$ at diameter D_c can be derived by the frequency of crater population per bin-size:

$$F(D_c) = \frac{n[D_a, D_b]}{(D_b - D_a)}$$

The data is plotted as $F(D_c)$ versus D_c with the mean bin center:

$$D_c = \left[\frac{D_a + D_b}{2} \right]$$

4.3.3. Relative Size-Frequency Plot

The *relative (R)* plots (Arvidson et al., 1978; Neukum, 1983; Michael, 2013; Fassett, 2016) remove a D_c^{-3} differential slope (D_c^{-2} cumulative, Figure 4.2/C) power law from size-frequency distributions. With other words, the relative crater frequency plot measures how the cumulative crater frequencies vary from a -2 slope. While this, in turn, can be related to the measured crater densities, the relative plot provides further information to the cumulative crater frequencies. The relative crater size-frequency $R(D_c)$ at diameter D_c can be calculated by:

$$R(D_c) = \frac{n[D_a, D_b]}{(D_b - D_a)D_c^{-3}}$$

and plotted as $R(D_c)$ versus D_c . Relative plots are commonly used to study different impactor populations. In this thesis 10/decade crater binning has been used.

4.4. Deriving Absolute Model Age on the Lunar Surface

To convert the CSFD into AMA, the model requires the crater formation rate on the surface. The crater formation rate describes how fast craters on a given size are formed on a given unit area:

$$\phi(D, t) = \frac{dN}{dt}$$

Both ϕ and N highly dependent on the crater diameter and time. Smaller craters form more often than larger ones. The crater formation rate is expected to be different on other planets due to the differences in impactor properties (size-frequency distribution (SFD), velocity, and density) (Le Feuvre & Wieczorek, 2008, 2011) and target

properties (strength and gravity) (Dundas et al., 2010; van der Bogert et al., 2017). Neukum et al. (2001a) and (2001b) translate the lunar chronology function to other terrestrial planets (e.g., Mercury) by using the estimated SFD of projectiles bombarded the lunar surface and crater-scaling rule (Schmidt & Housen, 1987; Housen & Holsapple, 2011). Based on the Neukum model (1983, 2001a) the shape of the SFD of impacting projectiles has not changed with time, and thus, crater formation rate can be divided into two functions: production function (PF) and chronology function (CF).

4.4.1. Production Function

The production function (PF) describes the number of impact craters produced on the lunar surface (Neukum, 1983). To describe the shape of the PF, measuring impact crater size-frequency distributions on various, geologically undisturbed areas is crucial. However, most of the planetary surfaces were overprinted by complex geologic processes, making difficult to account for exact crater densities (Hartmann, 1995). The first attempt to derive the shape of the PF used to fit power laws and plotted the results on a $\log N$ versus $\log D$ plots (Young, 1940; Brown, 1960; Hartmann, 1964).

Since 1964, higher resolution data become available, it has become obvious that a simple power law was not enough to describe the lunar CSFD, but at least three different “segments” were necessary (e.g., Hartmann, 1969). Some researchers have favored to combine three different power law functions (Hartmann, 1969; Baldwin, 1971; Hartmann & Wood, 1971; Shoemaker, 1977; Hartmann et al., 1981), while others proposed to apply a polynomial function to fit to the CSFDs (Neukum et al., 1975; Neukum & König, 1976; König, 1977; Neukum, 1983; Neukum et al., 2001a; Ivanov, 2001). Neukum (1983) and Ivanov (2001) have published the unchanging form of the lunar PF:

$$\log N = \sum_{j=0}^{11} a_j (\log D)^j$$

where N is the frequency of craters equal to or larger than D crater diameter in kilometers, a_j is one of the eleven production function coefficients (Table 4.2), and a_j for $j = 0$ describes the y-axis shift. The shape of the PF is illustrated on Figure 4.2.

4.4.2. Chronology Function

The Apollo and Luna missions collected several rock samples from specific regions on the lunar surface and the K-Ar radiometric age of impact melt clasts from these samples provide the calibration points for the chronology function (CF). However, Stöffler & Ryder (2001) noted that those collected samples should be handled with high caution regarding their provenance and the resulted radiometric and exposure ages derived with different isotopic systems.

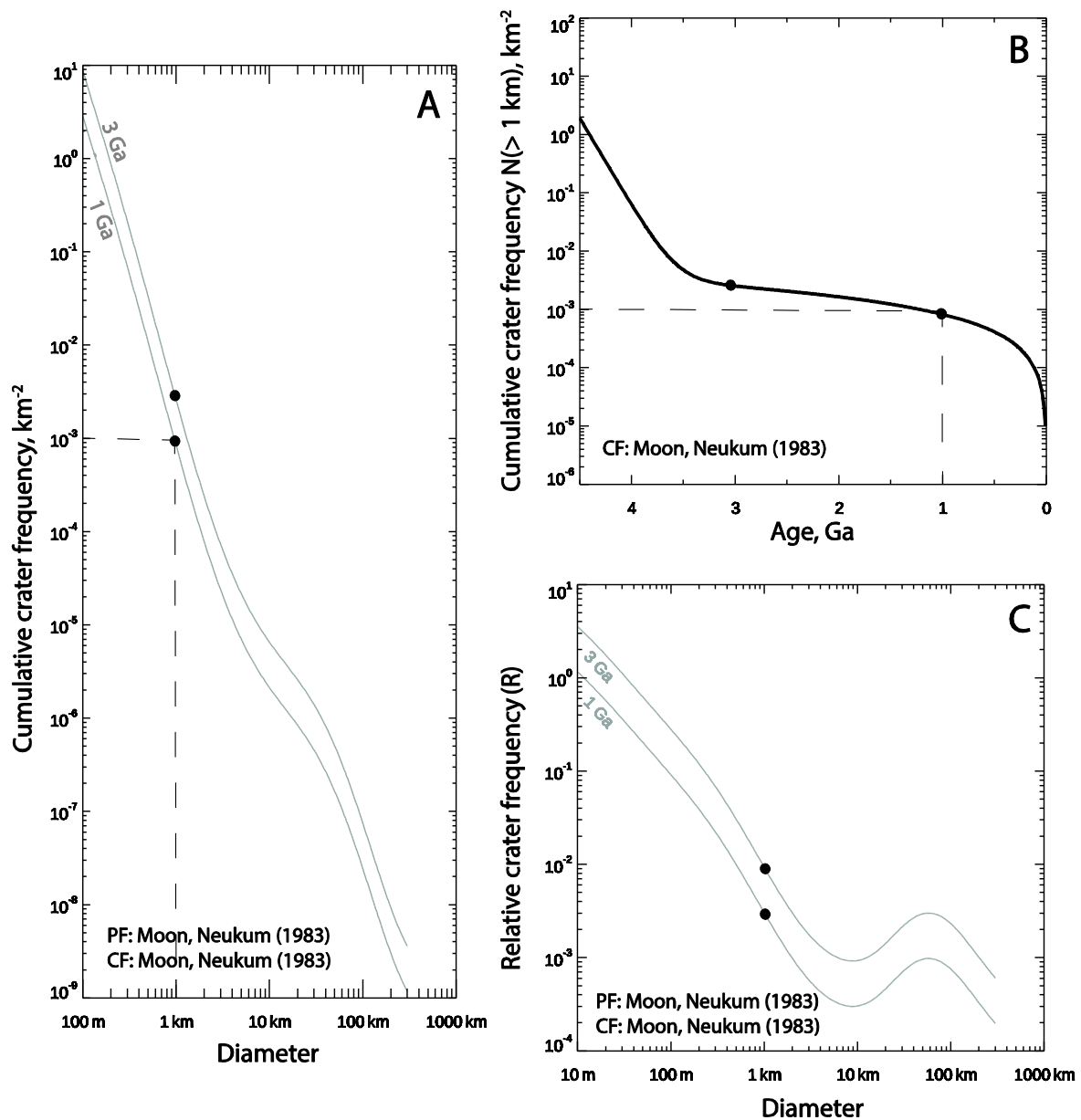


Figure 4.2: Functions used for CSFD-based AMA determinations. (A) Cumulative representation of the lunar crater PF as described by Neukum (1983). The PF (solid lines) is shown for a surface of 1 Gyr and 3 Gyr. The black dots represent the frequency of the reference diameter, $D \geq 1 \text{ km}$, which is used to extract an age from the chronology function. (B) Lunar chronology function (CF). Black dots correspond to the frequency of the reference diameter shown in panel A giving an absolute age of 1 Gyr and 3 Gyr. (C) Relative crater frequency representation of the lunar PF. Black dots represent the frequency of the reference diameter shown in panel A.

Table 4.2. The production function coefficients for different chronology models on the Moon and Mercury. The difference in the coefficients on the Moon and Mercury is due to the different crater formation rates on the two planetary bodies.

| Coefficient | Neukum (1983) Moon | Neukum et al. (2001a) Moon | Neukum et al. (2001b) Mercury | Le Feuvre & Wieczorek (2011) non-porous, Mercury |
|-----------------|-----------------------|-------------------------------|----------------------------------|--|
| a ₀ | -2.5339 | -3.876 | -3.016675 | -9.939 |
| a ₁ | -3.6269 | -3.557528 | -3.627417 | -3.994 |
| a ₂ | 0.43662 | 0.781027 | 0.6038601 | -1.116 |
| a ₃ | 0.79347 | 1.021521 | 1.026714 | 1.269 |
| a ₄ | 0.086468 | -0.156012 | -0.003767761 | 1.272 |
| a ₅ | -0.26485 | -0.444058 | -0.4204364 | -0.8276 |
| a ₆ | -0.066382 | 0.019977 | -0.03223500 | -0.3718 |
| a ₇ | 0.037923 | 0.086850 | 0.08044575 | 0.2463 |
| a ₈ | 0.010596 | -0.005874 | 0.003170165 | 0.02091 |
| a ₉ | -0.0022496 | -0.006809 | -0.006733922 | -0.02756 |
| a ₁₀ | -0.00051797 | 0.000825 | 0.0001334403 | 0.003659 |
| a ₁₁ | 0.0000397 | 0.0000554 | 0.0001428627 | |

The relationship of the sample ages to the CSFD measurements of the landing sites allowed to establish the cratering chronology model describing the impact cratering rate as a function of time on the Moon (Baldwin, 1971; Neukum, 1971; Neukum & Wise, 1976; Neukum, 1977, 1983). The lunar CF in cumulative form represents an exponentially decreasing cratering rate beyond 3 Gyr, and a constant impact rate from that time until today (Neukum, 1983; Neukum & Ivanov, 1994) (Figure 4.2/B and 4.3). This function can be described in the following form:

$$N(D \geq 1 \text{ km}) = 5.44 * 10^{-14}[e^{6.93T}-1] + 8.38 * 10^{-4}T$$

where, $N(D \geq 1 \text{ km})$ is the number of craters per km² equal to or larger than 1 km, and T is the crater accumulation time (or crater retention age).

Recent work from Iqbal et al. (2019a) revisited the CSFD of the Apollo 11 landing site and the most recent radiometric ages of samples from the literature (Figure 4.3). Figure 4.3 represents calibration points from Iqbal et al. (2019a) and previous works (Hiesinger et al., 2000, 2012a; Marchi et al., 2009; Robbins, 2014). The calibration point from Iqbal et al. (2019a) for the Apollo 11 landing site confirmed the Neukum (1983) and Neukum et al. (2001a) lunar chronology models. Additional studies from Hiesinger et al. (2000, 2012a), Iqbal et al. (2018, 2019b) and Borisov et al. (2019) re-investigated the CSFD of Apollo 12, 14, 17 and Luna 20 (van der Bogert et al., 2017) landing sites and their initial results are also consistent with the Neukum's chronology model.

Lunar Cratering Chronology

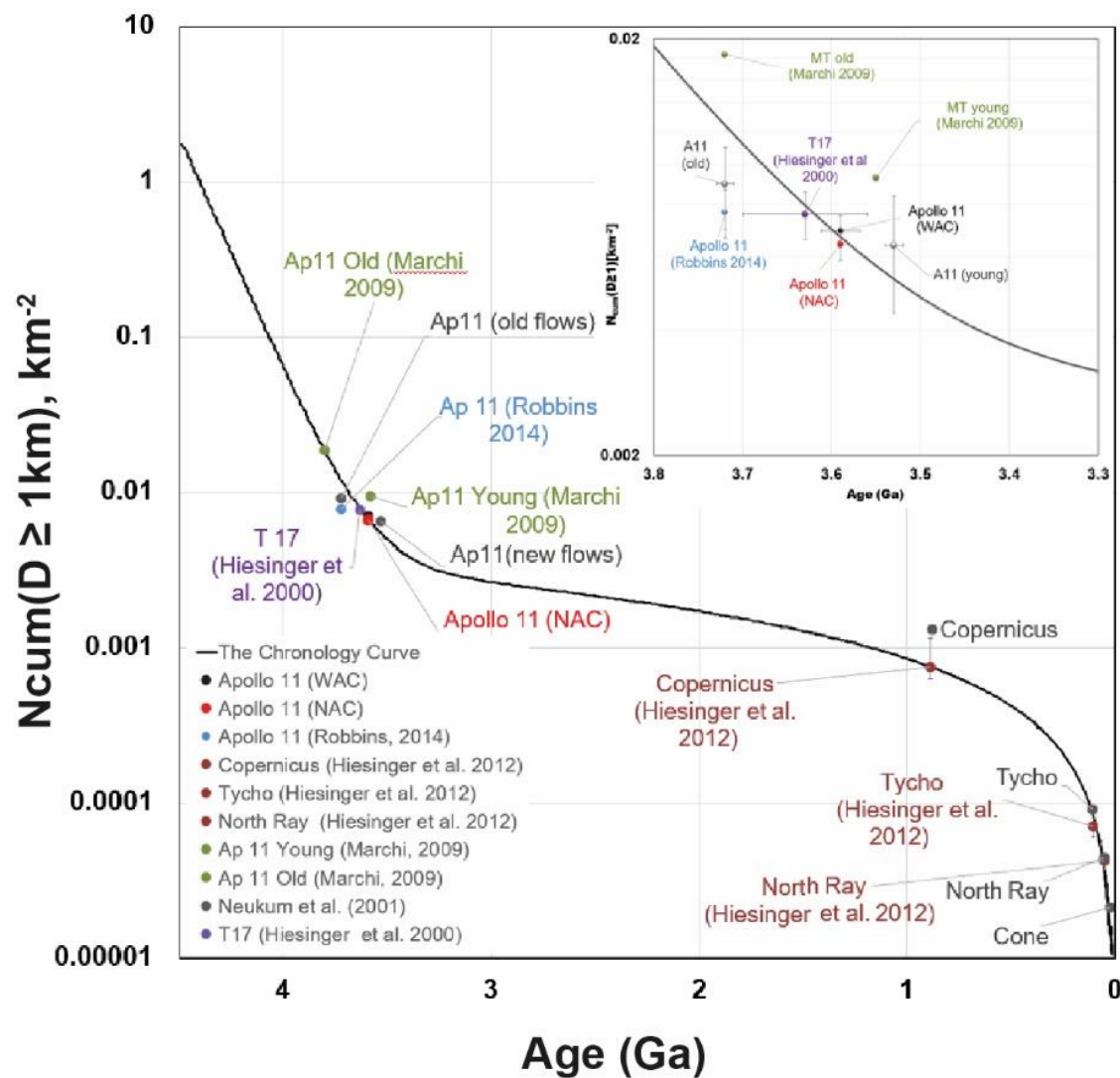


Figure 4.3: Lunar cratering chronology curve after Neukum (1983) from Iqbal et al. (2019a). The gray points display the values used by Neukum (1983), and Neukum et al. (2001a) for the calibration of the curve. The data points in red and black represent the new calculated value of the Apollo 11 landing site from Iqbal et al. (2019a), with NAC and WAC data respectively. Calibration points from Hiesinger et al. (2012a) in dark red, Marchi et al. (2009) in green, and Robbins (2014) in blue compared to the chronology curve. The inset shows the comparison of Iqbal et al. (2019a) updated values (red and black) to the old values measured by Neukum (1983) and Neukum et al. (2001a) (gray), Hiesinger et al. (2000) (purple), Marchi et al. (2009) (green), and Robbins (2014) (blue).

Using the crater-scaling rule from Schmidt & Housen (1987), Neukum et al. (2001b) calculated the chronology model for Mercury. Since the Mariner-10 images have low resolution, 10 km crater diameter was chosen as a reference diameter to derive the relative and absolute model ages. Assuming the same cratering decay rate as for the Moon and Mercury to Moon cratering rate ratios, Neukum et al. (2001b) proposed a similar time-depending chronology model as for the Moon:

$$N(D \geq 10 \text{ km}) = 2.63 * 10^{-16}[e^{6.93T}-1] + 4.05 * 10^{-6}T$$

The mercurian chronology function is slightly higher for the same reference crater diameter than the lunar chronology, where the lower impact rate on Mercury tends to be compensated by the larger impactor velocities. Alternatively, Le Feuvre & Wieczorek (2011) calculate PFs and CFs from a combination of astronomical observations of probable impactors and dynamical calculations to estimate the impact rate. However, due to the lack of mercurian samples the cratering chronology has high uncertainty in AMA on Mercury. Le Feuvre & Wieczorek (2011) have published the following chronology function for non-porous surface on Mercury:

$$N(D \geq 1 \text{ km}) = 2.74 * 10^{-24}[e^{14.44T}-1] + 1.150 * 10^{-1}T$$

4.5. Chronostratigraphy

On planetary bodies, the stratigraphic system is based on remote sensing observation. The stratigraphic relationship of terrains with the principles outlined by Gilbert (1893) can be combined with the cratering chronology model to create a chronostratigraphic system for the Moon (lunar chronostratigraphic system) and other planetary bodies, e.g. Mercury.

The first attempt to characterize the boundaries of the lunar epochs was carried out by Shoemaker & Hackmann (1962) using impact basins and several younger craters based on Earth-based telescopic observations. Later, a more comprehensive stratigraphic system was established by Wilhelms (1987) using the Lunar Orbiter and Apollo missions data. The relative and absolute ages of geologic units (Neukum & König, 1976; Neukum, 1977; Wilhelms, 1979) using the principles of crater statistics from Neukum (1983) served as a guideline to define the lunar chronostratigraphic system. From oldest to youngest time-stratigraphic systems are the pre-Nectarian (> 4.3 Gyr), Nectarian (4.1 – 3.9 Gyr), Imbrian (3.9 – 3.2 Gyr), Eratosthenian (3.2 – 1.5 Gyr), and the Copernican (< 1.5 Gyr). Table 4.3 lists the boundaries of each time-stratigraphic systems, which are related to the formation of basins and large craters. The pre-Nectarian System is characterized by the formation of large lunar basins including the South Pole-Aitken basin. The Nectarian System consists of geological units including the Nectaris (~ 885 km in diameter, Neumann et al., 2015) and other impact basins as well as all older materials before the Imbrium basin (~ 1321 km in diameter, Neumann et al., 2015) was formed. The Imbrium System includes the

youngest lunar basins (Imbrium, Orientale, Schrödinger, **Orgel et al., 2018**) and plains forming materials. Shoemaker & Hackmann (1962) defined the youngest chronostratigraphic units, which are the Eratosthenian and Copernican Systems, and mark the formation of Eratosthenes (~ 58 km in diameter) and Copernicus craters (~ 95 km in diameter), respectively.

Table 4.3: Lunar chronostratigraphic system with relative and absolute ages (Neukum, 1983).

| System | Boundary | Crater Frequency N(1) [km ⁻²] | AMA [Gyr] |
|---------------|---------------------|--|--------------|
| Copernican | Copernicus crater | $1.3 \cdot 10^{-3}$ | 1.5 |
| Eratosthenian | Eratosthenes crater | $3.0 \cdot 10^{-3}$ | 3.2 |
| Imbrian | Imbrium basin | $3.5 \cdot 10^{-2}$ | 3.9 |
| Nectarian | Nectaris basin | $1.2 \cdot 10^{-1}$ | 4.1 |
| Pre-Nectarian | Highlands | $3.6 \cdot 10^{-1}$ | >4.3 |

*Table 4.4: Mercurian chronostratigraphic system with relative and absolute ages (Spudis & Guest, 1988). *References: (1) Spudis & Guest, (1988), (2) Neukum et al. (2001b), (3) Ernst et al. (2017), (4) Banks et al. (2017), (5) Marchi et al. (2013).*

| System | Boundary | Crater Frequency N(20) [10 ⁶ km ²] | AMA [Gyr] | Ref.* |
|---------------|---------------|--|------------------|-------------|
| Kuiperian | Kuiper crater | | 1.0 | (1) |
| | | 1.3 ± 0.1 | 0.280 ± 0.06 | (4) |
| Mansurian | Mansur crater | | 3.0-3.5 | (1) |
| | | 8.9 ± 0.4 | 1.7 ± 0.2 | (4) |
| Calorian | Caloris basin | 41 ± 9 | 3.9 | (1),(2),(3) |
| Tolstojan | Tolstoj basin | 93 ± 15 | 3.9-4.0 | (1),(2),(3) |
| Pre-Tolstojan | | ~120 | > 4.0 | (1),(2),(5) |

Based on the Mariner-10 data, Spudis & Guest (1988) established the first lunar-like time-stratigraphic system with initial absolute age limits on Mercury. From oldest to youngest, these are the pre-Tolstojan (> 4.0 Gyr), Tolstojan (4.0 – 3.9 Gyr), Calorian (3.9 – 3.5 to 3.0 Gyr), Mansurian (3.5 to 3.0 – 1.0 Gyr), and Kuiperian (< 1.0 Gyr) (Table 4.4). The pre-Tolstojan System consists of ancient multi-ring basins and extensive intercrater plains with volcanic origin, while the Tolstojan System marks the formation of Tolstoj basin (~ 467 km in diameter, **Orgel et al., 2020**) and the oldest, smooth plains materials (Spudis and Guest, 1988; Denevi et al., 2009; Byrne et al., 2018) prior the formation of Caloris basin. The Caloris basin (~1556 km in diameter, **Orgel et al., 2020**) is the youngest basin and includes the youngest widespread smooth plains deposits on Mercury. The Mansurian and Kuiperian are the two youngest chronostratigraphic systems including impact crater-related deposits and are defined by the craters Mansur (~75 km in diameter, 3.9 – 1.7 Gyr) and Kuiper (~62 km in diameter, < 0.280 Gyr), respectively (Banks et al., 2017).

CHAPTER 5

ANCIENT BOMBARDMENT OF THE INNER SOLAR SYSTEM – REINVESTIGATION OF THE “FINGERPRINTS” OF DIFFERENT IMPACTOR POPULATIONS ON THE LUNAR SURFACE

Csilla Orgel, Gregory Michael, Caleb I. Fassett, Carolyn H. van der Bogert, Christian Riedel, Thomas Kneissl, and Harald Hiesinger (2018), published in *Journal of Geophysical Research*, 123, 748-762, <https://doi.org/10.1002/2017JE005451>

Abstract

The lunar cratering record provides valuable information about the late accretion history of the inner Solar System. However, our understanding of the origin, rate, and timing of the impacting projectiles is far from complete. To learn more about these projectiles, we can examine crater size-frequency distributions (CSFDs) on the Moon. Here, we re-investigate the crater populations of 30 lunar basins (≥ 300 km) using the buffered non-sparseness correction (BNSC) technique, which takes crater obliteration into account, thus providing more accurate measurements for the frequencies of smaller crater sizes. Moreover, we revisit the stratigraphic relationships of basins based on $N(20)$ crater frequencies, absolute model ages, and observation data. The BNSC-corrected CSFDs of individual basins, particularly at smaller crater diameters are shifted upwards. Contrary to previous studies, the shapes of the summed CSFDs of Pre-Nectarian (excluding South Pole-Aitken Basin), Nectarian (including Nectaris) and Imbrian (including Imbrium) basins show no statistically significant differences, and thus provide no evidence for a change of impactor population.

5.1. Introduction

The Moon has the best preserved impact record in the inner Solar System due to the absence of an atmosphere and the extremely low rates of surface modification. The lunar cratering record has long been used by the planetary community to determine relative and absolute surface ages (Öpik, 1960; Baldwin, 1964; Neukum, 1983) and provides valuable information about the late accretion history of the inner Solar System. Crater size-frequency distributions (CSFDs) have been used to define the lunar “production function” (PF) (Neukum, 1983), which describes the population of craters forming on the Moon's surface. The PF can be used to extrapolate the measured CSFD from a particular surface unit to a reference diameter (~ 1 km) whose frequency will give an absolute model age from the lunar “chronology function” (CF) (Neukum, 1983). Neukum's approach assumes that the PF has remained unchanged, but this is debated (Strom et al., 2005; Bottke et al., 2007; Head et al., 2010; Fassett

et al., 2012b; Marchi et al., 2012; Morbidelli et al., 2012). Neukum (1983) and Hartmann (1995) argued it is possible to use one PF to analyze CSFDs from surfaces of all ages, but if this is not correct, it would systematically affect the derived age results. If the PF has been unchanged, this could suggest the Moon had only one impactor population, or that multiple populations that contributed to its impact record had the same size-frequency distribution. For example, collisional evolution tends to cause all impactor populations to evolve to the same size-frequency distribution (Bottke et al., 2005). However, if it can be shown that the PF changed over time, it would also indicate that more than one impactor population may have contributed to the lunar cratering record (O'Brien & Greenberg, 2003). Therefore, constraining whether the PF shape changed over time is crucial for improving this widely used method of crater-based age determination on the Moon and other planetary bodies.

Many potential projectile families for the Moon exist, such as main-belt asteroids, asteroids from the hypothesized E-belt a proposed inner extension of the asteroid belt that is now mostly extinct, comets, or even remnant ejecta fragments from the giant impact that formed the Moon (Gomes et al., 2005; Strom et al., 2005; Morbidelli et al., 2010; Bottke et al., 2012; Bottke et al., 2015). These objects are characterized by specific projectile size-frequency distributions that can be scaled to crater sizes using crater scaling laws (Ivanov, 2001; Housen & Holsapple, 2011). Since the shape of the CSFD in the absence of modifying processes is directly connected to the size-frequency distribution of the impacting projectiles, this shape can be used to identify the projectile source(s). Determining the source region(s) of the impacting projectiles is of particular importance for understanding the timing of lunar basin ($D \geq 300$ km) formation.

The timing and sequence of impact basin formation are an important part of lunar geologic history. There are two major views about the origin of lunar basins. First, the basins result from the exponentially declining number of planetesimals from planetary accretion (Hartmann, 1995; Neukum, 1983; Neukum & Ivanov, 1994). Second, the basins formed in an impact spike, called Late Heavy Bombardment (LHB) or the terminal lunar cataclysm originally based on the radiometric ages of lunar samples, which concentrated around 3.9 Gyr (Tera et al., 1974; Stöffler & Ryder, 2001). However, the timing and nature of the cataclysm are both debated. It was proposed based on the Nice model (Gomes et al., 2005; Morbidelli et al., 2005; Tsiganis et al., 2005; Morbidelli et al., 2012) that the migration of the giant planets could have destabilized the Main Asteroid Belt and the hypothesized E-belt, and injected projectiles into the inner Solar System. Furthermore, numerical models (Marchi et al., 2012; Bottke et al., 2012; Morbidelli et al., 2012) and crater counting results from Fassett et al. (2012b) show an uptick in the impact flux near 4.1 Gyr, which could be consistent with the Nectaris basin forming event, however this is not fully consistent with the radiometric ages of the lunar samples, which show a peak in impact melt age of 3.9 Gyr at all landing sites.

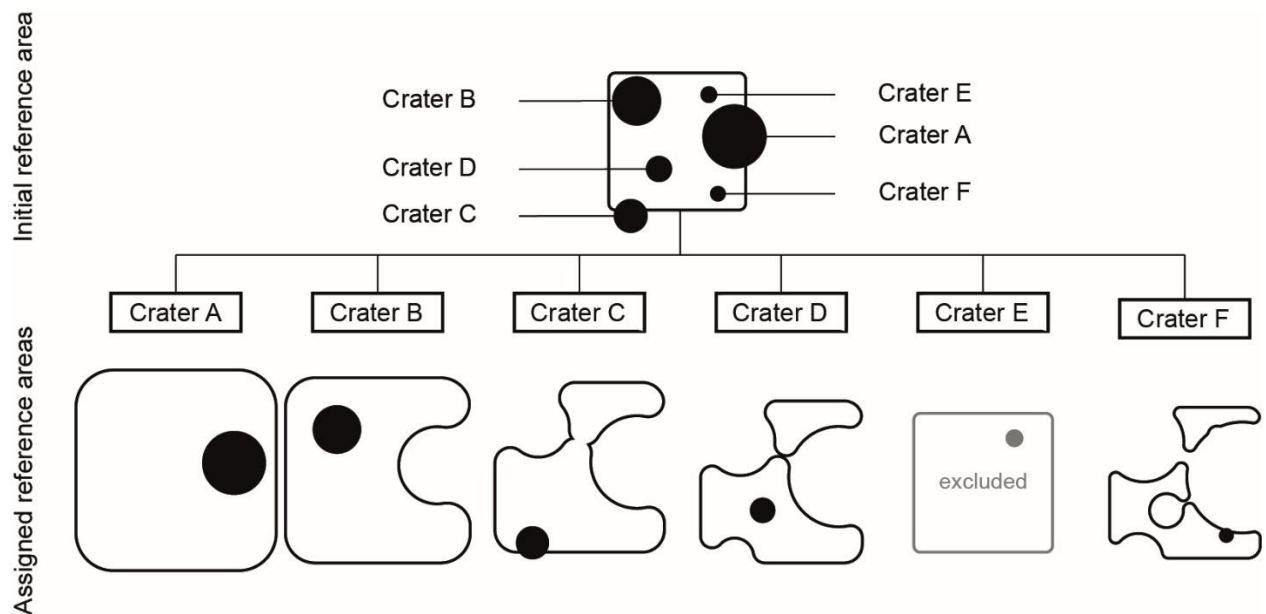


Figure 5.1: Assignment of individual reference areas during buffered non-sparseness correction. In this example, there is a rectangular reference area with six intersecting craters A-F, with crater A being the largest and crater F being the smallest crater. We assume a surrounding ejecta blanket of one crater radius in width for every crater. Accordingly, the area which is affected by crater obliteration is two times a crater's radius (crater rim plus ejecta blanket). For every crater, all larger craters plus their surrounding ejecta blankets are removed from the initial reference area. The remaining area is buffered by one crater radius of the crater which is currently under investigation. If the centroid of the crater is located inside the modified reference area, the investigated crater is considered for the CSFD measurement. In this example, crater E is excluded since it is located entirely on top of crater A's ejecta blanket.

Several authors have suggested that the shape of the PF changed over time and suggested that different impactor populations may have played a role during the formation of the lunar basins (Strom et al., 2005; Head et al., 2010; Fassett et al., 2012b; Marchi et al., 2012; Bottke et al., 2012; Morbidelli et al., 2012). However, different authors proposed different transition times for when the shape of the PF changed, as well as different characteristics for the older and younger populations. Strom et al. (2005) proposed two different impactor populations (Population 1 and Population 2), which formed the oldest lunar basins and bombarded the younger mare terrains, respectively. They argued from the CSFDs that a transition in impactor populations occurred between 3.9 – 3.8 Ga. These results are supported by a later CSFD study by Head et al. (2010). Head et al. (2010) identified two different populations with a transition during the Imbrian period at less than 3.9 Ga, close to the time of the Orientale basin event. Their findings were mainly based on the Nectaris, Imbrium, and Orientale cratering records. In contrast to the analysis by Head et al. (2010), Fassett et al. (2012b) normalized and combined the CSFDs of all basins assigned to the same period, then compared these summed CSFDs to each other.

They found that the transition between the two populations occurred earlier than mid-Nectarian, and that there was no change in the shape of the CSFDs between the Nectarian basins and the Imbrian basins.

In addition to the findings described above, Marchi et al. (2012) identified a third population of impactors, distinct from the “early” population on the lunar highlands and the “late” population on the lunar maria. According to their findings, the transition from the early population to an intermediate population, which they assign to the impactors that produced the LHB, occurred near the time of the Nectaris basin event. Marchi et al. (2012) interpreted their impactor population changes from the “early” population to an intermediate population to be caused by impactor velocities twice as fast as the “early” population, but without change in the impactor SFD. This is consistent with the model that the LHB projectiles came from an ancient E-belt at the inner margin of the asteroid belt (Bottke et al., 2012; Morbidelli et al., 2012). Head et al. (2010) and Fassett et al. (2012b), however, stated that their observed CSFDs agree with findings from Strom et al. (2005), who concluded that the LHB projectiles came from the Main Asteroid Belt, not just a specific region at its inner margin. However, Cuk et al. (2010) argued that the source of lunar cataclysm impactors could not be the Main Asteroid Belt.

These observations and findings on varying CSFDs on the lunar surface are at variance with one another and highly depend on the interpretation of asteroid belt evolution models and subsequent geological processes. Thus, to address the question of whether the PF has changed with time and when the potential transition occurred to produce differently shaped CSFDs, we re-investigated the crater frequencies of the key lunar basins as listed by Fassett et al. (2012b) using their crater measurements, but applying a new CSFD technique. The buffered non-sparseness correction (Kneissl et al., 2016) more rigorously accounts for crater obliteration on densely cratered surfaces. Then, we examined the basin stratigraphy based on both $N(20)$ value, i.e. the crater frequencies ≥ 20 km and the derived absolute model ages. We also used image and topographical datasets to explore the basin relationships, as well as previous studies (Wilhelms, 1987; Fassett et al., 2012b; Hiesinger et al., 2012b). Finally, we studied the shape of the summed CSFDs of Pre-Nectarian, Nectarian and Imbrian aged basins and inferred potential projectile populations.

5.2. Data and Methods

For the direct comparison of our corrected CSFDs with Fassett et al. (2012b), we use their crater measurements along with their geologic mapping. The mapping covers the remnants of each investigated basin and attempts to exclude the resurfaced areas (e.g. mare deposits or ejecta material from larger impacts). The crater measurements are based on the lunar crater catalog (Head et al., 2010), which was compiled using Lunar Reconnaissance Orbiter Lunar Orbiter Laser Altimeter (LOLA) data (Smith et al., 2010; Smith et al., 2017) and contains all impact craters with diameters ≥ 20 km.

Additional craters beyond that database were included from younger surfaces (Fassett et al., 2012b). First, we reloaded all the CSFD measurements into new shapefiles and recalculated the area and crater sizes in an updated CraterTools extension (Kneissl et al., 2011; Kneissl et al., 2015) in ESRI ArcGIS 10.3.

Then, we used the new CSFD method, the buffered non-sparseness correction (BNSC) (Kneissl et al., 2016) which was implemented in CraterTools in ArcGIS, but not yet released to the public. A standalone tool will be soon available (Riedel et al., 2017). The motivation for the new technique comes from the fact that smaller craters on highly cratered surfaces were previously undercounted with respect to their accumulation due to their obliteration by larger craters and their ejecta blankets.

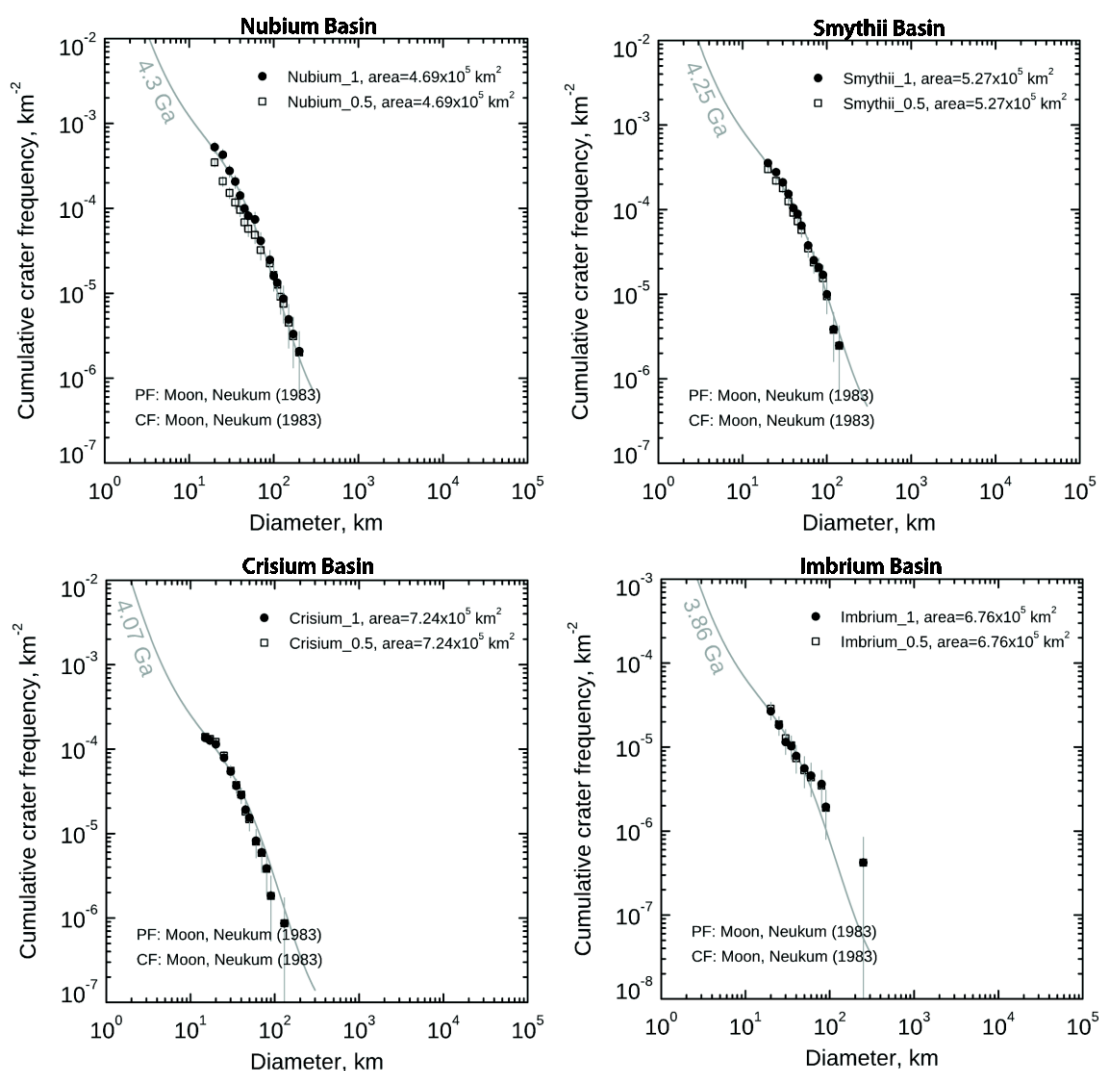


Figure 5.2: The figure compares the effect of different exclusion radius: 1 (black filled circle) and 0.5 (black empty square) from the crater rim. We can say that the different exclusion radii do not significantly change the results. Although, the Pre-Nectarian-aged Nubium and Smythii basins represent slightly larger difference than Nectarian-aged Crisium and Imbrian-aged Imbrium basin.

Thus, this technique takes non-sparseness into account (see in Kneissl et al. (2016) Figure 1, and this study Figure 5.1). It is important to mention that each crater is referenced to an area excluding regions in the study area that have been resurfaced by larger craters, thus the reference area becomes smaller for correspondingly smaller crater sizes. The other part of the new method makes use of buffered crater counting (BCC), which includes all craters overlapping the counting area with a buffer, but whose center is located outside of the region of interest (Fassett & Head, 2008; Fassett et al., 2012b; Kneissl et al., 2015). The use of the buffer allows us to increase the number of craters included in the measurements, giving better statistics. The width of the buffer depends on the estimated range of the ejecta blanket (Kneissl et al., 2015). In this study, we took the region affected by ejecta to be 1 crater radius radial from the crater rim. This removes the region obliterated by the craters and the thickest part of the ejecta. We could increase the area removed to be more certain, but at the cost of further decreasing the counting statistics. We compiled a figure to show different exclusion radius, namely 1 and 0.5 crater radius from the crater rim. We can say that the different exclusion radii do not significantly change the results. It has a larger effect in the case of older basins (Nubium, Smythii) (Figure 5.2). Thus, if a nearby, smaller crater's center falls into this 1 crater radius, the smaller crater will be excluded unless a portion of this crater still overlaps the counting area. In this case, the smaller crater will be taken into consideration with the buffer, because the crater has age information about the area under consideration. The included and excluded craters for each basins can be seen in the Appendix A and also in Figure 5.3. We represent the CSFDs using 2 different approaches: (1) BCC – as done by Fassett et al. (2012b), and the new approach (2) BNSC. To understand how crater obliteration affects the CSFDs we investigated the general influence of BNSC techniques on CSFD curves (Kneissl et al., 2016) (see in Figure 5.3) by comparing the results of different techniques applied systematically to different key regions used in the previous study (Fassett et al., 2012b).

We derived the $N(20)$ and $N(64)$ values, i.e., the frequency of craters ≥ 20 km and ≥ 64 km, as was done by Fassett et al. (2012b), and normalized these to an area of 10^6 km². Using $N(20)$ allows the comparison of the crater densities over a larger diameter range than $N(64)$. The error was calculated as follows: $N(X)$ crater frequency divided by the square root of the number of craters. The basins were listed in two tables: (1) based on $N(20)$ as presented in Fassett et al. (2012b) (see in Table 5.1), and (2) the determined absolute model age (Table 5.2) values. Table 5.1 shows the comparison of $N(20)^*$ from Fassett et al. (2012b) and $N(20)$ as well as $N(64)$ from this study. The factor in Table 5.1 shows the difference in $N(20)$ as a percentage for the individual basins. The changes in Table 5.1 refer to the differences in the ranking of the basins compared to Fassett et al. (2012b). Additionally, we studied the relationships of the crater frequencies and absolute model ages to stratigraphical observations from previous studies (Wilhelms, 1987; Fassett et al., 2012b).

We determined the absolute model ages of lunar basins (Table 5.2) making use of the CraterStats software (Michael & Neukum, 2010; Michael, 2013) and applied the lunar

PF and CF from Neukum (1983). To derive the absolute model ages, we used the cumulative fit and the μ -notation, which represents the compounded uncertainties of the particular chronology model (Michael et al., 2016). Here, we applied the cumulative and differential plots with pseudo-log crater binning (Neukum, 1983). All CSFD plots with corresponding counting areas are available in the Appendix A. Finally, to compare the nature of the impactor population(s) to Fassett et al. (2012b), we derived the shape of the summed CSFDs of Pre-Nectarian, Nectarian, and Imbrian-aged basins using an R-plot with 10/decade binning (Figure 5.4). Note that the only change in data analysis between Fassett et al. (2012b) and this study is the distinct CSFD analysis technique, because we aggregated the same basins from each time period as Fassett et al. (2012b). The bins were fitted to the lunar PF (Neukum, 1983) in the crater diameter range of 20 – 200 km (Pre-Nectarian basins), 20 – 130 km (Nectarian basins) to get compared to Fassett et al. (2012b) and 8 – 70 km (Imbrian basins) to show the shape of the CSFD curve.

5.3. Results and Interpretation

5.3.1. Crater Frequencies with BNSC

Due to their old ages, the lunar basins are non-sparsely cratered surfaces where craters overlap each other at various sizes. We derived the crater densities of key lunar basins (Fassett et al., 2012b) using 2 different CSFD techniques: BCC and BNSC (Figure 5.3). The crater frequencies given by the BNSC technique reflect an increase in the measured frequencies of smaller craters (Table 5.1), seen as upward shifted crater bins in the CSFD with respect to the crater frequencies derived from the BCC technique alone (Figure 5.3). Our results show that crater frequencies increase by a factor of 24% (Table 5.1/Factor) compared to Fassett et al. (2012b). The shift is due to the corrected reference areas, namely that the density of smaller craters become higher in the correspondingly smaller reference areas when areas resurfaced by larger subsequent craters have been removed. This difference in the CSFDs grows systematically larger for older surfaces, such as Pre-Nectarian and Nectarian basins. However, there is little to no effect of the BNSC technique on Imbrian basins, because craters are sparse on these younger surfaces. In fact, almost no craters were excluded from the analysis because of their sparse distribution. Furthermore, the results of all individual basins correspond better to the lunar PF (Neukum, 1983) over a larger diameter range, than those CSFDs derived with BCC, as shown in Figure 5.3.

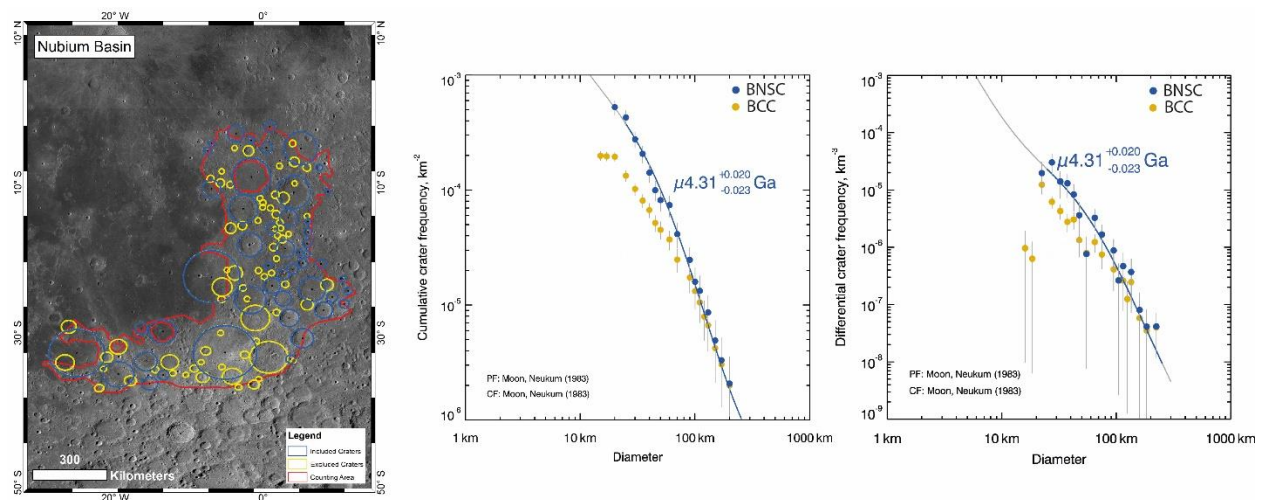


Figure 5.3: Crater measurement map and derived CSFD with absolute model age of Nubium Basin after Neukum (1983). Counting area over Lunar Reconnaissance Orbiter Camera Wide Angle Camera (LROC WAC) 100 m/pixel mosaic base map. Craters marked with blue circle were counted during calculation, craters marked in yellow were excluded. CSFD cumulative and differential plots of Nubium Basin using two different crater counting techniques: BCC (yellow filled circle), and BNSC (blue filled circle). The BNSC data shows that the smallest crater bins are corrected to higher crater frequencies when accounting for crater non-sparseness. Absolute model age was derived from Neukum (1983) and included the μ -notation, which shows the uncertainty of calibration of the chronology model.

5.3.2. Refined Basin Sequence

As a result of the improved CSFDs, our derived $N(20)$ crater frequencies for the individual lunar basins are different than Fassett et al. (2012b), which changes the basin sequence significantly. The differences increase on surfaces with higher crater densities, since these surfaces are where the largest corrections in CSFDs were made using the BNSC technique. Consequently, the changes in basin sequence are more noticeable on older (Pre-Nectarian-aged and Nectarian-aged) than younger (Imbrian-aged) surfaces (Table 5.1/Changes). Nubium basin has the highest $N(20)$ crater frequency (526 ± 77) with a high $N(64)$ (61 ± 14) as well. The difference (169%) compared to Fassett et al. (2012b) is the largest. The higher crater frequency can be explained by the exclusion of area that had been resurfaced by subsequent craters and their ejecta. Furthermore, Amundsen-Ganswindt basin with a factor of 77%, includes Schrödinger basin, which in turn causes the exclusion of a large portion of relatively smaller craters from the counting area, and increases the density of the rest of the craters in the area of interest. The discrepancy between $N(20)^*$ (Fassett et al., 2012b) and our $N(20)$ is lowest in Coulomb-Sarton (+3%) and Fitzgerald-Jackson (+5%) basins. Hertzprung basin shows a negative factor, namely a decreased crater frequency compared to Fassett et al. (2012b). This effect of the technique could be interpreted with the distribution of larger craters which are separated from each other

and relatively large craters are excluded from the calculation due to obliteration. The derived Imbrian crater frequencies are slightly lower or the same as Fassett et al. (2012b) reported. As mentioned above, the BNSC technique plays only a minor role for sparsely cratered surfaces (Kneissl et al., 2016). In the case of the Schrödinger basin, there is no difference between the crater frequencies. The outcome is due to the relatively large (318076 km²) counting area and the widely distributed craters, which means that crater obliteration is negligible in the investigated crater-size range. The same can be concluded for Imbrium and Orientale basins as for Hertzprung basin.

The absolute model ages are dependent on the chronology model and the crater diameter range which can be fitted to the PF (Neukum, 1983), thus we highlight the basin sequence based on the model ages in a separate Table 5.2. Birkhoff, Ingenii and Fitzgerald-Jackson basins represent relatively older ages and high $N(64)$ values (49 ± 19 , 63 ± 22 , 80 ± 36 , respectively), although very low $N(20)$ crater frequencies (223 ± 58 , 198 ± 53 , 184 ± 70 , respectively). This means that the larger craters were preserved better on the surface than smaller craters as also observed by Povilaitis et al. (2017). These old basins however, contain many large superposed craters that have destroyed craters in the 20 km range, thus resulting in low $N(20)$ values. Thus, these basins are shown in the lower section of the basin sequence based on $N(20)$. This is due to the fact that the PF (Neukum, 1983) appears more consistent with the larger crater sizes in the CSFD and the smaller craters < 30 km fall off from that PF suggesting there has been some loss at this scale and the low $N(20)$ could be explained by resurfacing.

We note the following differences between the stratigraphical observations and derived basin sequences. In the current study, to compare $N(20)$ with basin stratigraphy Freundlich-Sharanov was placed as a Nectarian basin, instead of Pre-Nectarian (Wilhelms, 1987; Fassett et al., 2012b). It has been debated whether Apollo basin belongs to the Pre-Nectarian period (Wilhelms, 1987; Fassett et al., 2012b; Hiesinger et al., 2012b), but according to our absolute model age it is clearly younger than the Nectaris basin forming event, although the error bars overlap in $N(20)$. Coulomb-Sarton and Lorentz pre-date Birkhoff basin in the stratigraphy (Wilhelms, 1987), and the $N(20)$ reflects the same relationship in Fassett et al. (2012b) and our work as well. However, the absolute model ages do not conform with this stratigraphy, because the $N(64)$ value for Birkhoff basin places it much higher in the sequence. Mendeleev basin is younger than Moscoviense basin (Wilhelms, 1987), in good agreement with our $N(20)$ result, but contradicts Fassett et al. (2012b). On the other hand the absolute model age shows the opposite stratigraphic relationship, due to the high $N(64)$ for Mendeleev basin, in agreement with Fassett et al. (2012b). It should be pointed out that the stratigraphic sequence is debated in the case of the Humboldtianum and Crisium basins. The observation from Fassett et al. (2012b) is consistent with both of our $N(20)$ results, namely that Crisium is older than Humboldtianum basin, although the error bars in the $N(20)$ overlap, as well as the

absolute model ages. The younger, Imbrian basin sequence retains the same stratigraphic position in our analysis as in Fassett et al. (2012b).

5.3.3. Impactor Population

To investigate the nature of the impactor population(s), we plotted the summed CSFDs of the Pre-Nectarian-aged basins (excluding South Pole-Aitken Basin (SPA)), Nectarian-aged basins (including Nectaris), and Imbrian-aged basins (including Imbrium) on an R-plot as was done by Fassett et al. (2012b). Figure 5.4 displays a comparison between the study by Fassett et al. (2012b) (Figure 5.4/a) and the current study (Figure 5.4/b), where the summed CSFDs were produced by two different CSFD techniques: (1) BCC and (2) BNSC, respectively. Figure 5.4/a (Fassett et al., 2012b) shows a distinct difference in the CSFD of the Pre-Nectarian distribution, in comparison to the Nectarian and Imbrian distributions, expressed as a steep slope in the CSFD below 100 km size range, that does not conform to the lunar PF (grey isochrons). This observation led to the conclusion that different impactor populations could explain the change in the CSFD from the Pre-Nectarian to the Nectarian period (Fassett et al., 2012b). However, our results show that the shape of the CSFD is in fact unchanged (Figure 5.4). The above mentioned steep slope does not appear in our Pre-Nectarian CSFD. The proper accounting of smaller craters corrects the crater bins in the CSFD upward, thus the slope is removed by using the non-sparseness correction. Moreover, the CSFDs correspond better to the PF (Neukum, 1983) over almost the entire crater diameter range. Nevertheless, a few crater bins in the larger end of Pre-Nectarian (150 – 170 km) and Nectarian (110 – 120 km) basins fall off from that PF, when applying the non-sparseness correction.

5.4. Discussion

5.4.1. Impactor Populations and the LHB

During the formation periods of the Pre-Nectarian and Nectarian basins, crater obliteration was an important process which affected the crater population on the surface (Kneissl et al., 2016). Applying the BNSC to the CSFDs for the lunar basins, we found $N(20)$ densities that were on average 24% higher than in Fassett et al. (2012b), who already reported 50% higher crater densities in comparison to Wilhelms (1987). This may be explained in part by the global data coverage both from the WAC and LOLA instruments on the Lunar Reconnaissance Orbiter, but the improvements are primarily due to the improved CSFD technique. The observed shift in the CSFDs come from the correct accounting of the smaller crater population on highly cratered surfaces by excluding those areas where obliteration has occurred. Thus, we can much more accurately measure crater production on a given surface.

5. REINVESTIGATION OF THE DIFFERENT IMPACTOR POPULATIONS ON THE LUNAR SURFACE

Table 1: Derived absolute model ages of lunar basins using the buffered non-sparseness correction, ranked by N(20) frequency. ^aData from Fassett et al. (2012b), ^bDifference in crater frequencies between N(20)_a and N(20) in %, ^cChange in sequence compared to Fassett et al. (2012b). The model ages quoted for each basin with the respected μ -notation do not include the systematic uncertainties in the chronology model.

| # | Lunar basins | Period | N(20) ^a | N(20) | N(64) | Factor ^b | Change ^c | Model Age |
|----|---------------------|--------|--------------------|---------|-------|---------------------|---------------------|---------------------|
| | | | | | | (%) | | μ (Ga) |
| 1 | South Pole-Aitken | PN | 156 ±7 | 254±21 | 39±5 | 62 | 0 | 4.31±0.019, 0.021 |
| 2 | Nubium | PN | 195±18 | 526±77 | 61±14 | 169 | ↑6 | 4.31±0.020, 0.023 |
| 3 | Cruger-Sirsalis | PN | 262±46 | 365±86 | 43±19 | 39 | ↑1 | 4.26±0.032, 0.041 |
| 4 | Amundsen-Ganswindt | PN | 202±37 | 359±108 | 56±25 | 77 | ↑3 | 4.26±0.038, 0.052 |
| 5 | Smythii | PN | 225±19 | 355±39 | 32±8 | 57 | 0 | 4.26±0.016, 0.018 |
| 6 | Dirichlet-Jackson | PN | 266±36 | 346±60 | 28±11 | 30 | ↓3 | 4.23±0.022, 0.026 |
| 7 | Serenitatis | PN | 298±60 | 334±73 | 6±6 | 12 | ↑7 | 4.22±0.027, 0.033 |
| 8 | Poincare | PN | 194±44 | 286±61 | 38±16 | 47 | ↑1 | 4.23±0.031, 0.040 |
| 9 | Coulomb-Sarton | PN | 271±54 | 281±63 | 26±13 | 3 | ↓8 | 4.23±0.025, 0.030 |
| 10 | Lorentz | PN | 179±31 | 275±60 | 37±14 | 53 | 0 | 4.20±0.029, 0.036 |
| 11 | Schiller-Zucchius | PN | 211±47 | 234±65 | 29±15 | 10 | ↓5 | 4.24±0.038, 0.052 |
| 12 | Birkhoff | PN | 170±33 | 223±58 | 49±19 | 31 | 0 | 4.29±0.035, 0.047 |
| 13 | Ingenii | PN | 167±33 | 198±53 | 63±22 | 18 | 0 | 4.28±0.035, 0.047 |
| 14 | Fitzgerald-Jackson | PN | 175±34 | 184±70 | 80±36 | 5 | ↓3 | 4.26±0.044, 0.063 |
| 15 | Freundlich-Sharanov | PN/N | 140±18 | 173±25 | 17±6 | 23 | ↑1 | 4.14±0.019, 0.023 |
| 16 | Nectaris | N | 135±14 | 172±20 | 15±4 | 27 | 0 | 4.17±0.012, 0.014 |
| 17 | Grimaldi | N | 126±28 | 165±43 | 28±13 | 30 | ↑3 | 4.14±0.033, 0.044 |
| 18 | Mendel-Rydberg | N | 125±17 | 158±26 | 14±5 | 26 | ↑3 | 4.13±0.022, 0.026 |
| 19 | Apollo | N | 151±23 | 158±29 | 12±6 | 4 | ↓5 | 4.14±0.024, 0.029 |
| 20 | Planck | N | 118±36 | 135±48 | 17±12 | 14 | ↑2 | 4.13±0.038, 0.053 |
| 21 | Moscoviense | N | 120±17 | 128±19 | 10±4 | 6 | ↑2 | 4.09±0.020, 0.024 |
| 22 | Korolev | N | 127±22 | 128±24 | 8±5 | 0.7 | ↓5 | 4.11±0.021, 0.025 |
| 23 | Mendeleev | N | 129±36 | 125±40 | 14±10 | -3.2 | ↓5 | 4.13±0.044, 0.064 |
| 24 | Humorum | N | 108±21 | 121±25 | 9±5 | 12 | ↑1 | 4.09±0.023, 0.027 |
| 25 | Hertzprung | N | 129±22 | 116±26 | 17±7 | -22.5 | ↓6 | 4.09±0.030, 0.037 |
| 26 | Crisium | N | 113±11 | 114±13 | 7±3 | 0.8 | ↓2 | 4.07±0.016, 0.018 |
| 27 | Humboldtianum | N | 93±14 | 109±19 | 9±4 | 17 | ↓1 | 4.08±0.026, 0.032 |
| 28 | Imbrium | I | 30±5 | 26±5 | 4±2 | -13.4 | 0 | 3.87±0.035, 0.046 |
| 29 | Schrödinger | I | 19±7 | 19±7 | 4±3 | 0 | 0 | 3.86±0.025, 0.030 |
| 30 | Oriente | I | 21±4 | 20±4 | 1±1 | -5 | 0 | 3.81±0.0081, 0.0085 |

5. REINVESTIGATION OF THE DIFFERENT IMPACTOR POPULATIONS ON THE LUNAR SURFACE

Table 2: Derived absolute model ages of lunar basins using the buffered non-sparseness correction, ranked by model age. The model ages quoted for each basin with the respected μ -notation do not include the systematic uncertainties in the chronology model. Data listed in "Stratigraphy" from Fassett et al. (2012) and Wilhelms et al. (1987). The sample ages are from the review of Stöffler et al. (2006), and references therein. (1) Stöffler et al. (2006), (2) Norman et al. (2006), (3) Norman and Nemchin (2014), (4) Swindle et al. (1991), (5) Schmitt et al. (2017), (6) Norman et al. (2010), and (7) Snape et al. (2016).

| # | Lunar basins | Period | Model Age μ (Ga) | Stratigraphy* (Fassett et al., 2012) | Stratigraphy* (Wilhelms et al., 1987) | Sample ages (Ga) | Ref. |
|----|---------------------|--------|----------------------|--|--|---|-------------------|
| 1 | South Pole-Aitken | PN | 4.31±0.019, 0.021 | Oldest lunar basin | | | |
| 2 | Nubium | PN | 4.31±0.020, 0.023 | > Humorum | > Imbrium, Humorum | | |
| 3 | Birkhoff | PN | 4.29±0.035, 0.047 | | > Imbrium, Hertzsprung | | |
| 4 | Ingenii | PN | 4.28±0.035, 0.047 | | | | |
| 5 | Amundsen-Ganswindt | PN | 4.26±0.038, 0.052 | > Schrödinger | > Schrödinger | | |
| 6 | Cruger-Siralis | PN | 4.26±0.032, 0.041 | | | | |
| 7 | Smythii | PN | 4.26±0.016, 0.018 | > Crisium | > Crisium | | |
| 8 | Fitzgerald-Jackson | PN | 4.26±0.044, 0.063 | > Freundlich-Sharanov | | | |
| 9 | Schiller-Zucchius | PN | 4.24±0.038, 0.052 | | > Orientale, Humorum | | |
| 10 | Dirichlet-Jackson | PN | 4.23±0.022, 0.026 | > Korolev | | | |
| 11 | Coulomb-Sarton | PN | 4.23±0.025, 0.030 | > Birkhoff | > Orientale, Imbrium, Hertzsprung, Lorentz, Birkhoff | | |
| 12 | Poincare | PN | 4.23±0.031, 0.040 | | > Schrödinger, Planck | 3.98±0.05 | (1) |
| 13 | Serenitatis | PN | 4.22±0.027, 0.033 | > Nectaris | > Imbrium | 3.89±0.01 3.87±0.03 | |
| 14 | Lorentz | PN | 4.20±0.029, 0.036 | | > Orientale, Imbrium, Birkhoff | | |
| 15 | Nectaris | N | 4.17±0.012, 0.014 | | > Imbrium | 3.85±0.05 4.10±0.10 3.92±0.03 3.75-3.96 4.22±0.01 | (1) (2) (3) |
| 16 | Grimaldi | N | 4.14±0.033, 0.044 | > Mendel-Rydberg | > Orientale | | |
| 17 | Freundlich-Sharanov | N | 4.14±0.019, 0.023 | > Moscoviense | > Moscoviense, Mendeleev, Korolev | | |
| 18 | Apollo | N | 4.14±0.024, 0.029 | > Korolev, Hertzsprung | > Orientale, Korolev, Hertzsprung | | |
| 19 | Mendeleev | N | 4.13±0.044, 0.064 | | | | |
| 20 | Planck | N | 4.13±0.038, 0.053 | > Schrödinger | > Schrödinger | | |
| 21 | Mendel-Rydberg | N | 4.13±0.022, 0.026 | | > Orientale | | |
| 22 | Korolev | N | 4.11±0.021, 0.025 | > Hertzsprung | > Orientale, Hertzsprung | | |
| 23 | Humorum | N | 4.09±0.023, 0.027 | | > Orientale, Imbrium | | |
| 24 | Hertzsprung | N | 4.09±0.030, 0.037 | | > Orientale | | |
| 25 | Moscoviense | N | 4.09±0.020, 0.024 | | > Mendeleev, Humboldtianum | | |
| 26 | Humboldtianum | N | 4.08±0.026, 0.032 | | | | |
| 27 | Crisium | N | 4.07±0.016, 0.018 | > Humboldtianum | > Imbrium, Serenitatis | 3.89±0.02 3.84±0.04 3.89±0.017 3.89-3.93 | (1) (4) (5) |
| 28 | Imbrium | I | 3.87±0.035, 0.046 | | | 3.91±0.01 3.85±0.02 3.77±0.02 3.86±0.09 3.93±0.02 | (1) (6) |
| 29 | Schrödinger | I | 3.86±0.025, 0.030 | | > Orientale | | |
| 30 | Orientale | I | 3.81±0.0081, 0.0085 | | | | |

A changing CSFD would indicate more than one impacting population. Tera et al. (1974) found an age of 3.9 Ga for the lunar rock samples and suggested the existence of the Late Heavy Bombardment. Based on crater size-frequency distribution measurements from the lunar surface, a changing impactor population between 4.1 – 3.8 Ga was suggested by numerous authors (Strom et al., 2005; Head et al., 2010; Fassett et al., 2012; Marchi et al., 2012). One possible scenario for a changing population could be an event in the Solar System which caused an impact rate spike or cataclysm on the Moon. For example, a migration of the giant planets might eject projectiles with an increased flux from the Main Asteroid Belt into the inner Solar System causing a higher impact rate on the Moon (Gomes et al., 2005; Morbidelli et al., 2005; Tsiganis et al., 2005; Morbidelli et al., 2012). Fassett et al. (2012b) saw a steep slope in the diameter range from 20 km to 100 km in the summed CSFD of the Pre-Nectarian basins and concluded a changing impactor population earlier than the mid-Nectarian period. In contrast, our results indicate that the steep slope is due to the under-counting of smaller crater densities in non-sparsely cratered terrain. We find a CSFD consistent with those from later periods without a steep slope in the distribution. Nevertheless, an unchanging population of the impacting projectiles likewise gives no timing information, and does not exclude the impact spike scenario. It does however constrain the spike scenario – if it occurred – to bombardment of the Moon with a similar SFD impactor population: this could be by excitement of the same source population, or alternatively a collisionally evolved population with similar SFD.

5.4.2. Basin Sequence and Sample Ages

The Apollo and Luna missions provided the samples to derive radiometric ages of mare basalts and impact events. The uncertainty of the provenance of impact melt breccias on the lunar surface makes the age dating of the lunar basins highly challenging. Because of the clustered locations and limited number of Apollo landing sites, the contamination of impact melt breccias from different impact events is highly possible (Stöffler et al., 2006). Nevertheless, these rock samples are the only direct age information from the lunar impact basins.

5.4.2.1. Serenitatis Basin

In earlier studies, Serenitatis was classified as a Pre-Nectarian basin (Baldwin, 1974; Fassett et al., 2012b; Head, 1974; Stuart & Howard, 1970; Wilhelms & McCauley, 1971), although Wilhelms (1987) thought Serenitatis was younger than the nearby Crisium basin based on stratigraphy. Dating of the Serenitatis basin was attempted by analyzing impact melt from the Apollo 17 mission, which landed in the Taurus-Littrow region, on the eastern rim of Serenitatis basin. Unfortunately, most of the impact melt breccias collected there have an uncertain provenance due to subsequent impact events, such as those forming the Imbrium and Crisium basins, or Tycho Crater. The radiometric ages of the impact melt breccias vary between 3.87 – 3.98 Ga (Stöffler et

al., 2006) and recalculated $^{40}\text{Ar} - ^{39}\text{Ar}$ analysis of samples shows ages between 3.89 – 3.93 Ga (Schmitt et al., 2017), which are not consistent with the CSFD results from Fassett et al. (2012b) or our study (4.22 +0.027, -0.033 Ga) (Table 5.2). Nevertheless, a recent study from Spudis et al. (2011) also placed Serenitatis stratigraphically in the middle of the Pre-Nectarian period and they explained the absence of older sample ages by the fact that impact melt from Serenitatis was not collected. They interpret the young radiometric ages as samples originating mostly from Imbrium. Furthermore, Fassett et al. (2012b) provided observational evidence that Serenitatis pre-dates Crisium: (1) sculptured ejecta from Nectaris and Crisium basins overlapping, (2) large and degraded craters which are filled with Imbrium ejecta material, and (3) crater densities on Serenitatis that are twice those on Crisium. The old age of Serenitatis from our study is consistent with the crater density and observational evidence from Fassett et al. (2012b). We agree that Serenitatis must be a Pre-Nectarian basin.

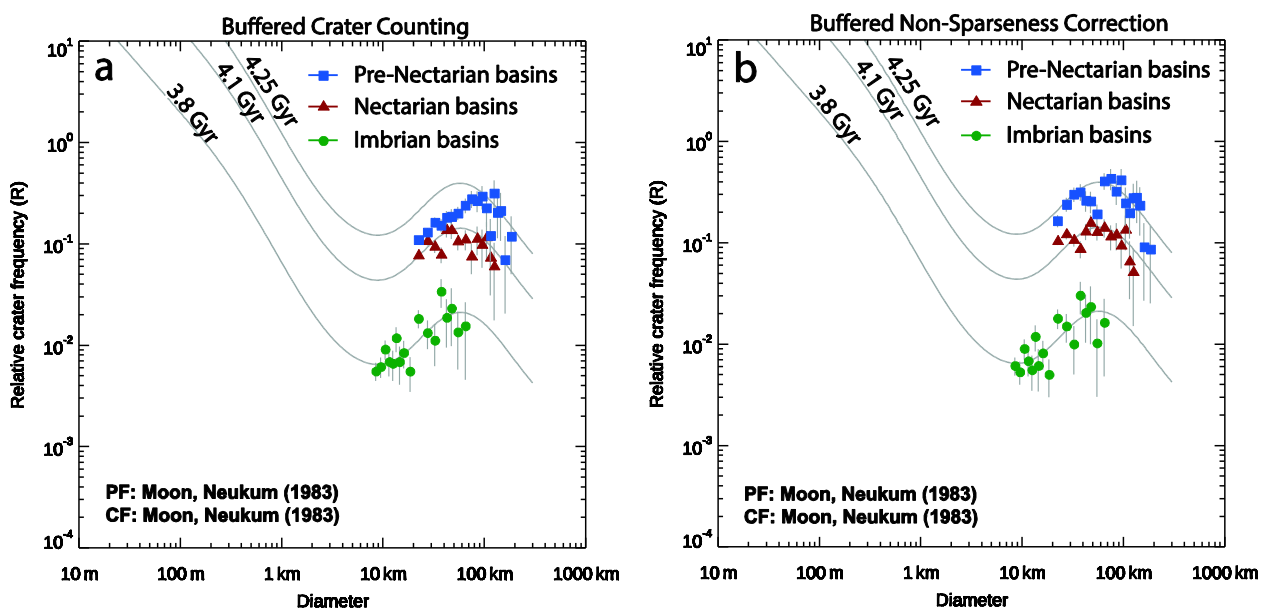


Figure 5.4: Summed CSFDs of the Pre-Nectarian-aged basins (excluding SPA, blue filled square), Nectarian-aged basins (including Nectaris, red filled triangle) and Imbrian-aged basins (including Imbrium, green filled circle) to study the impactor population(s) using an R-plot representation. a) Fassett et al. (2012b) found a change in the shape of CSFDs using the BCC method (Fassett & Head, 2008) and suggested different impactor populations with a transition occurred from Pre-Nectarian to Nectarian periods (blue filled square vs. red filled triangle), but earlier than mid-Nectarian. Note that the shape of Pre-Nectarian CSFD shows a steep slope in the diameter range from 20 km to 100 km. b) In contrast, our study shows similarities in the shape of the summed CSFDs derived using the BNSC technique for each period. The steep slope in the summed CSFD of the Pre-Nectarian basins is no longer present in our study. This figure has been modified after **Orgel et al. (2018)**, where the representation of the data has only changed, but the content remained the same.

5.4.2.2. Nectaris Basin

Apollo 16 landed on the highlands of Nectaris basin. The earlier studies (Stöffler et al., 2006) indicated that the most reliable age constraints for the age of Nectaris basin might come from analysis of the Descartes Formation. The samples show a range of ages between 3.85 – 4.1 Ga, the youngest of which represents the basement of North Ray Crater, and was proposed as the age of Nectaris basin forming event (Stöffler et al., 1985). Recent $^{40}\text{Ar} - ^{39}\text{Ar}$ analysis of impact melt breccias by Norman et al. (2006) indicated a radiometric age in the range from 3.75 Ga to 3.96 Ga. Only one sample (63525) from North Ray Crater gave an outlying result of 4.19 Ga. Moreover, Norman & Nemchin (2014) analyzed the zirconolite and apatite in another sample (67955) with the U-Pb system and derived an absolute age of $4.22 \pm 0.01, -0.01$ Ga indicating a basin-scale impact melting event. Additionally, Norman et al. (2010) determined a radiometric age of $3.866 \pm 0.09, -0.09$ Ga from the trace element composition of lunar breccias (67016 and 67455) from the Descartes region. Based on geochemistry, the provenance for the impact melt breccia might be the Procellarum-KREEP Terrane, thus most likely indicate the Imbrium impact, rather than Nectaris. In this study an age of $4.17 +0.012, -0.014$ Ga has been proposed for the Nectaris basin which corresponds well with the older age results from Norman et al. (2006), Norman et al. (2010), and Norman & Nemchin (2014), but exceeds the ages proposed in Stöffler et al. (1985), and Stöffler et al. (2006) (Table 5.2).

5.4.2.3. Crisium Basin

The robotic Luna 20 exploration mission visited the southern rim of Crisium basin and brought 30 g of samples back to Earth. The majority of the sample represented anorthositic highland material, however one fragment may represent Crisium (Swindle et al., 1991). In the review from Stöffler et al. (2006), the radiometric age is in the range from 3.84 Ga to 3.89 Ga, which might date the formation of the Crisium basin (see in Table 5.2), although it remains uncertain whether the samples represent Crisium or different impact event. The recent study from Schmitt et al. (2017) corrected radiometric ages of samples between 3.89--3.93 Ga, while traditional CSFD measurements on proposed impact melt exposures in Crisium give an absolute model age of $3.94 \pm 0.05, -0.05$ Ga (van der Bogert et al., 2018). Crater statistics from this study yield $4.07 +0.016, -0.018$ Ga which is slightly older than the radiometric ages of samples. Both the proposed radiometric and absolute model ages of Serenitatis are still older than Crisium, thus Crisium must be younger in age as our study also suggested.

5.4.2.4. Imbrium Basin

The extent of the lunar surface affected by the Imbrium impact event and the consequences for the sample collection is still debated. The Apollo 15 mission landed on the rim of Imbrium basin, but rock samples from Apollo 14, 16, and 17 landing sites might also contain ejecta material from Imbrium. The ages of impact melts from Apollo 15 vary between 3.77 Ga and 3.92 Ga (Stöffler et al., 2006; Norman et al., 2010; Snape et al., 2016) (see in Table 5.2). Impact melt rocks at Apollo 15 landing site were collected from the Apennine Front and have a radiometric age of 3.85 ± 0.02 , -0.02 Ga (Stöffler et al., 2006). The Fra Mauro Formation at Cone Crater near Apollo 14 is interpreted to be the continuous ejecta blanket of Imbrium, which has been dated as 3.85 ± 0.02 , -0.02 Ga (Stöffler, 2006). Apollo 16 polymict breccias and impact melt rocks of the Cayley Formation might also represent Imbrium discontinuous ejecta material, with an age of 3.86 Ga (Stöffler et al., 2006). Recent studies show slightly older ages such as 3.92 – 3.99 Ga based on U-Pb and Lu-Hf radiometric measurements (Snape et al., 2016; Haber et al., 2017). These radiometric ages are in reasonably good agreement with our CSFD measurements, which gives an absolute model age of $3.87 +0.035$, -0.046 Ga for the formation of Imbrium basin.

The differences between the absolute model ages and crater frequencies derived in our study (Table 5.1 and Table 5.2) are generally related to the relatively high $N(64)$ with respect to the $N(20)$ values in the cases of the older aged basins, which also tend to have more variable $N(20)$ values. The $N(20)$ provides point-like information about the crater frequency of craters ≥ 20 km. This position in the CSFD could be located off from the major trend of the CSFD, and therefore may not represent the entire CSFD. The absolute model ages give a better approach to establishing the basin sequence, because they reflect the formation age of the basins by using a wide range of crater diameter or so-called “population density” to fit a trend to CSFD. We argue that measuring the population density from the CSFD, is a more robust approach than any specific point such as $N(20)$. Such a value may be represented either by an extrapolated $N(1)$ value, or as we do here, by a model age found through a CF. Even if one disagrees with the choice of CF, we note that the CF preserves the sequence as ranked by population density, so that the relative age sequence is maintained. On the other hand, we show that in some cases the absolute model age does not correspond to the stratigraphical observations from Wilhelms (1987). It is noteworthy to mention that the image quality and the geographic coverage of data was limited in the 1980's. We may expect that we are able to make more comprehensive measurements of the crater populations and thus derive more accurate results. Our new analysis, on the basis of recent global lunar datasets provides an updated and more complete view of the basin sequence. Therefore, we believe that the basin sequence based on model age is more accurate than the use of $N(20)$, alone.

5.4.3. Saturation Equilibrium

Some areas of the lunar highlands exhibit crater densities for craters ≥ 20 km that may be close to saturation equilibrium (Head et al., 2010; Fassett et al., 2012b; Xiao et al., 2015; Povilaitis et al., 2017). Saturation equilibrium occurs when the formation of new craters destroy equal numbers of old craters, resulting in a steady state population density (Shoemaker, 1965; Gault, 1970; Woronow, 1977). Essentially, saturation equilibrium represents the highest level of non-sparseness that a count area can reach before that count area no longer provides absolute age information. Some heavily cratered areas, such as on the central farside, have CSFDs that cannot be fit with a PF, which might indicate a role of equilibrium processes at the small crater diameter bins, but these distributions can also not be fit with any existing equilibrium function (Povilaitis et al., 2017). These CSFDs likely exhibit a suppression of the smaller crater diameter frequencies due to the non-sparseness of the craters (Neukum, 1983), and would also benefit from the BNSC. After applying the BSNC, could the corrected CSFDs tell us something new about saturation equilibrium on the Moon?

To investigate this possibility, we compared the corrected count area extents for the small crater diameter bins in our study to their respective $N(20)$ crater frequencies for each basin (Figure 5.5). As expected, we see a linear decrease in the used counting area with increasing $N(20)$ value towards older surfaces, because the level of non-sparseness increases with basin age. For example, for Imbrian basins $N(20)$ values are determined using around 100% of the original area. $N(20)$ values for Nectarian basins are based on 40-90% of the defined count area, while most $N(20)$'s for Pre-Nectarian basins were derived from 20-40% of the original areas. Four Pre-Nectarian basins (Fitzgerald-Jackson, South Pole-Aitken, Amundsen-Ganswindt, and Nubium) have less than 20% of their original count area remaining after the BNSC for determination of an $N(20)$ (Figure 5.5).

This might suggest that these basins have almost reached saturation equilibrium at crater diameters of 20 km, because the remaining count area for craters of this diameter is approaching zero, where no pristine surface remains and almost 100% of the surface has been resurfaced by craters or their ejecta. However, the relatively small number of basins in this position on the graph, suggests that few basins are saturated with craters that have diameters of 20 km, a conclusion consistent with the findings of Povilaitis et al. (2017). The BNSC method may thus be a new approach to study equilibrium condition for various crater diameters on planetary surfaces.

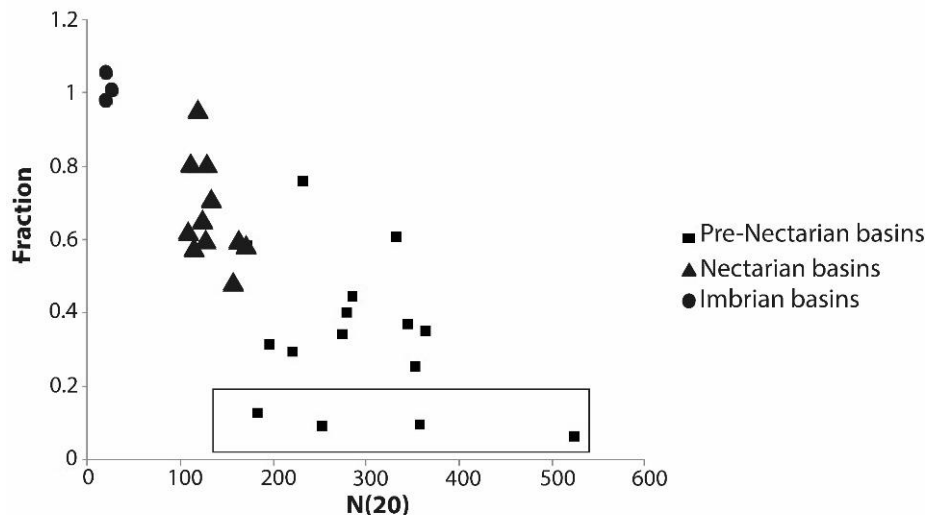


Figure 5.5: $N(20)$ versus fraction of original count area used to measure $N(20)$ crater density. The diagram shows the decrease of the remaining area after the correction “fraction”) and the increase of the $N(20)$ value towards older surfaces. The black box indicates the Fitzgerald-Jackson, South-Pole Aitken, Amundsen-Ganswindt and Nubium basins. These basins might be in saturation equilibrium. The $N(20)$ value of the corresponding basins is listed in Table 5.1.

5.5. Conclusion

We applied a buffered non-sparseness correction (BNSC) (Kneissl et al., 2016) to a crater-size frequency analysis of 30 key lunar basins. The shift in smaller crater density in the CSFD compared to the buffered crater counting technique (Figure 5.3) (Fassett & Head, 2008; Fassett et al., 2012b) represents the effect and scale of crater obliteration, and once corrected allows a larger range of the CSFD to be used to analyze the relative ages of the lunar basins, as well as shed light on the characteristics of the impactor population. This correction effect is greater on surfaces with higher crater frequencies. The corrected CSFDs better correspond to the PF from Neukum (1983) over a broader crater size range. The BNSC technique proved to make a significant difference in accounting crater densities on highly cratered surfaces.

In this study, we refined the basin sequence based on both $N(20)$ and absolute model ages. The difference in our results compared to Fassett et al. (2012b) comes from the fact that some basins such as Birkhoff, Ingenii and Fitzgerald-Jackson have relatively high $N(64)$ with respect to $N(20)$. The low $N(20)$ values placed these basins in the lower section of the Pre-Nectarian basin sequence, whereas our absolute model age results, using the full size-frequency range available in each case for the fit, provides an improved stratigraphy. Even though the relative stratigraphies from previous studies (Wilhelms, 1987; Fassett et al., 2012b; Hiesinger et al., 2012b) disagree in a few cases with our basin sequence based on absolute model ages, we still consider

that those measurements made from a broader crater size range to be more robust than establishing basin sequence based on $N(20)$ value, alone.

In contrast to previous studies (Head et al., 2010; Fassett et al., 2012b), which show a change in the shape of the CSFDs for the lunar periods, our results indicate no change in the shapes and thus, no evidence for a change in impactor population between the Pre-Nectarian and Nectarian periods.

In the future, the BNSC technique can be extended to heavily cratered surfaces of other planets in the inner Solar System, such as Mercury and Mars, because these planets have been bombarded by the same impacting projectile populations as the Moon and the lunar cratering chronology has been adapted for surface age dating on these other bodies (Ivanov et al., 2002; Neukum et al., 2001a; Strom et al., 2005). Using recently obtained MESSENGER, Mars Express, and Mars Reconnaissance Orbiter (MRO) data, reanalyzing the cratering record of these planets and applying appropriate crater-analysis techniques will provide further information about the history of different impactor populations in the inner Solar System.

As the oldest (our study: 4.31 ± 0.019 , -0.021 and Hiesinger et al. (2012b): 4.26 ± 0.03) and deepest impact structure on the Moon, the South Pole-Aitken Basin on the lunar farside remains a high priority candidate for exploration and sample return mission for NASA's third New Frontiers program, called MoonRise (NRC, 2011). Additionally, the Chinese Chang'e-4 mission proposed to visit the Apollo basin inside SPA by the end of 2018 (Wang et al., 2016). The question of the existence of the LHB and the relative and absolute stratigraphy of major lunar basins are still active questions. Sample return missions from various well preserved key locations from different time periods, such as Nubium, Smythii, Nectaris, Crisium, Humboldtianum, Orientale, and basins inside SPA (Kring & Durda, 2012; Potts et al., 2015; Steenstra et al., 2016; **Orgel et al., 2017**; Cohen et al., 2018) should be visited by robotic and human exploration missions, to help further constrain the lunar cratering chronology.

Acknowledgments

We would like to thank to David Minton, Simone Marchi and an anonymous reviewer their helpful comments to improve this manuscript. C. O. and C. R. were funded by the Deutsche Forschungsgemeinschaft (SFB-TRR 170, subproject A3-37). G. M. was supported by the German Space Agency (DLR Bonn), grant 50QM1702 (HRSC on Mars Express), on behalf of the German Federal Ministry of Economics and Technology. C. H. vdB and H. H. were funded by German Aerospace Center (DLR) project 50OW1504 and H. H. was also funded by the SFB-TRR 170, subproject A2. All the raw data for this work is available in the PDS. The original data is from Fassett et al. (2012). The derived data products are available at university data repository (http://www.planet.geo.fu-berlin.de/Orgel_etal_2017_Lunar_basins.zip) and as Supplementary Information.

CHAPTER 6

RE-EXAMINATION OF THE POPULATION, STRATIGRAPHY, AND SEQUENCE OF MERCURIAN BASINS: IMPLICATIONS FOR MERCURY'S EARLY IMPACT HISTORY AND COMPARISON WITH THE MOON

Csilla Orgel, Caleb I. Fassett, Gregory Michael, Christian Riedel, Carolyn H. van der Bogert, & Harald Hiesinger (2020), *Journal of Geophysical Research*, 125, e2019JE006212, <https://doi.org/10.1029/2019JE006212>

Abstract

Mercury has one of the best-preserved impact records in the inner Solar System due to the absence of an atmosphere and relatively unmodified ancient surface. However, our knowledge of the early impact record, and the nature of the impacting projectiles are far from complete. To get a better understanding of the early impact history, we examined large impact basins ($D \geq 300$ km) on Mercury. Here we catalogued 94 basins, 80 of which we classify as certain or probable, 1.7× times more than previously recognized. We re-evaluate the crater densities of basins using the buffered non-sparseness correction technique, which we successfully applied for the Moon. In contrast with a previous study, we find that basins have a slightly higher $N(300)$ crater density on Mercury than on the Moon, but similar $N(500)$ basin densities. Based on these results and comparison with the Moon, we infer that no more than half of the basin record remains observable and basins older than Borealis have generally been erased from the basin record. Furthermore, we establish the stratigraphic relationships of basins based on $N(25)$ crater frequencies, absolute model ages, and observations of cross-cutting relationships. Similarly to our previous study on the Moon (**Orgel et al., 2018**) we found no evidence for a change in the SFD of the impacting population, thus our results are consistent with a single impactor population that bombarded Mercury's surface.

6.1. Introduction

Mercury has one of the best-preserved impact records in the inner Solar System due to its relatively ancient surface and the absence of an atmosphere (Spudis & Guest, 1988; Strom & Neukum, 1988; Neukum et al., 2001b). The goal of this paper is to reinvestigate basin and crater densities, use these to probe the early impactor population on Mercury, and compare these with the Moon. Although Mercury and the Moon appear similar at first glance, Mercury experienced higher rates of surface modification than the Moon, as a consequence of both volcanism (Spudis & Guest,

1988; Denevi et al., 2009; Head et al., 2011; Ostrach et al., 2015; Whitten et al., 2014; Byrne et al., 2018) and impact-related resurfacing processes (Spudis & Guest, 1988; Strom & Neukum, 1988; Neukum et al., 2001b; Strom et al., 2011; Fassett et al., 2011; Fassett et al., 2012a; Braden & Robinson, 2013; Kreslavsky et al., 2014; Chapman et al., 2018). The earliest geological mapping (Trask and Guest, 1975) of the planet revealed a variety of important differences compared to the Moon, regarding both the impact basin ($D \geq 300$ km, where D is the basin diameter) and general cratering records, as well as its extensive volcanic plains.

Fassett et al. (2012a) catalogued and characterized the basin population ($D \geq 300$ km) on Mercury using data obtained by the MESSENGER spacecraft early in its orbital mission and found 46 impact basins, which were classified into three groups: certain (20) and probable (26), as well as a 41 tentative. Many of these tentative basins were proposed based on Mariner 10 and telescopic observation images, but could not be verified with the new MESSENGER data.

The nature and history of large impact basin formation on Mercury has been interpreted from two different viewpoints. The first is that the population of basins record a surge or increase in the impact rate during the early history of the Solar System, often called the Late Heavy Bombardment (LHB) (Tera, 1974; Stöffler & Ryder, 2001; Strom et al., 2005; Head et al., 2010; Fassett et al., 2012b; Marchi et al., 2012; Bottke et al., 2012; Morbidelli et al., 2012; Marchi et al., 2013; Strom et al., 2015). This increase is usually suggested to occur between ~ 3.8 and 4.1 Gyr based on the dating of lunar samples (Tera, 1974; Stöffler & Ryder, 2001; Stöffler et al., 2006), though the intensity of the postulated change in the impact flux varies substantially between different workers. It has also been proposed that the LHB included impacts from an impactor population that was distinct from the later one, which would be revealed in a crater size-frequency distribution (CSFD), or production function (PF) that changed over time. Such a hypothesis was made based on an observed difference between the CSFDs of the oldest lunar and mercurian surfaces and younger surfaces (Strom et al., 2005, 2011, 2015; Head et al., 2010, Fassett et al., 2012b). Strom et al. (2005, 2011, 2015) investigated the crater populations on the terrestrial bodies and proposed two different impactor populations: Population 1 and Population 2. They proposed that Population 1 impactors from the Main Asteroid Belt formed the oldest, heavily cratered surfaces on Mercury, Moon and Mars during the LHB. They predicted that LHB began sometime before ~ 3.9 Gyr and lasted ~ 100 to 300 Myr. Subsequently, near-Earth objects (NEOs) dominated the Population 2 impactors that cratered younger lightly cratered terrains after $3.8 - 3.7$ Gyr. Based on the CSFDs, they argued that a transition in impactor populations occurred between $3.9 - 3.8$ Gyr.

These results were supported by a later CSFD study by Head et al. (2010). Head et al. (2010) determined two different populations of impactors with a transition during the Imbrian period at less than 3.9 Gyr, close to the formation time of the Orientale basin. Their conclusions were mainly based on the pre- and post-mare crater

populations. In contrast to the study conducted by Head et al. (2010), Fassett et al. (2012b) normalized and summed the CSFDs of 30 key lunar basins assigned to the same chronostratigraphic period. Their results show a change in impactor population prior to the mid-Nectarian period, which would be consistent with an uptick of the cratering rate at 4.1 Gyr derived by Morbidelli et al. (2012).

The second view is that the basin population formed from an exponentially declining flux of planetesimals or planetesimal-derived debris following planetary accretion, or an accretion tail scenario (Hartmann, 1995; Neukum, 1983; Neukum & Ivanov, 1994; Baldwin, 2006; Ivanov, 2008; Werner, 2014; Zellner, 2017; Morbidelli et al., 2018). This scenario involves a collisionally-evolved impactor population, contributing to the cratering record within the inner Solar System, where the crater PF remained unchanged over time (Neukum, 1983; **Orgel et al., 2018**). Indeed, **Orgel et al. (2018)** showed that the apparent difference in the shape of the CSFD of the oldest lunar surfaces in comparison to the younger surfaces could be explained by the incomplete accounting for the smallest craters on heavily or nonsparsely cratered old surfaces. A non-sparse crater population causes the incremental obliteration of the smaller diameter craters in heavily cratered regions. A new technique to account for non-sparseness (Kneissl et al., 2016; **Riedel et al., 2018**) allowed **Orgel et al. (2018)** to re-examine the lunar data and correct for the effect.

Correct measurement, fitting, and interpretation of CSFDs on planetary bodies are critical for understanding the geological evolution of planetary surfaces. While the relative frequencies of craters can be used to establish relative ages for geological units, this information can also be converted to absolute model ages (AMAs) using a chronology function (CF), as established for the Moon from the radioisotope and exposure ages of lunar samples (Baldwin, 1971; Neukum, 1971, 1977; Arvidson et al., 1978; Neukum, 1983; Neukum et al., 2001b). This lunar cratering chronology can be extended for use on other planetary bodies by considering parameters such as the body's surface gravity, material properties and impact velocity (Neukum et al., 2001b). Alternatively, Le Feuvre & Wieczorek (2011) and Marchi et al. (2011) calculate PFs and CFs from a combination of astronomical observations of probable impactors and dynamical calculations to estimate the impact rate. However, due to the lack of mercurian samples, all current CFs for Mercury have substantial systematic uncertainty, which is then manifested in AMAs on Mercury.

Here, we re-examine the population of basins on Mercury as well as their superposed impact crater populations, as we also did for the Moon (**Orgel et al., 2018**). From this work, we re-examine the shape and nature of the PF on Mercury, which is critical for understanding early Solar System dynamics as well as to estimate AMAs for these major geological events on Mercury. To analyze the superposed impact crater populations, we use the buffered non-sparseness correction (BNSC) (Kneissl et al., 2016; **Orgel et al., 2018**; **Riedel et al., 2018**) and the buffered crater counting (BCC) (Fassett & Head, 2008; Fassett et al., 2012b) techniques. We also revisit the stratigraphic relationships of the basins based on crater densities and superposition

observations. As part of this process, we establish a new basin catalogue for Mercury. This list will serve as a useful basis for targeting for the upcoming BepiColombo mission.

6.2. Background

Observations from MESSENGER spacecraft data have enabled global re-examination of the cratering record of Mercury and characterization of its crater population for the first time. The new observations show a deficit in crater density in the crater diameter range of 20 – 128 km in heavily cratered terrains in comparison with the lunar highlands (Strom & Neukum, 1988; Fassett et al., 2011; Strom et al., 2011). However, the density of craters larger than 100 km is similar to the Moon. This may result from global resurfacing processes related to heavy bombardment and volcanism, where smaller craters are easily removed (Fassett et al., 2011; Marchi et al., 2013). Despite the fact that crater formation rates on Mercury are approximately three times higher than on the Moon for a given size. Consequently, the observed large craters and basins from the same impactor SFD are larger on Mercury than on the Moon (Fassett et al., 2011; Le Feuvre & Wieczorek, 2011; Marchi et al., 2011; Strom et al., 2011; Strom et al., 2015).

Baker et al. (2011) and Baker & Head (2013) catalogued complex craters, protobasins, and peak-ring basins ($D \geq 50$ km) on Mercury and the Moon. Their findings for Mercury compared with the Moon were: (1) the number of peak-ring basins and protobasins per unit area is higher, (2) the onset diameter of peak-ring basins is smaller, (3) the diameters of complex craters and peak-ring basins overlap more, and (4) complex craters are shallower. Moreover, clear multi-ring basins are absent on Mercury which may be explained by (1) lithospheric relaxation, (2) post-impact volcanic resurfacing, or (3) failure to form multi-ring structures (Fassett et al., 2012a; Chapman et al., 2018).

Generally, mercurian basins are morphologically more degraded than the lunar basins, and are commonly filled or partially filled with smooth plains. This is consistent with a more extended surface modification by volcanism and higher impact melt production (Denevi et al., 2009; Ostrach et al., 2012; Baker & Head, 2013; Ernst et al., 2015; Whitten & Head, 2015). Other surface degradation and obliteration processes may also play a role (e.g., Fassett et al., 2017), including the relatively more abundant secondary craters on Mercury (Strom, 1977).

Mercurian basin margins are often outlined by tectonic features such as wrinkle ridges, high-relief ridges and lobate scarps (Strom et al., 1975; Byrne et al., 2014; Byrne et al., 2018); these help make the identification of basins easier. The origin of these compressional landforms (thrust-faults and/or folds) have generally been interpreted to be a result of global contraction of the planet. Often, these features post-date the volcanic plains and some of these landforms follow and verge the basin perimeter (Fegan et al., 2017).

It is currently thought that major effusive volcanic activity started on Mercury earlier than 4.1 Gyr and ceased around 3.5 Gyr (Head et al., 2011; Ostrach et al., 2015; Byrne et al., 2016), but the AMAs are highly model dependent. However, small regions of plains and explosive pyroclastic deposits could be as young as few hundred million years old (Prockter et al., 2010; Thomas et al., 2014; Denevi et al., 2018a). The oldest interpreted volcanic units are the intercrater plains, which have a rough texture as well as high density of primary and secondary craters ($D < 15$ km) (Wilhelms et al., 1976; Strom, 1977; Oberbeck et al., 1977; Spudis & Guest, 1988; Head et al., 2009; Denevi et al., 2013b; Whitten et al., 2014; Weider et al., 2015; Denevi et al., 2018a). The oldest and most heavily cratered intercrater terrains on Mercury have been estimated to be about 4.0 – 4.1 Gyr old (Marchi et al., 2013). Younger smooth plains exhibit a sparsely cratered surface covering 25% of the planet with a thickness between 0.5 – 4 km (Trask & Guest, 1975; Denevi et al., 2009; Head et al., 2009; Prockter et al., 2010; Head et al., 2011; Denevi et al., 2013a; Ernst et al., 2015; Ostrach et al., 2015; Whitten & Head, 2015; Denevi et al., 2018a). Smooth plains are often geographically coincident with impact basins (Caloris, Rembrandt, and numerous other basins in the northern and southern hemisphere), however the northern smooth plains, which represent 9% of the surface, are not related to any clear large basin (Head et al., 2011). One explanation for the frequent relationship between smooth plains and basins is that large basin-scale impacts may have triggered mantle upwelling and enhanced the production of partial melt in the mantle, even some time after the impact event (Elkins-Tanton & Hager, 2005; Roberts & Barnouin, 2012).

6.3. Data and Methods

6.3.1 Data

The primary data for this study are optical images from MESSENGER's Mercury Dual Imaging System (MDIS) (Hawkins et al., 2007; Chabot et al., 2016) with a variety of solar incidence and illumination azimuths mosaicked into a 166 m/pixel global data set. Additionally, we used the color and enhanced color 665 m/pixel global data set (Denevi et al., 2016; Denevi et al., 2018b). Topography data from MESSENGER's MDIS DEM (665 m/pixel) (Becker et al., 2016) and Mercury Laser Altimeter (MLA) (250 m/pixel) (Cavanaugh et al., 2007) served as the main topographic datasets. All data products are available from the Planetary Data System (PDS). The data were analyzed in ESRI ArcGIS 10.3.

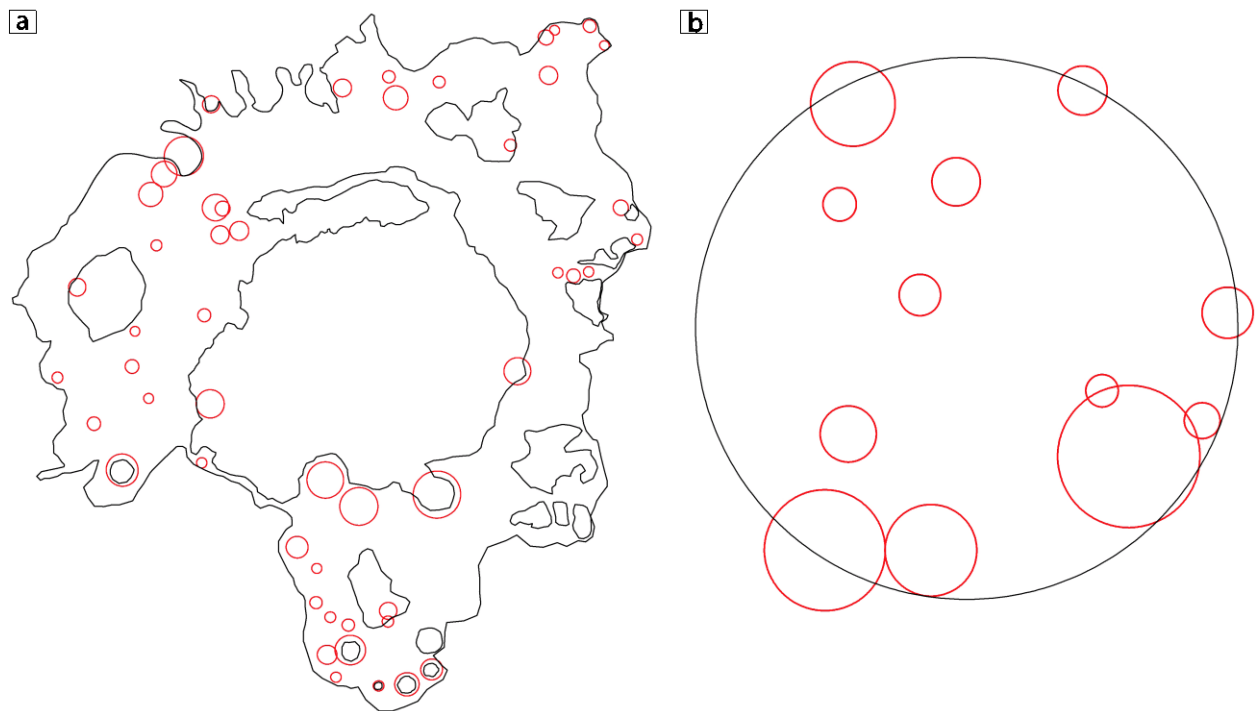


Figure 6.1: Different mapping approaches for the crater measurements. a) Craters (red circles) were counted on basin rim and ejecta deposit remnants (black outline), excluding all areas resurfaced by the smooth plains (e.g. Rembrandt basin). b) All craters were mapped inside the basin cavity (e.g. b102 basin).

We re-examined the basin catalogue of Fassett et al. (2012a), which was based on MESSENGER MDIS and MLA dataset. We also revisited previously unverified basins noted in Mariner-10 and telescopic observation studies (Table 6.2 and 6.3). To find potential new basins, we inspected the available datasets at a large range of scales. For the recognition and qualitative analysis of the basins, we visually assessed the completeness of the basin rim, ejecta deposit, topography, and additional associated tectonic features, such as lobate scarps and wrinkle ridges. We classified the basins ($D \geq 300$ km) as either “certain” (central interior depression and $> 75\%$ rim completeness), “probable” (central interior depression and $> 50\%$ rim completeness), or “tentative” (central interior depression and $< 30\%$ rim completeness), and these were inspected by several of the co-authors both independently and together. By percentage of rim completeness, we mean that circular arcs or segments were qualitatively inferred to exist, not necessarily quantitatively measured that a prominent topographic signature of a rim remains. Prominent rim topography is rarely complete on Mercury at basin scales, even for some of the freshest basins. We used both optical and topographic data sets to identify basins; however, the topographic data proved to be the most useful. For consistency, we refer to named basins by the assigned basin names from the IAU, and the alphanumeric identifiers (e.g., b1, b2, b3) used by Fassett et al. (2012a). For the newly discovered basins, we assign new alphanumeric identifiers \geq b69.

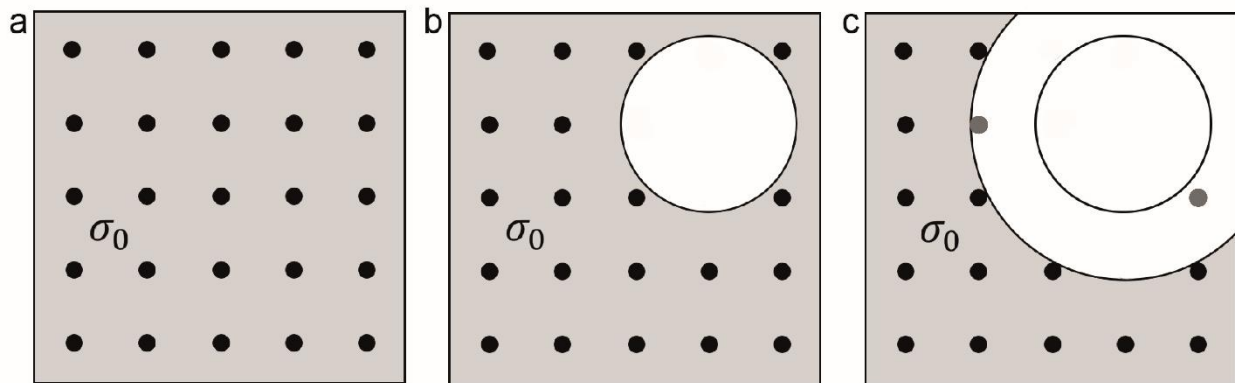


Figure 6.2: Schematic of non-sparseness correction. a) The aim is to determine the surface density (σ_0) of small craters. b) The occurrence of a large crater halfway through the geologic history of the surface diminishes the accumulated population within its boundary. Externally to it, σ_0 remains observable over the grey area. c) Some region is resurfaced by the large craters' ejecta (one crater radius from the crater rim, craters marked with dark grey circles), the remaining area where σ_0 is measurable is smaller. Note that if we choose the resurfaced area too large, this does not damage our measurement of σ_0 providing sufficient area remains.

6.3.2 Crater Size-Frequency Distribution Measurements

The CraterTools extension in ArcMap (Kneissl et al., 2011) was used to map the crater size-frequency distributions (CSFDs) for basins with diameters ≥ 25 km. We used two different mapping approaches for the crater measurements: (1) measuring craters on basin rims and ejecta deposits, excluding all areas resurfaced by smooth plains (Figure 6.1/a), and (2) mapping all craters inside the basins' rims, which only provides a lower limit on the accumulated superposed crater population due to resurfacing within the basins (Figure 6.1/b). For calculating the count areas and resulting CSFDs for each basin, we used three different approaches. In the first two approaches, we used the buffered crater count (BCC) method (Tanaka, 1982; Wichman & Schultz, 1989; Fassett & Head, 2008; Fassett et al., 2012b; Kneissl et al., 2015) applied to both mapping approaches, resulting in what we label as BCC1 and BCC2 CSFD measurements (Table 6.2). In some cases, the first mapping approach was not successful, because the basins are either fully or partially covered by volcanic plains of various thickness (e.g., Denevi et al., 2009; Fassett et al., 2012a; Whitten & Head, 2015; Denevi et al., 2018a), so we applied the second mapping approach. The BCC technique includes all craters crosscutting the region of interest within a buffer. The buffer in this study is one crater radius radial from the crater rim, which is the region affected by ejecta. **Orgel et al. (2018)** concluded that different exclusion radii do not significantly change the results.

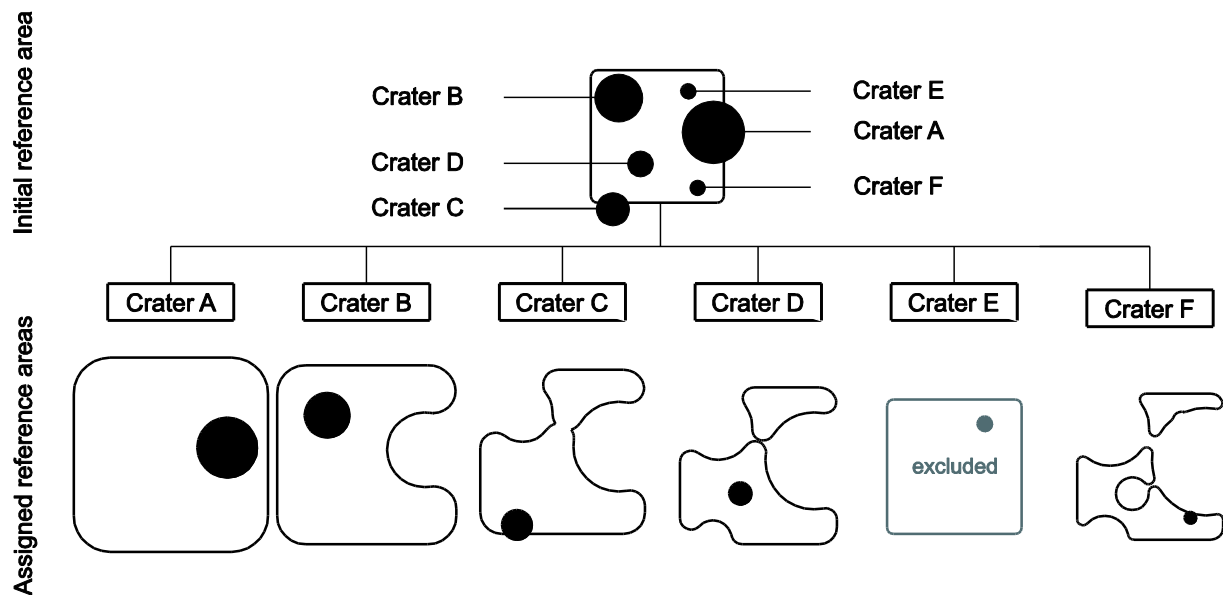


Figure 6.3: Each crater is assigned to a reference area during buffered non-sparseness correction. In this sketch, there is a rectangular reference area with six differently sized craters A-F, with crater A being the largest and crater F being the smallest crater. Individual craters affect the reference area by one crater radius from the crater rim. Therefore, the affected area by crater obliteration is two times a crater's radius. For every crater under consideration, all larger craters and their surrounding ejecta deposit are discarded from the initial reference area. The remaining area is buffered by one crater radius of the crater, which is currently under examination. If the centroid of the crater is located inside the modified reference area, the investigated crater is included for the analysis. In addition, the reference area for each crater becomes smaller for correspondingly smaller crater sizes. Moreover, in this example, crater E is excluded since it is located entirely on top of crater A's ejecta deposit. Consequently, some craters will be excluded during computation. **Orgel et al. (2018)** have published this figure.

Second, we used a new CSFD measurement approach developed to improve the measurement of the CSFDs of smaller diameter craters on heavily cratered surfaces. This buffered non-sparseness correction (BNSC) technique considers and corrects for crater obliteration of smaller diameter craters by larger craters and their ejecta deposits (Kneissl et al., 2016; **Orgel et al., 2018**; **Riedel et al., 2018**; Figure 6.2). Each crater is assigned a buffered reference area that excludes regions that have been modified by subsequent impacts; thus, the reference area becomes smaller for correspondingly smaller crater sizes (Figure 6.3). Details of the techniques, selection of buffer parameters, and improvements in the resulting datasets can be found in Kneissl et al. (2016), **Orgel et al. (2018)** and **Riedel et al. (2018)**. Thus, we used CSFD_Tools (**Riedel et al., 2018**), and applied a BNSC in concert with the first mapping approach (29 basins) (Table 6.2).

6.3.3 Determination of Absolute Model Ages

We determined the absolute model ages (AMAs) of the mercurian basins using the CraterStats software (Michael & Neukum, 2010; Michael, 2013; Michael et al., 2016) and applied both the production function (PF) and chronology function (CF) from Neukum et al. (2001b), as well as the Le Feuvre & Wieczorek (2011) non-porous scaling model (Table 6.2). The LeFeuvre & Wieczorek (2011) non-porous model defines crater production for large craters ($D > 20$ km) formed at depths larger than the given megaregolith thickness. We use the μ notation, which captures the systematic uncertainty in the overall chronology function used (Michael et al., 2016). We plotted the data in cumulative form using pseudo-log crater binning (Arvidson et al., 1978; Neukum, 1983), so that it can be directly compared with similar lunar datasets.

AMAs can be fit to any of the CSFDs that we derived via the BCC and BNSC techniques. However, we present AMAs that are fit to the BNSC-derived CSFDs, because of the improvement in the measurement of crater frequencies in the smaller diameter bins, which allows fitting of ages over a broader diameter range, thus improving the error bars (see e.g., Riedel et al., 2018; Orgel et al., 2018; see also Appendix B). Because of the high uncertainties on AMAs on Mercury, we also ranked the basins based on $N(25)$ derived by the BNSC approach to give the relative stratigraphy of the basins. We also compared this relative stratigraphy with values derived from using the BCC1 and BCC2 approaches (Table 6.2). As an independent check of our results, we compared the obtained ranking of basins with their observed relative stratigraphic relationships. Note that four basins (b11, b32, b96, Goethe) cannot be assigned AMAs due to the large scatter of their CSFDs.

6.3.4 Comparison with Lunar Basins

Orgel et al. (2018) used the AMAs and $N(20)$ values of the lunar basins to rank them in temporal sequence. Each derived $N(20)$ value represents the measured frequency of craters ≥ 20 km normalized to an area of 10^6 km². The error was calculated by dividing the $N(20)$ value by the square root of the number of craters in this population. In order to compare the crater densities of mercurian basins with the lunar basins, we rescaled the values of $N(20)_{\text{Moon}}$ to $N(X)_{\text{Mercury}}$. In other words, we estimated the size of the impactor that forms an impact crater with the diameter of 20 km on the Moon, and calculated the size of the impact crater that would be formed by that same impactor on Mercury. We applied the crater-scaling rule from Schmidt & Housen (1987) in Ivanov et al. (2008):

$$D_t/D_p = 1.21 * (d/f)^{0.427} * v^{0.564} / [g*(D_{sg}+D)]^{0.282} \quad (1)$$

where, D_t is the transient cavity diameter, D_p is the projectile diameter, d and f are target and projectile densities, v is impactor velocity, g is surface gravity, D_{sg} is the diameter strength to gravity transition, and D is the final crater diameter. Note D_{sg} is calculated from the lunar value presuming an inverse dependence of this term on gravitational acceleration and the same strength on both bodies. We used the equation from Chapman & McKinnon (1986) to calculate the transient diameter for a complex crater:

$$D_t = D_{sc}^{0.15} * D^{0.85} \quad (2)$$

where, D_{sc} is the transition diameter from simple to complex crater. All parameters are listed in Table 6.1. The results allow the comparison of the cumulative number of craters on each body that were formed by similarly sized impactors.

Finally, we derived the shape of the summed CSFDs of Pre-Tolstojan- (>4.0 Gyr, Neukum et al., 2001b), and Tolstojan-aged (4.0 – 3.9 Gyr, Neukum et al., 2001b) basins using an R-plot with 10/decade binning. If Neukum's model (1983, 2001b) about an unchanging population of impactors is correct, the CSFDs should fit with the isochrons of the PF represented on the R-plot, if the impactor population changed, the CSFDs should deviate from the Neukum PF.

*Table 6.1: Parameters used for equations (1) and (2) on the Moon and Mercury. *Calculated values in bold. ** (1) LeFeuvre & Wieczorek (2008), (2) Neukum & Ivanov (1994), (3) Neukum et al. (2001b), (4) Ivanov (2008)*

| | Moon | Mercury | Ref.** |
|--------------------------|--------------|----------------|---------------|
| v (km/s) | 19.4 | 42.5 | 1 |
| g (m/s ²) | 1.62 | 3.7 | |
| D_{sg} (km) | 0.3 | 0.13 | 2 |
| D_{sc} (km) | 15 | 11 | 3, 4 |
| d (kg/m ³) | 2500 | 2500 | 1 |
| f (kg/m ³) | 2700 | 2700 | 1,4 |
| D_p (km)* | 1.173 | 1.173 | |
| D_t (km)* | 19.15 | 22.17 | |
| D (km)* | 20 | 25 | |

6.4. Results

6.4.1. Updated Basin Inventory on Mercury

Most of the basins on Mercury are buried to variable degrees by thick smooth plains, intercrater plains, or impact melt on the surface of Mercury. In addition, candidate basins are often surrounded by scarps and other tectonic landforms, rather than obvious intact basin rims. Thus, the topographic data are extremely useful for identifying “hidden” basins not seen by earlier studies (Spudis & Guest, 1988; Neukum et al., 2001b; Fassett et al., 2012a).

Altogether, we identified and verified 49 certain, 31 probable (Figure 6.4 and Table 6.2) and 14 tentative basins (Figure 6.4 and Table 6.3) on the surface of Mercury. This is 1.7x more certain and probable basins than in the previous study (Fassett et al., 2012a), which was finished before the topography data used here were available.

- We discovered 30 new basins (alphanumeric identifiers \geq b69, Table 6.2) and verified 17 basins from the list of unverified basins from Fassett et al. (2012a).
- The remaining 24 on the list of unverified basins from Fassett et al. (2012a) were not confirmed to exist on topographic data, even though some of them (e.g., Bartok-Ives, Gluck-Holbein, Tir) have IAU approved names.

6.4.1.1. Examples of Newly Discovered Basins

Here, we present two examples out of 30 newly discovered basins (Figure 6.5 and Table 6.2).

6.4.1.1.1. The 375 km-Diameter Basin (b102) at 11.7°S, 75.4°W

The basin designated as b102 has a diameter of 375 km and was identified and classified as *certain*. It is located north of the Matisse-Repin and Raphael basins, and is centered at -11.7°S, -75.4°W (Figure 6.5 and Appendix B). Based on the $N(25)$ crater frequency using the BCC2 technique (Table 6.2), the basin belongs to the Tolstojan period, however, stratigraphically it pre-dates Raphael basin, which is a Pre-Tolstojan basin. Thus, the b102 basin must be older than the $N(25)$ value suggests. Smooth plains overprint the basin interior, which commonly exhibits low-reflectance material (Denevi et al., 2013a; Denevi et al., 2018a). The rim of the basin is hardly visible in optical data, but ~50% of the northern part of the rim is apparent topographically. Lobate scarps are localized at the western and northern/eastern basin rim, showing signs of tectonic faulting and folding. The scarp at the western rim shows tectonic faulting away from the basin center, while the eastern and northern scarps face towards the basin center.

6. RE-EXAMINATION OF THE POPULATION, STRATIGRAPHY, AND SEQUENCE OF MERCURIAN BASINS

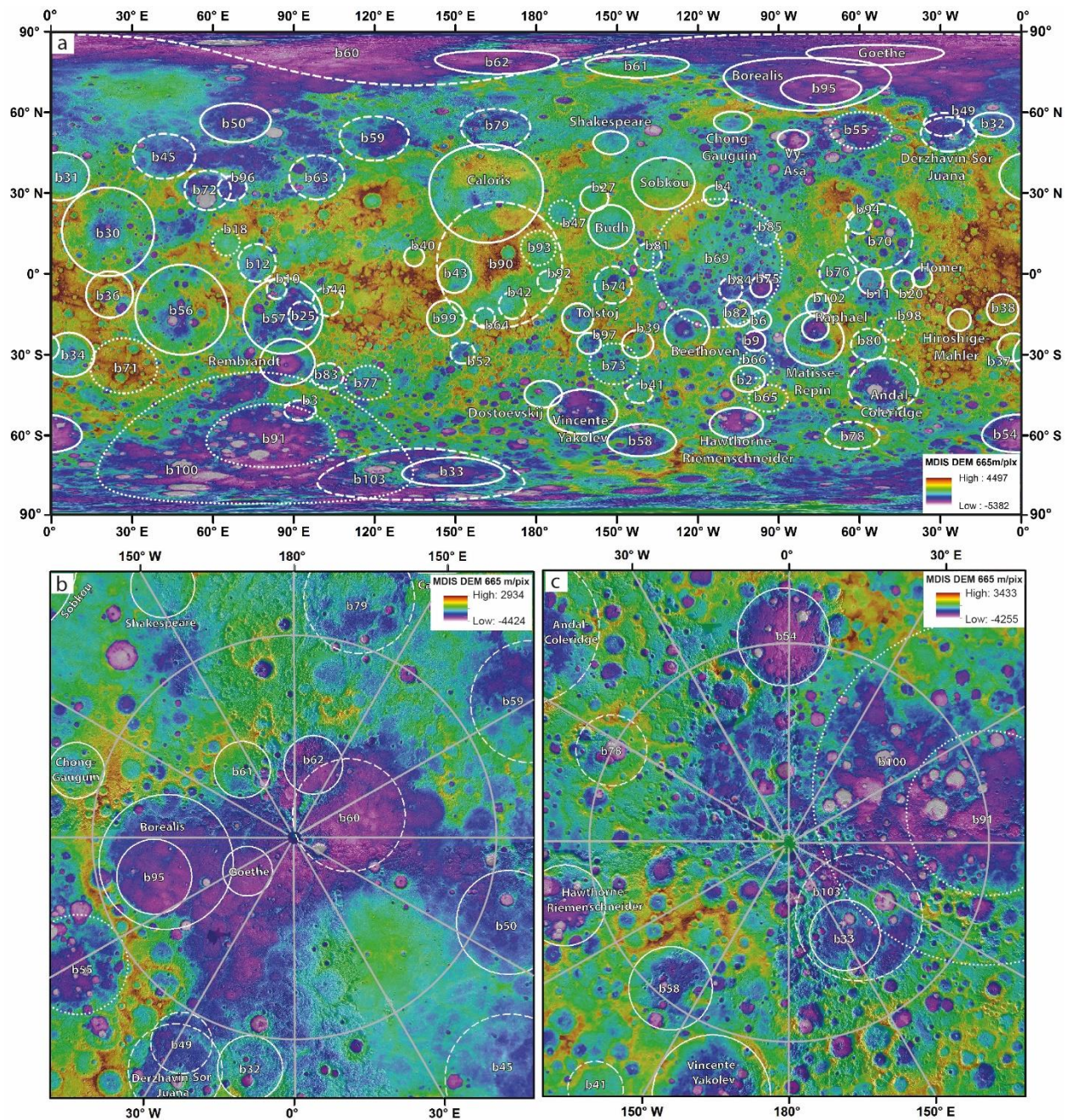


Figure 6.4: Global distribution of basins on Mercury determined from MESSENGER MDIS 166 m/pix data and MDIS DEM 665 m/pix resolution data. The basins were classified as (1) certain (solid line), (2) probable (dashed line), and (3) tentative (dotted line). a) Global distribution of basins in equidistant cylindrical projection. b) Polar stereographic projection of the North Polar Region and c), the South Polar Region with lines of longitude shown in 30° increments. The reference body is a sphere of 2440 km in radius.

6.4.1.1.2. The 645 km-Diameter Basin (b79) at 53.7°N, 164.8°E

A second example of a newly discovered basin (b79) is a degraded 645 km-diameter feature classified as *probable*. It is located north of the Caloris basin and lies beneath its ejecta (Figure 6.5 and Appendix B). Its geographic setting is analogous to the Mendel-Rydberg basin on the Moon, which is superposed by Orientale. The Caloris ejecta deposit (Odin Formation) that buries b79 is characterized by numerous kilometer-scale hummocky hills (see, e.g., Fassett et al., 2009; Ackiss et al., 2015). The basin rim is only recognizable as wrinkle ridges in topographic data, but is arcuate in its northern portion. The basin itself is a distinctive circular low area in the topography data, except where it is directly under the Caloris rim. Interestingly, the anomalous low topography created by b79 slightly extends into Caloris itself; similar inheritance of pre-crater topography is seen elsewhere on the Moon, Mars, and Mercury (Howard, 2007).

6.4.1.2. Examples of Newly Identified Tentative Basins

Here, we describe two examples out of 14 tentative basins. Of these 14 basins, nine were newly identified in this study (Table 6.3). The remaining five basins were already listed as *unverified* in Fassett et al. (2012a).

6.4.1.2.1. The 2032-Km-Diameter Basin (b69) at 3.9°N, 112.7°W

A tentative basin (b69) with a diameter of 2032 km is located beneath the ejecta NW of Sobkou basin at 3.9°N, -112.7°W (Figure 6.5 and Appendix B). If confirmed, b69 stratigraphically pre-dates a number of basins, including b4, b6, b75, b81, b82, b84, b85, Sobkou, and Beethoven. Thus, b69 would be a relatively ancient and much degraded Pre-Tolstojan basin. This location partly overlaps with the Mg-rich region on Mercury, where the existence of a basin has been previously suggested (Weider et al., 2015), but has never been clearly demonstrated on the basis of earlier geological analyses. The main lines of evidence for b69 being a candidate basin are (a) that its interior shows a depression that is approximately circular in outline, and (b) that it exhibits a number of lobate scarps that are circumferential to the tentative basin location. The reasons the basin is classified as *tentative* rather than *probable* are that a topographic high is present in the NW quadrant of the proposed location, and the basin rim is not visible in either topography or optical data.

Table 6.2: Certain and probable impact basins on Mercury, $D \geq 300$ km. Large mercurian basins ranked by crater densities using Buffered Non-Sparseness Correction (BNSC) and Buffered Crater Counting (BCC), respectively. Discrepancies between $N(25)$ and relative stratigraphy are marked with bold italics. Six basins (from b60 to b49) at the bottom of Table 6.2 are out of the sequence due to the paucity of craters or large uncertainty on the crater density measurements (e.g. b90, b60). * Data is from Fassett et al. (2012a), (a) Certain in *, (b) Probable in *, (c) Not verified by *, (d) This study, ** Visibility of basins, P = Possible, N = No, Y = Yes, ***Basins might be in saturation equilibrium.

| # | Mercury basins | Confidence | $N(25)$ BNSC | $N(25)$ BCC (1) | $N(25)$ BCC (2) | Factor (%) | AMA (Neukum et al. 2001) | AMA (Le Feuvre and Wicczorek, 2011) | Lat.(°) | Lon.(°) | Diameter (km) | Visibility | | Stratigraphy | Note* |
|----|-------------------------|------------|--------------|-----------------|-----------------|------------|-----------------------------|-------------------------------------|---------|---------|---------------|--------------|----------------|--|-------|
| | | | | | | | | | | | | Topography** | Optical data** | | |
| 1 | b42*** | Probable | 745±186 | 190±42 | 94±21 | 292 | $\mu 4.09 \pm 0.1, 0.14$ | $\mu 3.87 \pm 0.027, 0.045$ | -11.7 | 171.1 | 426 | Y | P | > Caloris | c |
| 2 | b50 | Certain | 286±86 | 112±31 | 91±15 | 155 | $\mu 4.14 \pm 0.081, 0.10$ | $\mu 3.84 \pm 0.025, 0.029$ | 56.1 | 68.4 | 615 | Y | Y | Undistinguishable relationship with b45 | c |
| 3 | b96*** | Probable | 195±87 | 108±32 | 90±22 | 81 | | | 31.8 | 67.1 | 386 | Y | P | > Rachmaninoff, b72 | d |
| 4 | b81 | Probable | | | 185±32 | | | | 6.3 | -138.6 | 425 | Y | P | - | d |
| 5 | b4 | Certain | | | 183±42 | | | | 29.0 | -113.7 | 322 | Y | Y | - | b |
| 6 | Borealis*** | Certain | 165±55 | 104±15 | 90±10 | 59 | $\mu 4.24 \pm 0.042, 0.059$ | $\mu 3.95 \pm 0.021, 0.031$ | 70.5 | -79.2 | 848 | Y | Y | > b95, b55, Chong-Gauguin, Vy-Asa, Goethe | b |
| 7 | b99 | Certain | | | 161±23 | | | | -16.5 | 146.3 | 562 | Y | P | > Caloris | d |
| 8 | b61 | Certain | | | 160±35 | | | | 77.1 | -142.6 | 360 | Y | Y | Undistinguishable relationship with Borealis | c |
| 9 | b64 | Probable | 158±79 | 146±73 | 87±27 | 8 | $\mu 3.99 \pm 0.11, 0.17$ | $\mu 3.80 \pm 0.044, 0.086$ | -16.3 | 160.8 | 314 | Y | Y | > Caloris, b90 | b |
| 10 | b84 | Probable | | | 155±47 | | | | -5.7 | -107.8 | 364 | Y | N | undistinguishable relationship with b82, b75 | d |
| 11 | b25 | Probable | | | 153±28 | | | | -15.4 | 93.3 | 444 | Y | N | > Rembrandt, b44 | c |
| 12 | b97 | Certain | | | 151±36 | | | | -25.9 | -160.4 | 334 | Y | Y | > Tolstoj | d |
| 13 | b82 | Certain | | | 150±29 | | | | -14.5 | -105.1 | 425 | Y | P | - | d |
| 14 | b63 | Probable | | | 149±18 | | | | 36.3 | 97.3 | 700 | Y | N | - | c |
| 15 | Haworth-Riemenschneider | Certain | | | 142±25 | | | | -55.4 | -105.7 | 481 | Y | P | - | b |
| 16 | b45 | Probable | 139±35 | 116±24 | 76±12 | 20 | $\mu 4.03 \pm 0.064, 0.077$ | $\mu 3.82 \pm 0.029, 0.036$ | 43.7 | 41.8 | 711 | Y | Y | > b72 | b |
| 17 | Dostoevskij | Certain | 136±29 | 109±21 | | 25 | $\mu 3.96 \pm 0.066, 0.80$ | $\mu 3.82 \pm 0.018, 0.020$ | -44.6 | -177.5 | 423 | Y | Y | - | a |
| 18 | Raphael | Certain | 128±32 | 100±23 | | 28 | $\mu 4.01 \pm 0.036, 0.040$ | $\mu 3.77 \pm 0.022, 0.026$ | -20.1 | -76.4 | 394 | Y | Y | - | a |
| 19 | Vincent-Yakolev | Certain | | | 126±17 | | | | -50.1 | -163.6 | 699 | Y | Y | > Dostoevskij | b |
| 20 | b78 | Probable | | | 118±25 | | | | -60.0 | -62.7 | 431 | Y | P | - | d |
| 21 | b54 | Certain | | | 117±18 | | | | -57.2 | -0.2 | 595 | Y | N | - | b |
| 22 | b52 | Probable | | | 116±30 | | | | -29.4 | 152.6 | 336 | P | N | - | b |
| 23 | b58 | Certain | | | 113±21 | | | | -61.7 | -140.9 | 513 | Y | Y | > Vincent-Yakolev | c |
| 24 | b70 | Probable | | | 113±11 | | | | 13.8 | -52.8 | 1028 | Y | P | > b94, b76, b11, b20, Homer | d |
| 25 | Hiroshige-Mahler | Certain | | | 112±30 | | | | -17.1 | -23.0 | 345 | Y | Y | - | b |
| 26 | b76 | Probable | | | 112±19 | | | | 0.6 | -68.1 | 577 | Y | N | > b11 | d |
| 29 | b103 | Probable | | | 106±13 | | | | -74.5 | 137.2 | 814 | Y | P | > b33 | d |
| 30 | b31 | Certain | | | 104±14 | | | | 36.2 | 3.0 | 758 | Y | N | > b30 | b |
| 31 | b59 | Probable | | | 102±15 | | | | 50.1 | 119.3 | 701 | Y | N | > Caloris | c |
| 32 | b57 | Certain | | | 100±9 | | | | -15.5 | 85.8 | 1203 | Y | N | > b44, Rembrandt, b25, b101, b12 | c |
| 33 | b62 | Certain | | | 95±25 | | | | 78.6 | 165.3 | 376 | Y | N | > Caloris | c |
| 34 | b43 | Certain | | | 95±18 | | | | -0.8 | 149.5 | 531 | Y | P | > Caloris | c |
| 35 | b92 | Probable | | | 94±28 | | | | -2.7 | -175.8 | 320 | Y | N | - | d |
| 36 | Sobkou | Certain | 92±17 | 83±13 | 64±9 | 11 | $\mu 3.99 \pm 0.029, 0.037$ | $\mu 3.77 \pm 0.018, 0.026$ | 33.6 | -132.9 | 821 | Y | Y | > b4, Budh, b27 | a |
| 37 | b41 | Probable | | | 89±29 | | | | -44.4 | -141.9 | 308 | P | P | - | b |
| 38 | Chong-Gauguin | Certain | 88±29 | 64±21 | | 38 | $\mu 4.08 \pm 0.071, 0.086$ | $\mu 3.85 \pm 0.030, 0.037$ | 56.4 | -107.1 | 332 | Y | Y | Undistinguishable relationship with Vy-Asa | a |
| 39 | b94 | Probable | | | 87±25 | | | | 19.2 | -60.2 | 364 | Y | N | - | d |
| 40 | b101 | Probable | | | 86±27 | | | | -5.6 | 83.6 | 311 | Y | P | - | d |
| 41 | b74 | Probable | | 86±16 | | | | | -4.1 | -151.5 | 589 | Y | N | > Tolstoj | d |
| 42 | Andal-Coleridge | Probable | | | 85±12 | | | | -41.1 | -51.2 | 828 | Y | P | - | b |
| 43 | b33 | Certain | | | 84±20 | | | | -73.5 | 149.1 | 452 | Y | Y | - | b |
| 44 | Budh | Certain | | | 84±14 | | | | 17.5 | -152.3 | 687 | Y | N | > b27 | b |
| 45 | b3 | Probable | | | 83±27 | | | | -50.7 | 92.3 | 318 | Y | P | - | b |
| 46 | b38 (Sanai) | Certain | 83±15 | 66±11 | | 26 | $\mu 3.94 \pm 0.056, 0.066$ | $\mu 3.75 \pm 0.035, 0.056$ | -13.3 | -6.9 | 485 | Y | Y | - | a |
| 47 | b56 (Lennon-Picasso) | Certain | | | 82±7 | | | | -13.3 | 48.4 | 1426 | Y | N | > b36 | c |
| 48 | Matisse-Repin*** | Certain | 82±16 | 64±8 | | 28 | $\mu 3.99 \pm 0.027, 0.034$ | $\mu 3.93 \pm 0.021, 0.031$ | -24.0 | -76.9 | 852 | Y | Y | > Raphael, b102 | a |
| 49 | b39 | Certain | 81±28 | 81±19 | | 0 | $\mu 3.98 \pm 0.085, 0.11$ | $\mu 3.84 \pm 0.028, 0.048$ | -26.1 | -142.4 | 444 | Y | Y | > Beethoven | a |
| 50 | Tolstoj | Certain | 81±17 | 77±14 | 77±13 | 5 | $\mu 3.97 \pm 0.034, 0.037$ | $\mu 3.76 \pm 0.021, 0.025$ | -16.5 | -164.7 | 467 | Y | Y | - | a |
| 51 | b30 (Calder-Hodgkins) | Certain | | | 80±7 | | | | 15.6 | 21.0 | 1404 | Y | P | > b36 | b |
| 52 | b40 | Certain | | | 80±26 | | | | 6.4 | 134.7 | 308 | Y | P | > Caloris | b |
| 53 | b75 | Certain | | | 77±24 | | | | -4.8 | -96.7 | 332 | Y | N | - | d |
| 54 | b95 | Certain | | | 74±18 | | | | 68.2 | -74.3 | 468 | Y | N | - | b |
| 55 | b11 | Certain | 73±42 | 129±49 | 94±23 | -44 | | | -2.9 | -56.0 | 396 | Y | Y | > b20 | b |
| 56 | b12 | Probable | 73±24 | 79±19 | 56±12 | -8 | $\mu 4.10 \pm 0.047, 0.070$ | $\mu 3.91 \pm 0.026, 0.043$ | 4.1 | 76.3 | 594 | Y | N | Undistinguishable relationship with b18 | b |
| 57 | b37 (Aneirin) | Certain | 71±21 | 56±16 | | 27 | $\mu 4.01 \pm 0.059, 0.069$ | $\mu 3.79 \pm 0.035, 0.049$ | -27.3 | -3.0 | 442 | Y | Y | - | a |

6. RE-EXAMINATION OF THE POPULATION, STRATIGRAPHY, AND SEQUENCE OF MERCURIAN BASINS

| # | Mercury basins | Confidence | N(25) BNSC | N(25) BCC (1) | N(25) BCC (2) | Factor (%) | AMA (Neukum et al. 2001) | AMA (Le Feuvre and Wicczorek, 2011) | Lat.(°) | Lon.(°) | Diameter (km) | Visibility | | Stratigraphy | Note* |
|----|----------------|------------|------------|---------------|---------------|------------|--------------------------|-------------------------------------|---------|---------|---------------|--------------|----------------|--|-------|
| | | | | | | | | | | | | Topography** | Optical data** | | |
| 58 | b36 | Certain | 71±15 | 53±8 | | 34 | μ4.08±0.039,0.053 | μ3.84±0.022,0.026 | -7.6 | 21.6 | 737 | Y | Y | - | a |
| 59 | b80 | Probable | | | 69±17 | | | | -26.2 | -56.7 | 498 | Y | N | > Matisse-Repin, Undistinguishable relationship with Andal-Coleridge | d |
| 60 | Homer | Certain | 68±19 | 62±16 | | 10 | μ4.02±0.054,0.063 | μ3.80±0.031,0.040 | -1.3 | -36.8 | 318 | Y | Y | - | a |
| 61 | b79 | Probable | | | 68±13 | | | | 53.7 | 164.9 | 645 | Y | N | > Caloris | d |
| 64 | b102 | Certain | | | 63±21 | | | | -11.7 | -75.4 | 375 | Y | P | > Raphael | d |
| 65 | b32 | Certain | | 55±22 | 48±12 | | | | 55.4 | -10.8 | 384 | Y | Y | > Derzhavin-Sor Juana | b |
| 66 | b44 | Probable | | | 51±11 | | | | -10.2 | 102.6 | 459 | Y | N | - | b |
| 67 | b34 | Certain | | | 51±10 | | | | -30.0 | 6.5 | 696 | Y | P | > b37 | b |
| 68 | Vy-Asa | Certain | 44±18 | 33±12 | | 33 | μ3.96±0.052,0.082 | μ3.82±0.050,0.11 | 49.7 | -84.7 | 317 | Y | Y | - | a |
| 69 | b20 | Certain | 42±21 | 56±20 | | -25 | μ3.87±0.064,0.12 | μ3.94±0.050, 0.075 | -3.0 | -44.0 | 364 | Y | P | > Homer | a |
| 70 | b72 | Probable | | | 42±10 | | | | 31.0 | 58.0 | 629 | Y | P | > Rachmaninoff | d |
| 71 | Beethoven | Certain | 40±9 | 38±8 | | 5 | μ3.85±0.053,0.062 | μ3.70±0.034,0.059 | -21.0 | -124.2 | 661 | Y | Y | - | a |
| 72 | b2 | Certain | 40±16 | 51±17 | 58±16 | -22 | μ3.90±0.077,0.099 | μ3.71±0.039,0.094 | -38.9 | -101.4 | 420 | Y | Y | - | a |
| 73 | Rembrandt | Certain | 35±6 | 36±6 | | -3 | μ3.86±0.028,0.035 | μ3.65±0.038,0.15 | -32.7 | 87.5 | 731 | Y | Y | - | a |
| 74 | Caloris | Certain | 35±7 | 28±7 | | 25 | μ3.78±0.035,0.047 | μ3.66±0.078,0.50 | 29.9 | 161.4 | 1556 | Y | Y | - | a |
| 75 | b60 | Probable | | | 123±16 | | | | 80.4 | 134.3 | 877 | Y | N | > b61, b62 | c |
| 76 | b90 | Probable | | | 44±3 | | | | 3.4 | 166.3 | 1977 | Y | N | > Caloris, b99, b64, b42, b43, Tolstoj, b92 | d |
| 77 | b27 | Certain | | | | | | | 28.0 | -158.5 | 393 | Y | N | - | a |
| 78 | b6 | Certain | | | | | | | -17.2 | -96.7 | 312 | Y | P | > b82, b9 | b |
| 79 | b9 | Certain | | | | | | | -25.0 | -99.0 | 316 | Y | N | - | b |
| 80 | b49 | Probable | | | | | | | 55.5 | -28.8 | 362 | Y | P | > Derzhavin-Sor Juana | c |

Table 6.3: Tentative impact basins on Mercury, $D \geq 300$ km. * Data is from Fassett et al. (2012a), (a) Certain in *, (b) Probable in *, (c) Not verified by *, (d) This study, ** Visibility of basins, P = Possible, N = No, Y = Yes.

| # | Mercury basins | Confidence | Lat.(°) | Lon.(°) | Diameter (km) | Visibility | | Stratigraphy | Note* |
|----|----------------|------------|---------|---------|---------------|--------------|----------------|--|-------|
| | | | | | | Topography** | Optical data** | | |
| 1 | b18 | Tentative | 11.8 | 64.8 | 424.97 | P | P | undistinguishable relationship with b12 | c |
| 2 | b47 | Tentative | 22.9 | -170.5 | 370.95 | Y | N | pre-dates Caloris | c |
| 3 | b55 | Tentative | 53.4 | -59.5 | 579.81 | P | N | undistinguishable relationship with Vy-Asa | c |
| 4 | b65 | Tentative | -46.2 | -93.9 | 425.48 | Y | N | pre-dates b2, might pre-date Hawthorne-Riemenschneider | b |
| 5 | b66 | Tentative | -33.5 | -98.4 | 446.74 | Y | N | pre-dates b2, b9 | c |
| 6 | b69 | Tentative | 4.0 | -112.7 | 2032.31 | Y | N | pre-dates b85, b4, Sobkou, b81, Beethoven, b82, b84, b75, b6 | d |
| 7 | b71 | Tentative | -34.1 | 26.8 | 872.79 | P | N | undistinguishable relationship with b56, pre-dates b34 | d |
| 8 | b73 | Tentative | -33.4 | -151.3 | 646.45 | Y | P | pre-dates b39, b97 | d |
| 9 | b77 | Tentative | -40.5 | 117.5 | 537.00 | Y | N | Undistinguishable relationship with b83 | d |
| 10 | b85 | Tentative | 14.6 | -94.9 | 343.50 | Y | N | | d |
| 11 | b91 | Tentative | -60.1 | 81.7 | 1001.09 | Y | N | pre-dates b3 | d |
| 12 | b93 | Tentative | 9.6 | -179.3 | 542.88 | Y | N | pre-Caloris | d |
| 13 | b98 | Tentative | -20.6 | -47.5 | 358.39 | Y | P | | d |
| 14 | b100 | Tentative | -61.0 | 75.7 | 2081.86 | P | N | pre-dates b91, b3, Rembrandt, b83, b77, b54, b33, b103 | d |

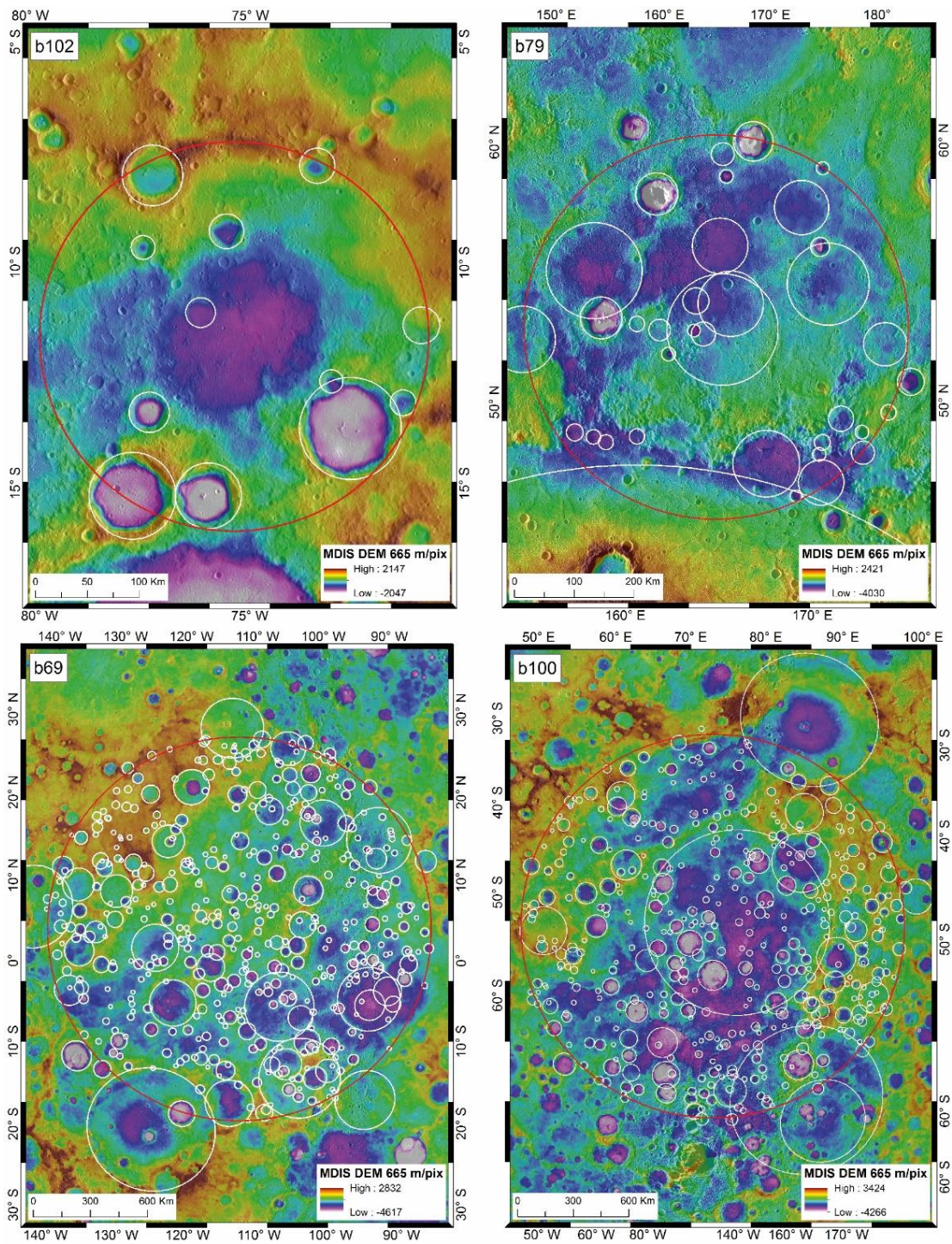


Figure 6.5: Examples of newly discovered basins overlaid on MDIS DEM 665 m/pix and MDIS monochrome data set. B102 is a certain basin with an almost completely preserved rim. B79 is categorized as probable and is situated north and beneath Caloris basin. B69 is a tentative basin overlapping with the proposed Mg-rich region on Mercury (Weider et al., 2015). B100 is a tentative basin covering a large portion of the South Polar Region on Mercury.

6.4.1.2.2. The 2081 km-Diameter Basin (b100) at 60.9°S, 75.7°E

Another example of a tentative basin is a 2081 km-diameter basin (b100) at -60.9°S, 75.7°E) with an uncertain extent, but an interior that is a broad topographic depression (Figure 6.5 and Appendix B). Some of the tectonic landforms in the region are broadly circumferential to the tentative basin location as well. Additionally, b91 could be a possible offset peak-ring for b100 as the size of this tentative basin would allow that. If confirmed, b100 pre-dates b3, b33, b54, b77, b83, b91, 103, and Rembrandt, which would mean it is one of the oldest basins on Mercury.

6.4.2. Crater Frequencies with Buffered Non-Sparseness Correction

The surface of Mercury went through extensive modification processes due to volcanic activity, which makes it challenging to measure accumulated crater densities corresponding to older basin surfaces. There is no method to compensate for the destruction of smaller craters on volcanically resurfaced areas. However, the BNSC technique corrects for the geometric obliteration of small craters by larger impacts and their corresponding ejecta deposits, and therefore can better estimate crater densities on surface units, where this form of obliteration dominates crater erasure (Kneissl et al., 2016; **Orgel et al., 2018**). The BNSC correction typically leads to an increase of the obtained smaller crater densities when compared to the BCC technique (Figure 6.6).

As described in the Data and Methods section, we derived the crater densities of mercurian basins using two different CSFD techniques: BCC and BNSC. The differences in measured crater frequencies using BCC and BNSC become systematically larger for older surfaces, such as Pre-Tolstojan basins, than on younger surfaces, due to the increasing role that crater obliteration plays on older surfaces. Thus, the $N(25)$ values for Mercurian basins derived using the BNSC technique are different from the $N(25)$ values obtained using with the BCC1 technique. The shifting of the results is in good agreement with improvements made to lunar basin CSFDs in our previous study (**Orgel et al., 2018**). The application of BNSC increases the obtained $N(25)$ values by an average of 35% compared to BCC1 (Table 6.2). If we exclude the anomalously high crater density of b42, this value drops to 25%. This difference is slightly higher on Mercury than on the Moon, where we measured 24% increase (**Orgel et al., 2018**).

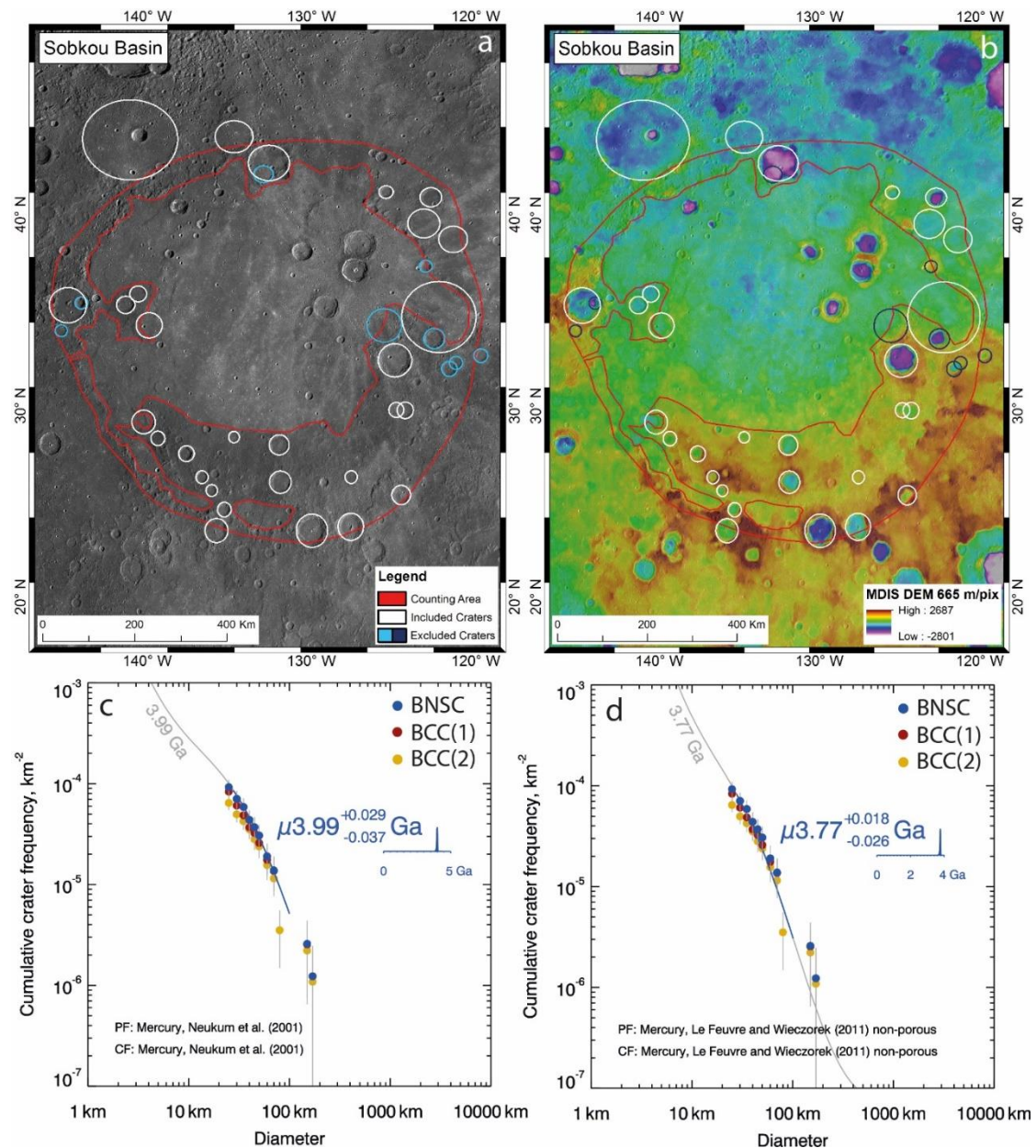


Figure 6.6: Crater measurement maps and derived CSFD with AMA of Sobkou basin after Neukum et al. (2001b) and Le Feuvre & Wieczorek (2011). a) Counting area on MESSENGER's Mercury Dual Imaging System (MDIS) 166 m/pixel mosaic base map. Craters marked in white were counted for BNSC age determination; whereas craters marked in blue were excluded during computation. We applied 1 crater radius radial from the crater rim, which removes the region obliterated by the craters and their proximal ejecta. b) Counting area on MESSENGER's Mercury Dual Imaging System (MDIS) DEM 665 m/pixel mosaic base map. Legend for panel "a" is the same as for panel "b". c-d) Cumulative CSFD plots of Sobkou basin using two different crater counting techniques: BCC (1: red circles, 2: yellow circles), and BNSC (blue circles). The BNSC data shows that the smallest crater bins were corrected to higher crater frequencies when accounting for crater non-sparseness. AMAs derived from the Neukum et al. (2001b) (c) and Le Feuvre & Wieczorek (2011) chronology functions (d) using Poisson age analysis.

The b42 basin has the highest $N(25)$ crater frequency (745 ± 186). The difference (292%) between the BNSC and the BCC1 results for this basin are also the largest. The higher crater frequency can be explained by the exclusion of area that had been resurfaced by subsequent craters and their ejecta in a relatively small counting area (Figure 6.7 and Appendix B). The discrepancy between the BNSC and BCC1 $N(25)$ values is lowest in b11 basin (-44%) (Figure 6.7 and Appendix B). The negative factor shows a decreased crater frequency compared to BCC1. This effect could be interpreted as resulting from the distribution of few larger craters, which are separated from each other over relatively large area. Additionally, the centers of intersecting craters fall within one crater radius, thus, are excluded from the calculation due to obliteration.

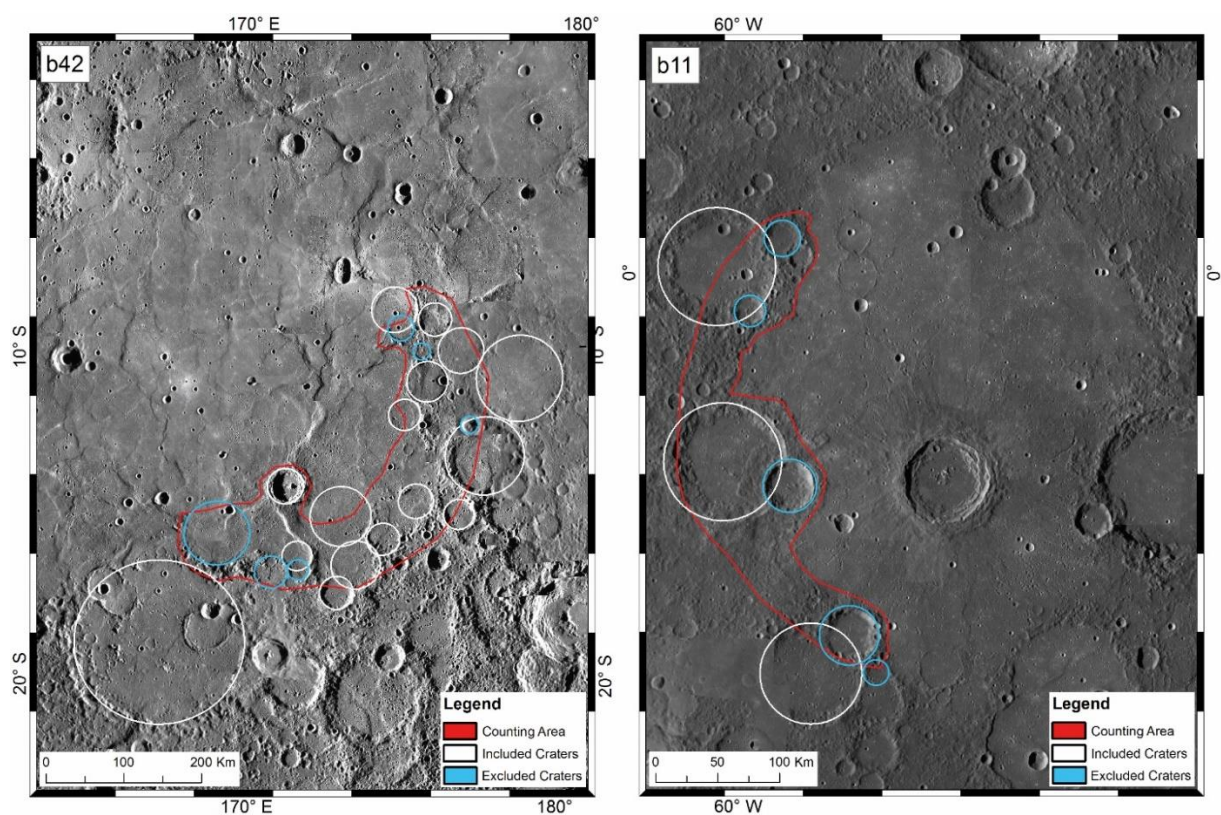


Figure 6.7: B42 has the largest difference between the BNSC and the BCC1 results (292%), while the discrepancy is the lowest (-44%) in b11. Craters excluded and included during computation are marked with blue and white, respectively.

6.4.3. Spatial Densities of Basins on Mercury and the Moon

The spatial densities of (1) certain and probable (altogether 80 basins) and (2) all basins including tentative basins (altogether 94 basins), respectively, allow a comparison between the basin populations on Mercury and the Moon. This can be done without rescaling the values of $N(300,500)_{\text{Moon}}$ to $N(X,Y)_{\text{Mercury}}$ due to the large uncertainties in scaling at basin scales. The spatial density of basins with $D \geq 300$ km per 10^6 km² on Mercury or the $N(300)_{\text{Mercury}}$ are 1.07 ± 0.12 (certain and probable) and 1.26 ± 0.13 (all basins), respectively. Similarly, the spatial density of basins with $D \geq 500$ km per 10^6 km² on Mercury or the $N(500)_{\text{Mercury}}$ are 0.44 ± 0.07 (certain and probable) and 0.54 ± 0.08 (all basins), respectively. To compare the basin density values with the updated data set from the Moon, we derived the spatial density of lunar basins (altogether 36 basins) using the data from **Orgel et al. (2018)** with additional basins from the Neumann et al. (2015) basin catalogue. We found that the spatial density of basins with $D \geq 300$ km and $D \geq 500$ km per 10^6 km² are an $N(300)_{\text{Moon}}$ of 0.94 ± 0.16 and an $N(500)_{\text{Moon}}$ of 0.55 ± 0.12 . In contrast to a previous study (Fassett et al., 2012a), we find that basins have a slightly higher $N(300)$ density on Mercury than on the Moon (Figure 6.8/a), but the difference is below the level of the 1-sigma uncertainties. The similar $N(500)$ basin density on Mercury and the Moon has substantial implications for the early history of both planetary bodies' crust. This result could be the consequence of saturation on both surfaces (Fassett et al., 2011).

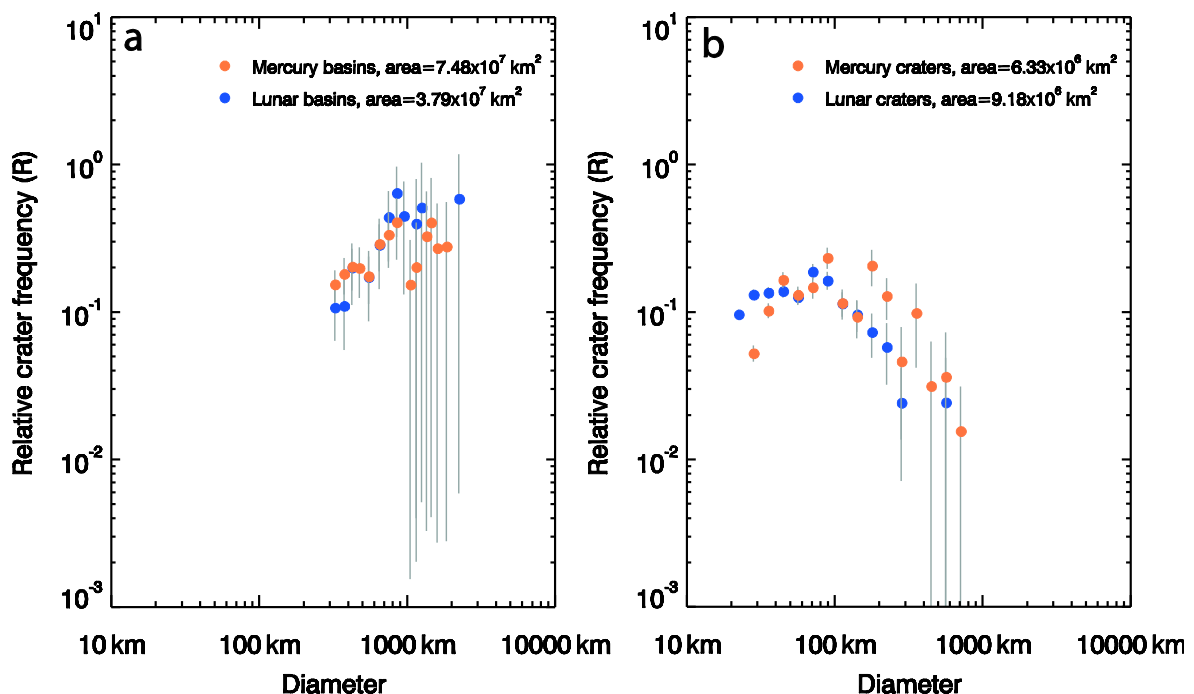


Figure 6.8: Relative crater frequency of (a) large basins ($D \geq 300$ km) and (b) craters superposing large basins on Mercury (Pre-Tolstojan, Tolstojan basins and Caloris), and compared to the Moon (Pre-Nectarian, Nectarian and Imbrian basins) (**Orgel et al., 2018**).

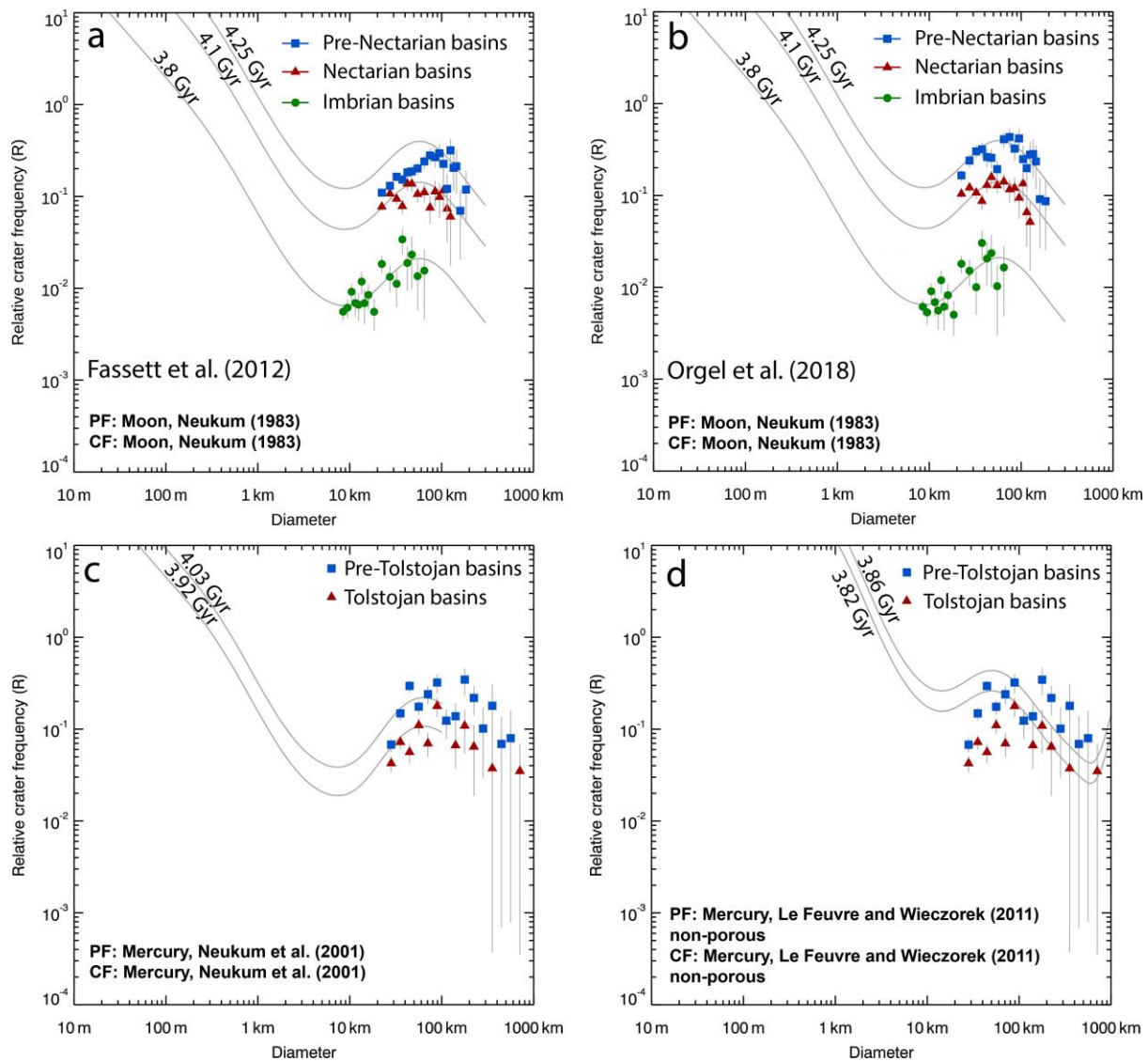


Figure 6.9: Summed CSFDs to study the impactor population(s) on the Moon (a-b) and Mercury (c-d) using an R -plot representation. a-b) Summed CSFDs of the Pre-Nectarian-aged basins (excluding SPA, blue squares), Nectarian-aged basins (red triangles) and Imbrian-aged basins (green circles) on the Moon using the BNSC technique (30 basins). The gray lines represent the isochrons of the PF. a) Fassett et al. (2012b) found a steep slope in the diameter range from 20 km to 100 km in the shape of Pre-Nectarian CSFD using the BCC method (Fassett & Head, 2008), and concluded different impactor populations (modified from Orgel et al., 2018). b) In contrast, Orgel et al. (2018) shows that CSFDs conform to the Neukum (1983) PF showing an unchanging shape of the distribution, thus indicating an unchanging SFD of impactors (modified from Orgel et al., 2018). c-d) Summed CSFDs of the Pre-Tolstojan-aged basins (blue squares) and Tolstojan-aged basins (red squares) on Mercury using the BNSC technique (29 basins). c) The shape of CSFDs do not follow the Neukum et al. (2001b) PF below 35 km diameter in Pre-Tolstojan distribution. d) The summed CSFDs do not conform to the Le Feuvre & Wieczorek (2011) non-porous PF below ~ 50 km diameter, but they fit at larger crater sizes.

We also summed the crater densities of certain and probable mercurian (Pre-Tolstojan, Tolstojan basins and Caloris basin, altogether 29 basins) and lunar basins (Pre-Nectarian, Nectarian and Imbrian basins, altogether 36 basins) (see also, **Orgel et al., 2018**) using the BNSC technique, alone (Figure 6.8/b). Compared to the Moon, the crater densities on Mercury are slightly higher or nearly equivalent at large crater diameters ($D > 100$ km). Below 100 km in diameter, the CSFD on Mercury falls below the lunar distribution, which is consistent with previous studies (Fassett et al., 2011, 2012a).

6.4.4. Impactor Population

To investigate the nature of the impactor population(s) on Mercury, we compared the summed BNSC CSFDs of the Pre-Tolstojan-aged basins and Tolstojan-aged basins (including Tolstoj) (Figure 6.9/c, d) to one another, and then to the summed CSFDs of Pre-Nectarian, Nectarian, and Imbrian basins on the Moon (Figure 6.9/a, b) (**Orgel et al., 2018**). Figure 6.9/a shows that Pre-Nectarian CSFD does not conform to the isochrons of the unchanging Neukum (1983) PF using the BCC method (Fassett et al., 2012b), concluding a change in impactor populations. The application of the BNSC method to the lunar basin population (Figure 6.9/b) allowed the correction of the smaller crater size bins on ancient Pre-Nectarian surfaces (**Orgel et al., 2018**). By removing areas that were affected by non-sparse cratering, and thus the destruction of smaller diameter craters by subsequent craters and their ejecta, a clearer view of the Pre-Nectarian CSFD was possible. Indeed, **Orgel et al. (2018)** were able to conclude that the shape of the CSFD between the Pre-Nectarian, Nectarian, and Imbrian periods did not change, which suggests that the SFD of the impacting population did not change as had previously been suggested (Head et al., 2010, Fassett et al., 2012b).

The shapes of the CSFDs for the Pre-Tolstojan and Tolstojan periods have similar shapes that generally follow the trend of the Neukum et al. (2001b) PF (Figure 6.9/c), but do not conform to the Le Feuvre and Wieczorek (2011) PF for non-porous material (Figure 6.9/d). As expected, the Pre-Tolstojan dataset plots above the Tolstojan due to their relative age differences. It is difficult to tell, based on the spread of the data points around the example isochrons whether there is a significant difference between the shapes of the two curves. Potentially, the smaller crater bins in the Pre-Tolstojan exhibit a lower crater spatial density than later in the Tolstojan.

6.5. Discussion

6.5.1. Geographic Distribution of Basins

Fassett et al. (2012a) suggested that the geographic distribution of the basins on the surface of Mercury is non-uniform. There are fewer basins observed on the eastern hemisphere than on the western hemisphere.

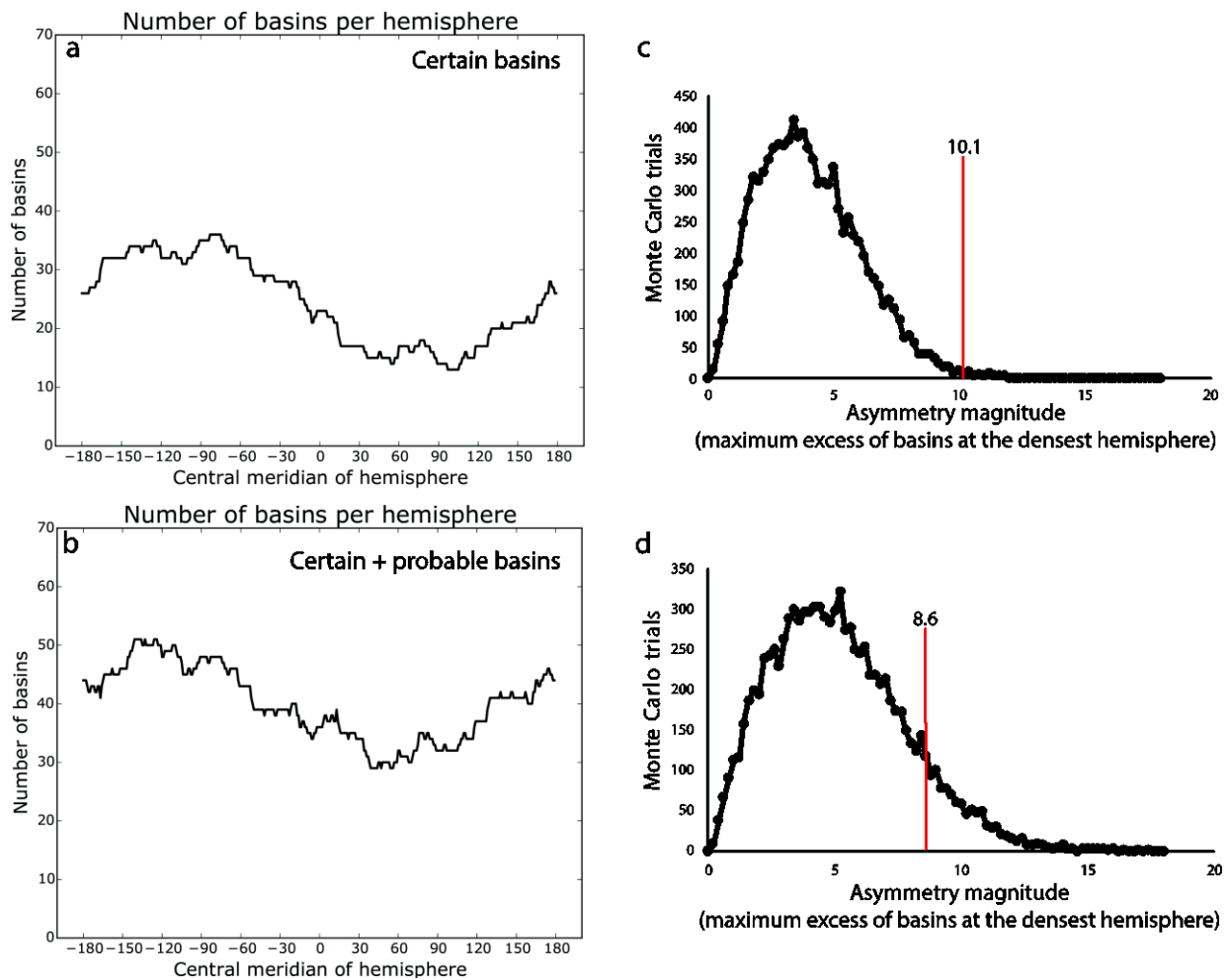


Figure 6.10: Basin asymmetry based on a) certain, and b) certain and probable basins. Number of basins per hemisphere shown in each 1° increments. The axes show the frequency of basins (y-axis) for a hemisphere with a given central meridian (x-axis); note that the dividing line between these two hemispheres is thus $x + 90^\circ$. c) Monte Carlo simulation of the probability to form certain, and d) certain and probable basins on the surface. The axes show the Monte Carlo trials (y-axis) to recreate the observed basin distribution, and the asymmetry magnitude (x-axis) represents the maximum excess of basins at the densest hemisphere. We found certain basins would have a lower basin asymmetry magnitude in 98% of cases with 10.1 asymmetry magnitude (red line), than the observed distribution (panel c). While, certain and probable basins would do so in 91% of trials with 8.6 basin asymmetry magnitude (red line) (panel d).

To analyze whether the basin distribution on Mercury is consistent with being drawn from a random population, we investigated the number of basins in hemispheres across the planet with a central meridian every 1° in longitude. Figure 6.10/a, b shows the number of basins is maximal for a hemisphere centered at roughly $120^\circ\text{W} \pm 30^\circ$, with a corresponding lower frequency in the opposite hemisphere. We ran a Monte Carlo simulation to test the probability of seeing a comparable magnitude for the observed basin asymmetry. We found certain basins would have a lower basin asymmetry magnitude in 98% of cases, while certain and probable basins would do so in 91% of trials (Figure 6.10/c, d). Note that this is a statistical probability calculation, where basins are treated as points, and target properties and geologic processes are assumed to be homogenous. Nonetheless, it tentatively suggests that the asymmetry in basin distribution would not be expected if basins were emplaced on the surface in a random manner.

This distribution could be explained by three major hypotheses: (1) different thermal properties of the crust due to orbital resonances and/or interior geodynamical processes (Vasavada, 1999; Siegler et al., 2013; Miljković et al., 2013; Chapman et al., 2018), (2) differential resurfacing by volcanism (Fassett et al., 2012a; Denevi et al., 2013a), or (3) that the basins on Mercury are spatially random but happened to end up in this configuration.

In the present day, Mercury's 3:2 spin-orbit coupling leads to a ~ 150 K difference in crustal temperatures as a function of longitude between the so-called "hot pole" (at 0°E and 180°E) and "cold pole" (at 90°E and 270°E) longitudes. Moreover, there is a $\sim 150 - 300$ K difference with latitude, with the larger contrast in the hot pole longitudes, which substantially depend on the orbital eccentricity (Vasavada et al., 1999; Williams et al., 2011). The orbital eccentricity of Mercury varied between 0.0 and 0.4 over its history (Correia & Laskar, 2004) and, thus the magnitude of lithospheric temperature anomalies may have varied substantially over billions of years. A complication for the importance of this effect is that it remains an open question when Mercury reached the 3:2 resonances (e.g., Tosi et al., 2015: > 1 Gyr after formation; Noyelles et al., 2014: < 20 Myr) that set up the current lithospheric thermal structure. If this happened well into Mercury's history, it is plausible that no differences in the observed size-frequency distribution as a function of lithospheric temperature would be expected, even with Mercury's present inhomogeneous distribution of temperature. Alternatively, Mercury might have once reached 1:1 spin-orbital resonance during its history with one hemisphere always facing the Sun and causing significant surface temperature difference on both sides (Correia & Laskar, 2009; Wieczorek et al., 2012). This thermal contrast could translate into differences in crater size, morphology, or morphometry, particularly for large impact events. The NASA's Gravity Recovery and Interior Laboratory (GRAIL) confirmed that the basins on the Moon are larger on the nearside than on the far side (Neumann et al., 2015). This asymmetry was explained by the increase of the heat-producing elements on the nearside; consequently, the nearside was initially hotter than the farside (Miljković et

al., 2013). Miljković et al. (2013) used the iSALE-2D hydrocode to model the size-frequency distribution (SFD) of basins on both hemispheres and found that lateral variations in target temperature could have greatly affected the SFD of basins. Specifically, the warmer nearside results in a SFD that shifts to larger crater diameters and hence larger diameter of basins on the warm hemisphere.

The second major hypothesis is that the formation of smooth plains is spatially non-uniform on the surface and coincides with basins; however, one-third of the smooth plains is located in the Northern Polar Region unrelated to any large basin forming impacts (Denevi et al., 2013a; Ostrach et al., 2015; Qingyun et al., 2018). The thickness of smooth plains varies between 0.5 and 4 km (Trask & Guest, 1975; Denevi et al., 2009; Head et al., 2009; Prockter et al., 2010; Head et al., 2011; Denevi et al., 2013a; Ernst et al., 2015; Ostrach et al., 2015; Whitten & Head, 2015; Denevi et al., 2018a). We observe basins ($D \geq 300$ km) completely infilled by smooth plains and outlined by wrinkle ridges or lobate scarps. Of course, the effectiveness of this large-scale resurfacing process is dependent on basin size and the thickness of volcanic plains. Thus, the complete erasure of basins cannot be excluded by a planet-wide differential resurfacing.

6.5.2. Basin Formation and Subsequent Geologic Activity

In this study, we derived the AMAs of individual basins using the CSFDs we measured using the BNSC technique. The AMAs are dependent on the chronology model, which in fact is extrapolated from the lunar one and thus, includes uncertainties (Neukum et al., 2001b; Le Feuvre & Wieczorek, 2011). We compared the results derived with the Neukum et al. (2001b) and Le Feuvre & Wieczorek (2011) non-porous chronology models and found a ~ 200 Myr difference between the AMAs (Figure 6.6, Table 6.4). We found that the AMAs for Pre-Tolstojan basins (Neukum et al., 2001b) range from $4.24 \pm 0.04/0.06$ Gyr (Borealis basin) to $3.94 \pm 0.06/0.07$ Gyr (b38) with an average AMA of $4.05 \pm 0.06/0.15$ Gyr. Whereas, the AMA of Pre-Tolstojan basins using the Le Feuvre & Wieczorek (2011) CF vary between $3.95 \pm 0.02/0.03$ Gyr (Borealis basin) and $3.75 \pm 0.03/0.06$ Gyr (b38) with an average AMA of $3.84 \pm 0.03/0.04$ Gyr. The AMAs of Tolstojan basins using the Neukum et al. (2001b) CF give results from $4.10 \pm 0.05/0.07$ Gyr (b12) to $3.85 \pm 0.05/0.06$ Gyr (Beethoven basin) with an average AMA of $3.96 \pm 0.05/0.06$ Gyr. Using the Le Feuvre & Wieczorek (2011) CF, the AMAs vary from $3.94 \pm 0.05/0.07$ Gyr (b20) to $3.65 \pm 0.04/0.15$ Gyr (Rembrandt basin) with an average of $3.79 \pm 0.04/0.07$ Gyr. Although we report AMAs to three significant digits, the systematic errors in the chronology function could be substantial (> 200 Ma), and errors resulting from resurfacing are also non-negligible (100s of Ma). Thus, these values should be treated with appropriate caution.

Table 6.4: AMA intervals for Pre-Tolstojan and Tolstojan basins.

| | Neukum et al. (2001b) AMA intervals (Gyr) | Neukum et al. (2001b) avg. AMA (Gyr) | Le Feuvre & Wieczorek (2011) AMA intervals (Gyr) | Le Feuvre & Wieczorek (2011) avg. AMA (Gyr) |
|---------------------------------|---|--|--|---|
| Pre-Tolstojan basins | Max. $4.24 \pm 0.04/0.06$ (Borealis) | $4.05 \pm 0.06/0.15$ | Max. $3.95 \pm 0.02/0.03$ (Borealis) | $3.84 \pm 0.03/0.04$ |
| | Min. $3.94 \pm 0.06/0.07$ (b38) | | Min. $3.75 \pm 0.03/0.06$ (b38) | |
| Tolstojan basins | Max. $4.10 \pm 0.05/0.07$ (b12) | $3.96 \pm 0.05/0.06$ | Max. $3.94 \pm 0.05/0.07$ (b20) | $3.79 \pm 0.04/0.07$ |
| | Min. $3.85 \pm 0.05/0.06$ (Beethoven) | | Min. $3.65 \pm 0.04/0.15$ (Rembrandt) | |

The sequence of basins on Mercury was ranked based on $N(25)$ crater frequencies using the BNSC, BCC1, or BCC2 CSFD techniques. We found that $N(25)$ and relative stratigraphy are in good agreement, with only seven basins showing discrepancies (Table 6.2, marked with bold italics). Figure 6.11 shows the sequence of basin formation on Mercury (74 basins) and the Moon (30 basins) including results of all CSFD techniques. In Table 6.2, we include six more basins, but because of the absence of reliable crater statistics, we do not indicate these basins on Figure 6.11. Note that mercurian basins with higher crater frequencies than Borealis are very few in number compared with the Pre-Nectarian lunar basins. The youngest large mercurian basins (Rembrandt: 35 ± 7 , BNSC, 36 ± 6 , BCC1; Caloris: 35 ± 6 , BNSC; 28 ± 7 , BCC1) have a crater density when rescaled comparable to Imbrium and significantly higher than Schrödinger or Orientale. Rembrandt basin has been suggested to be similar in age or slightly older than Caloris (Watters et al., 2009; Fassett et al., 2012a; Whitten & Head, 2015). According to this study AMA and $N(25)$ of it is slightly higher than the Caloris forming event, although the error bars overlap in $N(25)$. We consider Rembrandt basin as probably having formed in the Tolstojan period, which is in agreement with previous studies (Ferrari et al., 2015; Hynek et al., 2016; Gemperline et al., 2017).

Based on the 2.5 times higher crater production rate above 300 km (Le Feuvre & Wieczorek, 2011) and a factor of 2 greater surface area, we expect a factor of ~ 5 more basins to form on Mercury than on the Moon (Figure 6.11). Consequently, we should observe ~ 180 basins on Mercury, if we calculate with 36 lunar basins larger than 300 km using **Orgel et al. (2018)** data and 6 additional basins from Neumann et al. (2015). Note that the observed 36 lunar basins show only the basin record after the lunar magma ocean solidification, when the formation of impact basins was feasible on the solid surface. This study classified 94 basins, including 80 certain and probable as well as 14 tentative basins. Thus, we observe roughly half of the basin record, where older basins than Borealis are completely erased from the basin record, and this finding is in good agreement with Marchi et al. (2013). Their findings suggest

global resurfacing processes related to heavy bombardment and persistent volcanic activity about 4.0 – 4.1 Gyr ago. The questions are, what happened to Mercury's surface prior 4.1 Gyr, and where are the missing basins? Alternatively, other processes besides LHB and extensive volcanism could explain the absence of basins.

These include: (1) viscoelastic relaxation of impact basins (Kamata et al., 2015; Conrad et al., 2018) due to the aftermath of a prolonged global magma ocean (Brown & Elkins-Tanton, 2009; Vander Kaaden & McCubbin, 2015) by tidal heating (Meyer et al., 2010), or (2) enhanced impact melt production due to the higher impactor velocities (Gault, 1975; Pierazzo et al., 1997; Cintala & Grieve, 1998; Barr & Citron, 2011; Ostrach et al., 2012; Whitten & Head, 2015; Manske et al., 2019).

The first hypothesis is that the initial thermal conditions from planetary accretion and metal-silicate differentiation likely produced a global magma ocean on terrestrial planets and the Moon (Shearer et al., 2006; Brown & Elkins-Tanton, 2009). The cooling of the magma ocean led to fractional crystallization, where positively buoyant minerals formed a “primary” or “flotation” crust. Based on laboratory experiments this mineral for Mercury is likely graphite, which originated from a low-FeO melt (Vander Kaaden & McCubbin, 2015). The remnants of that layer might be exposed now as low-reflectance material (LRM) by larger impacts, which is significantly contributing to the low albedo of Mercury's surface (Robinson et al., 2008; Denevi et al., 2009). Furthermore, those basins that formed around or shortly after the solidification of the magma ocean exhibit viscoelastic relaxation and still might show observable structures. However, on the Moon most of the proposed old Pre-Nectarian basins on the Moon do not exhibit clear topographic or gravity signatures (Kamata et al., 2015). Kamata et al. (2015) investigated the viscoelastic deformation of impact basins on the Moon using crustal thickness models to infer their thermal state at the time of basin formation. They find that a Moho temperature $> 1300 - 1400$ K is required for substantial viscous relaxation of the topography, and such a high temperature can be maintained only for a short time (< 50 Myr), or after a possible mantle overturn ≥ 150 Myr after magma ocean solidification. However, the magma ocean solidification may have been prolonged by tidal heating for 200 – 300 Myr on the early Moon (Meyer et al., 2010). Conrad et al. (2018) drew the same conclusions from GRAIL observations, where they assessed the age and relaxation state of lunar impact basins, and find a change in relaxation state likely caused by the cooling of the lunar crust between 4.21 – 4.45 Gyr. The solidification time of the magma ocean on Mercury is unknown, but similar processes could have affected Mercury's early crustal evolution (Padovan et al., 2015).

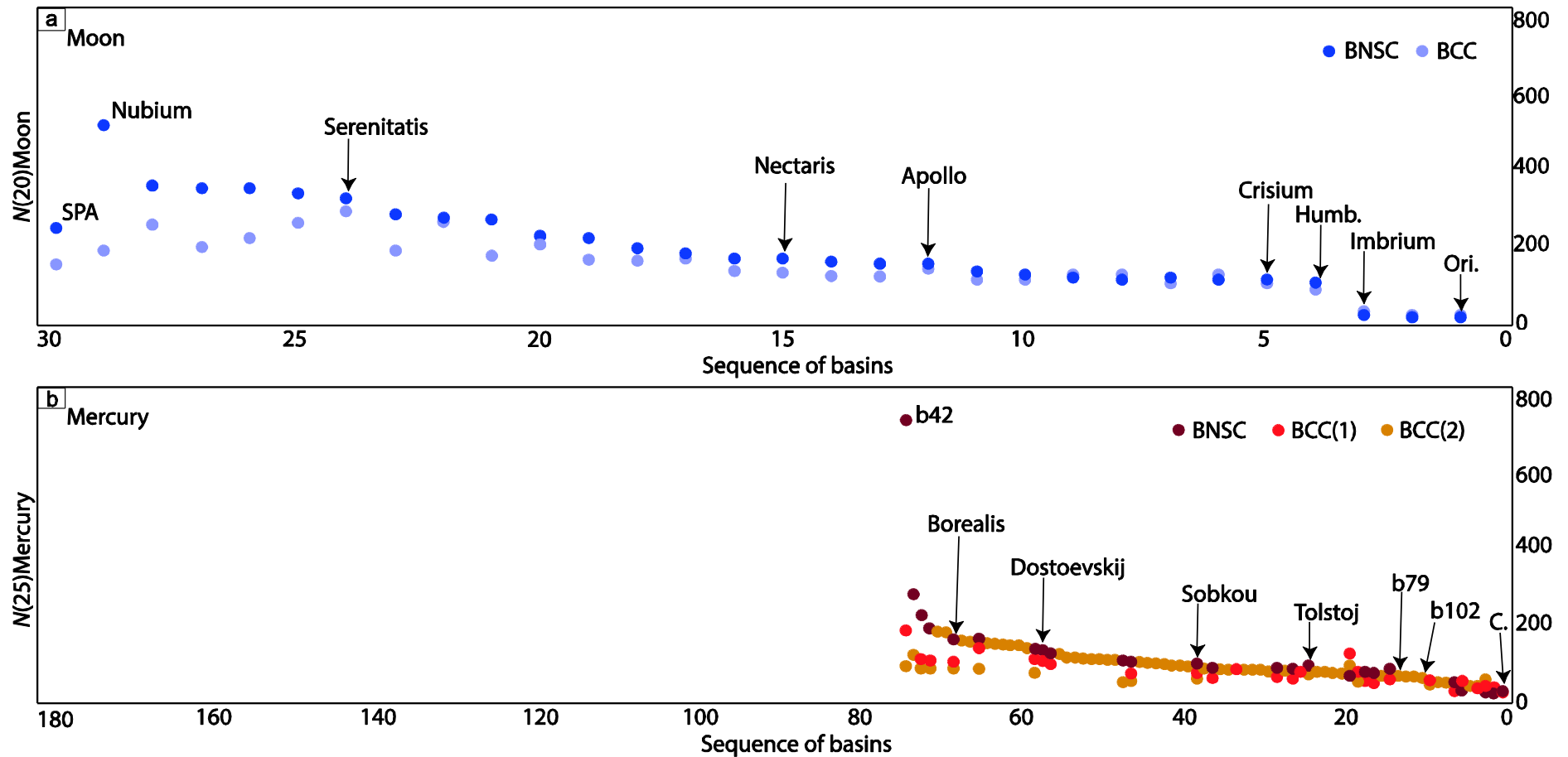


Figure 6.11: Sequence of basin formation on the Moon (a) and Mercury (b). Crater densities derived with (i) BNSC and (ii) BCC techniques with two different mapping techniques on Mercury: BCC1 measuring craters excluding all areas resurfaced by the smooth plains and, BCC2 mapping all craters inside the basin cavity. Crater densities derived with BNSC commonly show a higher density than with BCC technique on both planetary surfaces. Note the number of lunar and mercurian basins is 30 (Orgel et al., 2018) and 74, respectively. However, we assume that the Moon has 36 lunar basins (including 6 additional basins from Neumann et al. (2015))

*larger than 300 km after the lunar magma ocean solidification, we should observe ~5 times more basins (2.5 times higher crater production rate above 300 km and a factor of 2 greater surface area) to form on Mercury than on the Moon. Consequently, we expect to observe ~ 180 basins on Mercury. Lunar basins are spaced at a 5x interval to compensate for the higher impact rate and larger surface area on Mercury than the Moon; thus, roughly 5 basins should form for every lunar basin. Key basins are highlighted in the upper right corner of the symbols. Abbreviations: C. = Caloris basin, SPA = South Pole Aitken basin, Humb. = Humboldtianum basin, Ori. = Orientale basin, lunar data is from **Orgel et al. (2018)**.*

Second, considering higher impact rates, impact melt production was dominant in the early history of Mercury (Gault, 1975; Cintala & Grieve, 1998; Ostrach et al., 2012; Whitten & Head, 2015) and even more intensive than on the Moon. Manske et al. (2019) used hydrocode simulations to determine the amount of melt generated by an impact and found that the interior temperature and lithospheric pressure of the target planet significantly affects the final melt distribution and the crater morphology for impactors larger than 10 km in diameter on Mars. Additionally, large-scale collisions on a younger and hotter planet may result in the formation of an impact melt pool to fill up the entire crater resulting in the formation of an igneous province rather than a typical basin structure (Manske et al., 2019). This scenario could be relevant for Mercury, where the oldest basins are not observable on the surface. One plausible explanation is that they drowned in their own melt.

6.5.3. Saturation equilibrium

Saturation equilibrium is reached when the formation of new craters and their ejecta obliterate (on average) an equal number of pre-existing craters (Shoemaker, 1965; Gault, 1970; Woronow, 1977).

To investigate the possibility of saturation equilibrium on Mercury in crater diameters ≥ 25 km, we compared the fraction of the original and the BNSC modified count area sizes for each basin to its $N(25)$ crater frequencies (Figure 6.12/a). We expect that basins that show the highest level of non-sparseness to be close to or at saturation equilibrium. We observe a linear decrease in the effective counting area with increasing $N(25)$ value towards older surfaces, because the level of non-sparseness increases with basin age. This finding is in good agreement with the trends in saturation equilibrium of the lunar basins at diameters ≥ 20 km (**Orgel et al., 2018**). However, this linear decrease is steeper than on the Moon (Figure 6.12/b), which might provide additional evidence for an absence of basins older than Borealis on Mercury.

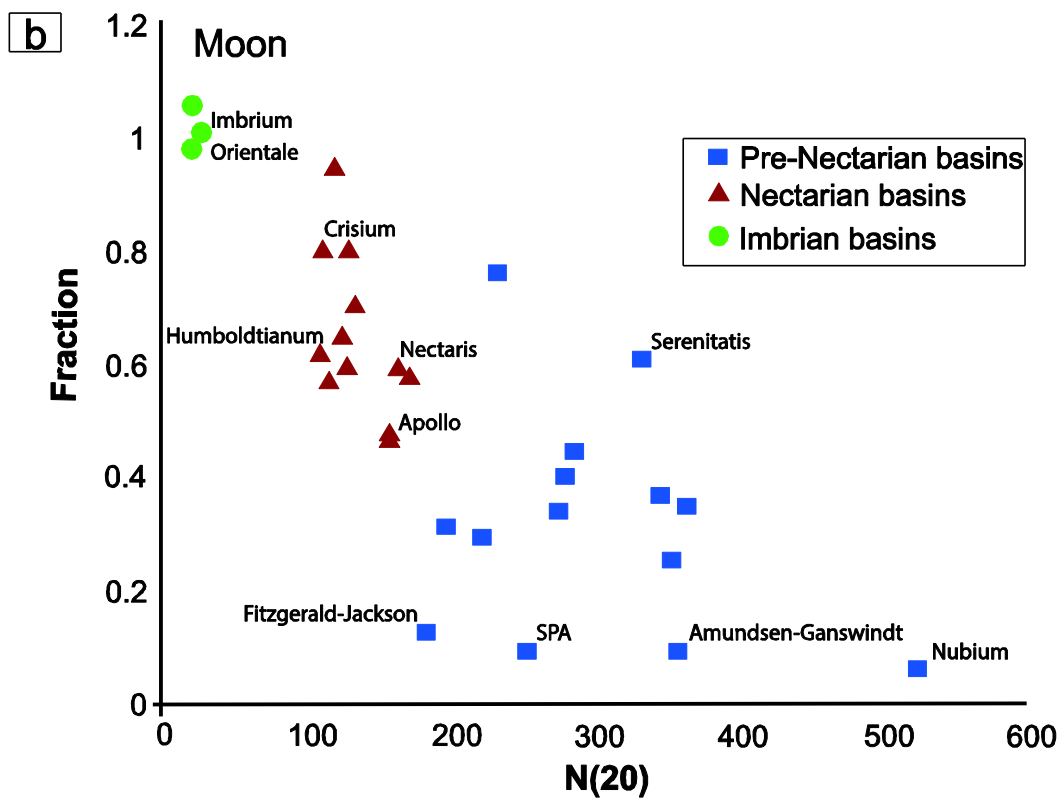
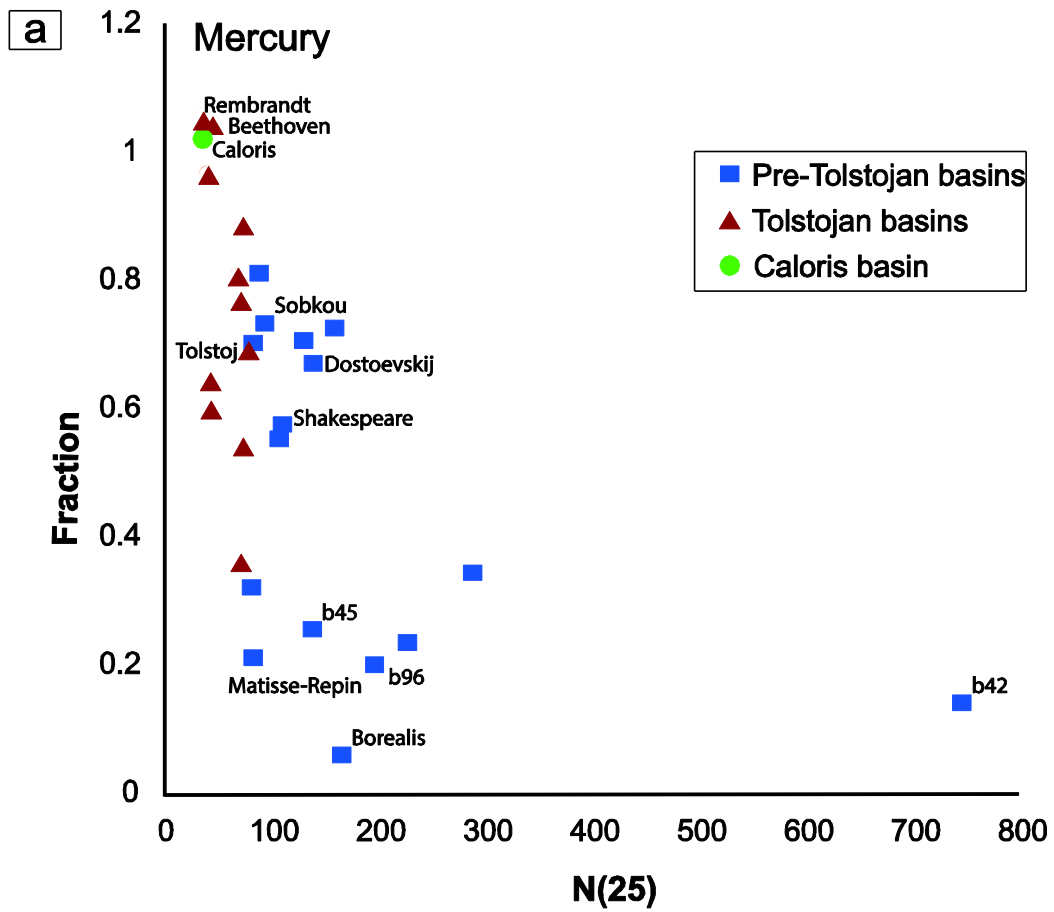


*Figure 6.12: Comparison of $N(20,25)$ versus fraction of original and BNSC-modified count area on Mercury (a) and the Moon (b). The BNSC-modified count area is the area size related to the smallest crater after computation. The diagrams present the decrease of the remaining area after the BNSC correction and the increase of the $N(20,25)$ value toward older surfaces. Fraction is calculated by 1.0 divided by the original count area size/BNSC-modified area size. Where the count area size/buffer area size is smaller than 1.0, the determined fraction could be larger than 1.0. a) Borealis, Matisse-Repin, b96, and b42 might be in saturation equilibrium on Mercury, where their original count area is less than 20% (fraction = 0.2). The $N(25)$ value derived by the BNSC technique of the corresponding basins is listed in Table 6.2. b) Fitzgerald-Jackson, South Pole-Aitken (SPA), Amundsen-Ganswindt, and Nubium might be in saturation equilibrium on the Moon, where their original count area is less than 20%, lunar data is from **Orgel et al. (2018)**.*

For example, Caloris, Beethoven, and Rembrandt basins' BNSC $N(25)$ values are calculated using nearly 100% of the original count area. Accordingly, the non-sparseness effect is negligible; we observed the same characteristic in the youngest basins on the Moon (**Orgel et al., 2018**). Consequently, these basins could belong to the same geologic time period. $N(25)$ values for Tolstojan basins are based on 40-90% of the initial count area, while most $N(25)$'s for Pre-Tolstojan basins were derived from 10-70% of the original areas.

At the largest crater diameters, four Pre-Tolstojan basins (Borealis, Matisse-Repin, b96, and b42) have less than 20% of their original count area remaining after the implementation of the BNSC (Figure 6.12/a, Table 6.2). This suggests that these basins have almost reached saturation equilibrium at crater diameters of ≤ 25 km, and that only 10-20% of their remaining count areas represent unmodified surfaces. Note that the crater population observed upon basins at, or close to, saturation cannot provide reliable AMAs due to the reduced number of craters that can be used for the fit. Thus, even though we provide AMAs in Table 6.2, those with the highest crater densities should be interpreted cautiously. The relatively small number of basins (Borealis, Matisse-Repin, b96, and b42) are saturated with craters that have diameters of ≤ 25 km, a conclusion consistent with previous results on the Moon (Head et al., 2010; Fassett et al., 2012b; Xiao & Werner, 2015; Povilaitis et al., 2017; **Orgel et al., 2018**). The BNSC method is, thus, useful for understanding the equilibrium conditions on Mercury and the Moon.

6.5.4. Impactor Population(s) and the Late Heavy Bombardment

Based on the observed crater populations on the Moon, Mars and Mercury, Strom et al. (2005, 2011, 2015) and Head et al. (2010) proposed two different populations of impactors. Fassett et al. (2012b) found a steep slope in the diameter range from 20 km to 100 km in the summed CSFDs of the Pre-Nectarian basins on the Moon and concluded that the impactor population changed in nature earlier than the mid-Nectarian period (Figure 6.9/a). However, **Orgel et al. (2018)** found that the steep slope is removed when the new BNSC technique is applied to the measurement of CSFDs on heavily cratered lunar basin (Figure 6.9/b). As a result, the CSFDs more closely follow the Neukum (1983) PF for all periods. This means that the shape of the impactor SFD across the Pre-Nectarian, Nectarian, and Imbrian periods did not change (**Orgel et al., 2018**). This implies that there was either one population of impactors or different populations with the same SFD.

One of the goals of our current work was to evaluate the nature of the impactor population(s) on Mercury using the same approach as for the Moon. We find that applying the BNSC to the CSFDs for the mercurian basins gives $N(25)$ densities that are on average 25% (excluding b42) higher than when using BCC approaches alone. The observed increase in crater densities using BNSC in the CSFDs come from the improved accounting of the small crater populations on these highly cratered surfaces by excluding areas where geometric crater obliteration occurred. This effect results in an increase in the measured crater spatial densities in these diameter bins, similar to what was seen for the BNSC on lunar data.

Again, if the Neukum (1983) and Neukum et al. (2001b) theory that the impactor population in the inner Solar System did not change over time, we would expect that the CSFDs for mercurian basins in different time periods maintain a single shape following the PF. With our new data analyses, we find that the shapes of the Pre-Tolstojan and Tolstojan basins are similar, although it is not possible to say conclusively whether the SFD of the Pre-Tolstojan basins drops off more sharply at < 50 km diameters due to the scatter of the dataset around the PF, which is more consistent with the Neukum et al. (2001b) PF than the Le Feuvre and Wieczorek (2011) non-porous model. Above 50 km diameters, the SFDs of both time periods show similar shapes and slopes. In summary, while inconclusive for craters < 50 km diameter, our results support a single impactor population or different populations with the same impactor SFD for Mercury. This study does not preclude changes to the CSFD in more recent epochs, i.e. in the Calorian and younger periods (Strom et al., 2011; Banks et al., 2017).

6.6. Conclusions

Altogether, we cataloged 94 basins, 1.7× times *certain* and *probable* basins as many as in earlier work (Fassett et al., 2012a). We performed crater size-frequency distribution (CSFD) analysis of 74 basins using the buffered crater counting (BCC) and the buffered non-sparseness correction (BNSC) techniques. Applying the BCC technique only allowed us to determine minimum values for CSFDs, so the relative ages of these basins are uncertain. The BNSC proved to be a useful technique to correct the effect of geometric crater obliteration due to heavy cratering on Mercury, which was successfully applied in previous study of the Moon (**Orgel et al., 2018**). Based on the CSFDs, we established a relative basin sequence, which proved to be generally in good agreement with the observed relative basin stratigraphy. We estimated that roughly half of the expected basin record is missing, where basins older than Borealis have been obscured by different processes (e.g., higher impact melt production, volcanism, subsequent impacts, and viscoelastic relaxation of basins) – a finding is in agreement with Marchi et al. (2013). We investigated the summed CSFDs of Pre-Tolstojan and Tolstojan basins to shed light on the impactor populations. In contrast to previous studies (Head et al., 2010; Fassett et al., 2012a, 2012b; Marchi et al., 2013; Strom et al., 2015), which demonstrate a change in the shape of the CSFDs prior 3.9 Gyr, our results are consistent with **Orgel et al. (2018)**, that one impactor population can explain the bombardment history of the surface of Mercury.

Acknowledgments

We would like to thank Lillian R. Ostrach, and an anonymous reviewer for their helpful comments that improved this manuscript. C. O. and C. R. were funded by the Deutsche Forschungsgemeinschaft (SFB-TRR 170, subproject A3), and H. H. via subproject A2. C. F. was supported by a NASA Discovery Data Analysis Program grant, Analysis of Large-scale Resurfacing Processes on Mercury. G. M. was supported by the German Aerospace Center (Deutsches Zentrum für Luft- und Raumfahrt) project 50QM1702, and C. H. vdB by the German Aerospace Center (Deutsches Zentrum für Luft- und Raumfahrt) project 50OW1504. All the raw data for this work are available on the NASA Planetary Data System (PDS).

The derived data products are at <http://dx.doi.org/10.17632/vf2sfbdvzr.1>. The dataset can be cited as Orgel, Csilla; Fassett, Caleb; Michael, Gregory; Riedel, Christian; van der Bogert, Carolyn H. Hiesinger, Harald (2020), "Re-examination of the population, stratigraphy, and sequence of mercurian basins: Implications for Mercury's early impact history and comparison with the Moon", Mendeley Data, V1, doi: 10.17632/vf2sfbdvzr.1

CHAPTER 7

TRAVERSES FOR THE ISECG-GER DESIGN REFERENCE MISSION FOR HUMANS ON THE LUNAR SURFACE

Elyse J. Allender, Csilla Orgel, Natasha V. Almeida, John Cook, Jessica J. Ende, Oscar Kamps, Sara Mazrouei, Thomas J. Slezak, Assi-Johanna Soini, & David A. Kring (2018). published in *Advances in Space Research*, 63,(1), 692-727, <https://doi.org/10.1016/j.asr.2018.08.032>

Abstract

This study explores the Design Reference Mission (DRM) architecture developed by Hufenbach et al. (2015) as a prelude to the release of the 2018 Global Exploration Roadmap (GER) developed by the International Space Exploration Coordination Group (ISECG). The focus of this study is the exploration of the south polar region of the Moon, a region that has not been visited by any human missions, yet exhibits a multitude of scientifically important locations – the investigation of which will address long-standing questions in lunar research. This DRM architecture involves five landing sites (Malapert massif, South Pole /Shackleton crater, Schrödinger basin, Antoniadi crater, and the South Pole-Aitken basin center), to be visited in sequential years by crew, beginning in 2028. Two Lunar Electric Rovers (LER) are proposed to be tele-robotically operated between sites to rendez-vous with crew at the time of the next landing. With engineering parameters in mind, we explore the feasibility of tele-robotic operation of these LERs between lunar landing sites, and identify potential high interest sampling locations en-route. Additionally, in-depth sample collection and return traverses are identified for each individual landing site across key geologic terrains that also detail crew Extra-Vehicular Activity (EVA). Exploration at and between landing sites is designed to address a suite of National Research Council (NRC, 2007) scientific concepts.

7.1. Introduction

As the international community continues to move forward with its vision for Solar System exploration, it is important to articulate a framework for inter-agency discussion and collaboration so that vital scientific questions may be addressed, and the overall strategic vision enhanced. The Global Exploration Roadmap (GER) provides such a framework. Developed by the International Space Exploration Coordination Group (ISECG) and last updated in 2018, the GER communicates a vision for collaborative and coordinated exploration of the Solar System, beginning with the International Space Station (ISS), continuing to the Moon and, eventually, leading to human missions on Mars (ISECG, 2018).

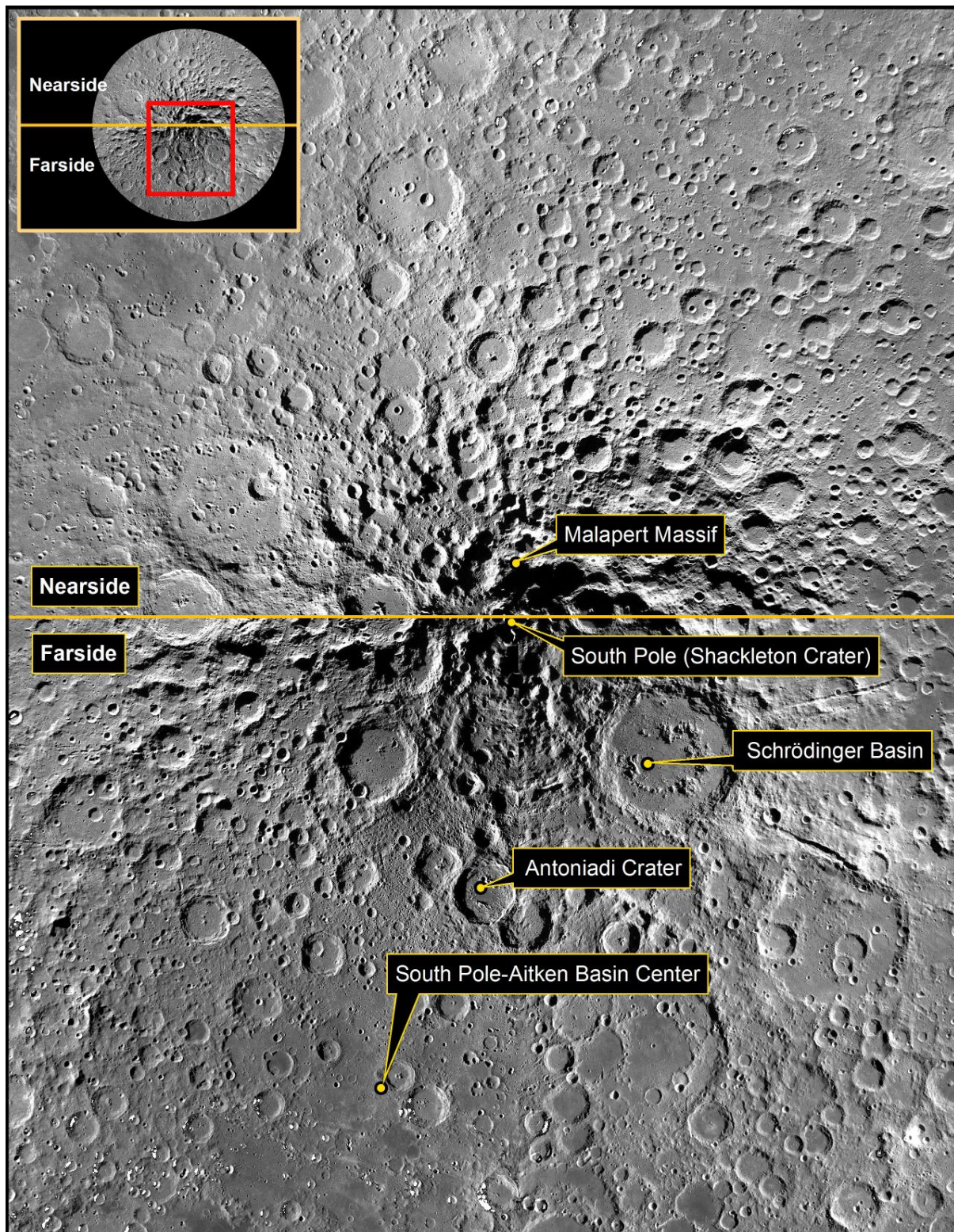


Figure 7.1: An overview of all landing sites considered in this study displayed on a LROC WAC mosaic of 100 m/pix. Projection is south polar stereographic.

Prior to the publication of the 2018 GER, envisaged updates to the 2013 version (ISECG, 2013) were presented by Hufenbach et al. (2015), who summarized the status of Design Reference Missions (DRM) targeting the lunar vicinity and surface, and highlighted the value these missions have for advancing the implementation of the GER. Hufenbach et al. (2015) also identified several opportunities for international cooperation and outlined a set of mission themes. This study examines the third theme – Humans to the Lunar Surface – and, in particular, its second phase “Human Lunar Surface Missions”.

The plan for Human Lunar Surface Missions is shaped by science, strategies for surface campaigns, and a Mars-forward perspective. The proposed missions focus on the south polar region and target five sites of diverse scientific interest: Malapert massif (85.99°S, 2.93°W), the South Pole/Shackleton crater (89.3°S, 130.0°W), Schrödinger basin (75.40°S, 138.77°E), Antoniadi crater (69.7°S, 172.0°W), and the South Pole-Aitken (SPA) basin center (60.0°S, 159.9°W). Here, we adjust the latitude and longitude of those sites slightly (Figure 7.1) in order to maximize scientific return within a 100 km Mars-forward exploration zone (Hufenbach et al., 2015). This exploration zone represents the maximum distance crewed rovers can travel from the landing site in order to return to a Lunar Orbital Platform-Gateway (LOP-G) within a 36 hr window in the event a mission abort is necessary (Whitley et al., 2017).

These sites are to be explored sequentially, beginning with Malapert massif. Before the first crew lands, two small pressurized rovers (SPRs), flight versions of the Lunar Electric Rover (LER), are delivered to the landing site. Once a crew arrives, it uses the rovers to explore the local region. After crew return to a LOP-G with the ascent vehicle and deliver samples back to Earth using the Orion, the rovers are tele-robotically driven to the next landing site where they can be used by a second crew. At each landing site, a crew of four is deployed, with two assigned to each SPR.

Here, we design (i) traverses between the landing sites and (ii) traverses in the vicinity of each landing site. To guide the design of those traverses, we utilize the key science concepts and investigative goals summarized by the National Research Council (NRC) (NRC, 2007). We list the prioritized and ranked concepts below:

- (1) The bombardment history of the inner Solar System is uniquely revealed on the Moon.
- (2) The structure and composition of the lunar interior provide fundamental information on the evolution of a differentiated planetary body.
- (3) Key planetary processes are manifested in the diversity of lunar crustal rocks.
- (4) Lunar volatiles increase our understanding of the composition state and distribution of volatiles in the lunar polar regions.
- (5) Lunar volcanism provides a window into the thermal and compositional evolution of the Moon.

(6) The Moon is an accessible laboratory for studying the impact process on planetary scales.

(7) The Moon is a natural laboratory for regolith processes and weathering on anhydrous airless bodies.

(8) Processes involved with the atmosphere and dust environment of the Moon are accessible for scientific study while the environment remains in a pristine state.

Within these eight concepts are 35 specific science goals to be addressed. Concepts 1 to 7 and their associated goals provide the framework against which the feasibility of each location within this study is assessed. Concept 8 has been addressed by the Lunar Atmosphere Dust and Environment Explorer (LADEE) mission and is not considered further here as we focus on addressing lunar interior and surface goals.

These concepts and goals were previously evaluated in a global lunar landing site study (Kring & Durda, 2012) which objectively identified scientifically-rich landing site locations. One of the sites, the Schrödinger basin, was identified in that study to be the highest priority landing site on the lunar surface because of the broad range of science and exploration objectives that could be addressed within that single location. Design reference missions, like those of Hufenbach et al. (2015) and Whitley et al. (2017), utilize a set of high-priority landing sites identified from Kring & Durda (2012) to realize exploration architecture set forth in the Global Exploration Roadmap (ISECG, 2013; ISECG2018).

This study ‘closes the loop’ in that we demonstrate how the design reference mission and engineering concepts of Hufenbach et al. (2015) can achieve the NRC (2007) goals and objectives using the mission architecture set forth in the Global Exploration Roadmap (ISECG, 2013; ISECG, 2018). We also utilize contributions from other landing site and traverse studies (Steenstra et al., 2016; Sruthi & Kumar, 2014; Kramer et al., 2013; Kring & Durda, 2012; Borst et al., 2012; Gibson & Jolliff, 2011). Steenstra et al. (2016), in particular, utilizes architecture from ISECG’s European Space Agency led Human-Enhanced Robotic Architecture and Capability for Lunar Exploration (HERACLES) mission concept (Landgraf et al., 2015), demonstrating the growing interest in human-robotic partnership for future exploration. Insights and implied trade studies (Section 7.6) arising from this work will help to further international collaboration on human-assisted robotic missions. It should be noted that once a formal landing site selection process has been performed by the international community the assessments within this paper can (and will) be performed again on the finalized selection.

Our results will be presented as follows: Section 7.2 provides a general overview of the geology of the SPA basin and each proposed human landing site, Section 7.3 details concept of operations information such as mission architecture elements, SPR functionality, sample collection requirements, and communication requirements.

Section 7.5 details traverses between landing sites, and at and around each site – taking parameters such as safe driving distances, trafficability, orbital communications coverage, and sample collection masses into account. Also, the ability to address NRC (2007) is assessed. In Section 7.6 we present recommendations for future trade studies, and Section 7.7 contains the study’s findings.

7.2. SPA Geology and Landing Sites

The South Pole-Aitken (SPA) basin is the largest (Smith et al., 2010) and oldest recognized impact structure (Wilhelms, 1987; Hiesinger et al., 2012; **Orgel et al., 2018**) in the Solar System with a diameter of 2500 km and a depth of approximately 13 km (Smith et al., 2010). Such a large basin-forming impact may have had significant thermal and geophysical effects both locally and globally. Based on Gravity Recovery and Interior Laboratory (GRAIL) data SPA basin exhibits a crustal thickness of < 20 km with local variations less than 5 km at Apollo and Poincare basins (Wieczorek et al., 2013). Because of the large extent of the SPA basin forming impact surface components may represent some of the deepest lunar materials, such as lower crust and upper mantle, which could be available to study (Cintala & Grieve, 1998; Vaughan & Head, 2014). Significant olivine exposures have not yet been detected within the SPA interior, only localized exposures of olivine in central peak/peak ring structures have been observed in Schrödinger basin and Zeeman crater (Kramer et al., 2013; Yamamoto et al., 2012).

Generally, SPA materials show enrichment in mafic minerals (pyroxenes) relative to the feldspathic highlands (Lawrence et al., 2002; Pieters et al., 2001; Moriarty and Pieters, 2018). There is a zoning in the distribution of low-Ca pyroxenes (Mg-rich pyroxenes) across the basin (Pieters et al., 2001; Nakamura et al., 2009) and high-Ca pyroxenes in a 700 km region in the SPA basin interior, distinct from both mare basalts and Mg-pyroxenes (Moriarty and Pieters, 2016; Ohtake et al., 2014). Additionally, the SPA interior exhibits a distinctive high-FeO chemical signature (Lucey et al., 1998a; Jolliff et al., 2000; Gibson & Jolliff, 2011; **Ivanov et al., 2018**) called the SPA Compositional Anomaly (SPACA). This compositional signature extends across the SPA basin (including to Schrödinger basin) and is likely a relict of impact melt produced by the SPA impact event (Hurwitz & Kring, 2013; Hurwitz & Kring, 2014; Hurwitz & Kring, 2015) or could reflect pre-impact stratification of the lunar crust (**Ivanov et al., 2018**).

As a consequence of its advanced age, the SPA basin interior has undergone extensive modification via processes such as impact cratering, mare/cryptomare and pyroclastic emplacement (Stuart-Alexander, 1978; Wilhelms et al., 1979; Gibson & Jolliff, 2011; Hiesinger et al., 2012; Kramer et al., 2013; Pasckert et al., 2018; **Ivanov et al., 2018**). Despite the thin crustal thickness across the entire SPA, the basin shows only a minor extent of volcanic activity (Wieczorek et al., 2013). A recent study from Pasckert et al. (2018) revealed the absolute model ages (AMA) of volcanic patches

within SPA and found two peaks in volcanic activity. The first major peak occurred between 3.6 Ga and 3.2 Ga, which is in agreement with the timing on the nearside (Hiesinger et al., 2002; Hiesinger et al., 2003) and the rest of the farside. However, the second volcanic peak (2.2 – 2.5 Ga) is not observed within SPA basin. Pyroclastic material has been detected at several locations within the SPA (Wilhelms et al., 1979; Gaddis et al., 2003). Schrödinger basin has a large volcanic vent, and a fracture running north from the vent. The vent and the surrounding dark-albedo region has a high-FeO abundance compared to the surrounding basin floor material (Kramer et al., 2013). Additionally, pyroclastic materials within Antoniadi crater (Sruthi & Kumar, 2014) and potentially in the SPA basin center (Borst et al., 2012) could be found at or near the landing sites.

Additionally, an asymmetric distribution of KREEP (Potassium-Rare-Earth-Elements-Phosphorous) material was detected by the Lunar Prospector mission (Lawrence et al., 1998; Lawrence et al., 2003; Lawrence et al., 2007). The Procellarum KREEP Terrain on the nearside is enriched in heat producing elements (K, Th, U) (Korotev et al., 2000) which could increase melt production for volcanic activity (Wieczorek et al., 2000). On the other hand, SPA has been defined by Jolliff et al. (2000) as a distinct geochemical terrane due to its intermediate Fe, and low Th signatures, which suggest the absence of a KREEP layer on the farside. Thus, there is a fundamental asymmetry in the thermal evolution of the Moon, including the distribution of heat sources in the lunar interior.

The first proposed landing site, Malapert massif, occurs along the edge of the basin while the final landing site is located near the center of the basin. As a whole, traverses planned at and around these proposed landing sites cross geologic terrains of various ages, and possibly various natures, defined by Wilhelms et al. (1979) and Spudis et al. (2008). We introduce each site in this section and provide detailed geological content of individual sites in Section 7.5.2.

7.2.1. Malapert Massif

Malapert massif is a mountainous surface feature located on the lunar nearside at 85.99°S, 2.93°W (Figure 7.1). The massif rises ~ 5 km above the lunar basal ellipsoid. Lunar massifs are postulated to form during large impact events in which underlying material is thrust above the surface creating a topographic high demarcated by faults or flexures (Harland, 2008). Thus, massifs are of particular geologic interest as they expose cross sections of the lunar crust. The ridge of Malapert massif contains two regions which are illuminated for 74% of the lunar year (Bussey et al., 2010) which may be used for solar energy collection if LER parameters allow. Additionally, the near-side (north) face of the ridge and portions of its summit are the only regions along the 5-landing site traverse that are in constant line-of-sight communication with Earth. The area surrounding Malapert massif also contains various small-scale permanently shadowed regions (PSR) which are accessible for exploration and will provide

information about extreme conditions in lunar polar environment and volatile composition.

7.2.2. Shackleton Crater

Shackleton crater is at the South Pole (Figure 7.1). It is a simple crater with a diameter of approximately 21 km at the rim and walls with slopes of $\sim 30^\circ$ that descend to a depth of 4.2 km (Haruyama et al., 2008). The crater floor is 6.6 km in diameter and is a PSR that may contain icy deposits of volatiles suitable for in-situ resource utilization (ISRU) (Mazarico et al., 2011), as well as lunar volatile-bearing regolith gardening processes. The crater walls are too steep, however, for the rovers (Section 7.3.2) to traverse, so crew will only be able to explore the crater rim and surrounding terrain including small and large-scale PSRs. In addition to PSRs, ‘cold traps’ – areas whose temperatures are cold enough to host H₂O, CO₂, and other volatiles (Watson et al., 1961) – are widely distributed within the South Pole region (see Appendices C4-B5 and C4-B6).

7.2.3. Schrödinger Basin

The landing site within the Schrödinger basin is located at 75°S, 133.5°E (Figure 7.1). The Schrödinger basin is inside the SPA basin and formed at the end of the basin-forming epoch on the Moon (Tera et al., 1974; Cohen et al., 2000; Stöffler & Ryder, 2001; Head et al., 2010; Morbidelli et al., 2012; **Orgel et al., 2018**). It is the best-preserved basin of its size in the Earth-Moon system. Schrödinger basin is ~ 320 km in diameter, 4.5 km deep, and has a well-preserved peak ring with a diameter of ~ 150 km that rises up to 2.5 km above the basin floor. The peak ring structure exposes a variety of minerals such as olivine, low and high-Ca pyroxenes, as well as anorthite (Kramer et al., 2013; Yamamoto et al., 2012). These minerals could show sequences of differentiated rock types from the upper mantle to the upper crust, respectively. Anorthosite (>97% anorthite) and pyroxene-bearing anorthosite may represent material similar to the highlands – the upper crystallization product of the magma ocean (Kramer et al., 2013). Moreover, pyroclastic material within an area of approx. 1250 km² with a localized source vent makes the Schrödinger basin a high-priority ISRU location (Wilhelms et al., 1979; Gaddis et al., 2003; Kramer et al., 2013).

Because it was previously identified as a high-priority site for lunar surface missions, it has received a lot of study (O’Sullivan et al., 2011; Bunte et al., 2011; Burns et al., 2013; Kramer et al., 2013; Kring et al., 2013; Senthil Kumar et al., 2013; Kring, 2014; Potts et al., 2015; Kring et al., 2016; Senthil Kumar et al., 2016; Steenstra et al., 2016), see Section 7.5.2.3. Samples collected from this basin can be used to address most of the science goals of the NRC (2007) report.

7.2.4. Antoniadi Crater

The landing site within *Antoniadi crater* is located at 69.5°S, 170°W (Figure 7.1). Antoniadi crater is ~ 143 km in diameter with a rim-to-floor depth of 4 km. The crater is noteworthy because it contains the lowest point on the Moon. A small crater puncturing the floor of Antoniadi extends the depth to 9.2 km below the lunar basal ellipsoid (Smith et al., 2010). Antoniadi crater contains both a central peak, and a central peak ring structure and is, thus, sometimes classified as a 'proto-basin' (Dominov & Mest, 2009). This crater is an attractive site to address some of the NRC (2007) objectives (Fagan et al., 2010) due to its relatively high thorium abundance – which may be a tracer for KREEP material (Lawrence et al., 1998) – the presence of some of the youngest mare on the far side of the Moon with an AMA range from 2.2 Ga to 3.7 Ga (Wilhelms et al., 1979; Pasckert et al., 2018), and pyroclastic materials (Sruthi & Kumar, 2014).

7.2.5. SPA Basin Center

The landing site within the *SPA basin center* on the lunar farside is located at 55.4°S, 163.3°W just northeast of Bhabha crater (Figure 7.1).

The proposed landing site is situated near the Mafic mound (60.0°S, 159.9°W) whose unusual composition has led to some controversy surrounding its origins – the mound may represent the remnants of SPA impact melt (Hurwitz & Kring, 2013; Hurwitz & Kring, 2015), be an impact-induced volcanic structure, or be a hybrid of these possibilities (Moriarty & Pieters, 2015). Mafic mound is approximately 75 km long and 1 km high and is also associated with a Bouguer anomaly that implies it is associated with significant excess mass relative to its surroundings (Zuber et al., 2013). The proposed landing site is also located within the SPACA. This area has additionally been proposed to be the landing site for the MoonRise sample return mission (Jolliff et al., 2003; Jolliff et al., 2010; Jolliff et al., 2017). To the northwest of the landing site is Bose crater, which is approximately 90 km in diameter and contains a central peak and terraced crater wall. Its central peak exhibits low-Ca pyroxene that could underlie the high-Ca pyroxene layer and also could provide impact melt from the SPA basin forming event. Additionally, pyroclastic materials from Bose and Bhabha craters may be exposed in this region (Borst et al., 2012), but unfortunately our planned traverses were not able to access these locations.

7.3. Concept of Operations

Here we introduce the mission architecture based on Hufenbach et al. (2015), crew rover capabilities, geologic sample requirements, and communication requirements used to develop a concept of operations.

7.3.1. Mission Architecture

The design reference mission scenario (Hufenbach et al., 2015) utilizes the Space Launch System (SLS), the Orion multi-purpose crew vehicle, an evolvable Deep Space Habitat (eSDH), a human lander with a reusable ascent stage, and two small pressurized rovers for crew who will be delivered to the surface for 28 days of exploration. Multiple SLS launches are needed to deliver those assets to the Moon. For this study we assume five SLS launches, one year apart, with each launch delivering a team of four crew to eDSH for subsequent surface exploration. The eDSH is a prototype habitat that builds on the expertise, capabilities, and lessons learned from the International Space Station (ISS). The conceptual vehicle has, more recently, been called the Deep Space Gateway (DSG), or the Lunar Orbital Platform-Gateway (LOP-G). In order to adhere to current nomenclature, we hereby refer to the eDSH as the LOP-G. In this DRM, the LOP-G is in a halo orbit around the second Earth-Moon LaGrange Point (EM-L2) where it will also serve as a communication relay from the lunar farside to Earth. A dual stage lander will perform descent/ascent, rendezvous, and docking manoeuvres with the LOP-G. The DRM assumes the ascent vehicle can be reused up to five times, provided it receives maintenance and refueling (Hufenbach et al., 2015).

Hufenbach et al. (2015) notably uses architectural elements from NASA's cancelled Constellation program of the new millennium. The SLS is a redeveloped version of the Ares V, however, the SLS will launch both crew and cargo together rather than relying on the dual launch combination of Ares I and Ares V, which were to rendez-vous in Low Earth Orbit (LEO) before continuing toward the Moon (Connolly, 2006). The Orion crew vehicle also has undergone redevelopment from the days of Constellation with the Crew Exploration Vehicle (CEV) being modified to the Multi-Purpose Crew Vehicle (MPCV).

In terms of lunar surface scenarios, the DRM of Hufenbach et al. (2015) (and thus, the ISECG) differs from that of Constellation in that it does not establish a permanent polar outpost. The lunar habitats are instead the rovers themselves (Section 7.3.2). The goals of "pervasive mobility" – enabling the scientific exploration of large areas of the lunar surface, "global connectivity" – enabling communication throughout exploration activities between astronauts and ground staff on Earth, and "long duration missions"

Table 7.1: Summary table of concept of operations.

| Characteristics | Tele-robotic operation | Crew operation |
|--------------------|---|-----------------------------------|
| Average speed | 0.36 km/h (0.1 m/s) | 5 km/h (1.38 m/s) |
| Maximum slope | 25° | 25° |
| Preferred slope | Under 15° | Under 15° |
| Driving capability | Only sunlit periods | Sunlit periods and lunar darkness |
| Driving limitation | Only during direct communication with Earth | Max. 14-days |

– allowing comprehensive lunar exploration activities to be performed and providing a proving ground for ISRU and other technologies applicable for Mars exploration (Mazanek et al., 2009) – are still maintained in the Hufenbach et al. (2015) DRM.

7.3.2. Small Pressurized Rovers (SPR)

Two Small Pressurized Rovers (SPR) will be used to explore the lunar surface. Their design is assumed to be a flight-evolved version of the Lunar Electric Rover (LER), which has been field tested in 3-day, 14-day, and 28-day-long mission simulations (Kring, 2017; Kring et al., 2017; Eppler et al., 2013). Because we utilize the capabilities of the LER in our analysis, we will refer to the rovers as LERs rather than SPRs in the remainder of this report.

The LER utilizes the Chariot chassis of Harrison et al. (2008), which has the ability to adhere to the surface better than the Apollo Lunar Roving Vehicle (LRV). A post-Apollo analysis recommended future rovers have the capacity of ascending and descending slopes of $\sim 25^\circ$ (Lunar Exploration Science Working Group, 1995). The Chariot chassis was designed to climb up 15° slope in terrestrial 1 g test conditions. When outfitted with a cabin to simulate an SPR, the LER climbed $18^\circ - 20^\circ$ slopes on the flank of a cinder cone (Öhman & Kring, 2012), suggesting 25° is a reasonable limit for lunar conditions. For the present study, we adopt a maximum slope limit of 25° as a ‘no-go’ value, but generally plan traverses on much shallower $< 15^\circ$ slopes. The average slope of our traverses is $\sim 4.3^\circ$. A summary of LER capabilities used in the study is given in Table 7.1. We also note that the slope is generally downhill from the first landing site at Malapert massif to the SPA basin center (Figure 7.4).

LERs may be operated by crew around landing sites and tele-robotically from the LOP-G or Earth (via the LOP-G or satellite relay) between landing sites. When crewed, the LERs typically accommodate two crew members, however, in the event of an emergency a single LER is capable of supporting all four crew members for a limited time. As per simulations carried out during NASA’s Desert Research and Technology Studies (DRATS) simulations in Northern Arizona (Eppler et al., 2013), crew may conduct LER-enabled traverses away from the landing site for a maximum of 14 days – this number reflects the total volume of consumables that can be carried by the rover. Each LER is equipped with a Portable Utility Pallet (PUP) – a portable charging station that also provides exterior storage for consumables, and a Portable Communications Terminal (PCT) to provide additional communications flexibility when crew are performing Extra-Vehicular Activities (EVA).

The LER is also a geological tool that accommodates Intra-Vehicular Activity (IVA) (Kring, 2017; Kring et al., 2017). It includes high-visibility windows that provide a 180° field-of-view and incorporates a minimum of six cameras – ForeCam, AftCam, port and starboard cameras, and docking cameras – which are utilized for safety, traversing and scientific purposes. These features facilitate observations and imagery of both local and distant geological features. The DRATS simulation illustrated that

IVA could provide high quality scientific characterization, similar to those enabled by EVA. EVA capability incorporates a SuitCam, enables mobile observations, and allows for in-situ sampling which is assisted using the onboard geologic tool rack, which contains rock hammers, tongs, a scoop, sample bags, and a sample storage compartment.

Table 7.2: NRC (2007) goals addressed with the addition of notional instrumentation to the LER. See Appendix C5 for a breakdown of all NRC goals.

| Unit Type | NRC goals (GPR) | NRC goals (chem. Analysis/APSX) | NRC goals (Gigapan) | NRC goals (Neutron detector) |
|----------------------|--------------------|------------------------------------|------------------------|------------------------------|
| Simple crater | 3d, 6a, 6c, 6d | 3a, 3b, 3c, 3d, 6a, 6c, 6d, 7a | 2a, 3d, 3e, 6a, 6b, 6c | |
| Complex crater | 3d, 6a, 6b, 6c, 6d | 3a, 3b, 3c, 3d, 6a, 6b, 6c, 6d, 7a | 2a, 3d, 3e, 6a, 6b, 6c | |
| Ejecta blanket | 3d, 6b, 6d | 3d, 6d | 3d, 6b | |
| Impact melt sheet | 3d, 6a | 3d, 6a | 2a, 3d, 6a | |
| Megaregolith | 3d, 3e | 3d, 3e | 3d, 3e | |
| Regolith | 3d, 4e, 7a, 7b, 7c | 4d, 7a, 7b, 7c, 7d | 2a, 3d | |
| Volatiles | 3d, 4a, 4c, 4d | 3d | 3d | 4a, 4b, 4c |
| Pyroclastic material | 3d, 5c | 3d, 5c | 2a, 3d | |
| Mare deposit | 3d, 5a | 2d, 3a, 3d, 5a, 5d, 6c | 2a, 3d | |

Without accurate estimations of the reduced productivity of the LERs during lunar darkness, this study assumes the same rate of both IVA and EVA ability for daytime and nighttime operations. There is a need for a trade study, which investigates both, driving and sampling (Section 7.3.3) in limited illumination conditions (Section 7.6).

At the time of this study, several uncertainties remain regarding the instrumentation payload that will be employed on the LER. Table 7.2 provides an overview of NRC (2007) goals that could be addressed along each ‘between landing site traverse’ if each of the additional notional instruments were included. The instruments considered for this study are adapted from Steenstra et al. (2016) who utilized the HERACLES mission concept, they are: Ground Penetrating Radar (GPR) – for lateral and vertical subsurface structure observations (we assume this is deployed at every landing site), a GigaPan camera – which provides oblique, color images at gigapixel resolution for panoramic and detailed visualization of geologic features of interest, an Alpha Particle X-Ray Spectrometer (APXS) and a Laser Induced Breakdown Spectrometer (LIBS) – for in-situ chemical analyzes, and a neutron spectrometer to detect H-bearing volatiles. Although we did not assume the LER would have a robotic arm for sample collecting, it became clear during the course of our study that an arm and ability to collect samples would greatly enhance our ability to address NRC (2007) science objectives and ISRU objectives.

A notable advantage of conducting either tele-robotic or crewed traverses with the LERs is that close-up imagery of exposed stratigraphy can be captured with the range

of cameras onboard – particularly the Gigapan – which can provide high-resolution detail about exposures on side-facing slopes which are not visible in orbital imagery.

The LER is designed to travel at speeds up to 5.56 m/s (20 km/hr) (Harrison et al., 2008), approximately twice the maximum designed speed of an Apollo-era LRV (Costes et al., 1972). Speeds adopted for use in this study are 1.39 m/s (5 km/hr) for crewed traverses, and 0.1 m/s (0.36 km/hr) for tele-operated traverses. The reduced speed for tele-operations will make it easier to avoid hazards and, importantly, will allow for continuous subsurface surveys with a GPR and volatile detection with a neutron spectrometer.

7.3.3. Sampling Requirements

When tele-robotically operated between human landing sites, the LER – at its current stage of development – has no sample collection ability. We show in Table 7.2 and in Section 7.5.1, that such an ability may be warranted given the terrain traversed and the number of NRC (2007) objectives these samples may address. This information is also presented in detailed tabular form in Appendix C1. When LERs are crewed at landing sites, sample collection is possible via EVA – the NRC (2007) objectives able to be addressed at each site are discussed in detail in Section 7.5.2 and a detailed summary of all planned EVAs (location, addressed NRC (2007) objectives, sample types, sample masses) is presented in Appendices C2-1 to C2-5.

A key constraint when estimating total sample mass requirements for the EVAs mentioned above concerns the complexity of lunar geology. The rock type and analytical methods suitable for that rock type dictate the sample size required to address any given science goal. Here we estimate minimum samples masses using parameters recommended by the Curation and Analysis Planning Team for Extraterrestrial Materials (CAPTEM) (Shearer et al., 2007). For example, CAPTEM (their Table 5) recommends 500 g for a mare basalt sample, 5000 g for a complex impact breccia, 0.5 g/clast for a rake sample, and 2000 g for an unsieved regolith sample. As each lithology is encountered in our traverses, sample masses are collected using those guidelines (Table 7.3).

An alternative way to estimate sample mass is by using a sampling rate per EVA hour. An analysis of Apollo missions determined that the astronauts collected 2.3 kg per crew member per EVA hour (Kring, 2007). Applying that metric, our traverses would produce larger masses than those estimated using minimum CAPTEM recommendations (Table 7.4). In this table, sample masses are also given in the case that only a single LER crew goes EVA each day.

Table 7.3: Summary of minimum sample masses collected for traverses at each site in this study. These are minimum sample masses because they assume only a single sample of each type is collected per station using CAPTEM recommendations (Shearer et al., 2007). In reality, multiple samples are likely.

| Sample type (collection method) | Malapert massif | South Pole (Shackleton crater) | Schrödinger basin | Antoniadi crater | SPA basin center |
|---|-----------------|--------------------------------|-------------------|------------------|------------------|
| Pyroclastic material (scoop) | - | - | 10 | 14 | - |
| Pyroclastic material (hand specimen) | - | - | - | 3.5 | - |
| Peak ring/central peak material (hand specimen) | - | 4 | 2.5 | 1.5 | 1 |
| Mafic mound (hand specimen, breccia) | - | - | - | - | 15 |
| Mare/cryptomare basalt (hand specimen) | - | - | 1.5 | 4 | 2 |
| Impact melt (breccia, hand specimen) | 55 | 1.5 | 35 | 45 | 25 |
| Wall material (breccia, rake) | - | - | 23 | 1.5 | 20 |
| Ejecta (rake, scoop, breccia) | 26 | - | 4 | 5 | 11 |
| Volatile-rich regolith (scoop) | 16 | 36 | 2 | - | - |
| Regolith (scoop) | 34 | 5 | 10 | 8 | 16 |
| Total (kg) | 126 | 46.5 | 88 | 82.5 | 90 |

Table 7.4: Sample masses per landing site calculated using a sampling rate of 2.3 kg per crew member per EVA hour (Kring, 2007). The number of EVA at each landing site are 24, 18, 34, 23, and 18 respectively.

| Sample Mass (kg) at each landing site | | | | | |
|---------------------------------------|-----------------|--------------------------------|-------------------|------------------|------------------|
| Collection rates | Malapert massif | South Pole (Shackleton crater) | Schrödinger basin | Antoniadi crater | SPA basin center |
| Four crew members (9.936 kg/hr) | 238.5 | 178.8 | 337.8 | 228.5 | 178.8 |
| Two crew members (4.968 kg/hr) | 119.2 | 89.4 | 168.9 | 114.3 | 89.4 |

7.3.4. Communications

When assessing the feasibility of communications coverage for this study we considered several options: direct Earth-Moon-Earth communications achieved via radio communications, based on calculations performed by Massachusetts Institute of Technology (2016), Earth-Moon-Earth communications using a relay tower on Malapert massif, and Earth-Moon-Earth communications using the LOP-G at EM-L2.

The north-facing ridge of Malapert massif and portions of its summit are the only regions along the 5-landing-site traverse that are in direct line-of-sight communication with Earth. The south-facing side of the massif, as well as much of the region south of the massif (traversing toward the lunar farside) cannot be in direct contact with Earth as they are shielded by the topography of the massif. See Appendix C3 for details of communications scenarios using the direct-to-Earth methods tested in this study.

For a humans-to-surface mission, continuous contact with Earth is desired and, thus, we select a halo orbit around EM-L2 (Hopkins et al., 2013). Hopkins et al. (2013) states that there are two broad classes of halo orbit available, a northern-class halo, which spends more time over the northern hemisphere of the Moon, and a southern-class halo, which spends more time over the southern hemisphere of the Moon. Of these two classes, the southern-class is the most suitable for observation of all of the proposed landing sites in the south polar region. Another important consideration in selecting an orbital configuration for all proposed landing sites is the amount of coverage at each site. Thus, there are two additional orbital sub-configurations to be considered – small and large halos. Large halos are positioned further from EM-L2 and closer to the Moon, giving them an orbital period of approximately 9 days, while small halos are positioned closer to the EM-L2 point, which increases the length of their orbital period to approximately 14.8 days (Hopkins et al., 2013). As seen in Figure 7.2 the large southern-class halo provides consistent coverage of the majority of our proposed landing sites (Lockheed Martin, 2016). The small southern-class halo provides superior coverage for three of our five sites, however, Malapert massif and the Shackleton crater experience severely reduced coverage, with only 2.96 and 4.44 days of communication respectively, see Table 7.5. Therefore, using the Hufenbach et al. (2015) architecture, the LOP-G would be placed into the large southern-class configuration.

Though not pursued in this study, another feasible option is to place the LOP-G into a Near Rectilinear Halo Orbit (NRHO) using DRM architecture from Whitley et al. (2017). If the NRHO were selected as the orbital configuration for the LOP-G in this study up to 86% coverage for all landing sites would be possible (Whitley et al., 2016), an improvement of up to 2% coverage at four of the five proposed landing sites. While the NRHO is comparable to the large and small halo configurations in terms of propellant cost, this configuration offers additional advantages in that it has very short transfer times (0.5 day vs 3 days for an EM-L2 halo), reducing crew time on the landing vehicle, decreasing the mass required for air, supplies and related systems, and allowing for an increase in propellant mass (Whitley et al., 2017).

Table 7.5: Communication coverage at landing sites utilizing a relay in a halo EM-L2 configuration. The calculated values are provided by Lockheed Martin (2016), based on a previously published analysis for a small halo orbital period of 14.8 days and a large halo orbital period of 10.6 days (Hopkins et al., 2013).

| Proposed Landing Site | Small Halo (days / % coverage) | Large Halo (days / % coverage) |
|--------------------------------|--------------------------------|--------------------------------|
| Malapert massif | 2.96 / 20-30 | 8.90 / 84 |
| Shackleton crater | 4.44 / 30-40 | 8.90 / 84 |
| Schrödinger basin | 11.84 / 60-90 | 9.01 / 84-85 |
| Antoniadi crater | 14.80 / 100 | 9.01 / 85 |
| South Pole-Aitken basin center | 14.80 / 100 | 9.12 / 85-86 |

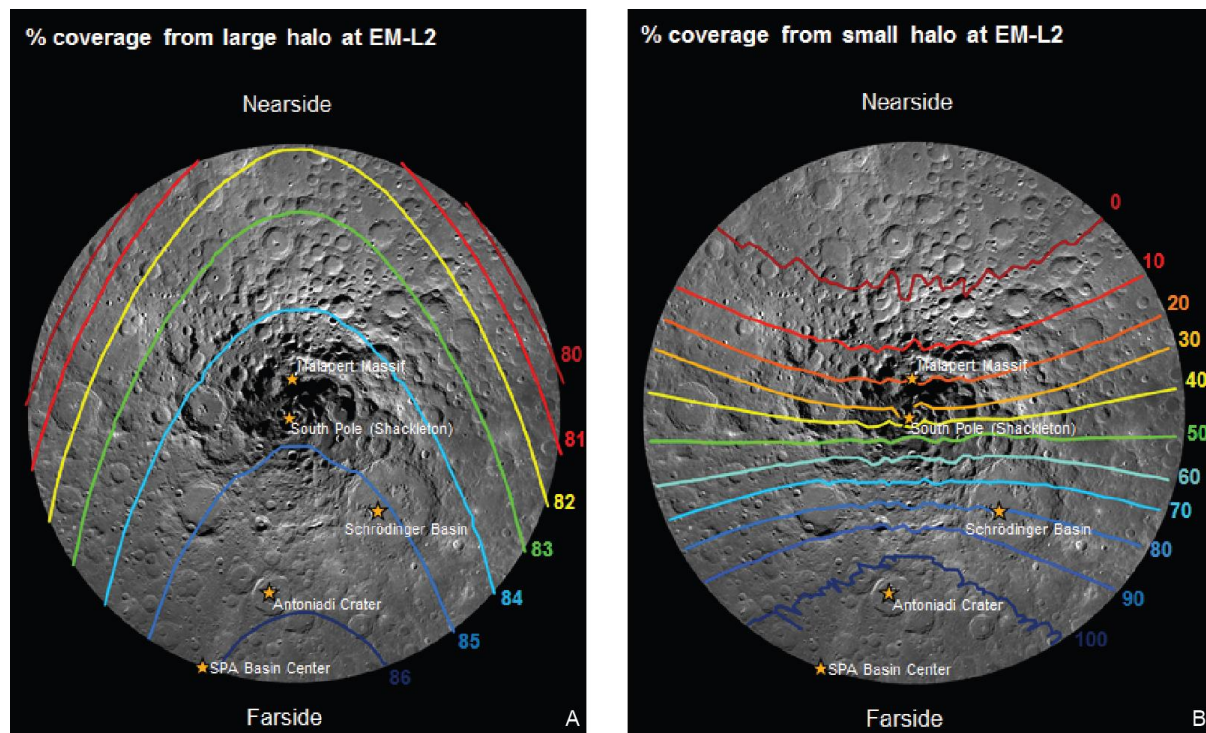


Figure 7.2: Percentage communication coverage for landing sites provided by large (A) and small (B) halo orbital configurations (Lockheed Martin, 2016).

7.4. Methodology

We design tele-robotic traverses between landing sites and crew traverses at landing sites in ESRI ArcGIS 10.1. Trafficability information is obtained by deriving slope maps and hillshaded Digital Elevation Models (DEM) from Lunar Orbiter Laser Altimeter (LOLA) (Smith et al., 2010) data available at resolutions from 10 to 100 m depending on latitude (Malapert massif: 20 m/pix, South Pole/Shackleton 10 m/pix, Schrödinger basin and Antoniadi crater: 60 m/pix and SPA basin center: 100 m/pix). Slope profiles were derived using LOLA DEM at resolutions from 10 to 100 m/pix (Appendix C4-A1, C4-B2, C4-B3, C4-C4, C4-C5, C4-C6, C4-D2, C4-D3). 3-D visualizations of landing site accessibility are created in ArcScene by combining Lunar Reconnaissance Orbiter (LROC) (Chin et al., 2007) Narrow Angle Camera (NAC) (1m/pix) imagery with LOLA DEMs at 60m/pix resolution for Schrödinger basin and Antoniadi crater. We processed these raw NAC images using the Ames Stereo Pipeline (Moratto et al., 2010).

To assess notional traverses, LROC Wide Angle Camera (WAC) (100 m/pix) images are overlaid with a selection of geologic maps (Wilhelms et al., 1979; Spudis et al., 2008; Gibson and Jolliff, 2011; Borst et al., 2012; Kramer et al., 2013; Sruthi & Kumar, 2014) in order to optimally locate sampling stations. Furthermore, we use these maps and their associated literature to identify scientifically interesting geologic features to visit en route. Additional data are extracted from Sruthi & Kumar (2014) and Kramer et al. (2013) concerning boulder availability and volcanic cones for Antoniadi crater, and M³ (Green et al., 2011) spectral data for Schrödinger basin. LROC NAC images

are used to refine station locations to specific deposits, outcrops, contacts, or boulders, as well as avoid hazards such as small craters below the detectable resolution of existing regional DEMs. Sample collection is designed in order to maximize the number of NRC (2007) concepts and goals that can be addressed at each site and across the study as a whole.

To obtain information about lunar volatile and cold-trap locations we use various datasets (Paige et al., 2010; Mazarico et al., 2011; Mandt et al., 2016). In order to identify regions where H₂O and CO₂ ice are present, temperature data from LRO's Diviner Lunar Radiometer Experiment is used (Paige et al., 2010). This data includes maximum, average, and minimum annual surface temperatures at 240 m/pix resolution. ArcGIS was used to create binary raster data indicating areas where H₂O and CO₂ ice can be stable. The H₂O ice stability map (Appendix C4-B5) is created based on regions where temperatures are lower than the H₂O sublimation temperature of 106°K, and CO₂ ice stability map (Appendix C4-B6) is based on areas where temperatures are lower than the CO₂ sublimation point of 54°K (Zhang & Paige, 2009; Zhang & Paige, 2010). We use a map of permanently shadowed regions from Mazarico et al. (2011) at a resolution of 240 m/pix (Appendix C4-B4). We also derive hydrogen concentration maps in 100 ppm, 125 ppm, and 150 ppm from Lunar Prospector Neutron Spectrometer (NS) data (Appendix C4-B5) (Elphic et al., 2007).

Traverse routes were located between the refined sampling stations using a least cost approach with a high weight given to the slope dataset in order to adhere to the slope capabilities of the LERs.

7.5. Results

7.5.1. Tele-Robotic Traverses Between Landing Sites

This section considers the feasibility of traversing between human landing sites in the allotted traverse period of one year between crew landings (Hufenbach et al., 2015).

As illustrated below, we found that it is possible for LER to navigate from the first landing site to the fifth landing site, although access to the floor of Antoniadi crater and one of two potential access routes to the floor of the Schrödinger basin need to be confirmed.

For between site traverses, we design two types of traverse to fully investigate potential options; a 'direct' traverse, and a 'science' traverse (Figure 7.3). The first utilizes the most direct route between human landing sites (given the slope capabilities of the LERs) and, thus, takes much less time to complete.

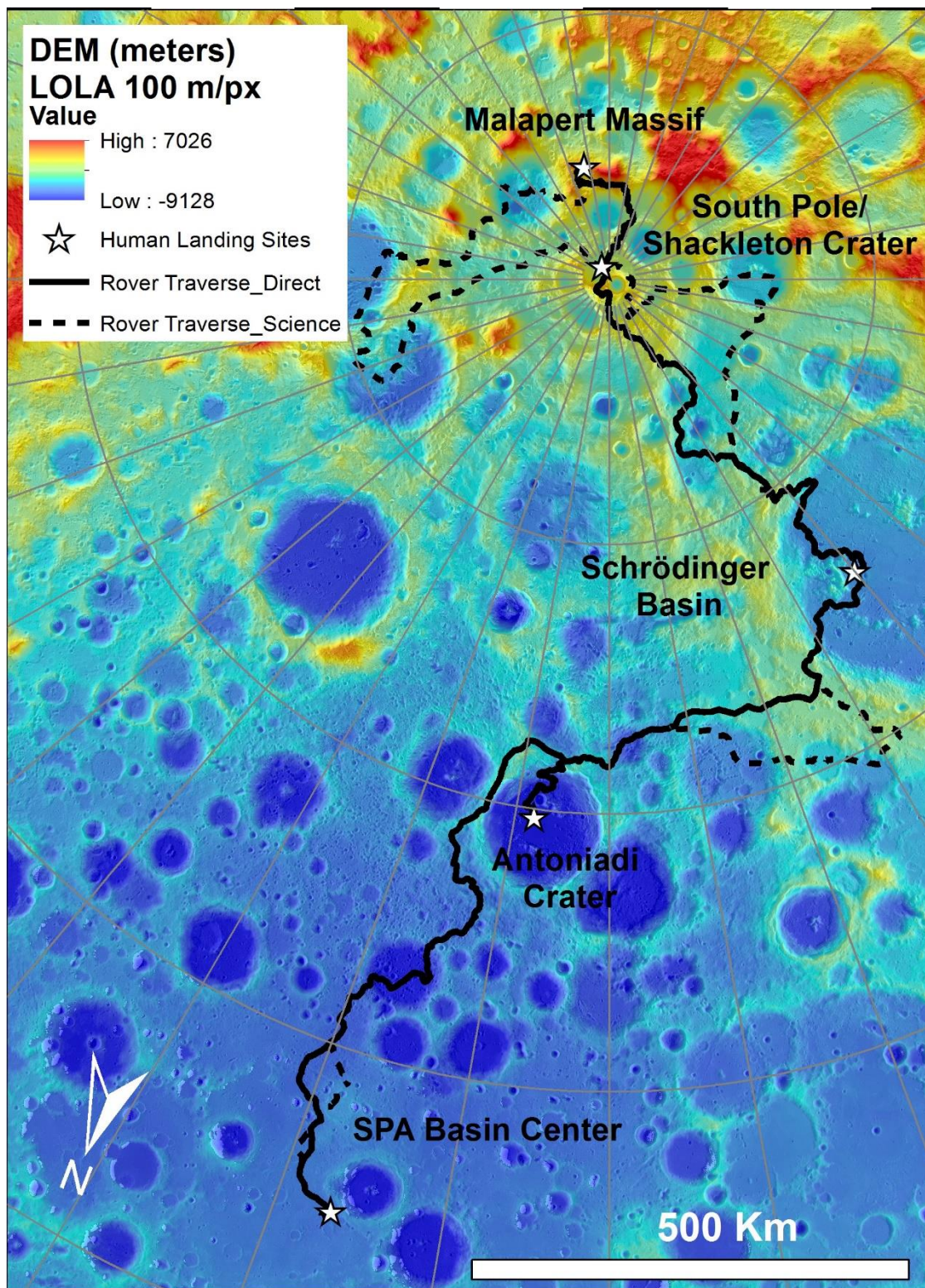


Figure 7.3: Colorized DEM of between landing site traverses from Malapert massif to South Pole-Aitken basin center displayed on a LRO LOLA mosaic of 100 m/px. Direct traverse shown with a solid line, while science traverse shown with a dotted line and landing sites with white stars. North is towards every direction from the South Pole shown by the grey polar stereographic grid. The traverses progress gradually north, as shown with an arrow in their direction.

7. TRAVERSES FOR HUMANS ON THE LUNAR SURFACE

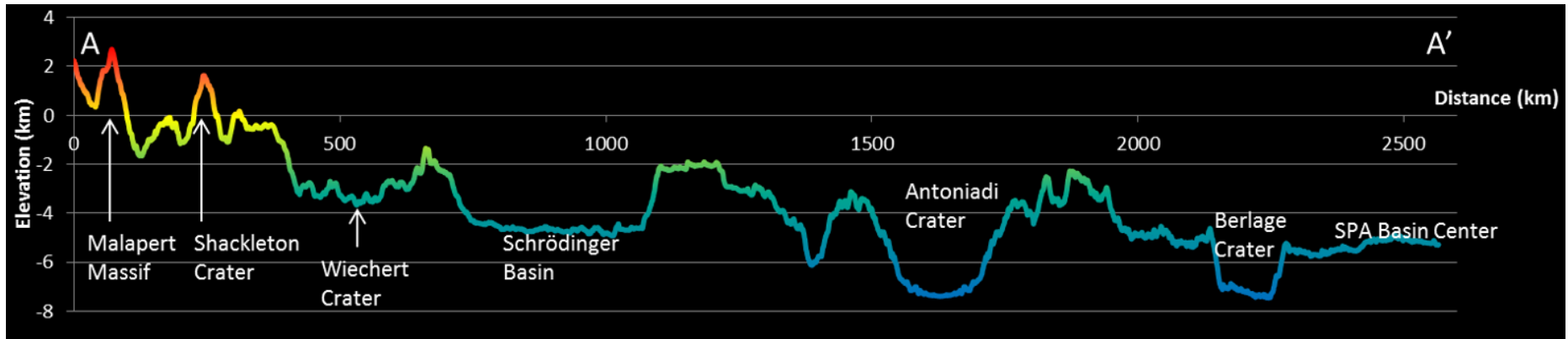


Figure 7.4: Colorized slope profile corresponding with the legend from Figure 7.3 of between landing site traverses from Malapert massif to South Pole-Aitken basin center. Note that the overall route progresses downhill into the center of the basin.

Through examination of multiple datasets along these direct routes we determine that no additional observational/sampling opportunities exist that provide information (with respect to the NRC (2007) concepts) that we do not already address with the at-landing site traverses. Thus, no time is allocated for observation along these routes and the LERs arrive at the next landing site early and sit waiting for the arrival of the next crew for up to several months.

The second type of traverse, the ‘science’ traverse, takes into account additional scientific gains that could be made if the entire year were utilized for observation and potential sampling (depending on notional LER instrumentation). Thus, science traverses deviate from the direct traverse routes in order to travel longer distances to sites of interest that may offer additional scientific merit with respect to the NRC (2007) concepts. For these traverses, we also consider deployment of notional instrumentation that may offer scientific gain if included on the LER; see Section 7.3.

With respect to risk, these science traverses are designed with slope and terrain factors in mind, as well as the 365-day travel time constraint; see Figure 7.4 for an overview of the route, in which it can be seen that the entire travel route progresses downhill into the basin center. With respect to the travel time constraint, the total driving time for the LERs is further limited by communications coverage (see Section 7.3.4), which may not be continuous, as they are to be tele-operated between human landing sites.

We assume that the surface is illuminated for 50% of the year (simply due to the day/night transition), and that the LERs will only be tele-operated in the daytime to maximize hazard avoidance. We then use communication data from Lockheed Martin (2016) to calculate maximum driving times for each traverse given orbital coverage for each landing site (Table 7.6 and Figure 7.2). The maximum driving distance is then calculated by multiplying this number with the allowable speed of the LERs while tele-operated (0.1 m/s or 0.36 km/hr). An assumed contingency margin of 30% is taken into account along all traverses, which is also subtracted from the maximum number of possible driving days. As a result, this provides the ‘safe’ driving distance (due to full communications and hazard avoidance) for the traverses between human landing sites in one year (see Table 7.6).

Table 7.6: Direct and science traverse lengths with respect to ‘safe’ driving distance with the LER tele-operated from EM-L2.

| From | To | Safe distance (km) | Direct traverse (km) | Direct traverse time (days) | Science traverse (km) | Science traverse time (days) |
|-------------------|--------------------------------|--------------------|----------------------|-----------------------------|-----------------------|------------------------------|
| Malapert massif | Shackleton crater | 932.7 | 208.4 | 24 | 911.4 | 105 |
| Shackleton crater | Schrödinger basin | 938.2 | 739.7 | 86 | 923.5 | 106.8 |
| Schrödinger basin | Antoniadi crater | 943.7 | 681.9 | 79 | 935.9 | 108 |
| Antoniadi crater | South Pole-Aitken basin center | 949.2 | 939.5 | 108 | 946.9 | 109 |

Detailed tables for each ‘science’ traverse are available in Appendix C1, documenting potential sampling stations, geologic units, and NRC (2007) goals able to be addressed with cameras, with sample return and with additional instruments. Note that in this study we find no opportunity to explore lava tubes during tele-robotic traverses between landing sites, or crewed traverses at and around landing sites.

Slope profiles for each of the direct and science traverses are given in Appendix C6.

7.5.1.1. Malapert Massif to Shackleton Crater

The direct and science traverses from Malapert massif to Shackleton crater are presented in Figure 7.5.

The direct traverse lies south of the Malapert massif, circumnavigates Haworth crater in a clock-wise direction, and passes the western rim of Shoemaker crater before approaching the South Pole/Shackleton crater landing site. It is 208.4 km in length and takes ~ 24 days (579 hrs) to complete. This leaves a 93% (331 day) contingency margin for the first long-distance, tele-operated LER direct traverse. The average slope across the entire traverse is 5.2° (Appendix C6).

The science traverse passes through Cabeus crater, which is one of the most critical sites for studying the distribution and composition of volatiles and the Moon. Cabeus crater contains one of only three large PSRs in the southern region which exhibit epithermal neutron suppression – suggestive of high hydrogen abundance and water ice deposits (Sanin et al., 2012).

The Lunar Prospector Neutron Detector measured a high concentration of hydrogen in Cabeus crater (Elphic et al., 2007), while the impact of the Lunar Crater Observation and Sensing Satellite (LCROSS) at this location caused an impact generated plume where the total water, ice and vapor was estimated to be 3-4% (Colaprete et al., 2010).

Additionally, LRO’s Diviner Lunar Radiometer Experiment recorded temperatures that suggest the PSRs within Cabeus could host CO₂ ice (Paige et al., 2010). During the traverse, multiple GPR and neutron detector measurements across Cabeus crater’s floor can help provide an understanding of the lateral and vertical distribution of lunar volatiles at this much studied location and broadly address NRC (2007) Concepts 4 and 7.

Using imagery from the LERs onboard optical cameras, or a Gigapan, stratified outcrops can also be studied in detail. As the traverse progresses through Cabeus, Drygleski and Ashbrook craters, images can help obtain a better understanding of the complexity of the current lunar crust, and determine the structure of multi-ring impact basins (NRC (2007) Concepts 3, and 6). Due to time constraints previously discussed, the LERs will only traverse along the rim of Drygleski crater rather than visit its central peak to remain within ‘safe’ driving distance.

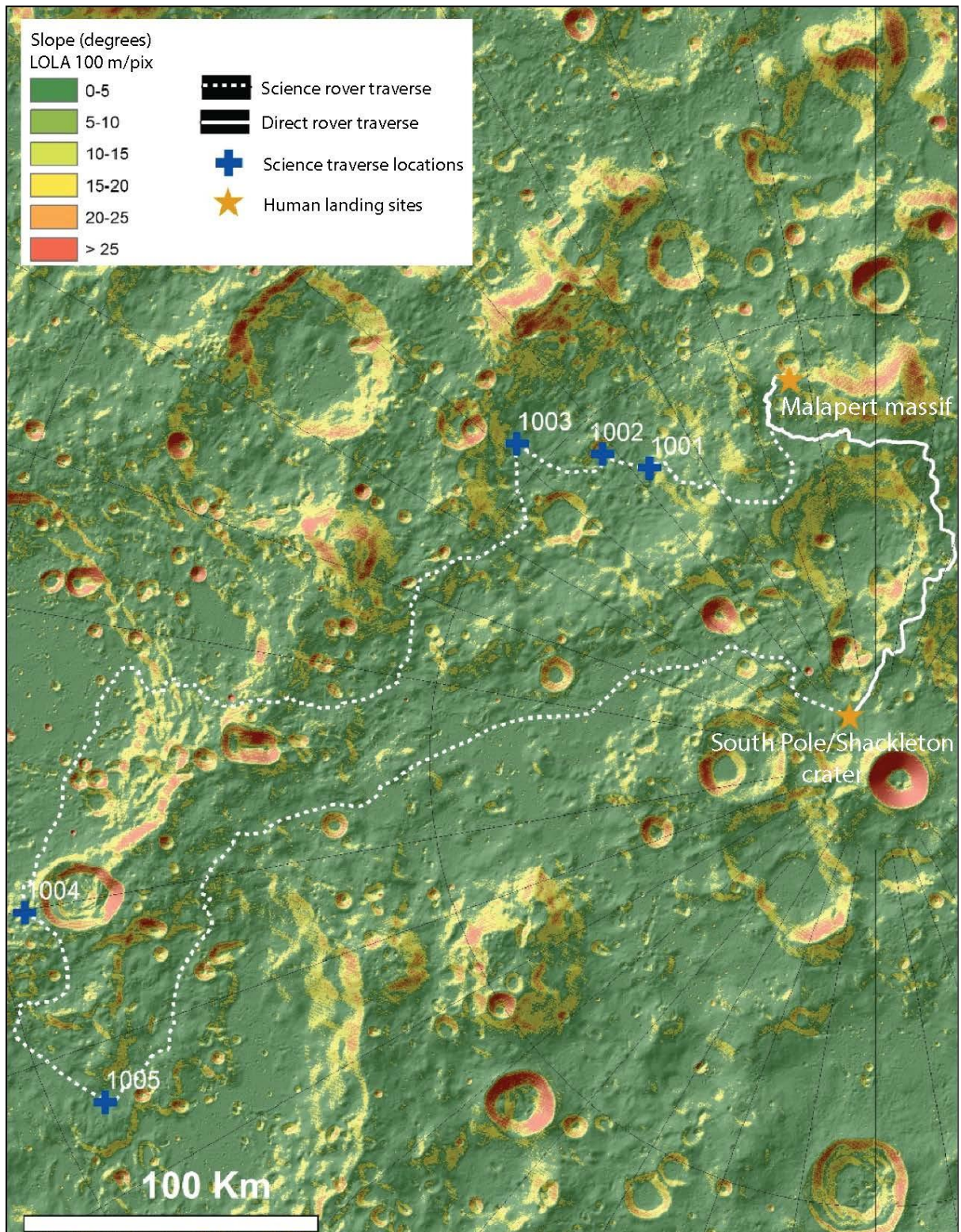


Figure 7.5: Direct and science traverses from Malapert massif to South Pole/Shackleton crater. Direct traverse shown with a solid line, while science traverse shown with a dotted line and stations of interest marked with blue crosses. The slope base map created from a LOLA 100 m/pix DEM overlaid on a LOLA hillshade. North is along every grid direction from the South Pole as shown by the polar stereographic projection.

The science traverse is 911.4 km in length, and takes ~ 105 days (2532 hrs) to complete. This leaves a ~ 70% (250 day) contingency margin for the first long-distance, tele-operated LER science traverse. The average slope across the entire traverse is 5.4° (Appendix C6).

7.5.1.2. Shackleton Crater to Schrödinger Basin

The direct and science traverses from Shackleton crater to Schrödinger basin are presented in Figure 7.6.

The direct traverse travels south in an anti-clockwise direction from the landing site nearby Shackleton crater before progressing north (once the limb and pole is crossed) to an access point in the southern rim of Schrödinger basin and terminates at the landing site beside a pyroclastic vent. The direct traverse is 739.7 km long and takes ~ 86 days (1894 hrs) to complete. The average slope across the entire traverse is 3.6° (Appendix C6).

The science traverse departs the landing site near Shackleton crater and travels south in a clockwise direction before crossing the nearside/farside boundary. The traverse then moves west toward Amundsen crater which has been proposed as an interesting site for the study of lunar volatiles (Lemelin et al., 2014; Runyon et al., 2012) as the relatively low slope of the crater facilitates LER access. Temperatures within PSRs in this region were measured with LRO's Diviner instrument and it was observed that specific sites within these PSRs contain maximum temperatures that do not exceed 54°K (see Appendices C4-B5 and C4-B6). This implies that Amundsen crater is one of the few areas in the south polar region where CO₂ ice may be found (Figure 7.7); thus it provides an opportunity to examine the lateral composition and distribution of lunar volatiles and provide additional valuable information to address NRC (2007) Concept 4.

With respect to geology, as Amundsen crater is classified as a complex crater its central peak is of particular interest, because it may contain uplifted basement material (Runyon et al., 2012) (NRC (2007) Concept 3). Estimates of the original depth of this excavated material are currently dependent on the equation used to summarize uplift. For example, using the depth of melting of Cintala & Grieve (1998) material may have been excavated from approx. 16 km. Using a stratigraphic uplift equation from Kring & Durda (2012) may return values of approx. 18 km. Thus, it is sensible to estimate that material exposed in central peaks could originate from depths greater than 15 km. Sampling of this material will help to refine its age. Impact melt from Amundsen will also be sampled so age determination can be performed in order to calibrate the impact flux rate (Kring, 2014) (NRC (2007) Concept 1). Additionally, this traverse visits some geological contacts from different epochs around Shackleton, such as Imbrian plains, and pre-Nectarian crater material (Spudis et al., 2008). These may be studied by direct sampling or through chemical measurements and analysis.

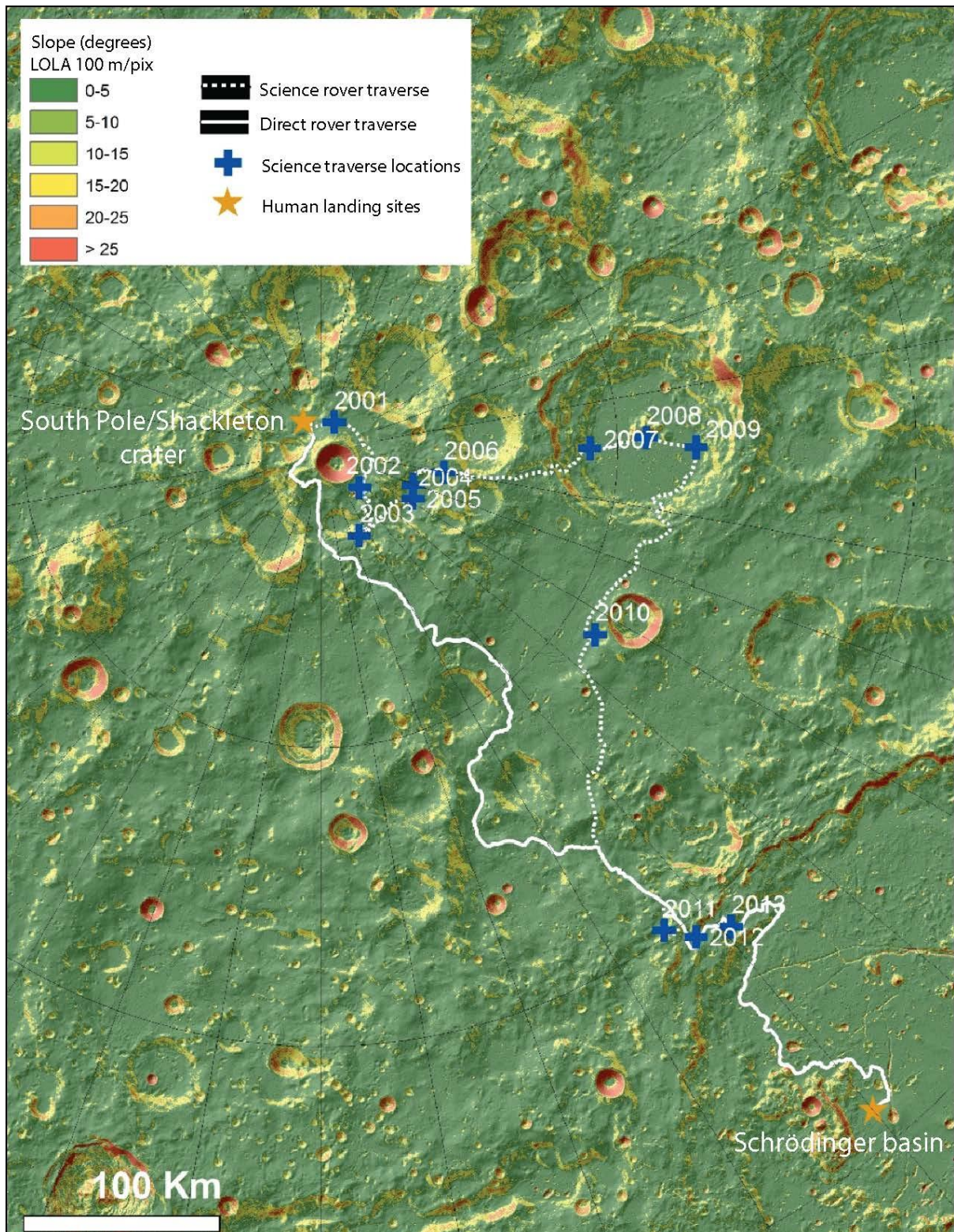


Figure 7.6: Direct and science traverses from South Pole/Shackleton crater to Schrödinger basin. Direct traverse shown with a solid line, while science traverse shown with a dotted line and stations of interest marked with blue crosses. The slope base map created from a LOLA 100 m/pix DEM overlaid on a LOLA hillshade. North is along every grid direction from the South Pole as shown by the polar stereographic projection.

7. TRAVERSES FOR HUMANS ON THE LUNAR SURFACE

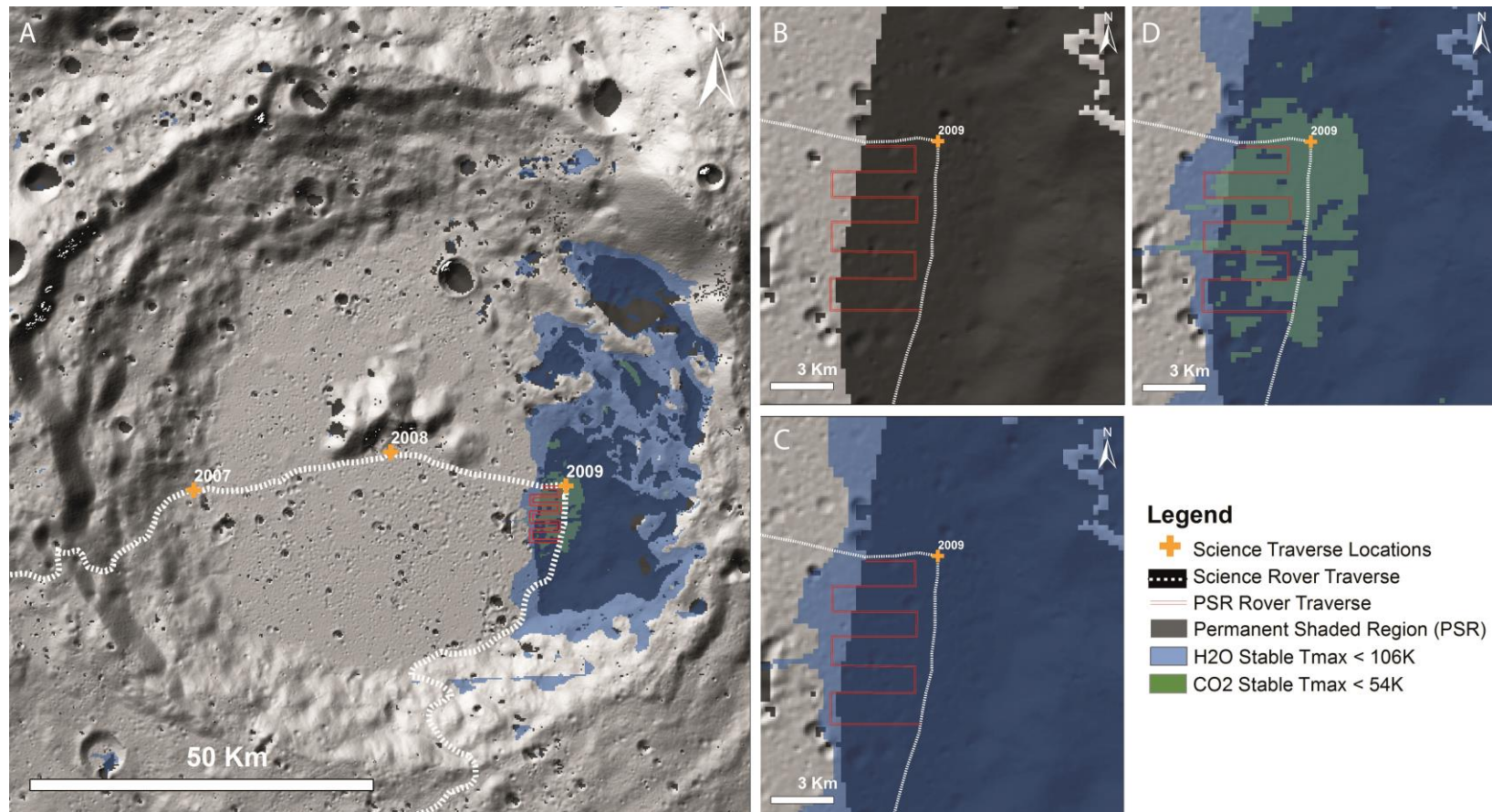


Figure 7.7: (A) The science traverse is shown descending to the interior of Amundsen crater. Stations of interest are marked in orange. (B) The path of the science traverse passing through a PSR, with an additional prospecting route shown in red. (C) Shows panel B route overlaid with a blue region in which H₂O ice is stable (at temperatures < 106°K). (D) Shows panel C additionally overlaid with regions in which CO₂ ice is stable (at temperatures < 54°K). Prospecting through these regions would enable the lateral composition and distribution of lunar volatiles to be examined.

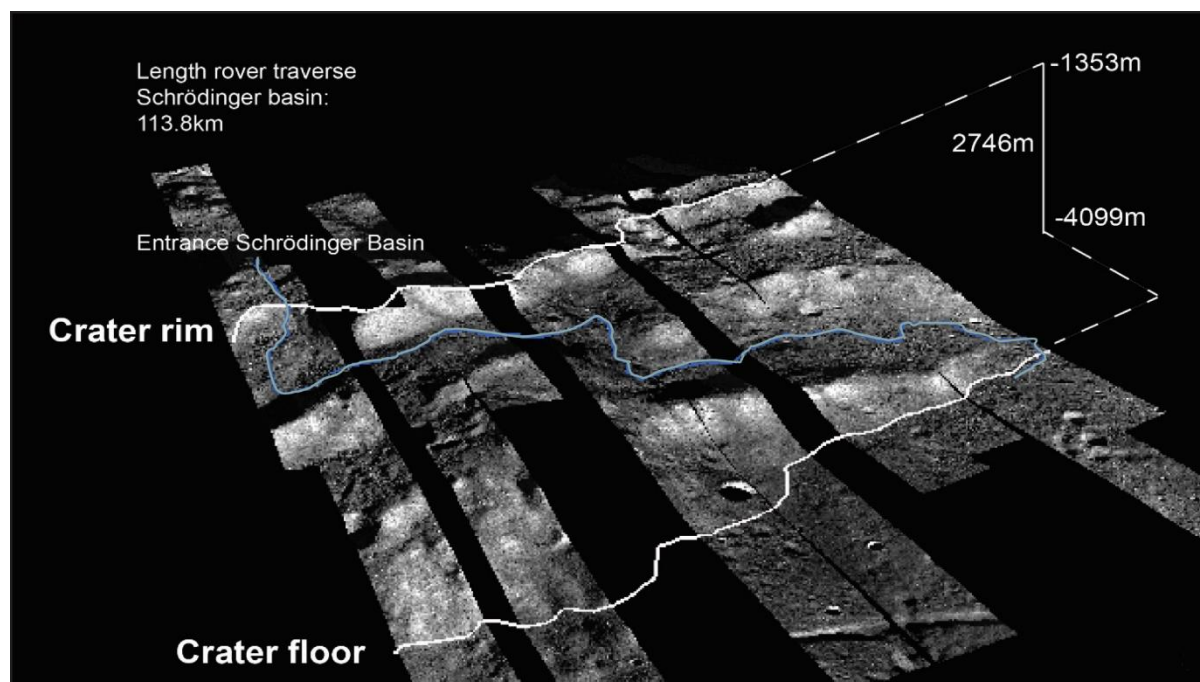


Figure 7.8: 3D image of Schrödinger basin wall. NAC mosaic draped over 60m resolution DEM. Blue line represents proposed rover traverse.

Trafficability measurements from NAC images, in combination with a 60 m LOLA DEM (Figure 7.8) and the slope map in Appendix C4-C3, are used to identify two ingress/egress points on the southern and eastern rim. To minimize driving distances, the southern access point is used to access the basin floor en route from the South Pole and the other is used to depart en route to Antoniadi crater. The southern ingress point is particularly challenging (Figure 7.6), but seems feasible based on slope limits. Nonetheless, this ingress point will need to be verified with additional study (Section 7.6). If this ingress point becomes suspect, then the LERs can access the basin floor from the east. That will, however, reduce the time available for the LERs to survey the floor of Amundsen crater between the South Pole and the Schrödinger basin.

The science traverse is 923.5 km in length and takes ~ 106.8 days (2563.2 hrs) to complete. The average slope across the entire traverse is 4.3° (Appendix C6).

7.5.1.3. Schrödinger Basin to Antoniadi Crater

The direct and science traverses from Schrödinger basin to Antoniadi crater are presented in Figure 7.9.

The direct traverse exits Schrödinger basin through the eastern rim and travels in a northeastern direction to Antoniadi crater following the most direct path of lowest slope. The direct traverse is 681.9 km in length and takes ~ 79 days (1894 hrs) to complete. The average slope across the entire traverse is 3.7° (Appendix C6).

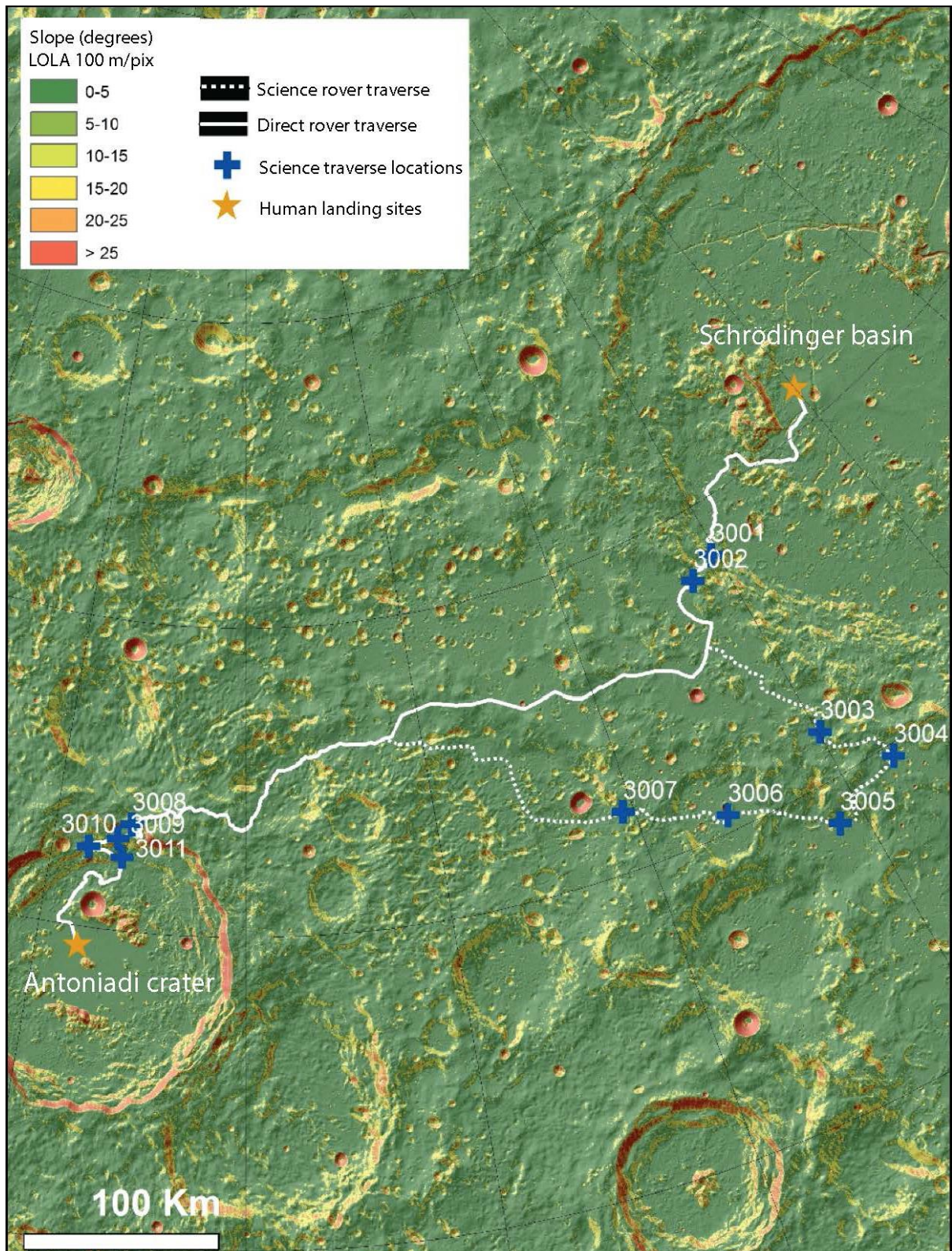


Figure 7.9: Direct and science traverses from Schrödinger basin to Antoniadi crater. Direct traverse shown with a solid line, while science traverse shown with a dotted line and stations of interest marked with blue crosses. The slope base map created from a LOLA 100 m/pix DEM overlaid on a LOLA hillshade. North is along every grid direction from the South Pole as shown by the polar stereographic projection.

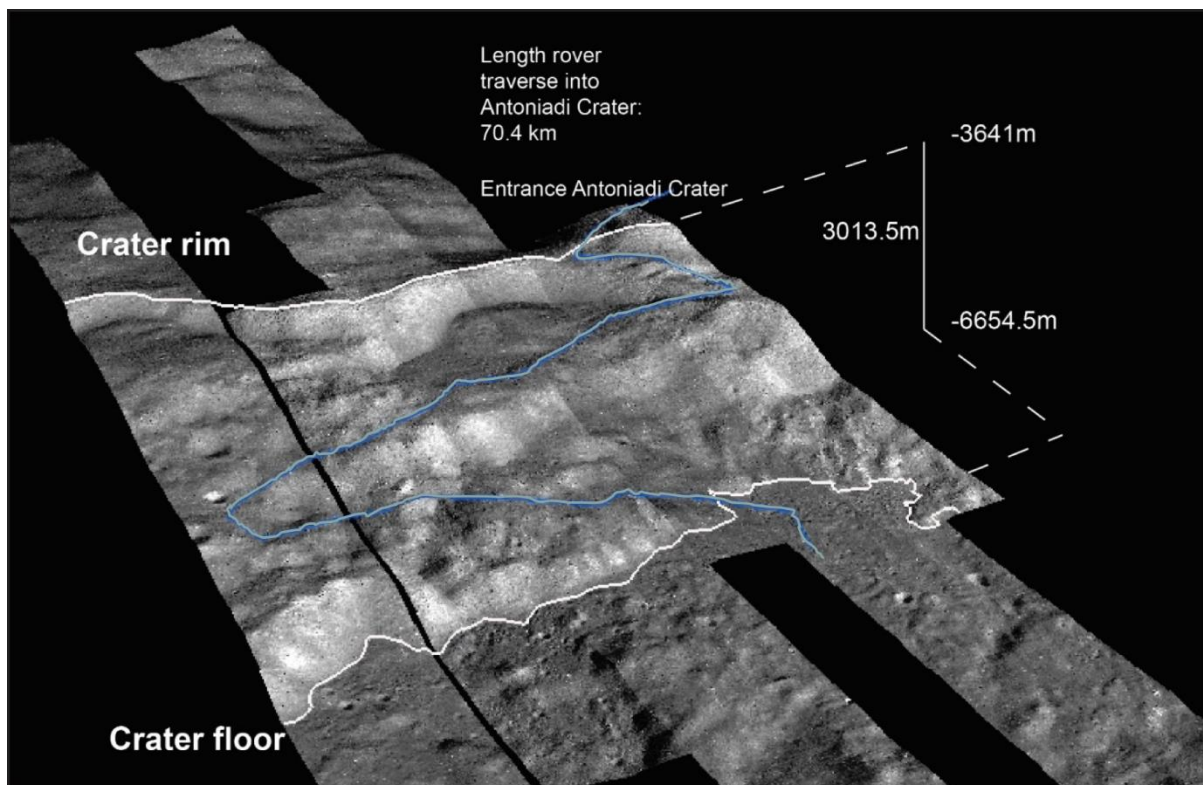


Figure 7.10: 3D image of Antoniadi crater wall. NAC mosaic draped over 60 m resolution DEM. Blue line represents proposed rover traverse.

The scientific traverse from Schrödinger basin to Antoniadi crater follows the path of the direct traverse exiting Schrödinger. It then diverges in a northerly direction to study excavated material in the vicinity of the basin. In particular, this traverse targets the secondary crater field from Antoniadi crater and impact melt ponds of Schrödinger basin as described by Kramer et al. (2013) (NRC (2007) Concept 1). The traverse then travels east, rejoining the direct traverse to enter Antoniadi crater from the south. Along this traverse the walls of both Schrödinger basin and Antoniadi crater will also be studied because they have the potential to contain stratification of the SPA melt sheet (NRC (2007) Concept 6).

As in Section 7.5.1.2, we use trafficability measurements from NAC images, in combination with a 60 m LOLA DEM and the slope map in Appendix C4-D1B to identify an ingress point into Antoniadi crater through its southern rim (Figure 7.10). The science traverse is 935.9 km in length and takes ~ 108 days (2599 hrs) to complete. The average slope across the entire traverse is 4.2° (Appendix C6).

7.5.1.4. Antoniadi Crater to South Pole – Aitken Basin Center

The direct and science traverses from Antoniadi crater to the South Pole-Aitken basin center are presented in Figure 7.11.

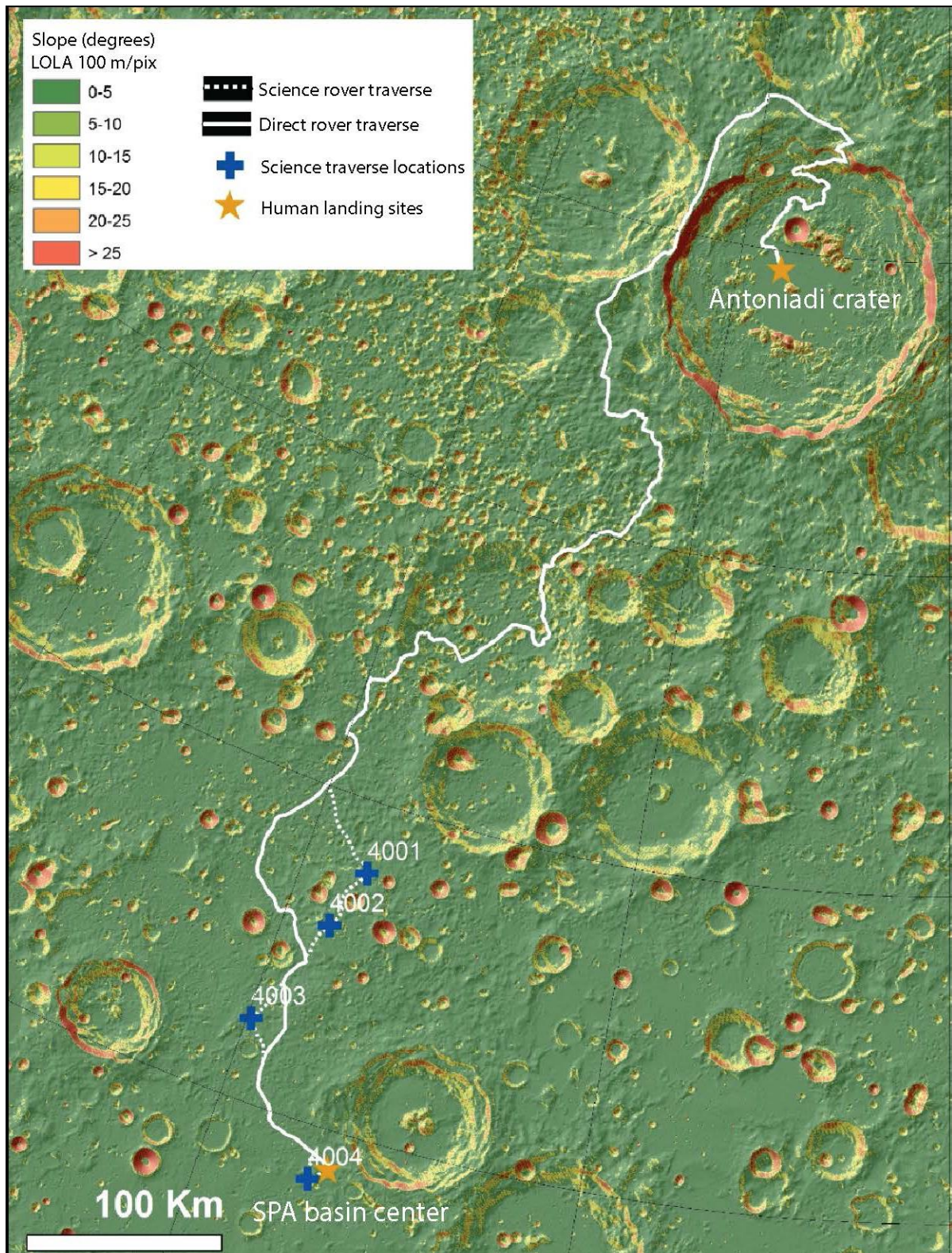


Figure 7.11: Direct and science traverses from Antoniadi crater to South Pole-Aitken basin center. Direct traverse shown with a solid line, while science traverse shown with a dotted line and stations of interest marked with blue crosses. The slope base map created from a LOLA 100 m/pix DEM overlaid on a LOLA hillshade. North is along every grid direction from the South Pole as shown by the polar stereographic projection.

The direct traverse from Antoniadi crater to the South Pole-Aitken basin center leaves Antoniadi from the access point on its southern rim and progresses north through the interior of Berlage crater before continuing toward the fifth human landing site. The total length of the traverse is 939.5 km, it takes ~ 108 days (2609 hrs) to complete. The average slope across the entire traverse is 4.4° (Appendix C6).

The science traverse from Antoniadi crater to SPA basin center does not allow for much extra science exploration due to the driving time constraints mentioned in the introduction to this section. The only divergence from the direct traverse occurs while approaching Mafic mound, as the science traverse approaches from a different direction. This allows for further science observations to be made that can provide additional information to constrain the origins of Mafic mound. If it consists of melt sheet from SPA, it can be used to determine the age of this basin (NRC (2007) Concepts 1 and 3). Mare basalts and cryptomare can be studied closer to the SPA basin center landing site and will therefore provide a better understanding of the age of volcanic events on the lunar farside (NRC (2007) Concepts 3 and 5).

The science traverse is the longest of all between site traverses, with a length of 946.9 km which takes ~ 109 days (2630 hrs) to complete. The average slope across the entire traverse is 4.5° (Appendix C6).

7.5.2. Crew Traverses At and Around Landing Sites

For four of the five landing sites, we designed two traverses to address NRC (2007) and to illuminate issues that need to be addressed by additional studies. Each traverse is <14 days long and is a loop that brings the crew back to the landing site either to restock consumables for subsequent traverse loops, or to return to the LOP-G. Potentially, one loop could be done in a 14-day-long sunlit period and the other in darkness, during a 28-day-long mission. If it is determined that crew cannot operate the LER during darkness, then either one of the loops could be chosen for daytime operations. For extended 42-day missions, e.g., as identified in the current edition of the Global Exploration Roadmap (ISECG, 2018), both traverse loops can be conducted in sunlight within an intervening nighttime stay at the landing site. We designed a 40-day, three loop traverse for Schrödinger basin to explore this option, leaving 2-days of contingency margin.

The rest of this section is structured as follows: for the first human landing site at Malapert massif, we fully describe its scientific potential, constituent traverse loops, slope profiles, individual sampling stations, and sample collection information in the main text, and refer readers to the corresponding attribute table for this landing site in Appendix C2-1. For subsequent human landing sites all detailed traverse information such as traverse loops, sampling stations, recommended samples, collection methods and masses, as well as the NRC (2007) concepts and the individual goals these samples address are given in their respective attribute tables available as individual appendices, see Appendices C2-2, C2-3, C2-4, and C2-5. Those traverses will only

be broadly described in the main text. Note that in figures where the field-of-view allows, an exploration zone with a Mars-forward radius of 100 km from the landing site is outlined in white. We also calculate approximate times needed for each traverse given landing site setup and breakdown operations, LER driving speeds, communication coverage requirements, and an EVA time allowance of approximately 1 hour for each sampling station. A tabular visualization of all NRC concepts and goals addressed at each landing site is provided in Appendix C5.

We assume that after initial descent onto the lunar surface (at the first human landing site) LERs need to be deployed from their stowed position on the lander, have their systems activated and checked, and be stocked with consumables. In addition, the lander may be prepared for hibernation while crew are completing traverses. Notional time allocations for these logistics are presented for the Schrödinger basin site in Appendix C4-C2.

7.5.2.1. Malapert Massif Traverse

As discussed in Section 7.2, Malapert massif is a mountainous surface feature located on the lunar nearside at 85.99°S, 2.93°W (Figure 7.1). The landing site for Malapert massif is situated on a flat area of high albedo on its western flank. Figure 7.12 shows the proposed dual loop Malapert massif traverse overlain on a 20 m/pix LOLA DEM.

In terms of geology, Figure 7.13A contains the Spudis et al. (2008) geologic map overlain over a 20 m/pix hillshaded elevation model. From this Figure, it can be seen that Traverse 1 (Stations 1-12) crosses four distinct terrains, including pre-Nectarian terra material, pre-Nectarian massif material, pre-Nectarian platform massif material, and Orientale basin secondary crater material. Traverse 2 (Stations 13-24) additionally crosses 7 distinct geological terrains: pre-Nectarian terra material, pre-Nectarian massif material, pre-Nectarian crater materials, Imbrian crater materials, Imbrium basin secondary crater material, pre-Nectarian platform massif material, and Orientale basin secondary crater material (Spudis et al., 2008). Samples are collected from each of these terrains in order to better constrain lunar chronology.

Figure 7.13B shows the proposed Malapert massif traverse overlain on a 20 m/pixel slope map to illustrate the LER access between stations. These average values are under the preferred slope of 15°, and the maximums are below the LER slope constraint of 25°. If adherence to smaller slope values becomes necessary, future study is required to pinpoint the locations of 'choke points' along the traverses planned in this study.

These 'choke points' are regions along the traverse in which slopes are highest (according to the 20 m/pixel slope maps) and care must be taken to traverse these points in the LER. However, none of these regions are above the LER slope constraint value of 25°. A slope profile for the first loop of the Malapert traverse is presented in Figure 7.14, which shows that regions of high slope (> 15°) are concentrated

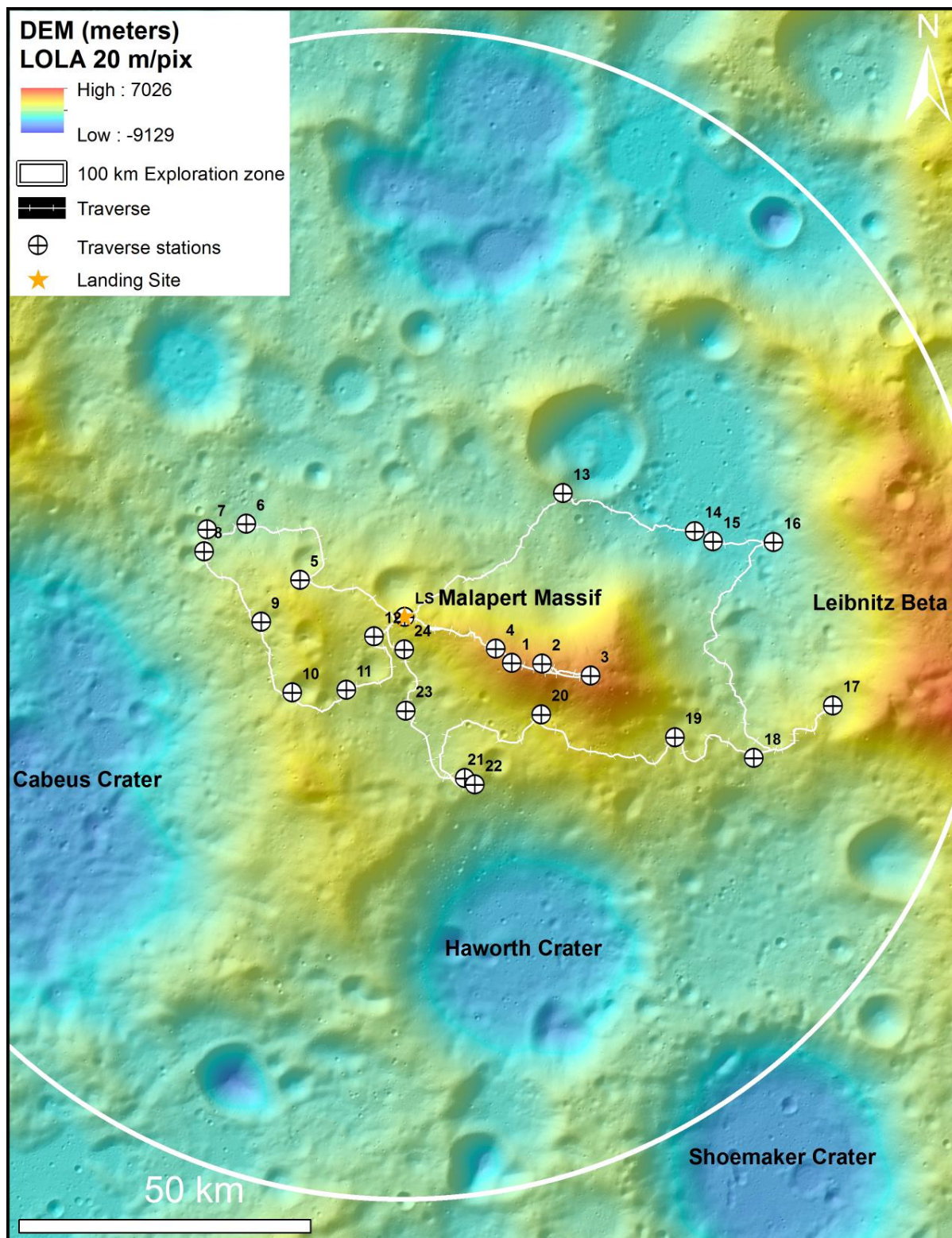


Figure 7.12: Colorized Lunar Orbiter Laser Altimeter (LOLA) Digital Elevation Model (DEM) of Malapert massif overlaid on an LROC WAC mosaic of 100 m/pix. Includes traverses, sampling stations, and 100 km Mars-forward exploration zone for reference.

7. TRAVERSES FOR HUMANS ON THE LUNAR SURFACE

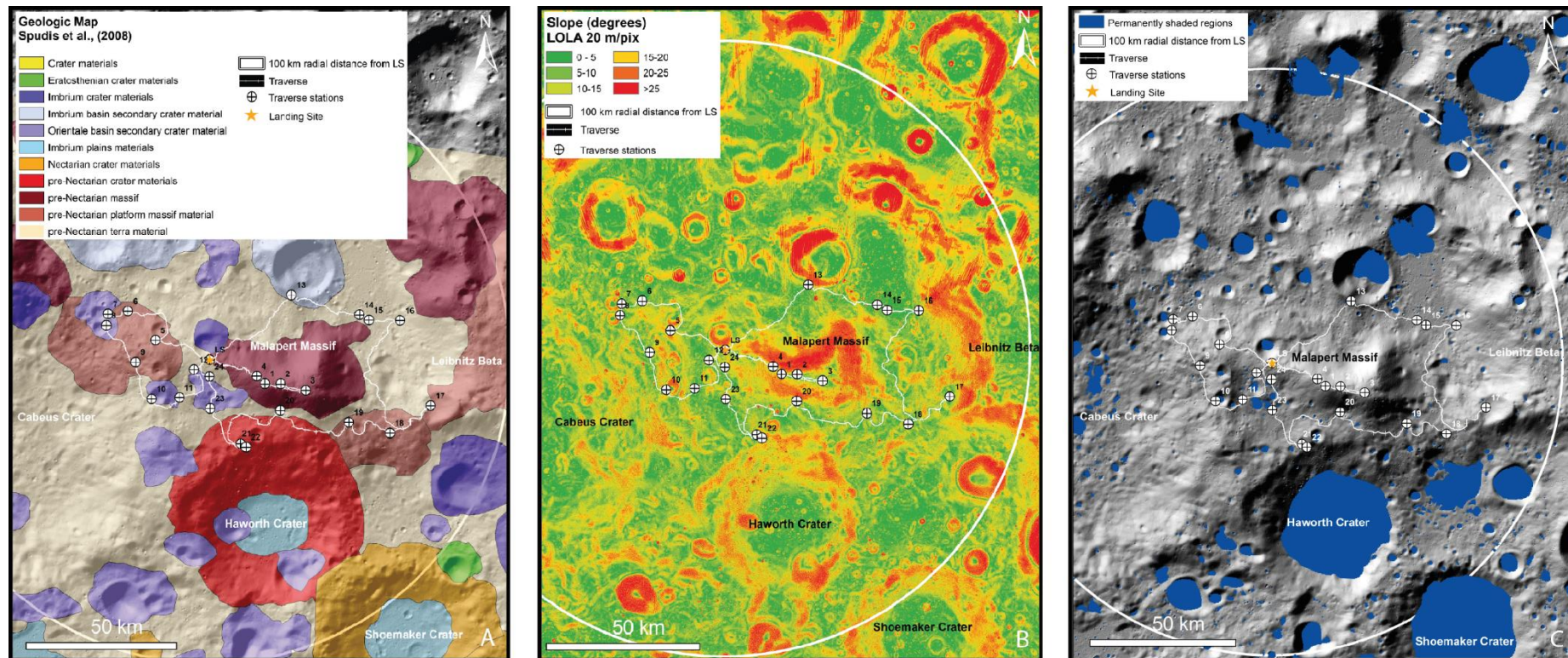


Figure 7.13: A: Spudis et al. (2008) map of geologic units combined with Malapert massif at-site traverse and a 20 m/pixel hillshaded LOLA DEM. B: Slope map (20 m/pixel from LOLA DEM) combined with the Malapert massif at-site traverse. C: Locations of Permanently Shaded Regions in the region of Malapert massif overlain on a LROC WAC 100 m/pix mosaic.

approaching Malapert ridge (Stations 1, 2, 3, and 4) – if these regions were unable to be traversed access to the ridge would not be possible and observation of massif structure, as well as highly illuminated regions, would be lost (see Traverse Loop 1 section below). To address this issue, in future studies higher resolution DEMs need to be constructed from LROC NAC images (1 m/pixel) in order to calculate slopes more accurately and pinpoint the locations of ‘choke points’ at the scale of the LER, as it is possible there may be room to maneuver around them given finer scale information.

Figure 7.13C shows the locations of PSRs in and around the proposed Malapert massif traverse. Sampling stations have been positioned to collect volatile-rich regolith within several of these regions to address NRC (2007) Concept 4. Additionally, along the ridge of the massif are two regions which experience constant illumination for 74% of the lunar year, these are referred to in Bussey et al. (2010) and De Rosa et al. (2012) as points M1 (86.04°S, 2.7°E) and M2 (86.00°S, 2.9°W).

These sites may be utilized for solar energy collection if LER parameters allow, as they are located on slopes of 20 – 25° (M1) and 15 – 20° (M2) respectively, midway between Stations 1 and 2. These highly illuminated regions provide excellent locations for the collection of solar energy, as solar arrays placed in these regions have the potential to support the power requirements of short-term missions. For longer-term exploration, permanent infrastructure could be established in these locations to provide long-term support. For this study, flexible exploration time has been allocated to deploy the Portable Utility Pallet (PUP) onboard the LERs for solar energy collection at these sites if required.

Based on communication calculations provided by Lockheed Martin (2016) the Malapert region receives coverage for only 84% (8.9 days) of a single 10.6 day orbital period; see Table 7.5 and Figure 7.2A. During the 1.7 day communication dropout, crewed LERs cease all exploration activities and remain at their current station until the next orbital period begins and coverage is regained. These communication pauses have been integrated into the total times calculated for Traverses 1 and 2.

Broadly speaking, traversing the Malapert massif region allows the NRC (2007) Concepts 1, 2, 3, 4, 6, and 7 to be addressed (Appendix C5-A).

Traverse Loop 1. Figure 7.12 illustrates a traverse loop that extends broadly east from the landing site up over the ridge onto the peak of Malapert massif where four EVA stations are to be located (Stations 1, 2, 3, 4). EVAs at these stations will involve the sample collection of massif material and observations of massif structure. The two regions of 74% illumination between Stations 1 and 2 can also be investigated with allocated flexible exploration time, and the PUP deployed for collection of solar energy.

If Ground Penetrating Radar (GPR) is included on board the LER it will be used at Station 3, located on the peak of the massif. GPR can gather structural information about the subsurface to varying depths depending on its frequency (Xiao et al., 2015) and can address goals within NRC (2007) Concepts 2 and 3. Due to the topography

of the massif and slopes along the ridge the only path off the massif retraces the ascent path taken by the LERs. Once the LERs have returned to the vicinity of the landing site, the traverse continues westward, traveling to the twin craters located on the massif adjacent to Cabeus crater. Sample collection of regolith and impact ejecta will be performed at Stations 5 and 6 on this traverse path before the twin craters are reached, and the structure of this secondary massif will be observed and documented using GigaPan imagery addressing NRC (2007) Concepts 3, 6, and 7.

The twin craters, mapped as secondaries from Orientale basin event (Spudis et al., 2008), will have samples collected from their rims at Stations 7 and 8. Collection of impact-reset lithologies associated with these craters may help provide an age for the Orientale impact addressing goals within NRC (2007) Concept 1.

The traverse continues south before making its way back to the landing site, traversing across the secondary massif by Cabeus crater and sampling volatile-rich regolith from a PSR location (Station 9, Station 11, Station 12), as well as crater ejecta and regolith samples (Station 10). Sampling of PSRs and regolith can broadly address NRC (2007) Concepts 4 and 7. Observations of massif structure will be taken at these stations, broadly addressing NRC (2007) Concept 6.

Traverse 1 is approximately 206.8 km long, taking a total of 10 days (64.0 hours) to complete with the inclusion of 12 EVA stations. It has an average slope of 6.8°, and a maximum slope of 19.2°. Making additional time allowances for communication dropout during each orbital pass, the total traverse time is approximately 12 days.

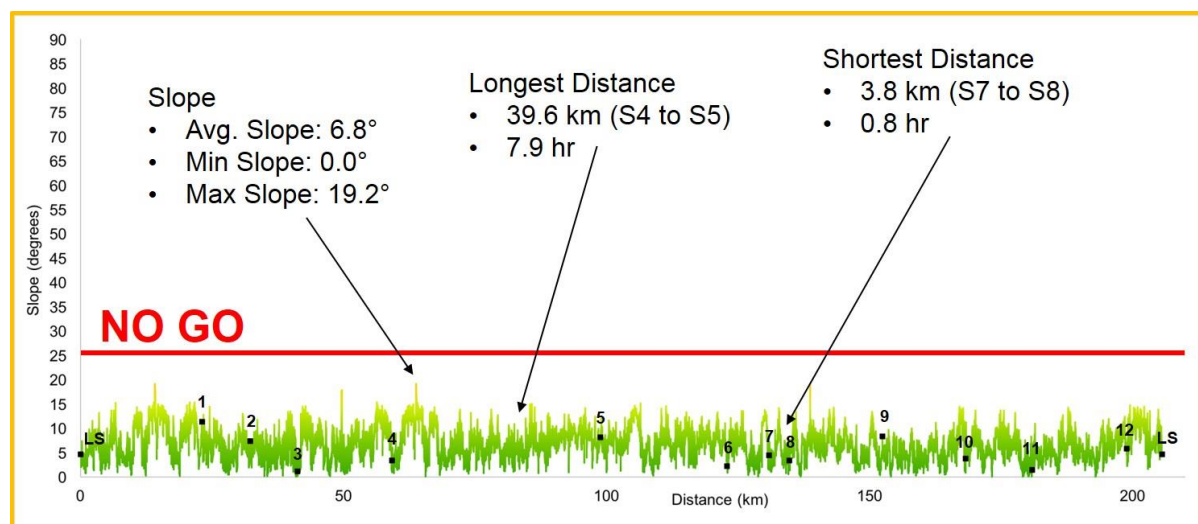


Figure 7.14: Slope profile for Traverse Loop 1 of Malapert massif. The point of highest slope ('choke point') is found en route to the summit of Malapert ridge, seen in this slope profile just before Station 1 is reached, and again returning along the ridge after passing Station 4. Given higher resolution LROC NAC DEMs it may be possible to maneuver around this point.

Additionally, this traverse has been notionally planned to take place during the lunar night and it is the initial human landing site using the proposed architecture, an additional two working days (15 hours) of margin have been allocated to allow for reduced exploration speeds bringing the total time taken for this traverse to 14 days. However, if it is determined that crew cannot operate the LER during lunar night, then this loop may be scheduled to occur in lunar daytime. As previously mentioned, the feasibility of nighttime operations needs to be addressed by additional studies.

Traverse Loop 2. The second traverse loop travels to a large impact crater north of Malapert massif. At this station sample collection of impact-reset lithologies can test the hypothesis that it is a secondary crater of the Imbrium basin-forming impact event (Spudis et al., 2008). Observations and potential sampling of ejecta associated with this crater will help to constrain models of secondary crater production and its effect on regolith mixing answering goals within NRC (2007) Concepts 1, 3, 6, and 7. The traverse continues east toward a small crater chain from which an ejected block can be collected (Station 14). This sample may be suitable for cosmogenic nuclide studies, which can help provide an age determination for the impact event by constraining the effects of space weathering and the flux of solar radiation with time.

Nearby, at Station 15 samples of volatile-rich regolith will be taken across a PSR boundary. This can help address the changes in composition throughout the transition from volatile-rich to typical lunar regolith.

Additionally, impact melt breccia will be collected at this station. NRC (2007) Concepts 1, 3, 4, 6, and 7 are addressed at stations in this region. Additionally, as the traverse is bounded on the east by the Leibnitz Beta plateau, sampling of this third massif structure is possible at two stations (16 and 17). From each station, regolith, massif, impact melt breccia material or volatile-rich regolith will be collected. Observations of the massif structure and stratigraphy will also be documented collected via GigaPan imagery. Samples from these stations can address goals from NRC (2007) Concepts 3, 6, and 7.

Stations 18, 19, and 20, which are on the south side of Malapert massif address the collection of volatile-rich regolith from PSR, excavated components from the Haworth impact, and the observation of Malapert massif structure (NRC (2007) Concepts 3, 4, 6, 7). Stations 21 and 22 overlooking Haworth crater will sample the impact-reset lithologies from the crater, providing one of the first ages of a pre-Nectarian impact crater and addressing NRC (2007) Concept 1. Excavated components entrained in impact breccia may provide a measure of lithological variation in the lunar crust addressing NRC (2007) Concept 3. Additionally, because of Haworth's significant excavation depth, it has the potential to provide information about the vertical extent and structure of the megaregolith, which will be documented using the GigaPan imagery, and broadly address NRC Concepts 3 and 6. PSRs will also be sampled here, addressing Concepts 4 and 7. Final EVA stations along this route will sample massif material and documenting the structure of the western edge of Malapert massif,

and additionally sample volatile-rich regolith from small PSR, addressing NRC Concepts 3, 4 and 7.

Traverse 2 is approximately 282.8 km long, taking a total of 12 days (83.6 hours) to complete with the inclusion of 12 EVA stations. It has an average slope of 5.6°, and a maximum slope of 19.5°, see Appendix C4-A1. Allowing for communications dropout during an EM-L2 orbital pass, the traverse takes 14 days. Traverse 2 is envisaged to take place within the duration of a lunar day to maximize the quality of stratigraphic Gigapan imaging, however, the feasibility of crew operations within lunar darkness needs to be studied.

These two Malapert area traverses are, in general, similar to those designed for Lunar Surface Systems during NASA's Constellation Program (Kring, 2011), which were then used for a 28-day-long, dual LER lunar mission simulation during NASA's Desert Research and Technology Studies (DRATS) campaign of late 2010.

7.5.2.2. South Pole (Shackleton Crater) Traverse

From Figure 7.15 it can be seen that Shackleton crater descends to a depth of approximately 4.2 km and its inner walls are fairly steep, with slopes of approximately 30° (Haruyama et al., 2008) (Appendix C4-B1).

As mentioned in Section 7.2, the interior of Shackleton crater is a PSR (see Appendix C4-B4), and several others are located in the region. In addition to PSRs, 'cold traps' (Watson et al., 1961), are widely distributed within the South Pole region (see Appendices C4-B5 and C4-B6). These provide ideal locations for addressing NRC (2007) Concept 4, which broadly aims to investigate volatile flux throughout the history of the Solar System. It can be seen from Appendices C4-B5 and C4-B6 that in addition to Shackleton crater, neighboring craters Faustini, Shoemaker, and Haworth also contain cold traps of interest for ISRU purposes and are also worthwhile targets for exploration. Faustini crater is the only neighboring crater able to be investigated in this work due to the capabilities of the LER (Section 7.3.2). Elphic et al. (2007) documented an increasing hydrogen gradient across the floor of Faustini crater with a north/south orientation. The presence of this gradient makes Faustini a prime location for sample collection and measurement of volatile concentration and depth relative to surface temperature. The walls of Faustini crater also provide an ideal location for sampling of material subject to a temperature change gradient, as they are steep, yet accessible given the parameters for this study.

Traverses and sampling stations for this landing site (Figure 7.15) are planned based on three main parameters: geologic unit (Spudis et al., 2008) (Appendix C4-B7), accessibility (slope) and volatile stability. Volatile maps used for this study are H₂O and CO₂ ice stability maps calculated from the temperature data from LRO's Diviner Lunar Radiometer Experiment (Paige et al., 2010) (see Appendices C4-B5 and C4-B6). NRC (2007) concepts addressed by the South Pole/Shackleton crater traverses

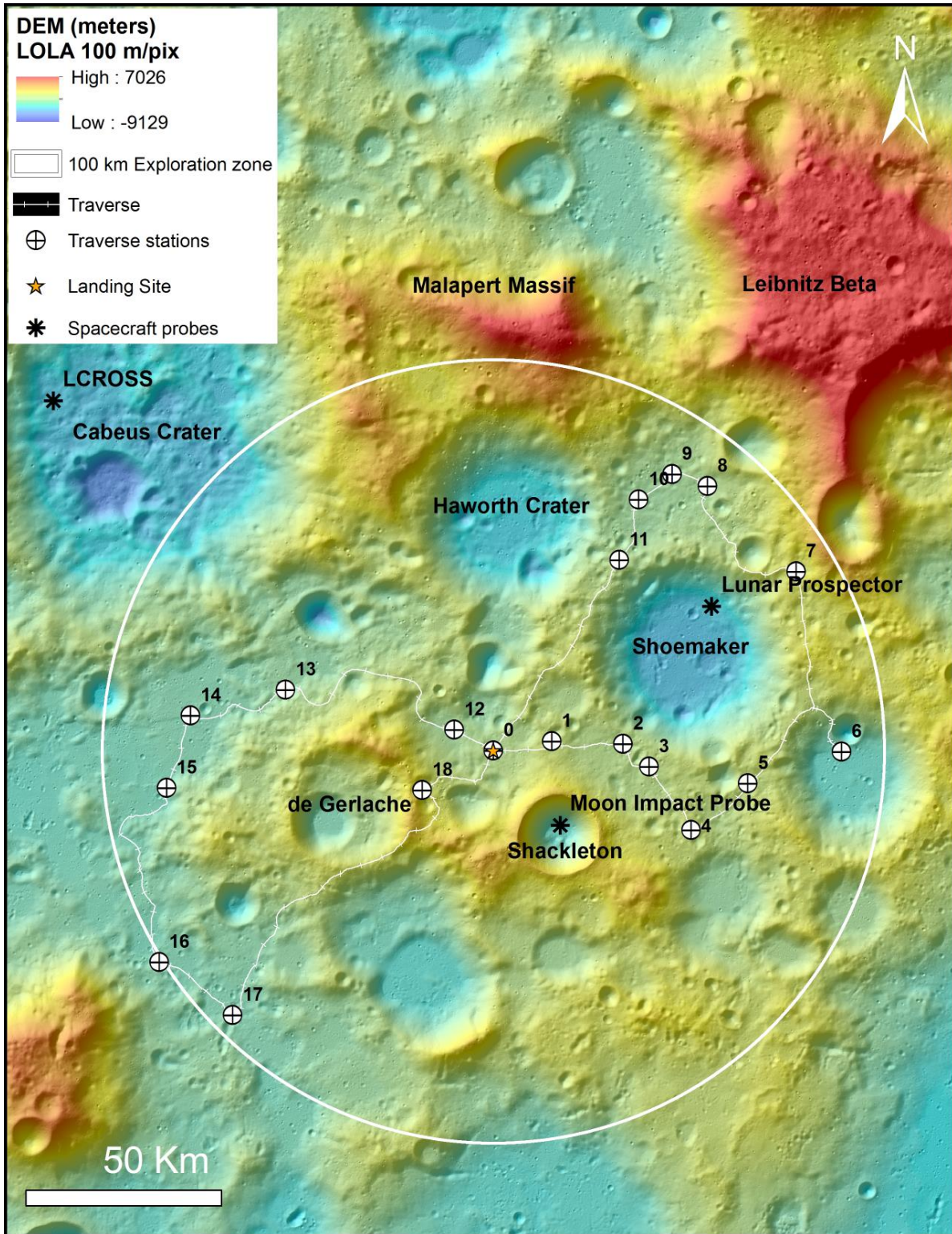


Figure 7.15: Colorized DEM of the South Pole region displayed on a LROC WAC mosaic of 100 m/pix. Includes traverses, sampling stations, spacecraft probes, and 100 km Mars-forward exploration zone for reference.

are 1, 2, 3, 4, 6, and 7. For detailed station information, sample collection methods, sample types, and masses, as well as NRC concepts and goals addressed with this traverse please refer to the tabular breakdown in Appendix C2-2 and Appendix C5-B.

Traverse Loop 1. Traverse 1 circumnavigates Shoemaker crater in an anti-clockwise direction, stopping to sample the hydrogen gradient across the floor of Faustini crater (Elphic et al., 2007), before continuing north to high priority Stations 8, 9, and 10 where extremely cold volatile rich regolith will be collected to address NRC (2007) Concept 4. LRO-LAMP (Lyman Alpha Mapping Project) data has detected geologically young impact crater in Faustini crater (Mandt et al., 2016) near Station 6, which could have excavated volatile-rich regolith directly to the surface and, thus, this station has a high priority. Station 11 is positioned between Haworth and Shoemaker craters, and is the only station in this traverse, which is not located in a PSR (in order to robustly address NRC (2007) Concept 4 samples are needed from a large number of volatile rich locations). However, its position renders it suitable for obtaining imagery of both craters, which will aid in the understanding of their stratigraphy and the vertical and lateral extent of volatiles in both Haworth and Shoemaker craters.

Traverse 1 is approximately 324 km long, taking a total of 12 days (77.7 hours) to complete with the inclusion of 11 EVA stations. It has an average slope of 6.3°, and a maximum slope of 23.4°, see Appendix C4-B2.

Traverse Loop 2. Traverse 2, which circumnavigates de Gerlache crater in an anti-clockwise direction, contains sample stations located on four geologic terrains (pre-Nectarian terra material, Imbrian plains material, Orientale basin secondary crater material, and Eratosthenian crater material) (see Appendix C4-B7). Station 15 in particular is located on the contact between pre-Nectarian terra material and Imbrian plains material, and samples collected from this station can be used for further characterization of these two units which can address NRC (2007) Concepts 1, 4, 6, and 7 (see Appendix C4-B8).

Traverse 2 is approximately 320 km long, taking approximately 11 days (71.5 hours) to complete with the inclusion of 7 EVA stations. It has an average slope of 5.5°, and a maximum slope of 23.2°, see Appendix C4-B3. Similar to Traverse 1, this traverse explores locations within PSRs to maximize the collection of volatile rich regolith.

7.5.2.3. Schrödinger Basin Traverse

Post-basin formation volcanism has resulted in the deposition of both mare basalts in the northern part of the smooth inner-peak ring floor of Schrödinger basin, and pyroclastic material emanating from a vent close to the center of the basin (see Appendix C4-C1). Such materials are not only significant for their insight into lunar magmatism, but also for potential ISRU applications. The identification of permanently shadowed regions (PSRs) within the basin (see Appendix C4-C1) indicate that volatile

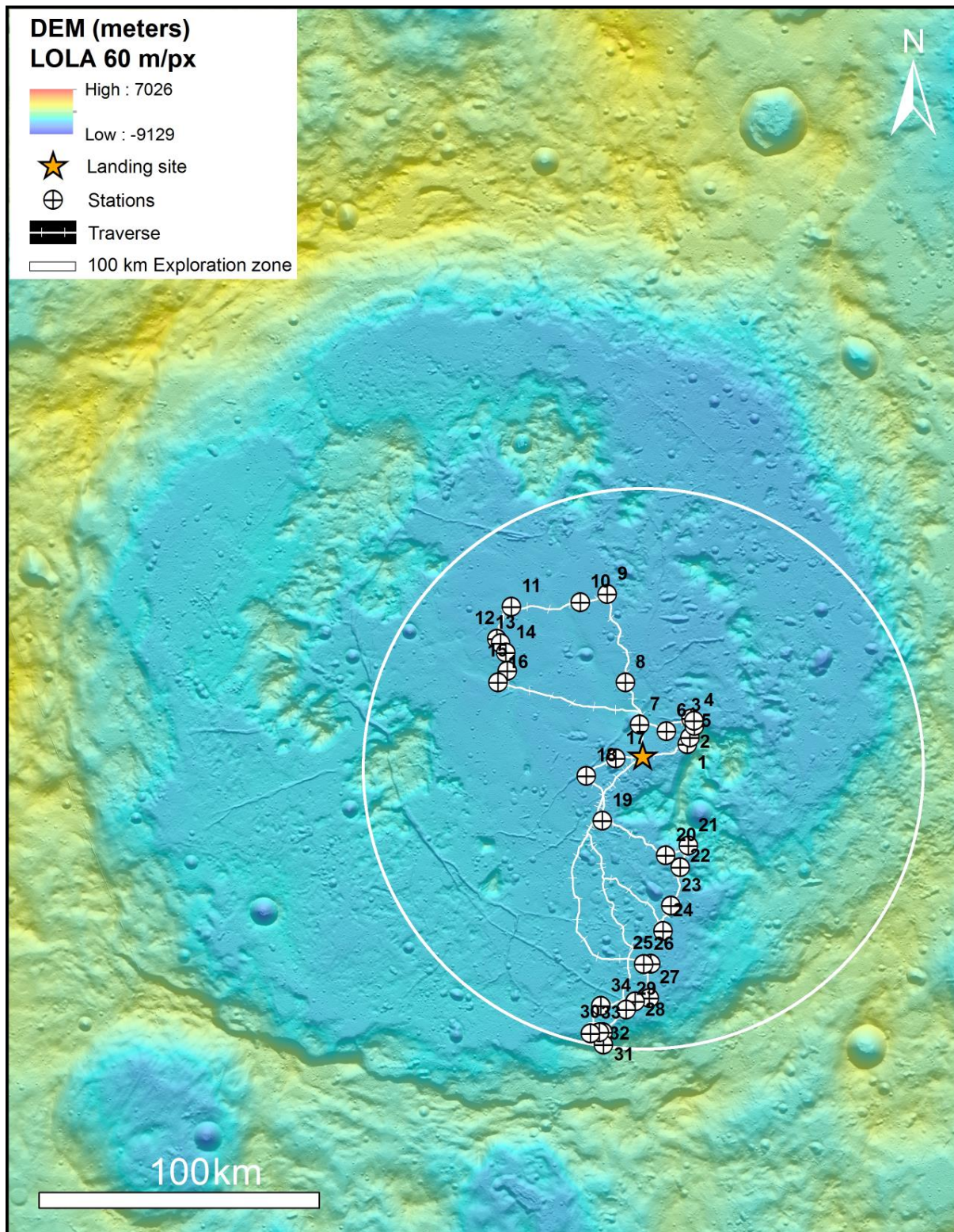


Figure 7.16: Colorized DEM of Schrödinger basin displayed on a LROC WAC mosaic of 100 m/pix. Includes traverses, sampling stations, and 100 km Mars-forward exploration zone for reference.

species may be present and stable on geological timescales. From the basin walls, it may be possible to sample the SPA basin impact melt sheet (Hurwitz & Kring, 2015).

Schrödinger basin has been well studied, with O'Sullivan et al. (2011) proposing three landing sites for human missions to its interior which focus on mare basalt deposits, the pyroclastic vent, the peak ring, impact melt breccia, or the Schrödinger melt sheet. Each site was constrained by a 10 or 20 km 'walkback' radius for the crew. Bunte et al. (2011) proposed a crewed sortie-reconnaissance mission in which a single landing site was located within the pyroclastic deposit, allowing access to the basin's inner ring and volcanic vent. Potts et al. (2015) designed two traverse routes for a 14-day solar-powered robotic mission to Schrödinger basin, while Steenstra et al. (2016) designed two traverses (a long and short route) based on a 3-year mission plan in support of the HERACLES mission concept (Landgraf et al., 2015). We incorporate all sampling locations from Steenstra et al. (2016) into this work.

In this traverse, we demonstrate the scientific gain from the longer duration, 42-day mission framework specified in the 2018 GER (ISECG, 2018). We provide three traverse options (Figure 7.16), all of which can be utilized if crew-LER operations are permitted at night, or two of which can be utilized if crew need to remain at the landing site during lunar night.

The diverse geological terrains inside the basin, as seen in Figure 7.17, allow all seven NRC (2007) concepts to be addressed (Appendix C5-C). A detailed explanation of how these NRC (2007) concepts and goals are addressed by the traverses in the following sections is found in Appendix C2-3.

If the interior of Schrödinger basin cannot be accessed via the identified access point by the LERs due to slope constraints (Section 7.6, and Figure 7.8), the crew would instead need to land outside of the basin. Such an exterior site would be limited in terms of geological context and notable features. In the external landing site, we propose in Figure 7.18, there is no access to young mare, pyroclastics, or feldspathic primary crust. External impact melts would also lack geological context, as the region is characterized by rough terrain dominated by the products of other impacts. We recommend detailed slope studies be performed on finer resolution LROC NAC DEMs (1 m/pixel) to ensure access to the interior landing site is possible.

Traverse Loop 1. Traverse 1 travels broadly north of the landing site, passing through five different units as defined by Kramer et al. (2013) (see Appendix C4-C1). The landing site is situated in the pyroclastic unit, and the traverse closely follows the 'short traverse' designed by Steenstra et al. (2016) which highlights the eastern peak ring as of particular interest, due to extensive M³ data availability and its close proximity to the pyroclastic vent (Bunte et al., 2011; O'Sullivan et al., 2011; Potts et al., 2015). The identification of boulders and associated trails in the Steenstra et al. (2016) mission enable the collection of peak ring material from locations that are accessible using the LERs in this study.

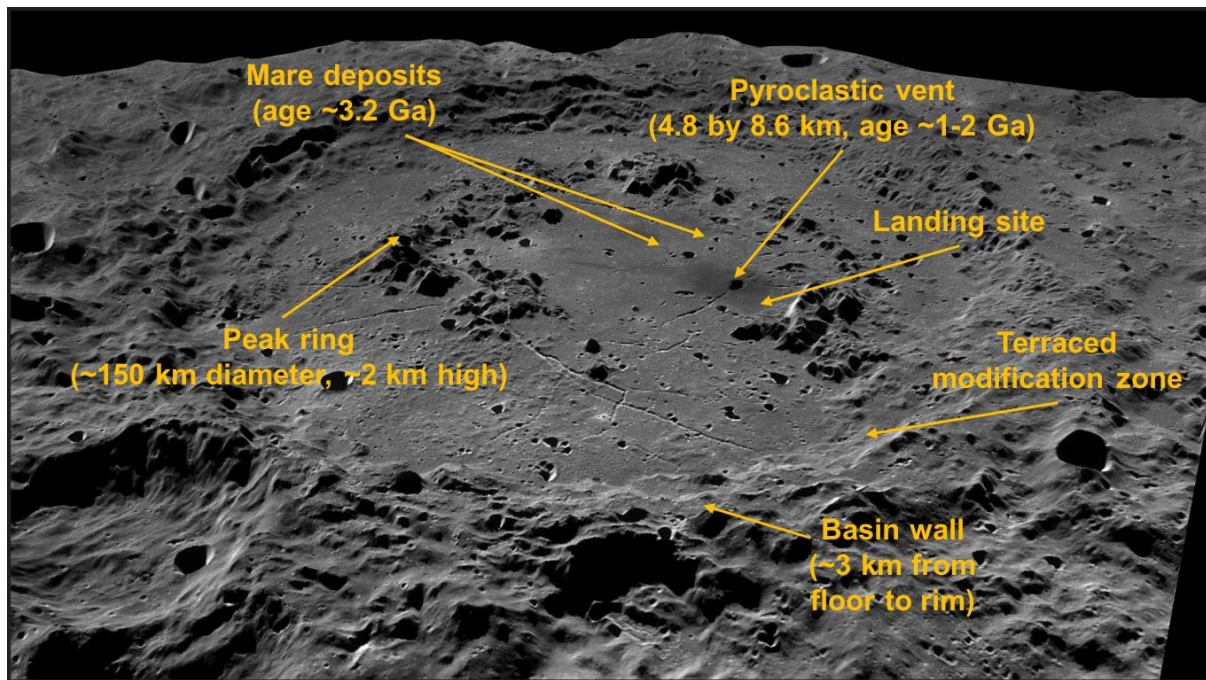


Figure 7.17: Oblique view of Schrödinger basin exploration zone from 100 m/pix LROC WAC mosaic. Units of interest are labeled.

Traverse 1 samples the base of the peak ring formation (Stations 1, 2, 3, and 4 addressing NRC (2007) Concepts 1, 2, 3, and 6) as well as the pyroclastic unit (Stations 5, 6, 7, 8, addressing NRC (2007) Concepts 1, 2, 3, 4, 5, and 7) before crossing the mare unit.

At Station 13, the traverse samples a PSR at a crater within the smooth inner peak ring impact melt unit of the basin, which may act as a cold trap where volatiles are incorporated into regolith (Kring et al., 2014). Station 16 samples the FeO-rich ridge described by both Shoemaker et al. (1994) and Kramer et al. (2013), which is thought to be the result of either buckling of the melt sheet or later extrusion. Samples from this ridge may address NRC (2007) Concepts 1, 5, and 7.

Traverse 1 is approximately 267 km long, taking a total of 12.5 days to complete with the inclusion of 16 EVA stations. It has an average slope of 3°, and a maximum slope of 14.8° (Appendix C4-C4). Soil trafficability studies have previously been carried out by Steenstra et al. (2016) and indicate that the pyroclastic terrain is amenable to traverse by an LER. Traverse 1 is intended to take part in lunar daytime, thus illumination is not a limiting factor to the activities planned.

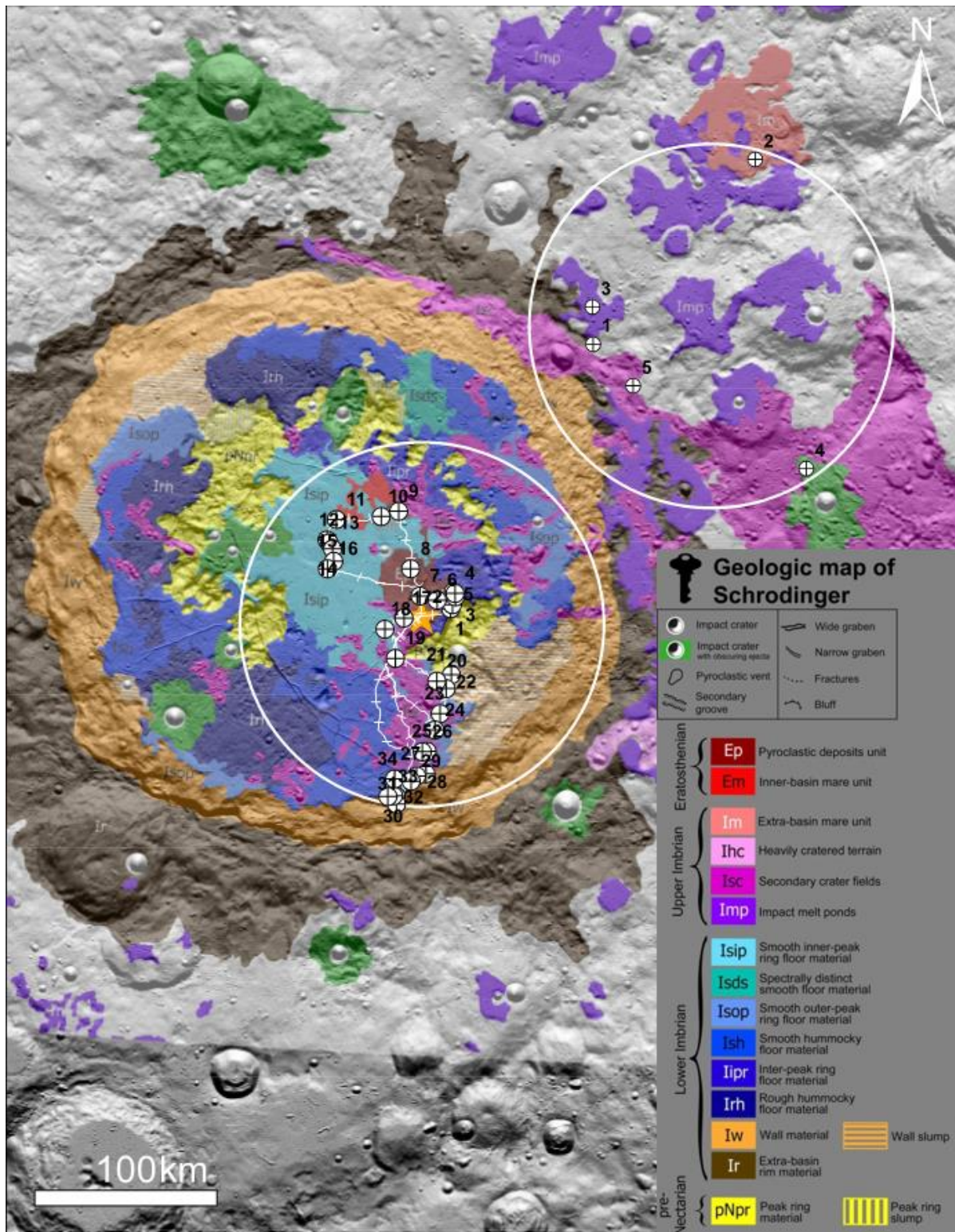


Figure 7.18: Proposed internal and external landing sites and exploration zones for Schrödinger basin. LOLA 100 m/pixel hillshade overlain with geological map from Kramer et al. (2013) demonstrates the loss of geological variety and novelty if the interior of the basin cannot be accessed by the LERs.

Traverse Loop 2. Traverse 2 travels south of the landing site, passing through six different units as defined by Kramer et al. (2013) (see Appendix C4-C1). Beginning from the landing site in the pyroclastic unit, the traverse closely follows the southern portion of the 'long traverse' designed by Steenstra et al. (2016) that draws on previous studies (Bunte et al., 2011; O'Sullivan et al., 2011, Potts et al., 2015). Eight stations are included, at which boulders from the peak ring, regolith from a secondary crater field, and impact melt breccias from the smooth and hummocky basin floor units are sampled.

Traverse 2 is approximately 205 km long, taking a total of 9.5 days (49 hours) to complete with the inclusion of 8 EVA stations. It has an average slope 2°, and a maximum slope of 9.7° (Appendix C4-C5).

Traverse Loop 3. After returning to the landing site to restock the LERs, crew travel farther south of Traverse 2 to explore the southern-most part of Schrödinger basin. Traverse 3 passes through six different units as defined by Kramer et al. (2013) (see Appendix C4-C1), continuing along the 'long traverse' designed by Steenstra et al. (2016) that draws on previous studies (Bunte et al., 2011; O'Sullivan et al., 2011; Potts et al., 2015). Ten stations are included, sampling boulders from the peak ring, regolith from a secondary crater field, and impact melt breccias from the smooth and hummocky basin floor units.

Slope maps and NAC imagery have been used to plan traverses within engineering constraints of the mission, however a thorough study of the trafficability of LERs along collapsed material at the base of the wall and along terraced material must be conducted in the future.

In the absence of additional studies concerning the feasibility of operations during lunar night, this traverse has been planned such that lunar daytime will begin as the crew approaches the first sampling station (Station 25), see Appendix C4-C2. Lighting conditions during this part of the mission are crucial as the crew will be observing the terrain changes and imaging the stratigraphy of the terraced zone. Stations in this traverse are closely spaced; collecting rakes, scoops and impact melt breccias from the wall material and smooth hummocky floor units.

Traverse 3 is approximately 284 km long, taking a total of 12.5 days to complete with the inclusion of 10 EVA stations. It has an average slope of 5.9°, and a maximum slope of 19.7° (Appendix C4-C6).

7.5.2.4. Antoniadi Crater Traverse

At Antoniadi crater we find that the presence of both a peak-ring and a central peak structure may provide the opportunity to sample material uplifted from the lunar crust, as well as the SPA impact melt sheet, which could be compared to similar samples from Schrödinger basin to address NRC (2007) Concept 6.

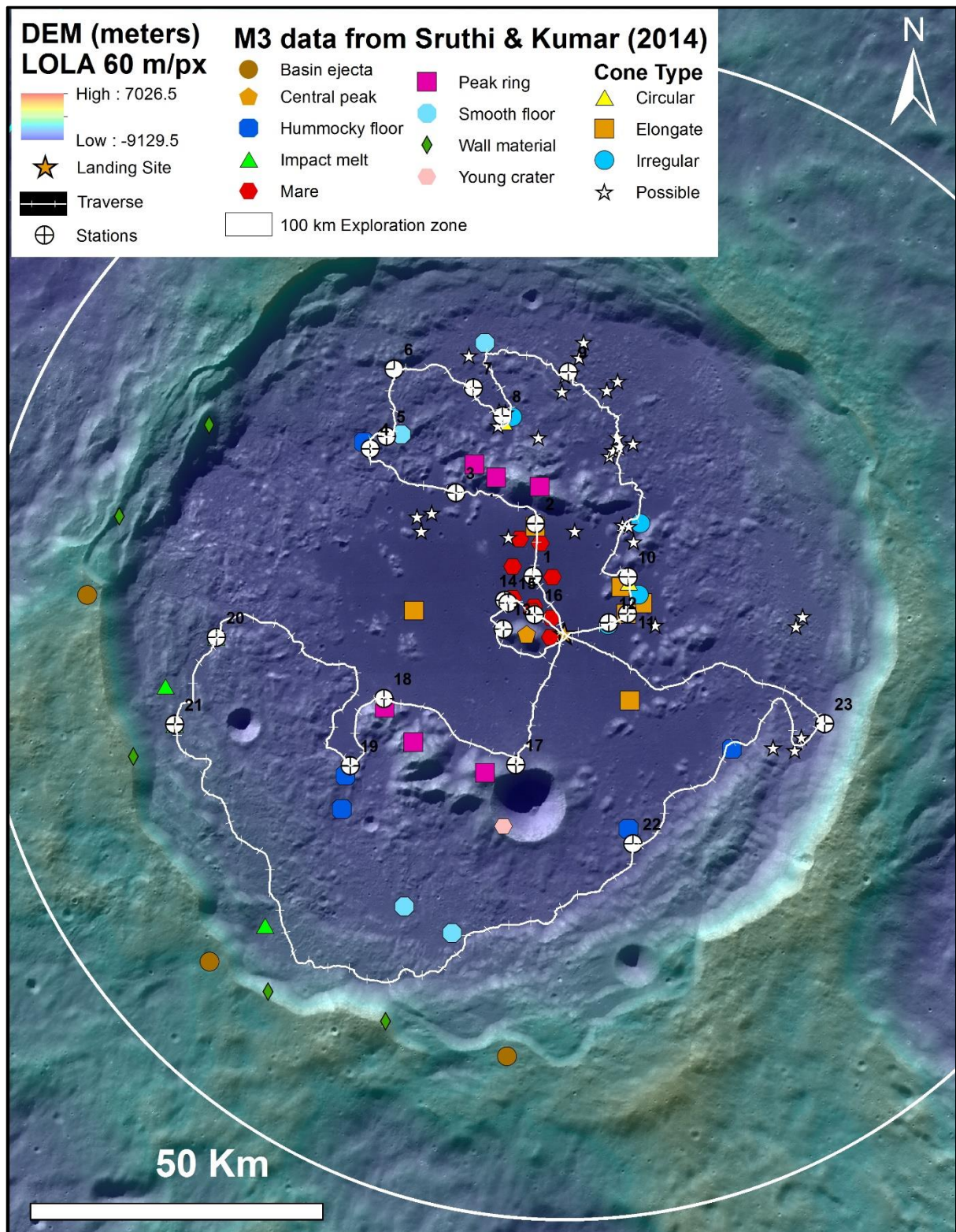


Figure 7.19: Colorized DEM of Antoniadi crater displayed on a LROC WAC mosaic of 100 m/px. Includes traverses, sampling stations, and 100 km Mars-forward for reference. Data from Sruthi & Kumar (2014) regarding the locations of their volcanic cones is also included.

Antoniadi crater contains nine geologic terrains mapped by Sruthi & Kumar (2014) (see Appendix C4-D1A), who also identified and classified 45 volcanic cones based on circular topography and the presence of central pits, using spectral data to refine their composition (Figure 7.19). Samples from these cones may also provide insight into lunar magmatic processes as pyroclastic material may be accessible, and would provide ground truth for imaging spectroscopy analyzes. Also noteworthy is the mare basalt in Antoniadi crater, which is thought to be some of the youngest on the farside of the Moon (Wilhelms et al., 1979; Pasckert et al., 2018). This may also be compositionally different from the nearside/equatorial mare basalts that have been sampled previously (Pasckert et al., 2018). Recent crater counts suggest an age of 1.6 Ga for the unit around the central peak and 2.6 Ga for the outer floor unit near the basin wall (Haruyama et al., 2009; Sruthi & Kumar, 2014). These divergent ages suggest episodic volcanism has occurred in the crater. Due to the wide range of geologic units within Antoniadi crater, we submit that all NRC (2007) concepts may be addressed at this site (see Appendix C2-4 and Appendix C5-D).

The exploration zone and related scientific goals are based on previous work by Clark et al., (2009), Fagan et al. (2010), and particularly Sruthi & Kumar (2014) as they have produced the most detailed and current geologic map of the basin.

If the interior of Antoniadi crater cannot be accessed via the identified access point by the LERs due to slope constraints (Figure 7.10), the crew would instead need to land outside of the crater. Such an exterior site would be limited in terms of geological context and notable features. In the external landing site, we propose in Figure 7.20, there is no access to young mare, or feldspathic primary crust. External impact melts would also lack geological context, as the region is characterized by terrain dominated by the products of other impacts.

Traverse Loop 1. Traverse 1 explores the northern portion of Antoniadi crater, as shown in Figure 7.19. The traverse passes through or along six geologic units as mapped by Sruthi & Kumar (2014). These units are: central peak, peak ring, hummocky floor, smooth floor, wall material, and mare basalt (see Appendix C4-D1A). A total of 16 stations are dispersed throughout these units as well as along key contact points to maximize and diversify sampling.

Traverse 1 is approximately 253 km long, taking a total of 12 days (90 hours) to complete with the inclusion of 16 EVA stations. It has an average slope of 2.6°, and a maximum slope of 13.2° (Appendix C4-D2). If crew-LER operations are permitted during lunar night, this traverse has been designed to be conducted during this time, as illuminated conditions are more essential for Traverse 2, in which photography of the crater wall has been planned.

Traverse Loop 2. Traverse 2 explores the southern portion of Antoniadi crater as illustrated in Figure 7.19. This 395 km traverse passes through or along seven geologic units as mapped by Sruthi & Kumar (2014). These units are young crater ejecta, peak ring, hummocky floor, smooth floor, impact melt, wall material, and mare

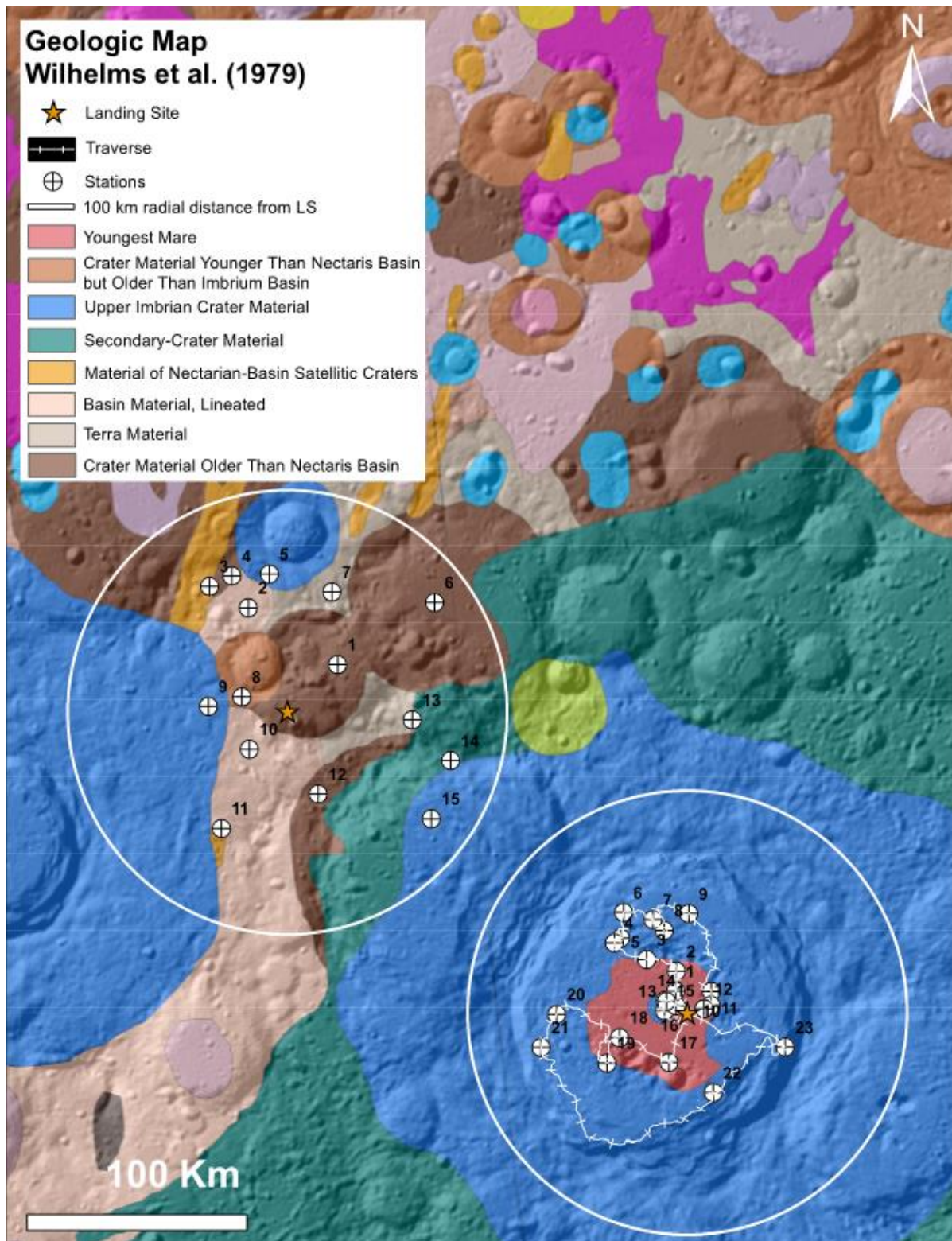


Figure 7.20: Proposed external (left zone) and internal (right zone) landing sites and exploration zones for Antoniadi crater. LOLA 100 m/pixel hillshade overlain with geological map from Wilhelms et al. (1979) demonstrates the loss of geological novelty if the interior of the crater cannot be accessed by the LERs.

basalt (see Appendix C4-D1A). A total of seven stations are dispersed throughout these units as well as along key contact points to maximize and diversify sampling.

Along the traverse from stations 20 through 23, documentation of the crater wall will be conducted via Gigapan imagery, addressing NRC Concepts 1, 2, 3, and 6. Whilst slope maps and NAC imagery indicate that traversing along the crater wall and through portions of terraced material is feasible, a thorough study of the trafficability of LERs along the collapsed material at base of the wall and along the terraced material needs to be conducted.

As this traverse is largely conducted along the basin wall, it is crucial that this traverse be conducted during the sunlit period of the lunar day to allow for photography of stratification within the wall material as well as ensuring a safe traverse for crew over potentially rough terrain.

Along this traverse, there is an average slope of 3.5° with a maximum slope of 14.3° (Appendix C4-D3). The total traverse time is 13 days (98 hours), including a total driving time of 79 hours, 7 EVA stations, communication dropout, and landing site breakdown operations.

7.5.2.5. South Pole-Aitken Basin Center Traverse

Traverses planned for this site can be seen in Figure 7.21. As mentioned in Section 7.2 despite its age the basin still maintains a distinctive FeO chemical signature (Gibson & Jolliff, 2011; Moriarty & Pieters, 2018). This compositional anomaly extends across the flat interior floor of the basin related to both volcanic and non-volcanic materials and is likely composed of impact-melt breccia leftover from the extreme event that created the basin. If able to be sampled, these impact-melts can be used to refine the age of the basin and address NRC (2007) Concepts 1 and 6.

Nearby the landing site are mare and cryptomare deposits mapped by Borst et al. (2012) and Gibson & Jolliff (2011) with conflicting extents. These volcanic materials would help to resolve these discrepancies and may address NRC (2007) Concepts 2, 3, and 5. Additionally, as mare basalts on the nearside range from 4.2 – 1.2 Ga, sampling from across the SPA basin would determine if farside volcanism shares a similar timeline (Jaumann et al., 2012; Pasckert et al., 2018).

To the northwest of the landing site is Bose crater, which is approximately 90 km in diameter and contains a central peak (of diameter 15 km) and a terraced crater wall. This central peak and crater wall (along with that of Bhabha crater) exhibit low-calcium pyroxene noritic composition, which is thought to represent thick impact melt breccia associated with the SPA-basin forming impact. No other regions of noritic composition have been identified, suggesting that the norite was uplifted by the rebound during the impact. Overlaying this noritic material is a gabbroic layer (Borst et al., 2012) which may represent the remnants of the differentiated mafic SPA impact melt sheet (Pieters et al., 2001). Sampling of this layer may address NRC (2007) Concept 6.

Furthermore, areas within the SPA basin have received some of the lowest contributions of non-SPA derived material, between 20 – 50% of both impact-melt and foreign materials (Petro & Pieters, 2004; Petro et al., 2011). Thus, samples of ancient regolith at this location will be less contaminated by non-SPA materials and address Concept 7.

The Mars-forward 100 km exploration zone within the SPA basin center involves investigation of the Mafic mound, Bose and Bhabha craters, a small, unnamed geologically young crater, mare and cryptomare deposits, and ancient regolith deposits (Figure 7.21).

The region contains 7 geologic terrains from pre-Nectarian to Imbrian age (Wilhelms et al., 1979). Borst et al. (2012) defined 9 geologic units for the study region, however, the mare/cryptomare boundaries are disputable when compared to those of Gibson & Jolliff (2011) (see Appendices C4-E1, C4-E2, C4-E3). Traversing in this region will help to address these discrepancies and comparison of samples from multiple adjacent flows would provide temporal and compositional context for volcanism in the SPA basin center.

The diverse set of lithologies within the proposed portion of the SPA basin center allows for NRC (2007) Concepts 1, 2, 3, 5, 6, and 7 to be addressed (Appendix C5-E). A detailed explanation of the specific NRC goals that can be addressed by the traverses in the following sections can be found in Appendix C2-5.

Traversal Loop 1. The first traversal travels broadly south, visiting the Mafic mound (Moriarty & Pieters, 2015). To investigate its origins we plan numerous opportunities to sample putative impact melt of the SPA basin forming event (Stations 4-7) and address Concept 1 to test the lunar cataclysm hypothesis. Furthermore, the ejecta blanket of Bhabha crater (Stations 1-3) can determine the age of the subsequent impact event, and ancient regolith collected from various locations (Stations 4-7, 9) can investigate the nature of regolith processes in the SPA basin center and address Concept 7. Additionally, cryptomare deposits (Stations 7-9, 11) can be sampled to address Concepts 2, 3 and 5 to reveal the nature of the lunar farside volcanism.

Traversal 1 is approximately 308 km in length, taking a total of 13 days (97 hours) to complete with the inclusion of 11 EVA stations and a 1.6 day pause due to orbital communication loss. It has an average slope of 3.6° and a maximum slope of 14.7° (Appendices C4-E4, C4-E5).

Traversal Loop 2. The second traversal circumnavigates north and explores the central peak (Station 14), crater wall (Stations 12, 15) and impact melt (Station 13) of Bose crater, sampling ancient regolith (Stations 12, 13, 15), as well as mare (Station 16) and cryptomare deposits (Stations 17, 18) (see Appendices C4-E2 and C4-E3). The impact melt pond of Bose crater can be used to accurately determine the age of crater-forming impact. Additionally, collecting samples of impact melt from a number of locations may provide insight on the nature of lunar history and chronology.

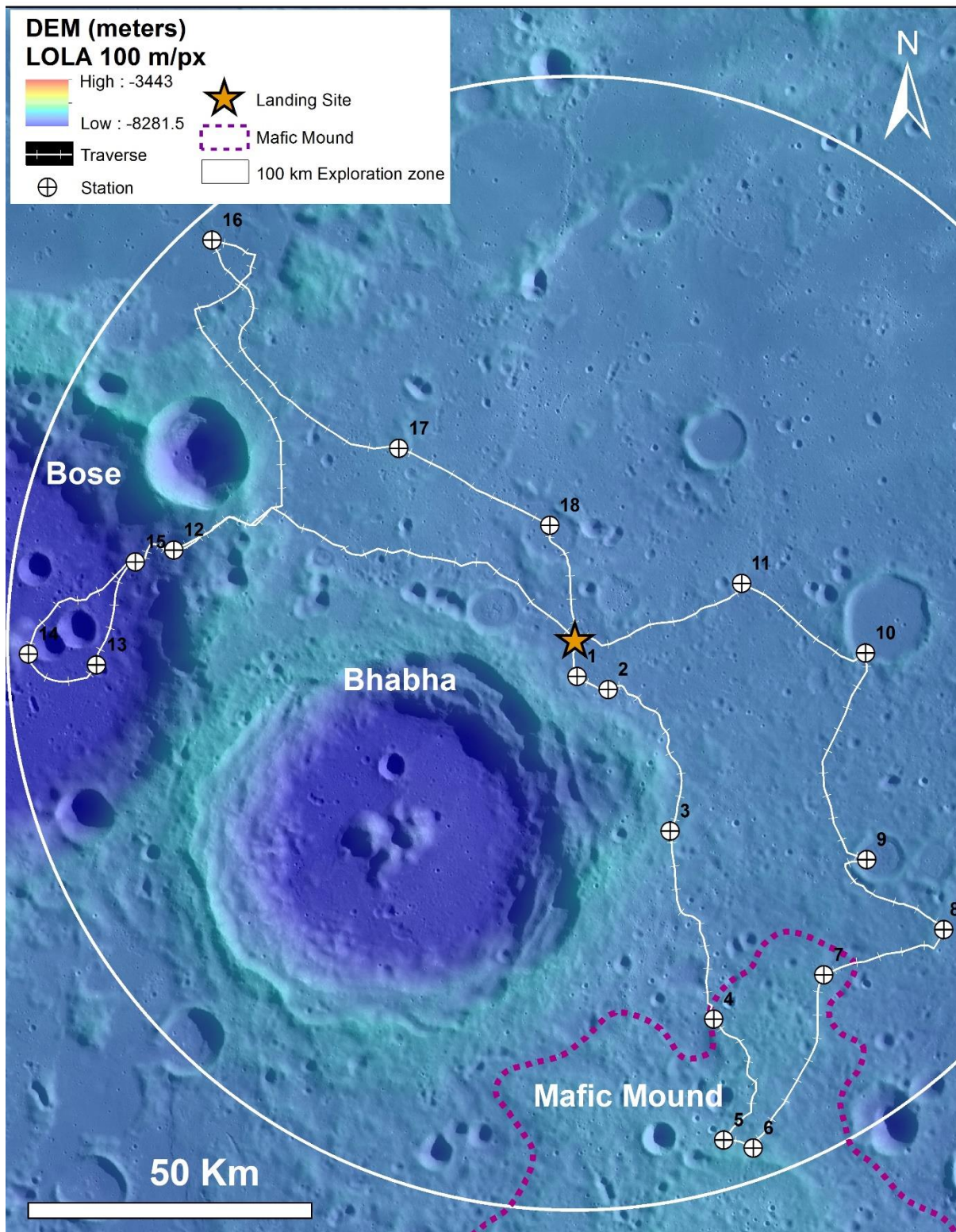


Figure 7.21: Colorized DEM of SPA basin center containing proposed landing site overlaid on LROC WAC mosaic of 100 m/pix. Includes traverses, sampling stations, and 100 km Mars-forward exploration zone for reference.

Sampling of the central peak of Bose crater may provide crucial information as to the presence, composition and possible differentiation of the SPA melt sheet. SPA impact melt sheet may be accessible from crater wall exposures, thus sampling stations have also been selected to sample wall material.

Traverse 2 is approximately 360 km long, taking a total of 14 days (103 hours) to complete with the inclusion of 7 EVA stations. It has an average slope 3.2°, and a maximum slope of 6.1° (Appendices C4-E4, C4-E6). We recommend this traverse take place in the lunar daytime due to the terrain variation when descending into Bose crater.

7.6. Implied Trade Studies

This study revealed several shortcomings in existing data and analysis. As such, we suggest that the following issues need more attention.

Detailed illumination studies were not possible for these sites due to the limited resolution of DEMs available in the edition of the Lunar Mapping and Modelling Project (LMMP) available at the time of the study. Thus, a future trade study must be conducted for all sites at a high resolution, especially along traverses where the LER is limited to daylight driving only to maximize hazard avoidance, increase visibility for crew and maximize scientific return from Gigapan deployment.

Also with respect to illumination, we assume the LERs are able to drive through PSRs, but the maximum duration of transit in darkness is not yet constrained and requires an additional trade study. Detailed illumination data should be collected and investigated in multiple dimensions (to determine if the entire LER will be in shadow, or partially in shadow) in order to assess thermal load on the LER and partially address the allowable time and distance it may travel in a PSR. Studies concerning the power source type, availability of solar power, and/or rechargability of the LERs are also required in order to factor in recharge times for all traverses.

Additionally, without accurate estimations of the reduced productivity of the astronauts and the LERs during lunar darkness, this study assumes the same rate of both IVA and EVA ability. Thus, there is a need for a trade study, which investigates both driving and sampling in limited illumination conditions. Also, visual and experimental time requirements are necessary for different instruments on board the LER(s) utilized along the scientific traverse between sites.

If an autonomous mode were considered for the LERs over terrain that had already been well-characterized, whether already traversed, characterized from high-resolution orbital imagery, or from Gigapan imagery taken along the traverse, LER speed would have to be slowed in order to minimize risk to the vehicles. This would have the follow-on effect of increasing traverse time, however, as long as this remains within the 30% contingency margin allotted to the 1-year travel time between landing sites then such a mode could be considered. Autonomy, or partial-autonomy, may also

be particularly useful when considering prospecting operations, or continuous sub-surface surveys over well-characterized regions. We recommend a future trade study be performed concerning the feasibility (time loss, risk minimization, hazard detection and avoidance) of autonomous navigation.

Future trafficability studies may be required to access to Schrödinger basin and Antoniadi crater in greater detail. This may involve the creation of high resolution NAC DEMs in order to facilitate hazard avoidance while the LER are tele-operated and elucidate the effect of poorly consolidated material on their access to human landing sites. Furthermore, additional hazard studies, such as rock abundance and crater density between, in, and around landing sites are necessary for more detailed traverse planning because 0.5 to 1.0 m resolution NAC imagery was not available along the entire routes we investigated.

Alternative traverse routes should be planned in the event that LER slope capabilities change in the future. This may be done parametrically, cycling through potential slope values in steps (e.g. 15, 20, 25, 30 degrees) and assessing how this affects the science able to be obtained from these alternate routes. Another angle to such a study would be to plan alternate traverse routes depending on the chosen orbital configuration – assessing how travel times, communications, and science gains will change if a Near-Rectilinear Halo Orbit is selected.

In terms of future LOP-G studies, a study to optimize LOP-G visibility by using its capability to change its orbital phase, and demonstrate its propulsion system, would be valuable. Additionally, detailed studies of LOP-G visibility from the lunar surface taking into account the occultation of the LOP-G by local terrain may be of interest.

In terms of additional data requirements, to maximize the scientific return detailed geologic maps of the South Pole (Malapert massif and Shackleton crater area) and South Pole-Aitken basin center would be required. While spectroscopic data is limited at such high latitudes, future studies may also wish to concentrate on the collection of this valuable data in order to further refine material composition for sample collection.

While our analyzes provide minimum mass estimates based on the assumption of rock and soil as the sampled material, volatile-rich and icy material should also be taken into account. It appears the landing sites and traverses will potentially provide access to them as well. Research into the transport and storage of volatile-containing samples must also be undertaken to ensure no sample context is lost upon transport back to Earth.

For this study, while ‘safe’ distances were calculated for traverses between landing sites, and a 100 km exploration radius was used for planning traverses at and around landing sites, in reality, traverses will be much shorter to take into account a variety of additional contingencies that arise from further detailed mission planning. In the course of this study, we did undertake preliminary crew activity planning in order to estimate overall traverse timing which is not discussed in this paper; however, an example crew

activity timeline for Schrödinger basin is included in Appendix C4-C2 to facilitate future research in this area.

We also suggest an investigation of notional instrument payloads (taking into account their dimensions, power consumption, and masses) which would maximize science return along the proposed traverses. For example, a visible to near-infrared (VNIR) multispectral camera or hyperspectral imaging spectrometer could aid in the ground-truthing of orbital data from Chandrayaan-1's M³ instrument. A mass spectrometer like NASA's Sample Analysis at Mars (SAM) instrument (Mahaffy et al., 2012), or ESA's Package for Resource Observation and in-Situ Prospecting for Exploration, Commercial Exploitation and Transportation (PROSPECT) Sample Preparation and Analysis (ProSPA) instrument (Carpenter et al., 2014; Barber et al., 2017) may be included for volatile analyzes. A drill, whether carried as an instrument by crew on EVA, or attached to the LER as with ESA's ExoMars 2020 rover (Vago et al., 2017), could also be used to investigate the vertical distribution of subsurface material and collect well-preserved material for analysis. Using the hole created by the drill, the crew could deploy a heat-flux experiment package to measure heat flow coming from the interior of the Moon and address NRC Goal 2d – characterize the thermal state of the interior. The PrActive or passive seismometers could also be carried as part of the instrument payload. Deployment of these seismometers at each proposed landing site, effectively forming a seismometer array, could help to characterize the lunar crust, mantle, and core and address NRC Concept 2.

Additionally, in order to address the recent impact flux (NRC Goal 1d) at (and potentially between) all proposed landing sites a camera positioned onboard the LOP-G could provide regular surface monitoring, which could be used to locate fresh craters for sampling by the crew on subsequent missions, or for the LERs to remotely investigate between crew landings if they are equipped with a sample collection ability.

Manual estimation of regolith thickness could be performed for traverses in this region by examining the size and morphology of concentric craters using the method described by Oberbeck & Quaide (1968) and as performed by Huang et al. (2018) for the Chinese lunar mission Chang'E-4. These regolith thickness estimations could then be "ground truthed" during the proposed mission using GPR measurements between and at all landing sites.

Once the results of the above trade studies have been obtained, traverse and EVA times presented here may be calculated more accurately depending on the task and priority of each station, and whether it is scheduled to be visited in lunar daytime or nighttime.

7.7. Conclusion

This study, based upon a Design Reference Mission by Hufenbach et al. (2015) as a prelude to the release of the 2018 GER, is a first-pass at the feasibility of a five-site, LOP-G enabled, lunar sample return mission scenario which utilizes both human and robotic assets. The findings of this study, obtained through integration of multiple remotely-sensed lunar datasets, robotic asset capabilities, and communications feasibility, show that a human-assisted robotic mission to the lunar south polar region, including farside locations, can address all seven NRC (2007) lunar science concepts, and would be a valuable resource for the early history and evolution of the Solar System.

The traverses between the five landing sites seem feasible within the known engineering capabilities of the LER(s). Our accessibility study identified possible access to the interior of Schrödinger basin and Antoniadi crater. Although, if future study of higher-resolution datasets, such as NAC DEMs, reveals that these basin floors are inaccessible, exploration zones must be limited to exterior surface locations, which would mean that significant geological context is lost (Figure 7.18 and 7.20).

We find that tele-operating the LERs between the five proposed landing sites along 'science' traverses can enable a significant amount of science to be performed while remaining within the allotted travel time and slope requirements with 30% contingency. Distances between landing sites are sufficiently short (approx. 1000 km) and LER speed is sufficiently fast (0.36 km/hr) to conduct significant geological surveys during 'science' traverses, some of which involve prospecting for icy volatiles in Cabeus and Amundsen craters. We recommend the addition of sample collection technology, such as a robotic arm, to facilitate this.

Given current engineering parameters it is not possible for the crew to fully explore a 100 km exploration zone in 28-day or 42-day missions, however, they are able to collect samples that address all, or a large fraction of the NRC (2007) objectives, depending on the landing site. In the future using variable rover speeds and EVA times on different terrain types will increase the maximum possible traverse distance adhered to in this study.

To maintain consistent communication across all landing sites we have selected a large southern-class halo orbit with an orbital period of 10.6 days for the LOP-G, based on calculations performed by Lockheed Martin (2016).

As the parameters for such a mission are likely to change based on results from future trade studies and asset engineering, components of this study are highly amenable to adaptation as necessary; similar assessments may be undertaken for any proposed landing site. We find that surface exploration and sample return from human-assisted robotic exploration of the lunar surface would allow the international community to progress in its vision for larger scale, Mars-forward campaigns and provide valuable insight for future lunar exploration activities.

Acknowledgments

This work was carried out through the 2016 Exploration Science Summer Intern Program hosted by the Lunar and Planetary Institute (LPI) and Johnson Space Center (JSC). This research was supported in part by the NASA Solar System Exploration Research Virtual Institute (SSERVI). Thank you to Josh Hopkins and Chelsea Welch at Lockheed Martin for their calculations of orbital coverage for the given landing sites, and the Lunar Mapping and Modeling Project (LMMP) support staff (now Moon Trek).

CHAPTER 8

CHARACTERIZATION OF HIGH-PRIORITY LANDING SITES FOR ROBOTIC EXPLORATION MISSIONS IN THE APOLLO BASIN, MOON

Csilla Orgel, Mikhail A. Ivanov, Harald Hiesinger, René Prissang, Gregory Michael, Carolyn H. van der Bogert, Jan Hendrik Pasckert, & Sebastian H. G. Walter, Manuscript in preparation to Planetary Science Journal

Abstract

As the oldest and largest visible impact structure on the Moon, the South Pole-Aitken (SPA) basin on the lunar far side is a scientifically high priority site for human and robotic exploration missions. The superposed Apollo basin is a 492 km diameter peak-ring, which is the largest and one of the youngest basins within the SPA basin. We selected three Regions of Interest (ROI) in the Apollo impact basin and addressed the National Research Council (NRC, 2007) scientific concepts and goals and Campaigns of the European Space Agency's Strategy for Science at the Moon (ESA, 2019), investigated landing and operational hazards as well as analyzed their ISRU potential. We demonstrated the scientific potential of two future robotic exploration mission architectures: (1) utilizing lander and rover assets on the lunar surface, and (2) with additional sample return capability. We conducted a series of data analyses concerning topography, slope, crater density, rock abundance, geology, mineralogy, and subsurface stratigraphy. The results showed that landing and operational hazards are manageable and that the terrains are safe for landing and navigation. The mare provinces have high In Situ Resource Utilization (ISRU) potential with relatively high FeO and TiO₂ contents ranging from 14-20 wt% and 3-5 wt%, respectively. In-situ observations with advanced rover and lander payload capabilities can help to address six of seven NRC concepts (1-3, 5-7) as well as Campaigns 1 and 5 of the European Space Agency's Strategy for Science at the Moon (ESA, 2019). However, there is a great loss in science benefit without a sample return capability. To test the cataclysm hypothesis and establish an accurate lunar chronology (Concept 1, NRC (2007)) a sample return mission scenario is required.

8.1. Introduction

As the oldest and largest visible impact structure (Wilhelms et al., 1979,1987; Garrick-Bethell and Zuber, 2009; Smith et al, 2010; Garrick-Bethell et al., 2020) on the Moon, the South Pole-Aitken (SPA) basin on the lunar far side is a scientifically high priority site for human and robotic exploration missions (National Research Council (NRC), 2007; Kring & Durda, 2012; **Allender et al., 2019**). Several national, international, and

commercial lunar lander and sample return missions directly or via the Lunar Orbital Platform-Gateway (LOP-G) are targeting the south polar region and SPA in the next decade (Steenstra et al., 2016; Ivanov et al., 2017; ISECG, 2018; **Allender et al., 2019**; Jawin et al., 2019; Flahaut et al., 2020). On January 3 2019, the Chinese Chang'e-4 exploration mission became the first landed mission on the far side of the Moon after a successful landing in Von Kármán crater in the NW portion SPA (Huang et al., 2018; Jia et al., 2018; Wu et al., 2019). Initially, the primary landing site for the Chang'e-4 robotic mission was the 492 km diameter Apollo basin in the NE quadrant of SPA basin (Wang & Liu, 2016), the location of which has been of interest for NASA's Constellation Program (Gruener & Joosten, 2009) (Figure 8.1). Because the Apollo basin is remained as one of potential landing site inside the SPA, we selected three Regions of Interest (ROI) with high priority on the central and southern mare deposits in the Apollo basin (Figure 8.1 and Figure 8.2). This work provides a series of geospatial analyses of various optical, topographical, and spectral datasets using Geographic Information System (GIS). We demonstrate that the Apollo basin allows us to address key lunar science objectives of NRC (2007) and Campaigns 1 and 5 of the European Space Agency's Strategy for Science at the Moon (ESA, 2019) and we investigate two future robotic exploration mission scenarios: (1) utilizing lander and rover assets, and (2) with additional sample return capability.

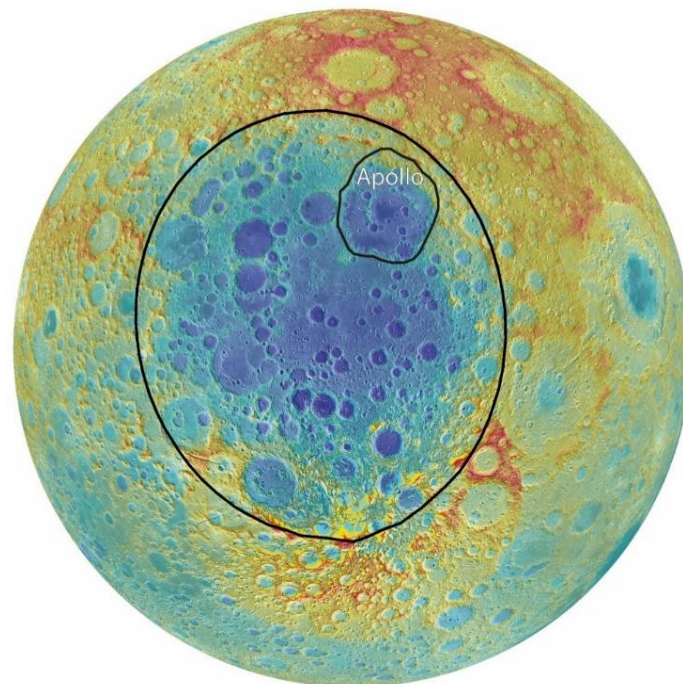


Figure 8.1: South Pole-Aitken basin overview. LROC WAC overlaid on LOLA DEM 100 m/pix data. The black solid lines represent the SPA basin outer rim and the Apollo basin, respectively.

8.2. Science Rationale

8.2.1. South Pole-Aitken Basin

The SPA basin has a diameter of 2400 by 2050 km and a depth of approximately 13 km (Garrick-Bethell and Zuber, 2009; Smith et al., 2010). Moreover, the SPA appears to be the oldest impact structure (Hiesinger et al., 2012b: 4.26 ± 0.03 Gyr, **Orgel et al., 2018**: $4.31 +0.019/-0.021$ Gyr) on the Moon. As a consequence of such a large basin-forming impact event, the crustal thickness beneath SPA is less than 20 km with local thicknesses of < 5 km beneath the Apollo and Poincaré basins (Wieczorek et al., 2013). Additionally, the floor of the SPA basin exhibits slightly enhanced thorium concentrations which, as a heat-producing element, could increase the melt production for volcanic activity (Wieczorek & Phillips, 2000). Despite both characteristics, the thin crustal thickness and higher thorium abundance, volcanic deposits cover the SPA basin floor to only a minor extent (Yingst & Head, 1999; Pasckert et al., 2018). However, a significant amount of olivine has not yet been detected within the SPA basin, and only the central peak/peak-ring structures of Schrödinger basin and Zeeman crater show olivine signatures (Yamamoto et al., 2012; Kramer et al., 2013). Additionally, there are several observations of pyroclastic deposits ranging from small (as in the Apollo basin) to large (as in the Oppenheimer crater and Schrödinger basin) (Wilhelms et al., 1979; Gaddis et al., 2003; Kramer et al., 2013) as well as proposed pyroclastics in the center of the SPA (Borst et al., 2012). Four distinct, mineralogical zones characterize the SPA basin (Lucey et al., 1998a; Jolliff et al., 2000; Pieters et al., 2001; Lawrence et al., 2002; Gibson & Jolliff, 2011; Moriarty & Pieters, 2018): (1) SPA Compositional Anomaly (SPACA) in the SPA basin center, which exhibits Ca, Fe-rich pyroxenes, (2) Orthopyroxene Annulus (OPX-A), dominated by Mg-rich pyroxenes, (3) Heterogeneous Annulus (HET-A), which shows a mixture of Mg-rich pyroxenes and feldspathic materials, and (4) SPA Exterior (SPA-X) with feldspathic composition.

8.2.2. Apollo Basin

Within the SPA basin, the Apollo basin (36.09°S , 159.69°W) is the largest peak-ring impact basin (492 km diameter, Baker et al., 2011). The inner peak-ring has a diameter of 247 km and reaches heights of ~ 1-2 km above the surrounding terrains (Baker et al., 2011). The inner peak-ring structure remained intact only in the west and northeast of the basin floor. The outer Apollo ring rises ~ 3 to 5 km above the basin floor and superposes the NE portion of the SPA basin rim (Figure 8.2 and Figure 8.3) (**Ivanov et al., 2018**).

The model crustal thickness beneath the Apollo basin is less than ~ 5 km, which is the thinnest in the entire SPA basin (Wieczorek et al., 2013). Baker & Head (2015) calculated the pre-impact crustal thickness in the range of 27.0 to 35.3 km and a maximum depth of excavation of 39 km. Similarly, numerical modeling from Potter et al. (2018) gives the estimates for pre-impact crustal thickness in the range of 25 to 40

km and a depth of excavation of ~ 32 km. These values for depth of excavation are larger than for the Schrödinger basin (26 km, Kring et al., 2016), which is a younger (Orgel et al., 2018) and smaller peak-ring impact basin closer to the south polar region. Therefore, the potential to find mantle material or more diverse rock types in the Apollo basin is higher than in the Schrödinger basin.

According to crater size-frequency distribution (CSFD) measurements, the Absolute Model Age (AMA) of Apollo basin varies from $3.91 \pm 0.04 / -0.06$ Gyr (Hiesinger et al., 2012b), $3.98 \pm 0.04 / -0.06$ Gyr (Ivanov et al., 2018) to $4.14 \pm 0.024 / -0.029$ Gyr (Orgel et al., 2018). Consequently, the Apollo basin is one of the youngest basins in SPA.

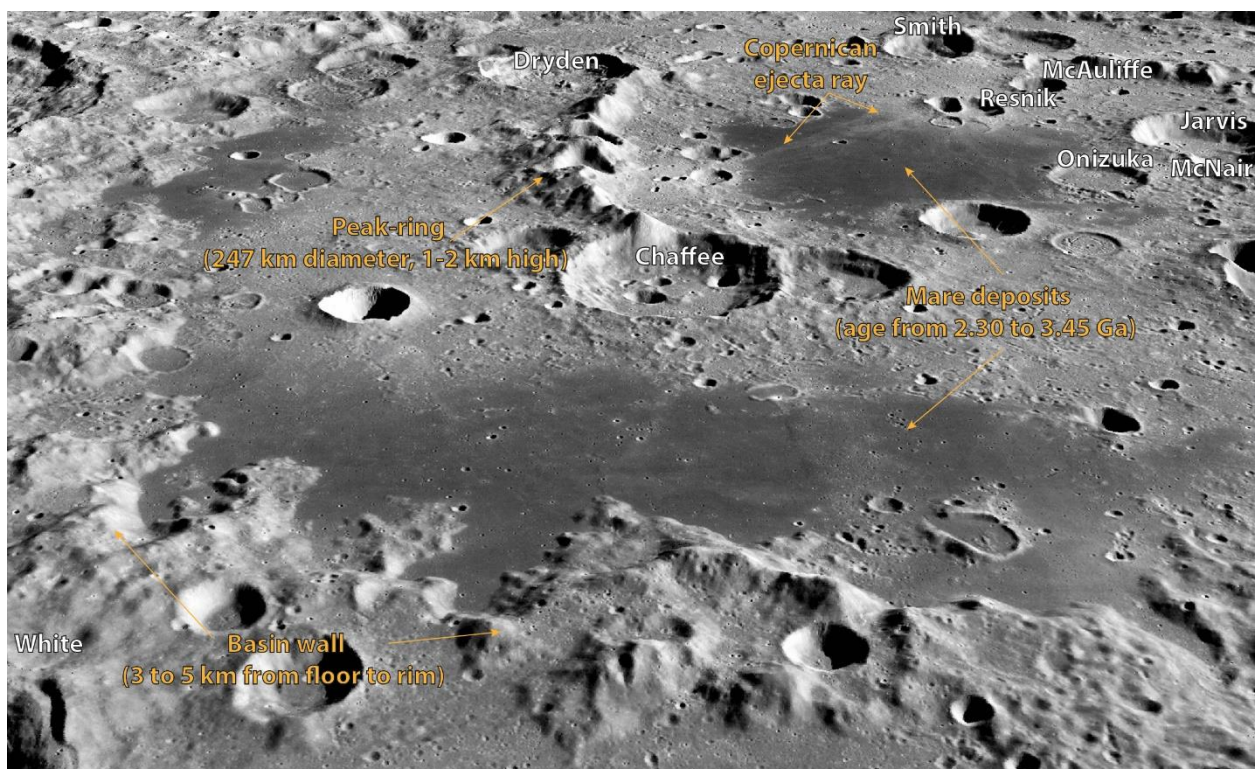


Figure 8.2. Oblique view of Apollo basin derived from a merged LRO LOLA and Kaguya TC 60 m/pix DEM and 100 m/pix LROC WAC mosaic. Units of interest are labeled. Vertical exaggeration is 2x.

Based on Apollo Imagery and Lunar Orbiter IV, the first geologic maps of the Apollo basin at 1:5M scale were compiled by Stuart-Alexander (1978) and Wilhelms et al. (1979). Based on new data from the Lunar Reconnaissance Orbiter Wide-Angle Camera (LROC WAC), Ivanov et al. (2018) have mapped the Apollo basin at 1:500K scale and found two major classes of landforms: (1) impact craters, and related features, and (2) plains-forming terrains of volcanic (dark plains) and impact (light plains) origin (Wilhelms et al. 1979; Thiessen et al. 2012; Meyer et al., 2018; Ivanov et al., 2018; Pasckert et al., 2018). The basin floor is mainly covered by four major

mare basalt provinces (center, south, west, and east), their AMAs ranging from 2.30 to 3.45 Gyr (central: 2.93 Gyr, southern: 3.31 Gyr and 3.45 Gyr, Pasckert et al., 2018) or from 2.44 Gyr (southern unit) to 2.49/3.51 Gyr (central unit) (Haruyama et al., 2009). The mare deposits have enhanced FeO and TiO₂ content, among the highest in the SPA basin (Figure 8.3) (Kring & Durda, 2012; Pasckert et al., 2018). Additionally, Gaddis et al. (2003) described a small pyroclastic deposit (42 km²) on the floor of a 20.5 km diameter crater on the outer ring of the Apollo basin. Based on low optical maturity, the lower returned Mini-RF radar signal, and slightly lower FeO abundance than the average green glass composition of 19.5 wt% FeO, Trang et al. (2010) suggested that materials in the Apollo basin could be a new type of pyroclastic deposit. Because of high FeO content, both mare and pyroclastic materials in Apollo basin have high In Situ Resource Utilization (ISRU) potential. Thiessen et al. (2012) mapped and derived AMAs from 3.4 to 3.8 Gyr for light plain deposits in the SPA, while **Ivanov et al. (2018)** report AMAs for three large fields of in-crater light plains in the NE portion of SPA ranging from ~ 3.80 to ~ 3.72 Gyr. Moreover, Meyer et al. (2016, 2018) mapped the light plain deposits at 1:300K scale around the Orientale basin and globally, respectively, and genetically linked 70% of all light plains to the Imbrium and Orientale basins.

The Apollo basin overlays both the HET-A terrain, and OPX-A mineralogical zone, unlike Schrödinger basin (Moriarty & Pieters, 2018). Baker & Head (2015) defined the Apollo basin as “Class C = ≤ 95% plagioclase (+ pyroxene)” spectral type. However, they did not detect crystalline plagioclase or shocked plagioclase on any outcrops. Furthermore, Potter et al. (2018) explain the lack of pure anorthosite by the magnitude of the impact, shocking the crust and erasing the anorthosite band in the 12.5 μm wavelength region. The peak-ring is dominated by pyroxenes (Klima et al., 2011; Baker & Head, 2015), which might originate from the lower crust, or can be explained by the possible presence of a differentiated melt sheet of SPA (Hurwitz & Kring, 2014; Vaughan & Head, 2014). Despite the thin crustal thickness (< 5 km) and maximum depth of excavation (32-39 km), olivine has not been detected in Apollo basin (Yamamoto et al., 2012). The lack of the remote sensing signature of olivine using remote sensing data suggests the presence of mafic-rich primary crust or cumulate pile at the depth of excavation (Potter et al., 2018), which is in good agreement with findings of Vaughan & Head (2014).

8. CHARACTERIZATION OF HIGH-PRIORITY LANDING SITES IN THE APOLLO BASIN, MOON

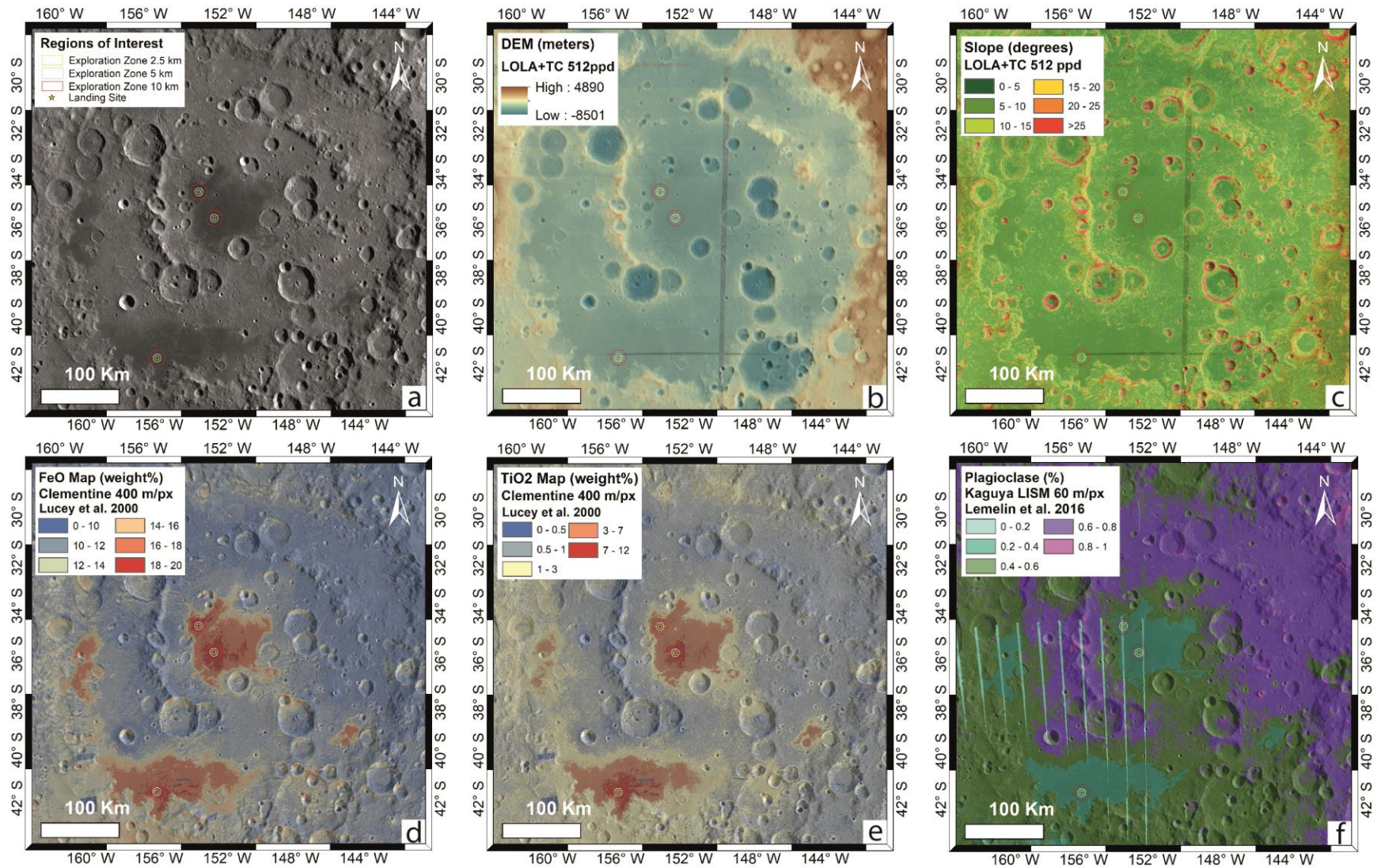


Figure 8.3: Maps of the Apollo basin. a) LROC WAC mosaic of 100 m/pix, includes three Regions of Interest (ROI) with proposed landing site (orange star), a 2.5 km (yellow), 5 km (white), and 10 km (red) exploration zone. b) Colorized LOLA and Kaguya TC DEM mosaic of 60 m/pix. c) Slope map at 60 m baseline derived from LOLA and Kaguya TC DEM. d-e) FeO and TiO₂ maps derived from Clementine UVVIS 400 m/pix global dataset, respectively (Lucey et al., 2000). ROI overlap with the highest abundance of FeO and TiO₂ concentrations. f) Plagioclase map of Kaguya MI 60 m/pix global dataset (Lemelin et al., 2016). Localized occurrences of plagioclase larger than 80 % are related to crater rims at the inner peak-ring of the Apollo basin. The striping results from data gaps.

8.3. Selection Criteria for Regions of Interest (ROI)

Typically, landing site assessments are based on criteria including: 1) terrain properties (hazards: slopes, crater density, rock abundance; landing precision; operations constraints), and 2) scientific potential. Additionally, ISRU potential of a future landing site became one of the driving forces to return to the lunar surface. Hazard analysis considers slopes (e.g., Luna-25: < 7°, Djachkova et al., 2017, Chang'E-3: < 7°, Wu et al., 2014) at baselines relevant to landing and operations safety. We use 60 m baseline data to derive slope maps. This resolution is relevant to other datasets, but does not provide accurate information for landing and operation safety. We mapped craters ≥ 70 m in various degradation states (Wu et al., 2014) in the selected areas. The threshold of 70 m diameter of impact craters requiring the crater to be resolved with 10 pixels across using TC 7 m/pix images. The depth-to-diameter ratio of young, fresh craters with similar diameters is 0.10 (Daubar et al., 2014), and they exhibit steep slopes ($> 25^\circ$, Basilevsky et al., 2014). Simple, small craters (up to a few hundred meters) become shallower and slopes become gentler with time (Fassett, 2016). The crater rims and proximal ejecta of these young craters are often characterized by materials with higher rock abundances, which are unsuitable for rovers. However, these young craters could provide data on the subsurface lithologies at different depths depending on their sizes.

Besides the requirements for terrain properties, several scientific objectives could be addressed following the recommendation of the NRC (2007) report. This report prioritizes eight science concepts and goals of lunar exploration. In this study, we only consider concepts 1 to 7 as we focus on addressing lunar surface and interior goals. To summarize the NRC (2007) concepts and goals, we list the concepts below:

1. The bombardment history of the inner Solar System is uniquely revealed on the Moon.
2. The structure and composition of the lunar interior provide fundamental information on the evolution of a differentiated planetary body.
3. Key planetary processes are manifested in the diversity of lunar crustal rocks.

4. Lunar volatiles increase our understanding of the composition state and distribution of volatiles in the lunar polar regions.
5. Lunar volcanism provides a window into the thermal and compositional evolution of the Moon.
6. The Moon is an accessible laboratory for studying the impact process on planetary scales.
7. The Moon is a natural laboratory for regolith processes and weathering on anhydrous airless bodies.

Campaigns 1 and 5 of the European Space Agency's Strategy for Science at the Moon (ESA, 2019) are the following:

Campaign 1: Analysis of new lunar samples

Campaign 5: Near surface geology, geophysics, mineralogy, and geochemistry

In addition to the scientific and engineering constraints, robotic missions will target landing sites with high ISRU potential to allow sustainable space exploration on the surface, where volatiles (e.g., H₂O) and mineral resources (e.g., ilmenite, FeTiO₃) can be extracted directly from the regolith and utilize to produce fuel, oxygen, and building materials (e.g., Allen et al., 2012; Allen, 2015; Ehresmann et al., 2017).

Combining all the elements discussed above, we selected three candidate landing sites for robotic exploration in the Apollo basin. Until today, there have been only four rover missions completed or are on-going on the lunar surface: Lunokhod-1 (completed roving distance: 9.436 km, Karachevtseva et al., 2013), Lunokhod-2 (completed roving distance: 39.16 km, Karachevtseva et al., 2017), Chang'E-3/Yutu-1 (completed roving distance: 114 m, Qiao et al., 2015), and Chang'E-4/Yutu-2 (on-going roving distance: > 358 m (as of January 5, 2020), Jones, 2020). Moreover, a previous solar-powered robotic mission study from Potts et al. (2015) designed short-distance traverses (3.7 km and 10.8 km), medium-distance traverses (22.5 km and 12.7 km) and long-distance traverses (28.8 km and 37 km) for 14-days missions to the Schrödinger basin. Steenstra et al. (2015) proposed a human-assisted robotic sample return mission concept in support of ESA's HERACLES human-assisted sample return mission concept based on a 3 year mission plan where two robotic mission traverses were planned within an ESA-specified total traverse distance of 100-300 km. Taking these values from previous missions and concept studies into account, we choose an exploration zone of 2.5 km, 5 km, and 10 km around each candidate landing sites for a nominal mission phase.

8.4. Data and Methods

8.4.1. Data

To evaluate the potential scientific return of each proposed ROI, we use all available datasets from previous lunar missions and studies (Kring and Durda, 2012). We integrated all datasets in ArcGIS 10.5. software environment. The terrain hazards are determined via digital elevation models (DEM), and slope maps derived from the Lunar Reconnaissance Orbiter Lunar Orbiter Laser Altimeter (LRO LOLA) instrument, with a baseline of ~ 60 m/pix (Smith et al., 2010). The terrains that compose the Apollo basin are visualized using Lunar Reconnaissance Orbiter Camera Wide Angle Camera (LROC WAC) mosaics of 100 m/pix (Robinson et al., 2010), Kaguya Terrain Camera (TC) images of 7 m/pix (Kato et al., 2010), and individual LROC Narrow Angle Camera (NAC) images of 1 m/pix (Robinson et al., 2010). We use the Kaguya TC images as the photobase for geologic mapping at 1:50,000 mapping scale for the central and southern portion of the Apollo basin, which in fact provides a higher resolution geologic map than that of Ivanov et al. (2018). For both safety and scientific purposes, we use the LRO Diviner Lunar Radiometer Experiment (DLRE) 236 m/pix data product to derive rock abundance. Rock abundance can be described in terms of the fraction of each pixel covered by exposed rocks (Bandfield et al., 2011). From the ISRU point of view we determine FeO and TiO₂ contents using Clementine 400 m/pix global maps (Lucey et al., 1998b, 2000), as well as the Kaguya Multiband Imager (MI) ~ 60 m/pix global data (Lemelin et al., 2016). To extract FeO and TiO₂ abundances (in wt%) from Clementine and Kaguya global raster datasets, we generated 50 random points within the 10 km exploration zone. To study the composition of the subsurface via impact craters (Ohtake et al., 2013, Huang et al., 2018, Fu et al., 2020) Chandrayaan M³ (Moon Mineralogy Mapper, global mode: 140 m/pix) and Kaguya MI data have been used (Pieters et al., 2009, Green et al., 2011).

8.4.2. Methods

8.4.2.1. Absolute Model Age (AMA)

We counted craters ≥ 70 m for hazard analysis and scientific purposes at each ROI. We are making use of the CraterStats software (Michael and Neukum 2010, Michael et al., 2013) to derive crater size-frequency distributions (CSFD) and absolute model ages (AMA) of the ROI and relevant geologic processes. We applied the lunar PF and CF from Neukum et al. (1983) to derive AMAs. We used the cumulative fit with pseudo-log crater binning and the μ -notation, which represents the compounded uncertainties of the particular chronology model (Michael et al., 2016). Respective crater counts were conducted in ESRI's ArcGIS 10.5, using the CraterTools extension (Kneissl et al., 2011). We are aware of the fact that the accuracy of our AMAs might be affected by the relatively small sizes of our count areas (van der Bogert et al., 2015). We used the buffered crater

counting (BCC) technique (Fassett and Head, 2008) which was implemented in CSFD_Tools (Riedel et al., 2018). This technique includes all craters overlapping the count area with a buffer. The use of the buffer allows us to increase the number of craters included in the measurements, giving better statistics. The measurements were carried out on Kaguya TC images with a pixel scale of 7 m/pix. For rover navigation purposes we calculated the low and high crater density areas within the 10 km exploration zone.

8.4.2.2. Regolith Thickness and Stratigraphy

We estimated the regolith thickness in the ROI using all LROC NAC images available by February 2018. The coverage was not complete and few images had poor quality. We followed the method from Quaide and Oberbeck (1968) to derive the regolith thickness using relatively fresh concentric craters (CC) with diameters less than 250 m. Small craters are strongly affected by variations in target properties (porosity, rock strength, and layering) and impact velocity (van der Bogert et al., 2017). According to Quaide and Oberbeck (1968) CC form when the impactor hits the lunar regolith-mare interface. We used the following equation:

$$\text{regolith thickness} = \left(k - \frac{D_f}{D_a} \right) D_a \tan(\alpha) / 2$$

where k is an empirical constant (0.86), D_f is the diameter of the inner concentric ring, D_a is the outer rim-to-rim diameter of a crater, and $\tan(\alpha)$ is the corresponding slope of inner walls of fresh craters ($31 \pm 2^\circ$). To map CC, we primarily considered NAC images with smaller incidence angle ($< 55^\circ$), but we also used images with higher incidence angle to fill gaps in image coverage. The distribution of CC is sparse in ROIs, thus we used the kriging statistic to interpolate the obtained regolith thickness values over the study areas. To study the deeper stratigraphy, we analyzed compositional variations within impact crater ejecta located on mare floor using Chandrayaan M³ pyroxene map and Kaguya MI plagioclase map. The diversity of minerals detected suggests chemical variations with depth, where smaller craters sample shallow strata, while larger craters exhibit deeper materials. We calculated the crater depth/diameter (d/D) ratio of Daubar et al. (2014) measured on lunar craters using LROC NAC images:

$$d = 0.096D^{1.07}$$

8.5. Results

The main focus of this study is on the central and southern mare provinces in the Apollo basin. We selected three ROIs based on hazard analyses as well as science, and ISRU potentials. We highlight exploration zones of 2.5 km, 5 km, and 10 km from each proposed landing site. Furthermore, we discuss each landing site in the context of key lunar science objectives from NRC (2007) and Campaigns 1 and 5 of the European Space Agency's Strategy for Science at the Moon (ESA, 2019), which could be addressed by robotic exploration missions (1) with lander and rover assets, and (2) with additional sample return capability.

8.5.1. Terrain Hazards: DEM, Slopes, Craters and Rock Abundance

On the basis of the studied data, all ROIs fulfil the general hazard requirements for a robotic exploration mission to the Apollo basin. The LOLA DEM serves as the basis to derive slopes at 60 m baseline, which do not exceed 5° except for few fresh craters with slopes $> 25^\circ$ (Figure 8.4). Taking landing precision and safety into account, slopes at 7 m baseline need to be investigated in the future. At shorter baselines, we expect larger variations in slopes. We found less than ~ 1000 craters ≥ 70 m within the 10 km exploration zones, and average crater diameters vary from 128 m (ROI 1) to 150 m (ROI 3) (Table 8.1, Figure 8.5). However, the largest maximum crater diameter is 983 m at ROI 2, and 233 m at ROI 3. The estimated average crater depths varies from ~ 10.7 m up to 12.8 m at ROI 1 and ROI 3, respectively (Table 8.1). The minimum crater depths vary 5.6 m at ROI 1 and ROI 2, and 9.2 m at ROI 3. The maximum crater depth varies from 54.5 m (ROI 1) up to 237 m (ROI 3). The crater density analyses showed that ROI 2 has the lowest crater density within the 10 km exploration zone. Additionally, 4.9% of the area of ROI 1 and 2 are covered by impact craters, while 7.5% of the area of ROI 3 are covered by craters. Younger craters have higher boulder densities at their rims and on their proximal ejecta radial to the crater centers. ROI 1 has the lowest areal rock density (3.5%), while ROI 3 (14.1) shows the highest rock abundance value within 10 km exploration zone (Table 8.2).

Table 8.1: Crater statistics of craters ≥ 70 m in diameter at within the three ROIs. Crater depths were derived using the empirical equation from Daubar et al. (2014).

| | ROI 1 | ROI 2 | ROI 3 |
|--------------------------------|--------|-------|--------|
| Min. crater diam. (m) | 70 | 70 | 70 |
| Max. crater diam. (m) | 588 | 983 | 233 |
| Average diameter (m) | 128 | 138 | 150 |
| Min. crater depth (m) | 5.6 | 5.6 | 9.2 |
| Max. crater depth (m) | 54.5 | 94.3 | 237.6 |
| Average crater depth (m) | 10.7 | 11.7 | 12.8 |
| Number of craters | 966 | 767 | 739 |
| Crater density/km ² | 0-11.9 | 0-9.9 | 0-10.3 |
| Fraction of the area (%) | 4.9 | 4.9 | 7.5 |

8. CHARACTERIZATION OF HIGH-PRIORITY LANDING SITES IN THE APOLLO BASIN, MOON

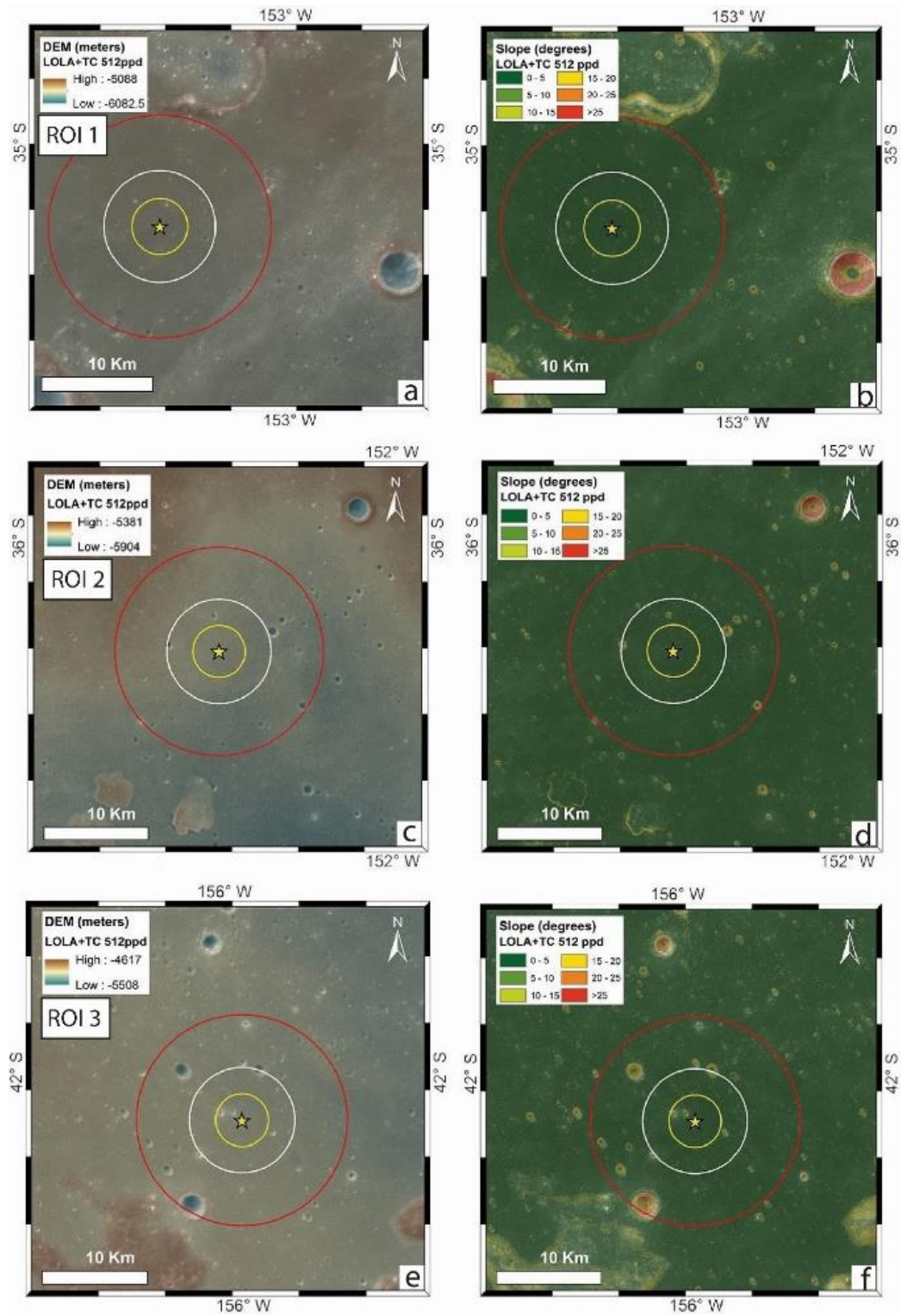


Figure 8.4: Digital elevation models (DEM; a, c, e) and slopes (b, d, f) derived from combined LRO LOLA and Kaguya TC 60 m/pix datasets for ROI 1, 2, and 3, respectively. The circles indicate exploration zones of 2.5 km, 5 km, and 10 km from the proposed landing site.

8. CHARACTERIZATION OF HIGH-PRIORITY LANDING SITES IN THE APOLLO BASIN, MOON

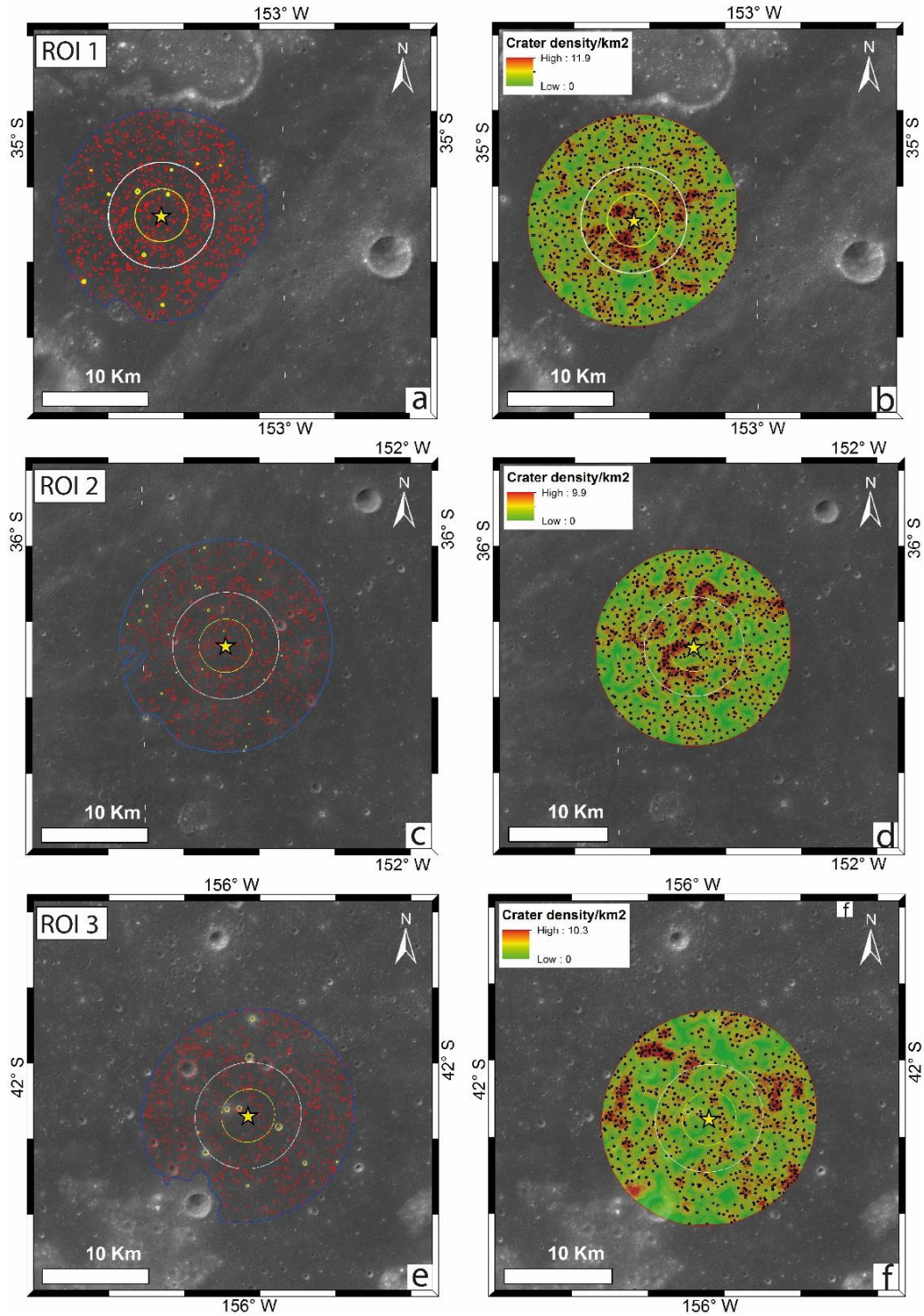


Figure 8.5: Maps of craters ≥ 70 m (a, c, e) and derived crater densities (b, d, f) based on Kaguya TC 7 m/pix data for ROI 1, 2, and 3, respectively. Red small circles are dark albedo craters, while small yellow circles represent bright ejecta craters. The circles indicate exploration zones of 2.5 km, 5 km, and 10 km from the proposed landing sites.

8. CHARACTERIZATION OF HIGH-PRIORITY LANDING SITES IN THE APOLLO BASIN, MOON

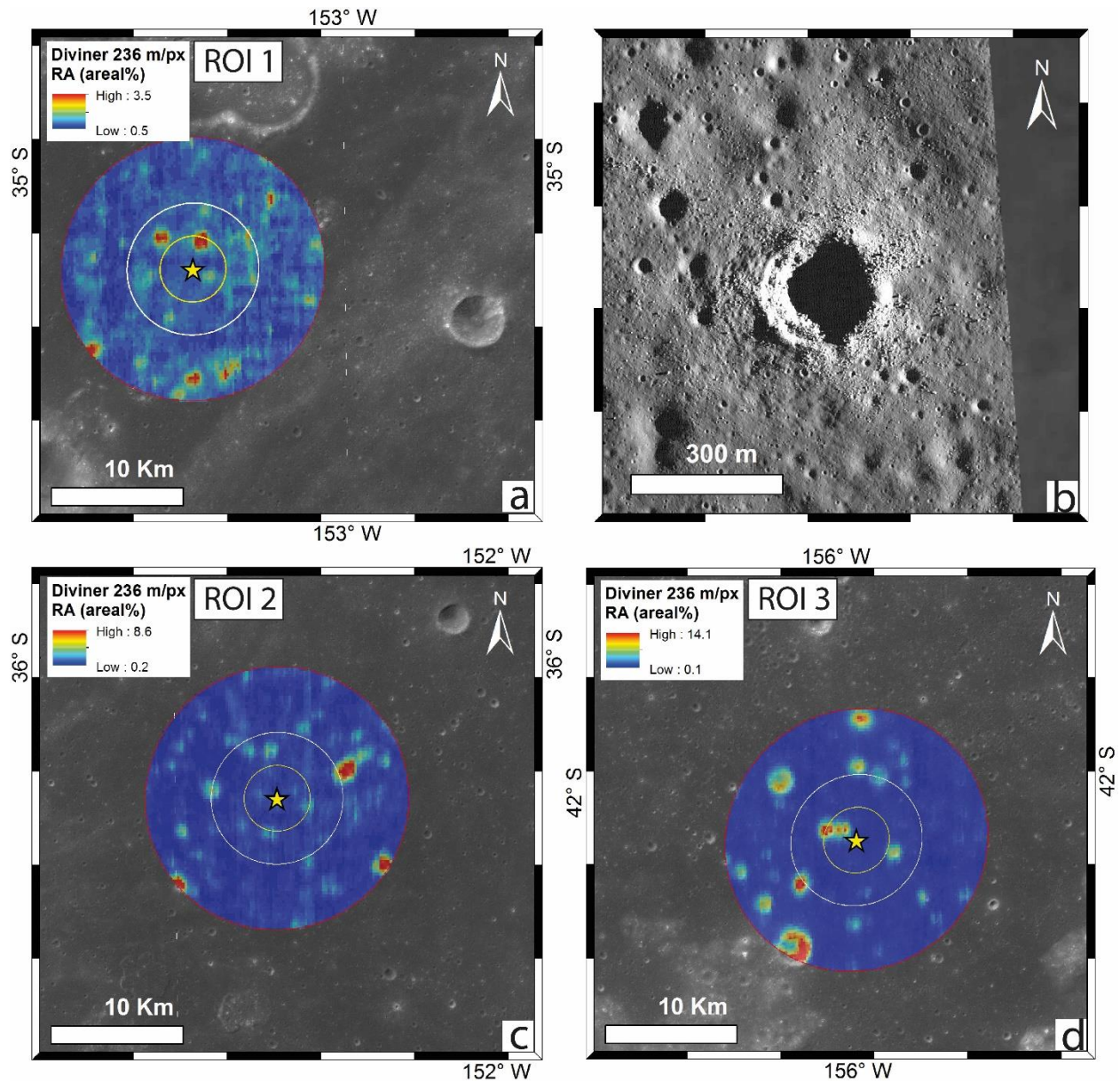


Figure 8.6: Rock abundance derived from LRO Diviner 236 m/px data (a, c, d) for ROI 1, 2, and 3, respectively. b) Example of “rocky” young crater. The circles indicate exploration zones of 2.5 km, 5 km, and 10 km from the proposed landing sites.

Table 8.2: Rock abundance (in areal %) based on LRO Diviner 236 m/px data.

| | ROI 1 | ROI 2 | ROI 3 |
|------|-------|-------|-------|
| Min. | 0.1 | 0.2 | 0.1 |
| Max. | 3.5 | 8.6 | 14.1 |

8.5.2. Science Potential

8.5.2.1. Geologic Mapping and Absolute Model Ages

There are three major classes of landforms mapped in the central and southern Apollo basin at 1:50,000 mapping scale (Figure 8.7 and Figure 8.8). We use a simplified terminology compared to Wilhelms et al. (1979) and **Ivanov et al. (2018)** but follow their general guidelines. A correlation chart of the mapped geologic units can be seen in Figure 8.9.

The Apollo basin formed on the NE portion of SPA basin rim during the pre-Nectarian/Nectarian period. It is characterized by a complex peak-ring basin structure (NpNbm) and hummocky terrain (NpNbh) interpreted as impact melt in the inner peak-ring and between the inner-peak ring and the outer ring. Immediately following subsequent craters (NpNc) overprinted the landscape of the Apollo basin and these craters usually are the most degraded large craters without ejecta deposits.

In the Imbrian period, light plains deposits (Ip), some of which originated from the Orientale impact event (Meyer et al., 2018), formed on the top of various older geologic units and are preserved in low-topographic areas. The surface of the light plain deposits is highly cratered. The formation of Ip unit was succeeded by the emplacement of the southern ($\mu 3.10 \pm 0.31 / -0.60$ Gyr) and the central ($\mu 2.42 \pm 0.67 / -0.81$ Gyr) mare provinces (Im). AMAs of mare provinces are in fairly good agreement with those of Pasckert et al. (2018), however, the AMAs derived in our study are uncertain due to the relatively small size of the crater count areas (van der Bogert et al., 2015), thus AMA must be taken with caution. Additionally, a well-preserved large crater (e.g. Imbrian-aged Dryden crater (Ic), Figure 8.2) with complex morphology and subdued ejecta deposit overlies the pre-Nectarian/Nectarian craters, and possibly is older than the central mare deposit. The visible ejecta of Dryden crater stratigraphically does not overlap with the mare deposit, either because of the ejecta deposit is rather degraded and the stratigraphic relationship is very uncertain or because Dryden crater was formed before the mare flooded the central area of Apollo basin. We favor the latter hypothesis.

The younger Eratosthenian craters (Ec) have sharp-crested rim morphologies without prominent ejecta rays, and the youngest Copernican craters (Cc) have crisp well-preserved impact morphologies with prominent ejecta rays and secondary craters. These Cc units overlay or cut across all other geologic units. Both mare provinces are affected by relatively larger Copernican craters: The southern mare deposit is probably affected by the ejecta of an unnamed crater ($\mu 924 \pm 57 / -58$ Myr) in the NE quadrangle of the mapping area (Figure 8.10.), where the ejecta deposit is poorly visible and cannot be mapped confidently. Similarly, the central mare province is superposed by a well-preserved ejecta deposit originating from an unnamed crater on top of Resnik crater ($\mu 861 \pm 54$ Myr) (Figure 8.10).

All proposed landing sites are on top of mare deposit (Figure 8.9). ROI 1 includes diverse geologic materials: Imbrian mare material (Im), Copernican-aged ejecta (Cc), which might contain SPA and Apollo impact melt breccia, as well as remnants of pre-Nectarian/Nectarian hummocky basin material (NpNbh). The NpNbh has a putative impact melt origin (Wilhelms et al., 1979), and forms “islands” (kipukas) within the 10 km exploration zone (Figure 8.9/a). ROI 2 lies on Imbrian mare deposit (Im) where the ejecta deposits from different Copernican-aged ejecta (Cc) from NE and SW directions merge at the SW part of the 10 km exploration zone (Figure 8.9/b). Moreover, these Copernican-aged ejecta deposits could have potentially excavated SPA and Apollo impact melt materials as is visible in Figure 8.12. ROI 3 is located on the Imbrian mare deposit unit (Im) in the vicinity of the outer ring of Apollo basin, namely to the pre-Nectarian/Nectarian basin-massif material unit (NpNbm) (Figure 8.9/c). This has a similar geologic setting to the Apollo 17 landing site, which was located at Taurus-Littrow valley on the eastern margin of Mare Serenitatis surrounded by the remnant of Serenitatis basin massif.

The following units were described:

(1) Basin-massif materials:

- pre-Nectarian/Nectarian basin-massif material unit (NpNbm): Forms the inner peak-ring massif and outer ring massif of the Apollo basin, originating from uplifted crustal material during basin formation.
- pre-Nectarian/Nectarian hummocky basin material unit (NpNbh): Forms the residual impact melt of basin formation.

(2) Plains-forming materials:

- Imbrian mare material unit (Im): Dark albedo unit of volcanic origin.
- Imbrian light plain material unit (Ip): Light albedo, highly cratered unit of impact ejecta origin from remote craters and basins. This unit overlies various older geologic units and is preserved in low-topographic areas.

(3) Impact crater materials: Identification of possible age is based on degradation state of the impact morphology.

- Copernican craters (Cc) have crisp well-preserved impact morphologies with prominent ejecta rays and secondary craters, and overlay or cut across all other geologic units.
- Eratosthenian craters (Ec) have sharp-crested rim morphologies without prominent ejecta rays.
- Imbrian craters (Ic) are well-preserved large craters with complex morphologies and subdued ejecta deposit.
- Pre-Nectarian and Nectarian craters (NpNc) are heavily degraded large craters without obvious ejecta deposit.

8. CHARACTERIZATION OF HIGH-PRIORITY LANDING SITES IN THE APOLLO BASIN, MOON

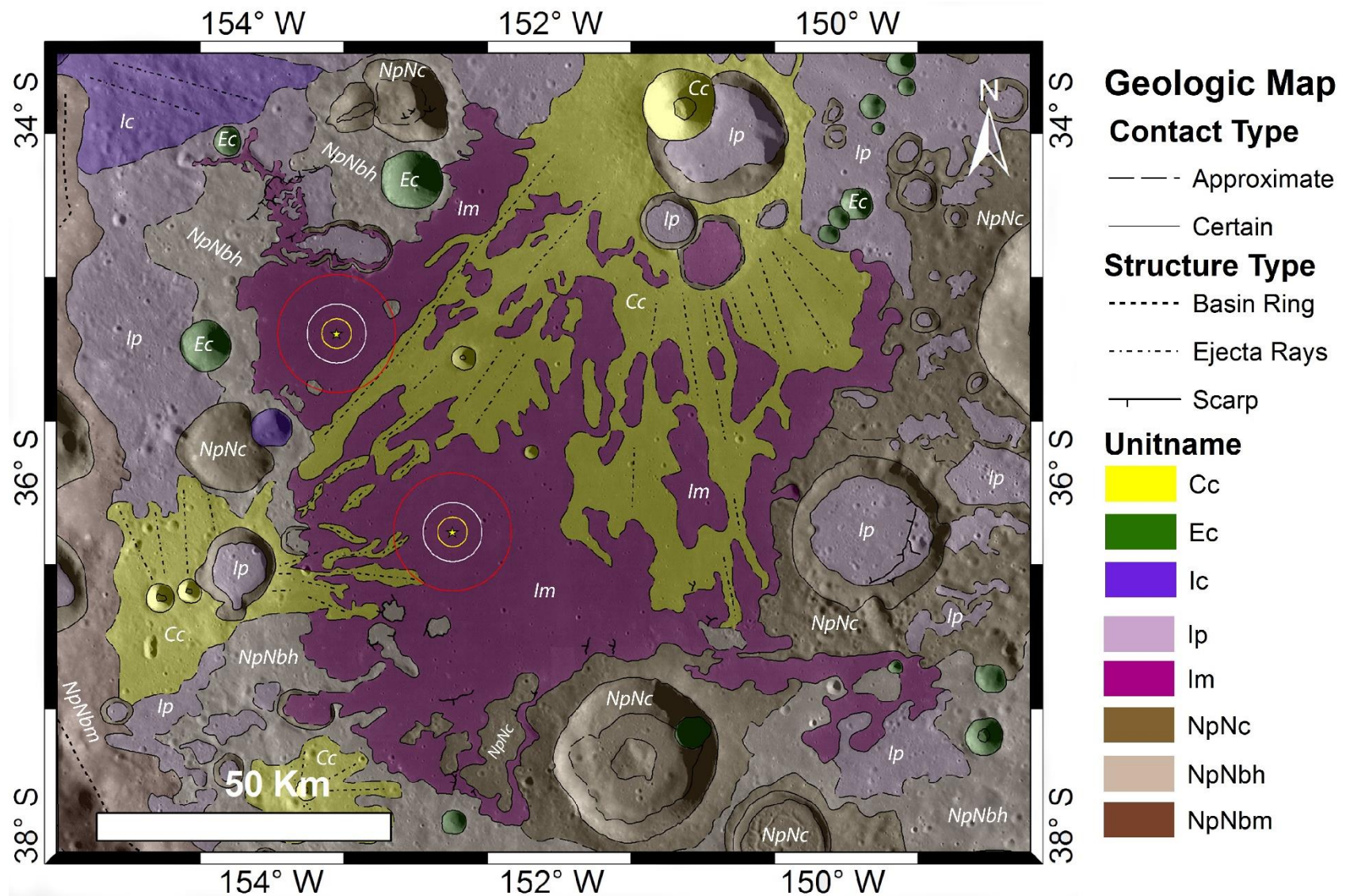


Figure 8.7: Geologic map of the central mare province of the Apollo basin with ROI 1 (upper) and ROI 2 (bottom) at 1:50,000 mapping scale. The circles indicate exploration zones of 2.5 km, 5 km, and 10 km from the proposed landing sites.

8. CHARACTERIZATION OF HIGH-PRIORITY LANDING SITES IN THE APOLLO BASIN, MOON

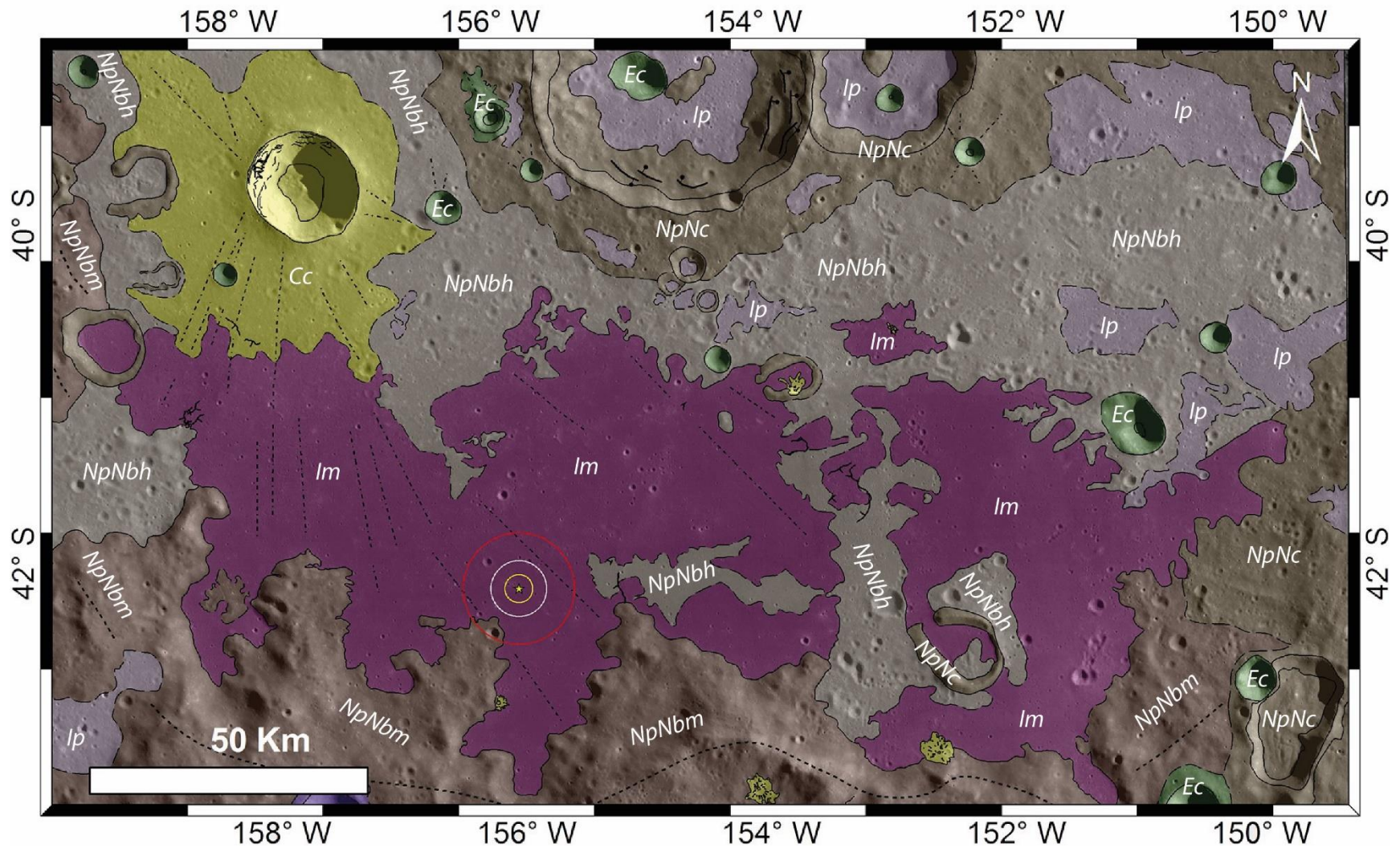


Figure 8.8: Geologic map of the southern mare province of the Apollo basin with ROI 3 at 1:50,000 mapping scale. The circles indicate exploration zones of 2.5 km, 5 km, and 10 km from the proposed landing site. Same legend as at Figure 8.7.

8. CHARACTERIZATION OF HIGH-PRIORITY LANDING SITES IN THE APOLLO BASIN, MOON

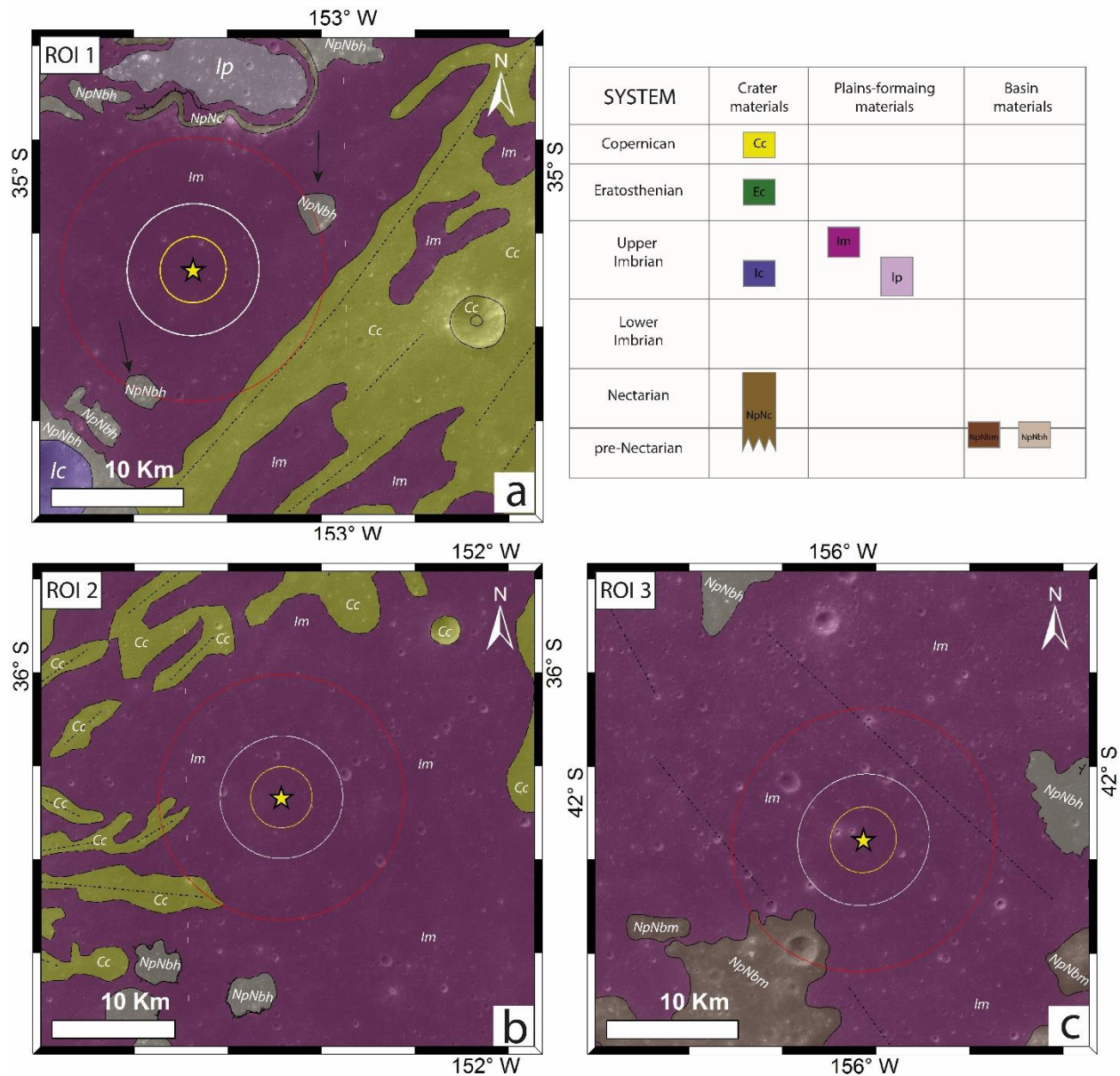


Figure 8.9: Geologic maps of ROIs with a correlation chart of the geologic units. The circles indicate exploration zones of 2.5 km, 5 km, and 10 km from the proposed landing site. a) ROI 1 has access to study Imbrian mare material (Im), Copernican-aged ejecta (Cc) which might excavate SPA and Apollo impact melt from the subsurface, as well as remnants of pre-Nectarian/Nectarian hummocky basin material (NpNbh) with putative impact melt origin (black arrows). b) ROI 2 could sample different Copernican-aged ejecta rays (Cc), potential SPA and Apollo impact melt materials, and Imbrian mare deposit. c) ROI 3 could investigate Imbrian mare deposit as well as pre-Nectarian/Nectarian basin-massif material (NpNbm).

8. CHARACTERIZATION OF HIGH-PRIORITY LANDING SITES IN THE APOLLO BASIN, MOON

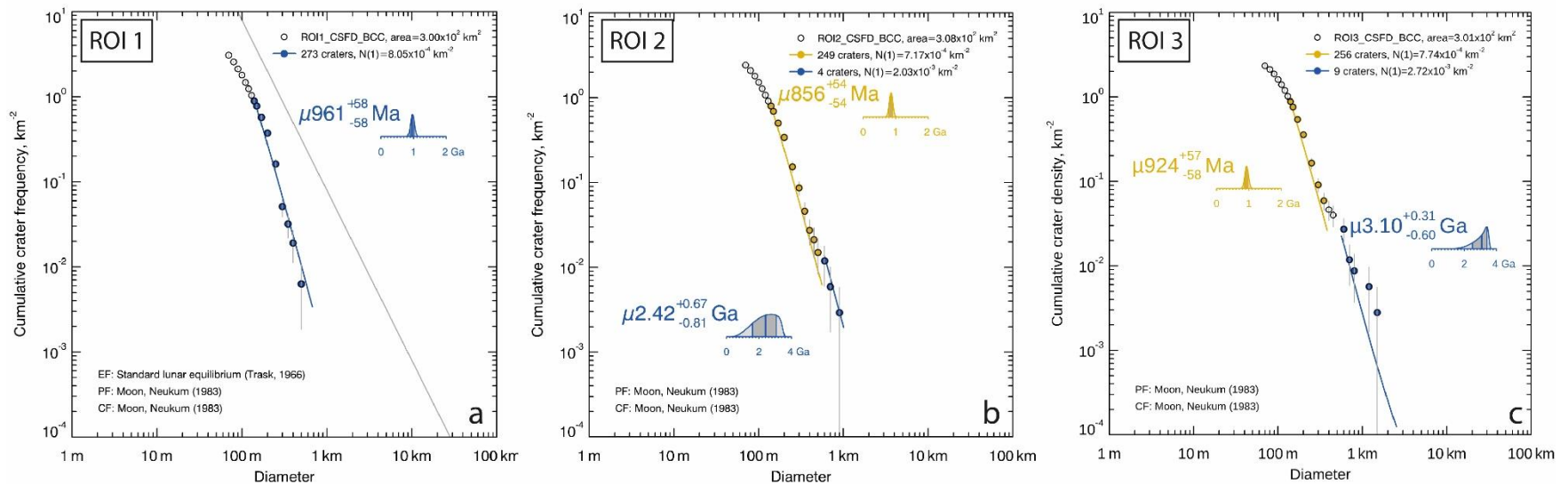


Figure 8.10: Crater size-frequency distribution and absolute model age of ROIs. a) AMA of ROI 1 might show a resurfacing age ($\mu 961 \pm 58$ Myr) originating from an unnamed Copernican-aged crater overlying the Resnik crater, rather than the mare deposit underneath. b) For ROI 2, a similar resurfacing age of $\mu 861 \pm 54$ Myr and a formation age of the mare deposit around $\mu 2.42^{+0.67/-0.81}$ Gyr have been derived. c) The formation age of the southern mare province is around $\mu 3.10^{+0.31/-0.60}$ Gyr, while the resurfacing age ($\mu 924^{+57/-58}$ Myr) might represent the formation of a large, unnamed Copernican-aged crater NW from the southern mare province.

8.5.2.2. Regolith Thickness and Subsurface Stratigraphy

The lunar surface is covered by a fine-grained regolith material, which is the result of impact gardening processes. In our work, we have found that the average regolith thickness varies from 4.6 m up to 8.3 m (Table 8.3), which is in good agreement with previous studies (Oberbeck & Quaide, 1968; Fa et al., 2014; Huang et al., 2018; Fu et al., 2020). We estimated regolith thickness by measuring the depth-to-diameter ratio of small concentric craters (CC) and interpolated the values over the 10 km exploration zone (Figure 8.11). However, based on their hydrocode simulations of CC craters, Prieur et al. (2018) suggest that (1) smaller strength discontinuities such as impact melt sheets within the regolith/target, and (2) low-impact velocities are sufficient to form CC. If that is the case, the estimated regolith thicknesses must be taken with caution, i.e., the values could indicate only a minimum regolith thickness.

Table 8.3: Regolith thickness (m) estimated using concentric craters (CC) and the equation from Oberbeck & Quaide (1968).

| | ROI 1 | ROI 2 | ROI 3 |
|-------------|-------|-------|-------|
| Min. (m) | 1.1 | 1.2 | 1.2 |
| Max. (m) | 24 | 18.5 | 19.9 |
| Average (m) | 5.7 | 8.3 | 4.6 |
| STDV | 3.9 | 3.2 | 3.3 |

To estimate local stratigraphy, we analyzed the mineralogy exposed by impact crater ejecta located on mare floor, where smaller craters expose shallow stratigraphy, while larger craters excavate deeper stratigraphy. The smaller craters show low-calcium pyroxene (LPC) signatures (green/yellow on Figure 8.12/a, b), and larger craters (e.g. Crater 1: 4491 m in diameter, 479 m depth; Crater 2: 2196 m in diameter, 223 m depth) expose a non-mare mineralogy (Figure 8.12/b, c).

We propose the following subsurface stratigraphy at ROI1 (Figure 8.13): The fine-grained regolith constitutes the upper part of the stratigraphy and on average is > 6 m in thick. Beneath that layer, the mare deposit could be reached between 6 and 11 m. This is an average depth exhibited by small craters of low-calcium pyroxene (LCP) (green/yellow on Figure 8.12/a, b). The two larger craters (Crater 1 and Crater 2) show non-mare materials, possibly impact melt-rich deposit on top of the mare province. Taking the excavation depth of Crater 1 and Crater 2 into account, the mare deposit is around ~ 200 m thick. Similarly, non-mare lithology exposed by the ejecta of large, unnamed Copernican-aged crater overlying Resnik crater at the NE part of the central mare province (Figure 8.7), which might have excavated the Apollo hummocky basin material (NpNbh) too.

8. CHARACTERIZATION OF HIGH-PRIORITY LANDING SITES IN THE APOLLO BASIN, MOON

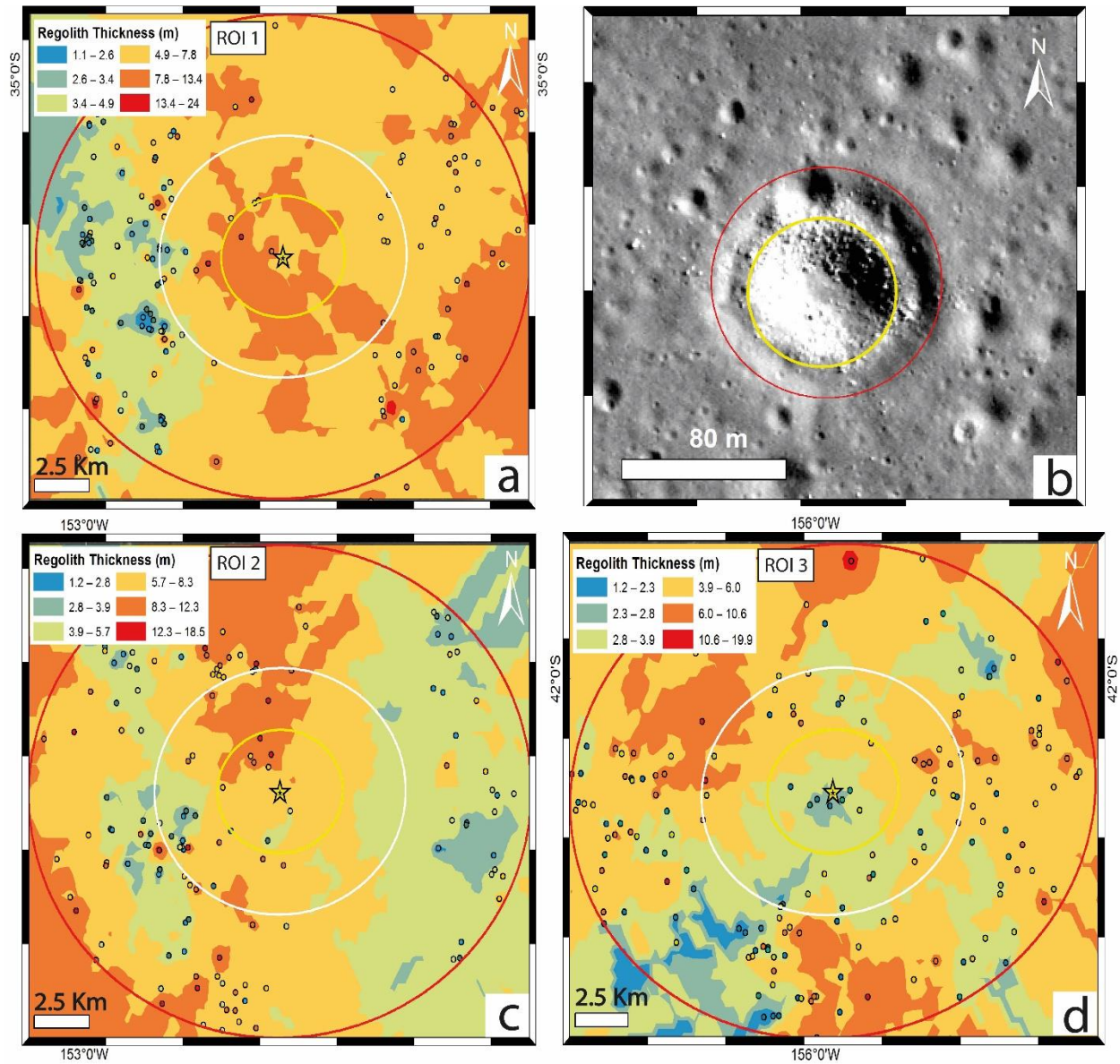


Figure 8.11: Map of regolith thickness estimation using the equation from Oberbeck & Quaide (1968). First, the data have been derived by measuring the depth-to-diameter ratio of concentric craters (panel b) using LROC NAC 1 m/pix data and second, the kriging technique has been applied to interpolate the results to the larger area. Points mark the measured values. The circles indicate exploration zone of 2.5 km, 5 km, and 10 km from the proposed landing site.

8. CHARACTERIZATION OF HIGH-PRIORITY LANDING SITES IN THE APOLLO BASIN, MOON

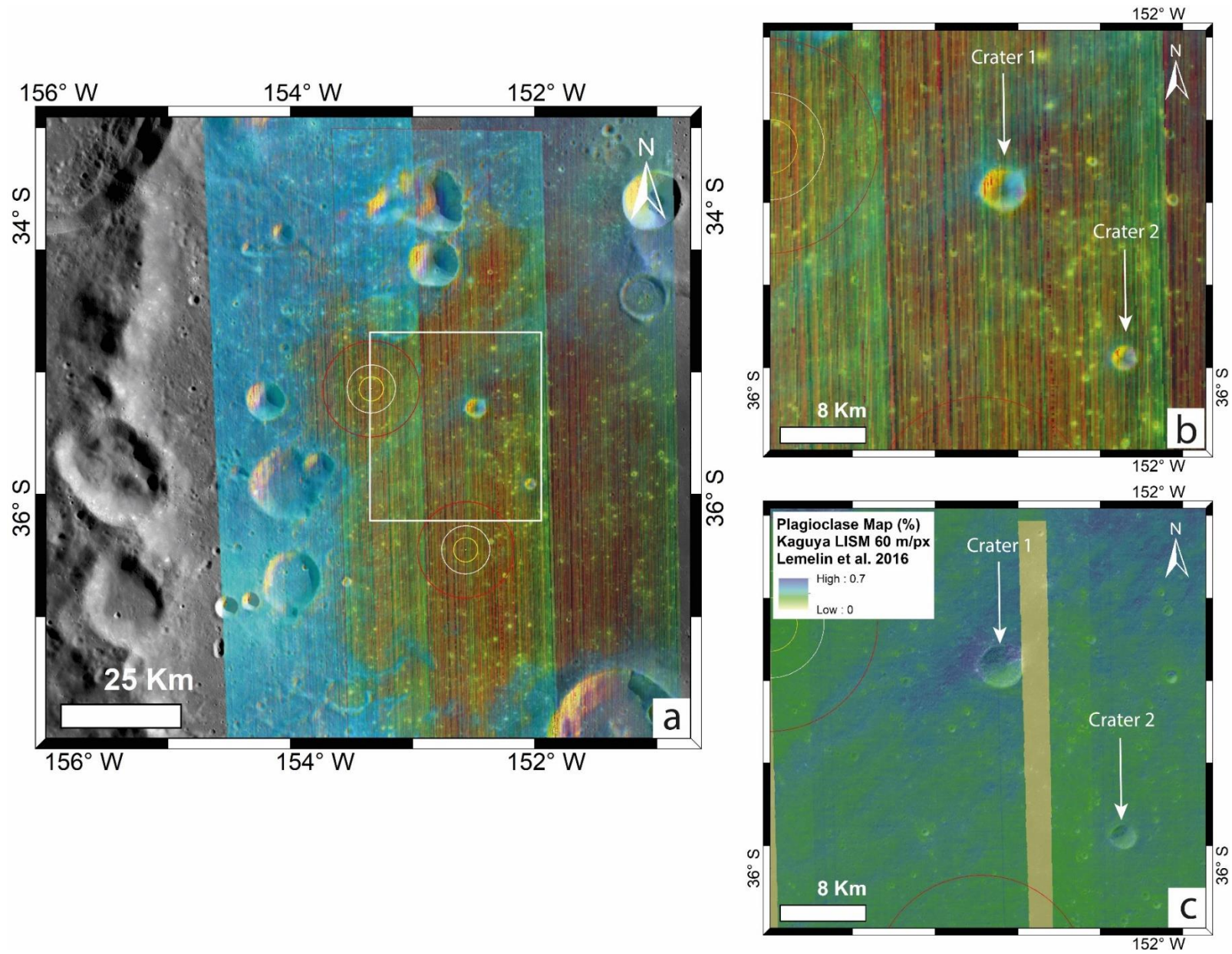


Figure 8.12: Chandrayaan M^3 pyroxene and Kaguya MI plagioclase spectral maps superposed on LROC WAC mosaic showing the central mare province region in the Apollo basin. Small green/yellow craters exhibit LCP mineralogy representing basaltic material (panel a and b). The ejecta of a large, unnamed Copernican-aged crater overlying Resnik crater is showing similar mineralogy than the hummocky basin material unit (NpNbh) (blue color), which crater might excavate non-mare material from the subsurface. The origin of this material might be impact melt from SPA and the Apollo basins. Additionally, panel b and c show two small craters (Crater 1: 4491 m in diameter and 479 m deep; Crater 2: 2196 m in diameter and 223 m deep) marked with white arrows, which indicate exhumation of non-mare material (blue color) as well. Panel b shows results of M^3 pyroxene map, while panel c represents Kaguya MI plagioclase map.

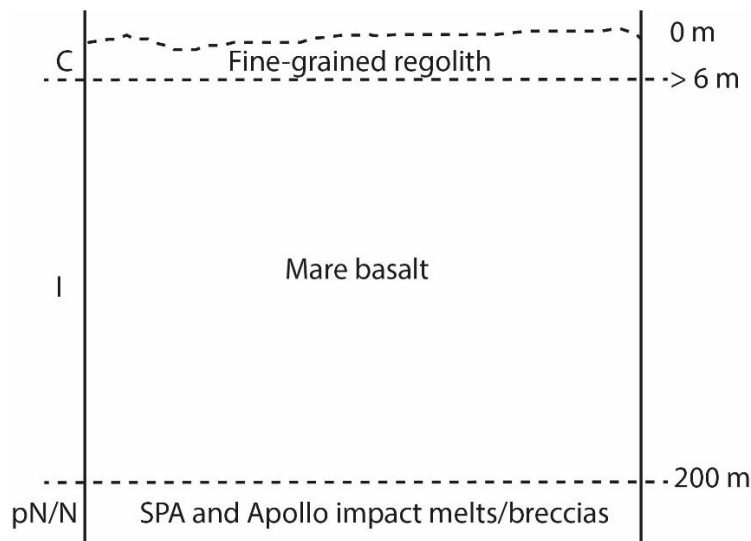


Figure 8.13: Simplified subsurface stratigraphy at ROI 1.

8.5.2.3. In Situ Resource Utilization (ISRU) Potential

In Situ Resource Utilization is important for sustainable human presence on the lunar surface and the Apollo basin has some of the highest FeO and TiO₂ contents inside the SPA basin (Figure 8.14, Figure 8.15, Table 8.4., and Table 8.5). ROI 2 has the highest average and maximum FeO contents, while ROI 1 has the lowest average and minimum FeO values. ROI 3 has the highest average and maximum TiO₂ contents, while ROI 1 has the lowest average and minimum TiO₂ values (Table 8.4).

8. CHARACTERIZATION OF HIGH-PRIORITY LANDING SITES IN THE APOLLO BASIN, MOON

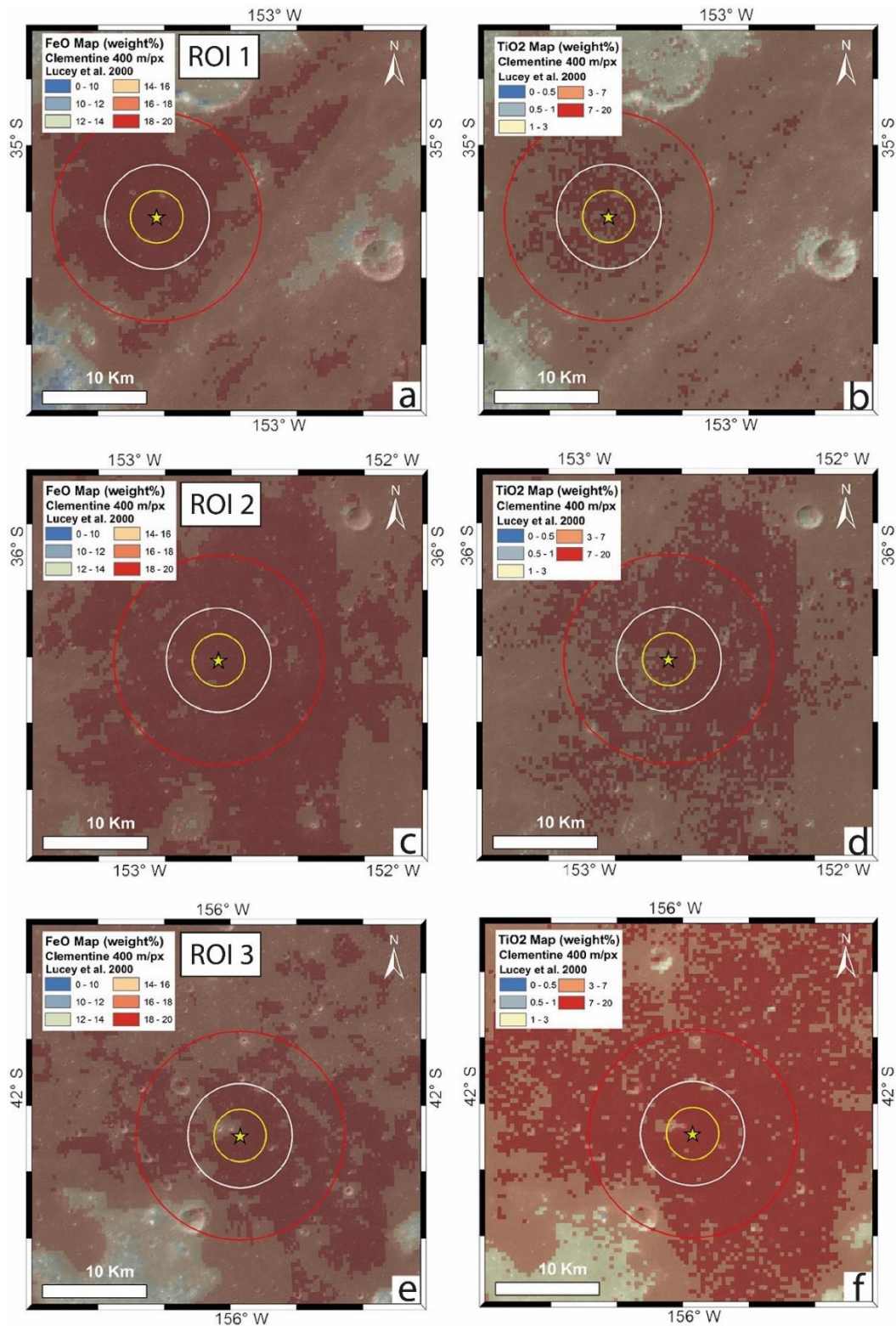


Figure 8.14: FeO and TiO₂ contents derived from Clementine 400 m/px data. a-b, c-d, e-f) FeO and TiO₂ contents of ROI 1, 2, and 3, respectively. The circles indicate exploration zones of 2.5 km, 5 km, and 10 km from the proposed landing site.

8. CHARACTERIZATION OF HIGH-PRIORITY LANDING SITES IN THE APOLLO BASIN, MOON

Table 8.4: FeO and TiO₂ weight percent (wt%) of mare deposits based on 400 m/pix Clementine data.

| | ROI 1 | | ROI 2 | | ROI 3 | |
|-------------|-------|------------------|-------|------------------|-------|------------------|
| | FeO | TiO ₂ | FeO | TiO ₂ | FeO | TiO ₂ |
| Min. wt% | 16.15 | 3.51 | 17.65 | 4.82 | 17.39 | 4.05 |
| Max. wt% | 18.58 | 7.74 | 18.80 | 8.77 | 18.58 | 9.59 |
| Average wt% | 17.90 | 6.35 | 18.33 | 7.18 | 18.18 | 8.09 |
| Stand. Dev. | 0.59 | 1.01 | 0.26 | 0.82 | 0.27 | 0.9 |

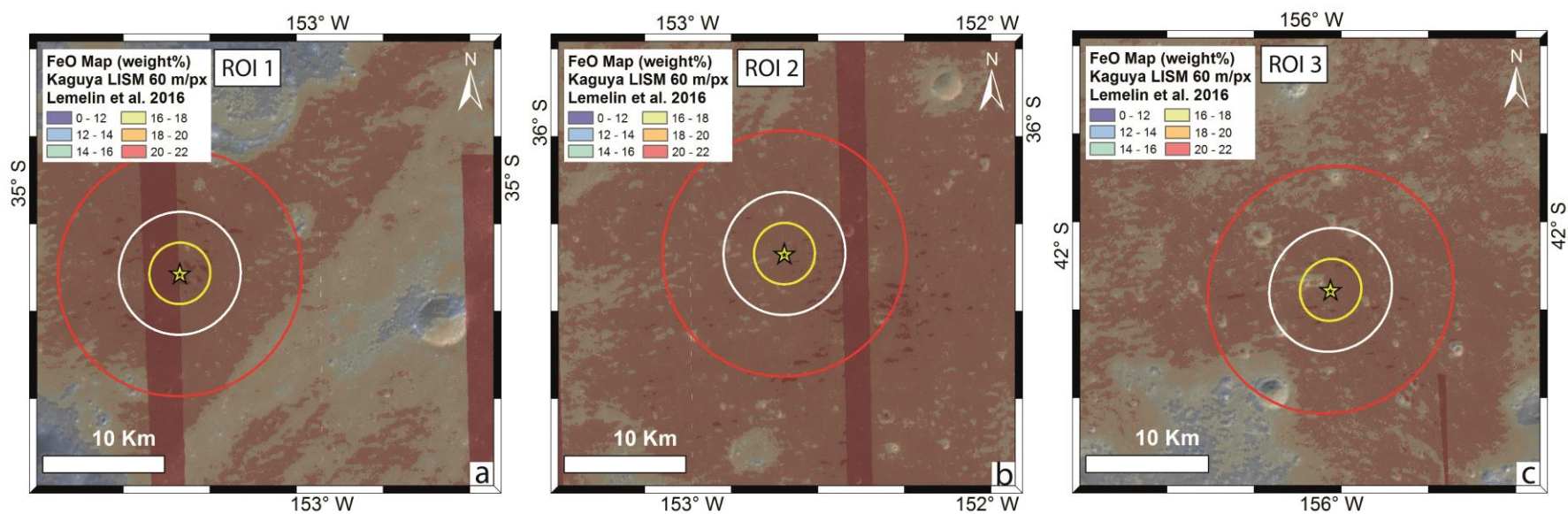


Figure 8.15: FeO abundances of mare deposits derived from Kaguya MI 60 m/pix data. Red, continuous stripes indicate no data.

Table 8.5: FeO weight percent (wt%) of mare deposits based on Kaguya MI 60 m/pix global dataset.

| | ROI 1 | ROI 2 | ROI 3 |
|-------------|-------|-------|-------|
| Min. | 14.09 | 16.59 | 17.41 |
| Max. | 20.54 | 20.15 | 20.39 |
| Average | 18.41 | 18.78 | 18.90 |
| Stand. Dev. | 1.2 | 0.71 | 0.71 |

8.6. Discussion

Figure 8.16 provides an overview of NRC (2007) goals that could be addressed by a robotic exploration mission with lander and rover capabilities. Altogether, we determined 12 plus 3 scientific goals of NRC (2007) that could be or may be addressed, respectively. A suggested payload would consist at least of a Ground Penetrating Radar (GPR) – for lateral and vertical subsurface structure observations, a GigaPan camera – which provides oblique, color images at gigapixel resolution for panoramic and detailed visualization of geologic features of interest, and a Laser Induced Breakdown Spectrometer (LIBS) – for in-situ chemical analyses. The following NRC (2007) goals could be addressed by a GPR: 3d, 3e, 5a, 5c, 6a, 6c, 6d, 7b,7c, a GigaPan: 1e, 2a, 3d, 3e, 6a, 6b, 6c, and a LIBS: 2b, 3a, 3c, 3d, 5a, 5c, 6a, 6c, 6d, 7d.

| NRC Concept/ Goal | a | b | c | d | e |
|--|--------------------------------------|---------------------------------------|--|-------------------------------------|--|
| 1. Bombardment history of the inner solar system | Test cataclysm hypothesis | Age of South Pole-Aitken | Establish absolute chronology | Recent impact flux | Secondary craters |
| 2. Structure and composition of lunar interior | Thickness/variability of lunar crust | Stratification of mantle | Size, composition, state of core | Thermal state of interior | N/A |
| 3. Diversity of lunar crustal rocks | Differentiation products | Age, distribution, origin of rocks | Composition of lower crust | Complexity of lunar crust | Extent/structure of megaregolith |
| 4. Lunar poles and volatiles | State and distribution of volatiles | Source of volatiles | Transport, alteration, loss, processes | Properties of polar regolith | Polar regolith and ancient solar environment |
| 5. Lunar volcanism | Origin/variability of basalts | Age of mare basalts | Range/extent of pyroclastic deposits | Lunar volcanic flux | N/A |
| 6. Impact processes | Melt sheet differentiation | Structure of multi-ring impact basins | Crater formation | Mixing of local and ejecta material | N/A |
| 7. Regolith processes | Characterize ancient regolith | Physical properties of regolith | Regolith modification processes | Rare minerals in regolith | N/A |

Addressed
 Not addressed
 May be addressed

Figure 8.16: NRC (2007) science concepts and goals in case of robotic exploration mission with rover and lander assets to the lunar surface. The highest ranked NRC (2007) science concepts and goals cannot be accomplished without sample return capability.

Figure 8.17 gives a summary of NRC (2007) goals that could be or may be addressed by a robotic exploration mission with lander and rover assets and additional sample return capability. The EL3 system is ESA's technology development, which will be capable of delivering up to 1700 kg of cargo to the Moon, including deploying a rover and retrieving 15 kg of samples from the surface, bringing them back to Earth for analysis. Altogether,

we identified 18 plus 5 scientific goals of NRC (2007) that could be targeted by a sample return mission to the Apollo basin. Almost all NRC (2007) concepts would be addressed. Collecting impact melt-bearing samples could help to constrain the age of one of the youngest impact basins within SPA basin and possibly the age of SPA as well. Impact melt on the mare provinces might be excavated by younger impact craters which could verify the hypothesis of impact melt sheet differentiation without landing on a rough, remnant impact melt sheet.

Determining the duration of the lunar basin-forming epoch and calibrating the lunar chronology are high priorities in lunar science. The Apollo basin offers the opportunity to sample a previously unsampled geochemical terrain on the Moon. This inner peak-ring basin formed at the boundary of SPA and the anorthositic highlands and provides a cross-section to constrain magma ocean crystallization processes and understand the thickness and variability of the lunar crust and mantle.

| NRC Concept/ Goal | a | b | c | d | e |
|--|--------------------------------------|---------------------------------------|--|-------------------------------------|--|
| 1. Bombardment history of the inner solar system | Test cataclysm hypothesis | Age of South Pole-Aitken | Establish absolute chronology | Recent impact flux | Secondary craters |
| 2. Structure and composition of lunar interior | Thickness/variability of lunar crust | Stratification of mantle | Size, composition, state of core | Thermal state of interior | N/A |
| 3. Diversity of lunar crustal rocks | Differentiation products | Age, distribution, origin of rocks | Composition of lower crust | Complexity of lunar crust | Extent/structure of megaregolith |
| 4. Lunar poles and volatiles | State and distribution of volatiles | Source of volatiles | Transport, alteration, loss, processes | Properties of polar regolith | Polar regolith and ancient solar environment |
| 5. Lunar volcanism | Origin/variability of basalts | Age of mare basalts | Range/extent of pyroclastic deposits | Lunar volcanic flux | N/A |
| 6. Impact processes | Melt sheet differentiation | Structure of multi-ring impact basins | Crater formation | Mixing of local and ejecta material | N/A |
| 7. Regolith processes | Characterize ancient regolith | Physical properties of regolith | Regolith modification processes | Rare minerals in regolith | N/A |

Addressed
 Not addressed
 May be addressed

Figure 8.17: NRC (2007) science concepts and goals in case of robotic exploration mission to the lunar surface with a rover, lander, and sample return capability. The highest ranked science concepts and goals can be achieved with sample return capability.

8.7. Conclusions

In this study, we analyzed the scientific potential for two future robotic exploration mission scenarios at three Regions of Interest (ROI) in the Apollo basin: (1) with lander and rover assets, and (2) with additional sample return capability. The proposed landing sites of the selected three ROI could fulfill the general engineering constraints, address several NRC (2007) scientific objectives, and show high ISRU potential in the Apollo basin. We conducted a series of data analyses. We investigated the topography, slopes, crater density, rock abundance, geology and mineralogy, and studied the subsurface stratigraphy.

The studied ROIs are generally smooth with average slopes of $< 5^\circ$ at baselines of 60 m with the exception of steeper slopes ($> 25^\circ$) associated with fresh craters. High local rock abundances still could allow for good traversability. The proposed ROIs reflect geologically complex areas, where mare deposits are covered by younger, Copernican-aged ejecta material with various thicknesses and distributions. These ejecta materials have low FeO and TiO₂ contents representing material beneath the mare deposit. The origin of that material could be SPA and Apollo impact melt, which is the key sample type to address the lunar cataclysm hypothesis. In addition, the mare deposits have high ISRU potential with relatively high FeO and TiO₂ contents ranging from 14-20 wt% and 3-5 wt%, respectively.

In-situ observations with advanced rover and lander payload capabilities can help to address six of seven NRC concepts (1-3, 5-7) as well as Campaigns 1 and 5 of the European Space Agency's Strategy for Science at the Moon (ESA, 2019). However, there is a great loss in science benefit without the sample return capability. The highest ranked NRC (2007) concept and goals are to test the cataclysm hypothesis and it would greatly benefit from a sample return mission scenario.

Acknowledgements

CO was funded by the Deutsche Forschungsgemeinschaft (SFB-TRR 170, subproject A3). CO is thankful for being hosted during the initial phase of this study at WWU in Münster.

CHAPTER 9

CONCLUSIONS

This Ph.D. thesis represents a cumulative dissertation and contains three published, peer-reviewed articles, one manuscript under preparation to a peer-reviewed journal, and one conference abstract. The publications presented in the previous chapters (5-8) contain their own summaries highlighting the conclusions of the specific article concerning a broader context. Chapters 5 and 6 are related to the re-investigation of the crater and impactor population using a new crater-size frequency distribution (CSFD) technique, the buffered non-sparseness correction (BNSC) method on the Moon and Mercury. Chapters 7 and 8 focus on the science potential of landing sites in the South Pole-Aitken (SPA) basin, which remains a high priority candidate for exploration and sample return missions. To help further constrain the lunar cratering chronology, sample return missions from various well preserved key locations inside the SPA basin (Kring & Durda, 2012; Potts et al., 2015; Steenstra et al., 2016; Cohen et al., 2018; **Allender et al., 2019**) should be visited by robotic and human exploration missions. This Ph.D. work uses available orbital remote sensing datasets, primarily visible camera and topographic datasets as well as various spectral datasets. The goal of this work was to test various accretion models and use the BNSC technique to re-evaluate the shape of the production function (PF) and infer potential impactor populations that bombarded the inner Solar System. The ongoing discussion about a time-changing PF has remained one of the major lunar research questions, which cannot be resolved in half a century. **The main research questions of this thesis related to early bombardment history of the inner Solar System are: (1) What is the timing, and nature of basin-forming impacts on the Moon and other terrestrial planets? (2) What is the origin of late-accreted materials? (3) Where are the key landing sites for future human and robotic exploration missions and how many National Research Council (NRC, 2007) objectives could be addressed there?** In order to achieve these goals, the necessary steps have been successfully completed. The application of the BNSC technique to analyze the CSFDs of 30 lunar and 29 mercurian basins was successful. The BNSC technique proved to make a significant difference in accounting crater densities on highly cratered surfaces, and corrects for crater obliteration of smaller diameter craters by larger craters and their ejecta deposits. The increase of the smaller crater density in the CSFD compared to the buffered crater counting (BCC) technique revealed the effect and scale of crater obliteration, and once was corrected allowed a larger range of the CSFD to be used to analyze the relative ages of the lunar and mercurian basins, as well as shed light on the characteristics of the impactor population. Before this sophisticated CSFD measurement approach was implemented, improvement of the measurement of the CSFD of smaller diameter craters on heavily cratered surfaces was lacking. Using this novel technique, a better understanding of the crater

populations of large lunar and mercurian basins was gained. Moreover, a relative basin sequence based on both crater frequencies and absolute model ages (AMA) proved to be generally in good agreement with the observed relative basin stratigraphy. Major conclusions related to the scientific objectives are:

O1. Understanding the history of cratering populations on the lunar and mercurian surface.

- *Re-examine the population of large impact basins ($D \geq 300$ km) on the Moon and Mercury using Geographic Information System (GIS).*
 - The lunar basin catalogue, which was compiled by Fassett et al. (2012b), has been successfully confirmed.
 - Altogether, 94 basins have been identified and verified on the surface of Mercury, 1.7× times more certain and probable basins than in previous work (Fassett et al., 2012a). The new catalogue comprises 49 certain, 31 probable, and 14 tentative basins.
 - 30 new basins and 17 basins from the list of unverified basins from Fassett et al. (2012a) have been discovered and verified, respectively.
- *Map the crater populations related to respective basins on the Moon and Mercury.*
 - The crater measurements and geologic mapping from Fassett et al. (2012b) on the Moon have been used for the direct comparison of the BNSC-corrected CSFDs with their results. All impact craters with diameters ≥ 20 km have been used and additional craters beyond that database were included from younger surfaces on the Moon (Fassett et al., 2012b).
 - The CraterTools extension in ArcMap (Kneissl et al., 2011) has been used to map the CSFDs for basins with diameters ≥ 25 km on Mercury.

O2. Investigating the origin of impactors and whether the impactor population size-frequency distribution changed over time and if so, when.

- *Analyze the shape of the summed CSFDs of basins from the same chronostratigraphic period on the Moon and Mercury using a relative plot.*
 - The apparent difference in the shape of the CSFD of the oldest lunar surfaces in comparison to the younger surfaces using the BCC technique have been explained by the incomplete accounting for the smallest craters on heavily or non-sparsely cratered old surfaces.
 - In contrast to previous studies (Head et al., 2010; Fassett et al., 2012b), which show a change in the shape of the CSFDs for the lunar periods, the shape of the Pre-Nectarian-aged basins (excluding SPA), Nectarian-aged basins and Imbrian-aged basins using the BNSC technique (30 basins) are not statistically distinguishable, the results indicated that only

one impactor population contributed to the lunar cratering record. This scenario involves a collisionally-evolved impactor population, contributing to the cratering record within the inner Solar System, where the crater PF remained unchanged over time (Neukum, 1983).

- However, the results did not completely exclude the impact spike scenario, where impactors could be originated by the excitement of the same source population, or alternatively a collisionally evolved population with similar SFD.
- Similarly to the lunar study, the summed CSFDs of the Pre-Tolstojan-aged basins and Tolstojan-aged basins on Mercury using the BNSC technique (29 basins) showed no evidence for a change in the SFD of the impacting population, thus the results are consistent with a single impactor population that bombarded Mercury's surface. This finding as well as the results for the Moon support the hypothesis of only one impactor population that bombarded the inner Solar System.

O3. Analyzing the influence of non-sparseness correction measurement technique on the CSFDs on the Moon and Mercury.

- *Derive the CSFDs using 2 different approaches: (1) Buffered Crater Counting (BCC) – as done by previous studies, and the new approach (2) Buffered Non-Sparseness Correction (BNSC). Derive the $N(20)$, i.e., the frequency of craters ≥ 20 km on the Moon, and $N(25)$ on Mercury and normalize these to an area of 10^6 km².*
 - The crater densities of 30 key lunar basins and 74 mercurian basins have been derived using 2 different CSFD techniques: BCC and BNSC.
 - CSFDs of 29 basins using the BNSC technique on Mercury have been obtained. In most of the cases, the BNSC approach was not successful, because the basins are either fully or partially covered by volcanic plains of various thicknesses. BNSC corrects for crater obliteration, but not for other geologic processes.
 - The BNSC correction typically leads to an increase of the obtained smaller crater densities when compared to the BCC technique. The application of BNSC increased the obtained $N(20)$ and $N(25)$ values by an average of 24% and 25% compared to BCC on the Moon and Mercury, respectively.
 - The spatial density of basins with $D \geq 300$ km and $D \geq 500$ km per 10^6 km² are an $N(300)_{\text{Moon}}$ of 0.94 ± 0.16 and an $N(500)_{\text{Moon}}$ of 0.55 ± 0.12 . In contrast to a previous study (Fassett et al., 2012a), the basins have a slightly higher $N(300)$ density of 1.07 ± 0.12 on Mercury than on the Moon. The similar $N(500)$ basin density of 0.44 ± 0.07 on Mercury and the Moon has substantial implications for both planetary surfaces being reached saturation at higher basin sizes.

- Compared to the Moon, the crater densities on Mercury are slightly higher or nearly equivalent at larger crater diameters ($D > 100$ km). Below 100 km in diameter, the CSFD on Mercury falls below the lunar distribution, which is consistent with previous studies (Fassett et al., 2011, 2012a).
- *Compare the results of different techniques applied systematically to different key regions on the Moon and Mercury.*
 - Crater densities derived with the BNSC commonly showed a higher density than with the BCC technique on both planetary surfaces. The differences in measured crater frequencies using BCC and BNSC become systematically larger for older surfaces, such as Pre-Nectarian and Pre-Tolstojan basins, than on younger surfaces, due to the increasing role that crater obliteration plays on older surfaces.
 - The derived Imbrian crater frequencies are slightly lower or the same as using the BNSC. The BNSC technique plays only a minor role for sparsely cratered surfaces.

O4. Studying how large-scale resurfacing events affect the shape of ancient CSFDs and the spatial distribution of basins.

- *Measure the effect of crater obliteration on ancient CSFDs.*
 - The application of the BNSC method to the lunar basin population allowed the correction of crater obliteration on the smaller crater size bins on ancient Pre-Nectarian surfaces, and a clearer view of the Pre-Nectarian CSFD was possible.
- *Study the effect of volcanism and other possible processes on the CSFDs and the spatial distribution of basins.*
 - The geographic distribution of the basins on the surface of Mercury is longitudinally non-uniform. The number of basins is maximal for a hemisphere centered at roughly $120^{\circ}\text{W} \pm 30^{\circ}$, with a corresponding lower frequency in the opposite hemisphere. This distribution could be explained by three major hypotheses: (1) different thermal properties of the crust due to orbital resonances and/or interior geodynamical processes (Vasavada, 1999; Siegler et al., 2013; Miljković et al., 2013; Chapman et al., 2018), (2) differential resurfacing by volcanism (Fassett et al., 2012a; Denevi et al., 2013a), or (3) that the basins on Mercury are spatially random but happened to end up in this configuration.
 - Based on the 2.5 times higher crater production rate above 300 km (Le Feuvre & Wieczorek, 2011) and a factor of 2 greater surface area, a factor of ~ 5 more basins is expected to form on Mercury than on the Moon. Consequently, ~ 180 basins should be observed on Mercury. 94

basins were classified on Mercury, including 80 certain and probable as well as 14 tentative basins. Thus, roughly half of the basin record might be only observed, where basins older than Borealis have been obscured by different processes (e.g., higher impact melt production, volcanism, subsequent impacts, and viscoelastic relaxation of basins) – a finding is in agreement with Marchi et al. (2013).

O5. Analyzing the saturation state of the lunar and mercurian basins.

- *Compared the fraction of the original and the BNSC modified count area sizes for each basin to its $N(20)$ and $N(25)$ crater frequencies on the Moon and Mercury, respectively.*
 - The oldest basins expected to show the highest level of non-sparseness to be close to or at saturation equilibrium. The linear decrease in the effective counting area with increasing $N(X)$ value towards older surfaces was observed on both planetary surfaces, because the level of non-sparseness increases with basin age. However, this linear decrease is steeper on Mercury than on the Moon, which might provide additional evidence for an absence of basins older than Borealis on Mercury.
 - Four Pre-Nectarian basins (Fitzgerald-Jackson, South Pole-Aitken, Amundsen-Ganswindt, and Nubium) and four Pre-Tolstojan basins (Borealis, Matisse-Repin, b96, and b42) have less than 20% of their original count area remaining after the BNSC was applied.

O6. Refining the lunar and mercurian basin stratigraphy and their AMAs.

- *To compare the crater densities of mercurian basins with the lunar basins, rescale the values of $N(20)$ Moon, to $N(X)$ Mercury.*
 - The size of the impactor that forms an impact crater with the diameter of 20 km on the Moon has been estimated to be 1.17 km. The size of the impact crater that would be formed by that same impactor on Mercury has been calculated to be 25 km in diameter, which resulted in $N(25)$ crater frequencies.
- *Derive AMAs of large basins on the Moon and Mercury using different chronology models.*
 - The AMAs of all individual basins on the Moon corresponded better to the lunar PF (Neukum, 1983) over a larger diameter range using BNSC technique, rather than those CSFDs derived with BCC technique.
 - The results derived with the Neukum et al. (2001b) and Le Feuvre & Wieczorek (2011) non-porous chronology models showed a ~ 200 Myr difference between the AMAs on Mercury. However, the systematic

errors in the chronology function could be substantial (> 200 Ma), and errors resulting from resurfacing are also non-negligible (100s of Ma).

- *Study the relationships of the crater densities and AMAs to stratigraphic observations and compare with previous studies.*
 - The AMAs and $N(20)$ values of the lunar basins have been used to rank them in temporal sequence. As a result of the improved CSFDs, the derived $N(20)$ crater frequencies for the individual lunar basins differ from the results from Fassett et al. (2012b), which changes the basin sequence significantly. The differences increase on surfaces with higher crater densities, because these surfaces are where the largest corrections in CSFDs were made using the BNSC technique. Consequently, the changes in basin sequence are more noticeable on older (Pre-Nectarian-aged and Nectarian-aged) than younger (Imbrian-aged) surfaces.
 - To compare $N(20)$ with the basin stratigraphy Freundlich-Sharanov was placed as a Nectarian basin, instead of Pre-Nectarian (Wilhelms, 1987; Fassett et al., 2012b). It has been debated whether Apollo basin belongs to the Pre-Nectarian period (Wilhelms, 1987; Fassett et al., 2012b; Hiesinger et al., 2012b), but according to the AMA it is clearly younger than the Nectaris basin forming event, although the error bars overlap in $N(20)$.
 - The sequence of basins on Mercury has been ranked based on $N(25)$ crater frequencies using the different CSFD techniques. The results showed that $N(25)$ and relative stratigraphy are in good agreement, with only seven basins showing discrepancies. This discrepancies could be explained by (1) extensive volcanic resurfacing, where the crater population of a given basin is highly modified and has “younger” AMA, than the stratigraphically overlaying basin, or (2) large crater(s) affect(s) relatively small counting area, which can produce a higher $N(25)$ value and higher ranking in basin sequence.

07. Characterizing potential landing sites for future human and robotic exploration missions with sample return capability and investigating how these missions could test the cataclysm hypothesis.

- *Study the potential exploration of the South Pole-Aitken basin including the south polar region of the Moon, a region that has not been visited by any human missions, yet exhibits a multitude of scientifically important locations.*
 - A human-assisted robotic mission to the lunar south polar region, including near-side location: the Malapert massif (85.99°S, 2.93°W), and farside locations: the South Pole/Shackleton crater (89.3°S, 130.0°W), Schrödinger basin (75.40°S, 138.77°E), Antoniadi crater (69.7°S, 172.0°W), and the South Pole-Aitken (SPA) basin center (60.0°S, 159.9°W)) can address seven National Research Council (NRC, 2007)

- lunar science concepts, and would be a valuable resource for the early history and evolution of the Solar System.
- Additionally, Apollo basin (36.09°S, 159.69°W) could serve as an excellent landing site for future robotic exploration mission. Prospecting the surface with diverse set of instruments and sampling in the Apollo basin could address six of seven NRC concepts (1-3, 5-7) as well as Campaigns 1 and 5 of the European Space Agency's Strategy for Science at the Moon (ESA, 2019). The Apollo basin showed that landing and operational hazards are manageable and that the terrains are safe for landing and navigation. Moreover, the mare provinces have enhanced FeO and TiO₂ contents, which are among the highest in the SPA basin. Thus, the Apollo basin provides high In Situ Resource Utilization (ISRU) potential.
 - *Explore the feasibility of tele-robotic operation of two Lunar Electric Rovers (LER) between five human lunar landing sites, and identify potential high interest sampling locations en-route using various datasets (e.g. optical, topographical and spectral).*
 - The traverses between the five landing sites seem feasible within the known engineering capabilities of the LER(s) allowing to collect a larger variety of samples.
 - Tele-operating the LERs between the five proposed landing sites along 'science' traverses can enable a significant amount of science to be performed (e.g. involve prospecting for icy volatiles in Cabeus and Amundsen craters) while remaining within the allotted travel time and slope requirements with 30% contingency.
 - *Plan sample collection activities and return traverses for each individual human landing site across key geologic terrains.*
 - Samples collected in the south polar region could address most of the NRC (2007) objectives, depending on the landing site. To address the lunar chronology, a few tens of kilograms of impact-melt bearing samples can be collected using parameters recommended by the Curation and Analysis Planning Team for Extraterrestrial Materials (CAPTEM) in a two times 14-day traverse loop on the Moon.
 - *Design exploration at and between landing sites to address a suite of US National Research Council (NRC, 2007) scientific concepts and goals.*
 - The two times 14-days traverses, sampling stations, recommended samples, collection methods and masses, as well as the NRC (2007) concepts and the individual goals successfully demonstrated the scientific potential of each human landing site.

The South Pole-Aitken basin on the lunar farside, and more specifically the south polar region, has drawn the attention of the biggest space agencies. A new era of space exploration is beginning, with multiple international and commercial partners engaged to return to the Moon. The major task would be to find the key landing sites and study those in more detail by testing different mission concept ideas. This renaissance in lunar exploration will offer new opportunities for science and technology demonstration missions whilst preparing for a human mission to Mars. Surface exploration and sample return from human-assisted robotic exploration of the lunar surface would allow the international community to progress in its vision for larger scale, Mars-forward campaigns and provide valuable insight for future lunar exploration activities.

BIBLIOGRAPHY

Ackiss, S. E., Buczkowski, D. L., Ernst, C. M., McBeck, J. A., & Seelos, K. D. (2015). Knob heights within circum-Caloris geologic units on Mercury: Interpretations of the geologic history of the region. *Earth and Planetary Science Letters*, 430, 542–550, <https://doi.org/10.1016/j.epsl.2015.08.003>

Ahrens, T. J., & O'Keefe, J. D. (1972). Shock melting and vaporization of lunar rocks and minerals. *Earth Moon Planets*, 4, 214–249.

Ahrens, T. J., & O'Keefe, J. D. (1977). Equations of state and impact induced shock-wave attenuation on the moon. *Impact and explosion cratering*. Ed. by D. J. Roddy, R. O. Pepin, and R. B. Merrill, Pergamon Press, New York, 639–656.

Allen, C. C. (2015). Taurus Littrow pyroclastic deposit: high-yield feedstock for lunar oxygen. 46th Lunar and Planetary Science Conference, The Woodlands, TX, Abstract #1140.

Allen, C. C., Greenhagen, B. T., Donaldson Hanna, K. L., & Paige, D. A. (2012). Analysis of lunar pyroclastic deposit FeO abundances by LRO Diviner. *Journal of Geophysical Research*, 117, E00H28, <http://doi:10.1029/2011JE003982>

Allender, E. J., Orgel, C., Almeida, N. V., Cook, J., Ende, J. J., Kamps, O., Mazrouei, S., Slezak, T. J., Soini, A.-J., & Kring, D. A. (2019). Traverses for the ISECG-GER Design Reference Mission for humans on the lunar surface. *Advances in Space Research*, 63, 1, 692–727, <http://doi:10.1016/j.asr.2018.08.032>

Arvidson, R., Boyce, J., Chapman, C., Cintala, M., Fulchignoni, M., Moore, H., Neukum, G., Schultz, P., Soderblom, L., Strom, R., Woronow, A., & Young, R. (1978). Crater analysis techniques working group – Standard techniques for presentation and analysis of crater size-frequency data. NASA Technical Memorandum 79730, Washington, D.C.

Baker, D. M. H., & Head, J. W. (2013). New morphometric measurements of craters and basins on Mercury and the Moon from MESSENGER and LRO altimetry and image data: An observational framework for evaluating models of peak-ring basin formation. *Planetary and Space Science*, 86, 91–116.

Baker, D.M.H., & Head, J.W. (2015). Constraints on the depths of origin of peak rings on the Moon from Moon mineralogy mapper data. *Icarus* 258, 164–180. <http://doi:10.1016/j.icarus.2015.06.013>

Baker, D. M. H., Head, J. W., Fassett, C. I., Kadish, S. J., Smith, D. E., Zuber, M. T., & Neumann, G. A. (2011). The transition from complex crater to peak-ring basin on the Moon: new observations from the lunar orbiter laser altimeter (LOLA) instrument. *Icarus*, 214, 377–393, <http://doi:10.1016/j.icarus.2011.05.030>

Baker, D. M. H., Head, J. W., Schon, S. C., Ernst, C. M., Prockter, L. M., Murchie, S. L., Denevi, B. W., Solomon, S. C., & Strom, R. G. (2011). The transition from complex crater to peak-ring basin on Mercury: new observations from MESSENGER flyby data and constraints on basin-formation models. *Planetary and Space Science*, 59, 15, 1932–1948, <http://dx.doi.org/10.1016/j.pss.2011.05.010>

Baldwin, R. B. (1964). Lunar crater counts. *Astron. J.*, 69, 377–392.

Baldwin, R. B. (1971). On the History of Lunar Impact Cratering: The Absolute Time Scale and the Origin of Planetesimals. *Icarus*, 14, 36–52.

Baldwin, R. B. (1974). On the accretion of the Earth and Moon. *Icarus*, 23, 97–107.

Baldwin, R. B. (2006). Was there ever a Terminal Lunar Cataclysm? With lunar viscosity arguments. *Icarus*, 184, 2, 308–318.

Bandfield, J. L., Ghent, R. R., Vasavada, A. R., Paige, D. A., Lawrence, S. J., and Robinson, M. S. (2011). Lunar surface rock abundance and regolith fines temperatures derived from LRO Diviner Radiometer data. *Journal of Geophysical Research*, 116, E12, E00H02, <http://doi:10.1029/2011JE003866>

Banks, M. E., Xiao, Z., Braden, S. E., Barlow, N. G., Chapman, C. R., Fassett, C. I., & Marchi, S. S. (2017). Revised constraints on absolute age limits for Mercury's Kuiperian and Mansurian stratigraphic systems. *Journal of Geophysical Research*, 122, 5, 1010–1020, <http://doi:10.1002/2016JE005254>

Barber, S., Smith, P., Wright, I., Abernathy, F., & Anand, M. (2017). ProSPA: the science laboratory for the processing and analysis of lunar polar volatiles within PROSPECT. 48th Lunar and Planetary Science Conference, The Woodlands, TX, Abstract #2171.

Barr, A. C., & Citron, R. I. (2011). Scaling of melt production in hypervelocity impacts from high-resolution numerical simulations. *Icarus*, 211, 1, 913–916.

Basilevsky, A. T., Kreslavsky, M. A., Karachevtseva, I. P., & Guskova, E. N. (2014). Morphometry of small impact craters in the Lunokhod-1 and Lunokhod-2 study areas. *Planetary and Space Science*, 92, 77–87.

Becker, K. J., Robinson, M. S., Becker, T., Weller, L. A., Edmundson, K. L., Neumann, G. A., Perry, M. E., & Solomon, S. C. (2016). First global digital elevation model of Mercury. 47th Lunar and Planetary Science Conference, The Woodlands, TX, Abstract #2959.

Borst, A. M., Foing, B. H., Davies, G. R., & Van Westrenen, W. (2012). Surface mineralogy and stratigraphy of the lunar South Pole-Aitken basin determined from Clementine UV/VIS and NIR data. *Planetary and Space Science*, 68, 1, 76–85.

Bottke, W. F., Levison, H. F., Nesvorny, D., & Dones, L. (2007). Can planetesimals left over from terrestrial planet formation produce the lunar Late Heavy Bombardment? *Icarus*, 190, 203–223.

Bottke, W. F., Nolan, M. C., Greenberg, R., & Kolvoord, R. A. (1994). Velocity distribution among colliding asteroids. *Icarus*, 107, 255–268.

Bottke, W. F., Vokrouhlicky, D., Marchi, S., Jackson, A., Levison, H. F., & Swindle, T. (2015). The Earliest Lunar Bombardment Produced by Moon-Forming Impact Ejecta. Workshop on Early Solar System Impact Bombardment III, 4–5 February, Houston, TX, LPI Contribution Nr. 1826, p. 3012.

Bottke, W. F., Durda, D. D., Nesvorny, D., Jedicke, R., Morbidelli, A., Vokrouhlicky, D., & Levison, H. F. (2005). Linking the collisional history of the main asteroid belt to its dynamical excitation and depletion. *Icarus*, 179, 63–94.

Bottke, W. F., Vokrouhlicky, D., Minton, D., Nesvorny, D., Morbidelli, A., Brassier, R., Simonson, B., & Levison, H. F. (2012). An Archaean heavy bombardment from a destabilized extension of the asteroid belt. *Nature*, 485, 78–81.

Braden, S. E., & Robinson, M. S. (2013). Relative rates of optical maturation of regolith on Mercury and the Moon. *Journal of Geophysical Research*, 118, 1903–1914.

Brown, H. (1960). The Density and Mass Distribution of Meteoritic Bodies in the Neighborhood of the Earth's Orbit. *Journal of Geophysical Research*, 65, 1679–1683.

Brown, S. M., & Elkins-Tanton, L. T. (2009). Compositions of Mercury's earliest crust from magma ocean models. *Earth and Planetary Science Letters*, 286, 446–455.

Bunte, M. K., Porter, S., & Robinson, M. S. (2011). A sortie mission to Schrödinger basin as reconnaissance for future exploration. *Special Paper of the Geological Society of America*, 483, 533–546.

Burns, J. O., Kring, D. A., Hopkins, J. B., Norris, S., Lazio, T. J. W., & Kasper, J. (2013). A lunar L2-farside exploration and science mission concept with the Orion multi-purpose crew vehicle and a teleoperated lander/rover. *Advances in Space Research*, 52, 2, 306–320.

Bussey, D., McGovern, J., Spudis, P., Neish, C., Noda, H., Ishihara, Y., & Sørensen, S. A. (2010). Illumination conditions of the south pole of the Moon derived using Kaguya topography. *Icarus*, 208, 2, 558–564.

Byrne, P. K., Klimczak, C., & Sengör, A. M. C. (2018). The tectonic character of Mercury. Eds. by Solomon, S. C., Nittler, L. R., Anderson, B. J., *Mercury: The view after MESSENGER*, Cambridge University Press, University of Cambridge, Cambridge, UK. 249–286.

Byrne, P. K., Klimczak, C., Sengör, A. M. C., Solomon, S. C., Watters, T. R., & Hauck, S. A. II. (2014). Mercury's global contraction much greater than earlier estimates. *Nature Geosciences*, 7, 301–307.

Byrne, P. K., Ostrach, L. R., Fassett, C. I., Chapman, C. R., Denevi, B. W., Evans, A. J., Klimczak, C., Banks, M. E., Head, J. W., & Solomon, S. C. (2016). Widespread effusive volcanism on Mercury likely ended by about 3.5 Ga. *Geophysical Research Letters*, 43, 7408–7416, <http://doi:10.1002/2016GL069412>

Carpenter, J., Barber, S., Cerroni, P., Fisackerly, R., Fumagalli, A., Houdou, B., Howe, C., Magnani, P., Morse, A., Monchieri, E., Reiss, P., Richter, L., Rizzi, F., Sheridan, S., Waugh, L., & Wright, I. (2014). Accessing and assessing lunar resources with PROSPECT. Annual Meeting of the Lunar Exploration Analysis Group, LPI Contribution No. 1820, Lunar and Planetary Institute, Houston, TX, Abstract #3018.

Cavanaugh, J. F., Smith, J. C., Sun, X., Bartels, A., Ramos-Izquierdo, L., Krebs, D. J., & Smith, D. E. (2007). The Mercury Laser Altimeter Instrument for the MESSENGER Mission. *Spacecraft. Space Science Reviews*, 131, Issue 1, 451–479.

Chabot, N. L., Denevi, B. W., Murchie, S. L., Hash, C. D., Ernst, C. M., Blewett, D. T., Nair, H., Laslo, N. R., & Solomon, S. C. (2016). Mapping Mercury: Global imaging strategy and products from the MESSENGER mission. 47th Lunar and Planetary Science Conference, The Woodlands, TX, Abstract #1256.

Chapman C. R., & McKinnon, W. B. (1986). Cratering of planetary satellites. Eds. by Burns J. A., Matthews M. S. *Satellites*. University of Arizona Press, Tucson, AZ, 492–580.

Chapman C. R., Baker, D. M. H., Barnouin, O. S., Fassett, C. I., Marchi, S., Merline, W. J., Ostrach, L. R., Prockter, L. M., & Strom, R. G. (2018). Impact cratering of

Mercury. Eds by Solomon, S. C., Nittler, L. R., Anderson, B. J., Mercury: The view after MESSENGER, Cambridge University Press, University of Cambridge, Cambridge, UK, 217–248.

Chin, G., Brylow, S., Foote, M., Garvin, J., Kasper, J., Keller, J., Litvak, M., Mitrofanov, I., Paige, D., Raney, K., Robinson, M., Sanin, A., Smith, D., Spence, H., Spudis, P., Stern, S.A., & Zuber, M. (2007). Lunar Reconnaissance Orbiter overview: the instrument suite and mission. *Space Science Reviews*, 129, 4, 391–419.

Cintala, M. J., & Grieve, R. A. F. (1998). Scaling impact melting and crater dimensions: Implications for the lunar cratering record. *Meteoritics & Planetary Science*, 33, 889–912.

Clark, P.E., Bleacher, J., Mest, S., Petro, N., & Leshin, L. (2009). Lunar field exploration scenarios for a south pole outpost. 40th Lunar and Planetary Science Conference, The Woodlands, TX, Abstract #1135.

Cohen, B.A., Swindle, T. D., & Kring, D. A. (2000). Support for the lunar cataclysm hypothesis from lunar meteorite impact melt ages. *Science*, 290, 1754–1756.

Cohen, B. A., Petro, N. E., Lawrence, S. J., Clegg, S. M., Denevi, B. W., Dya, M. E., Elardo, S. M., Grinspoon, D. H., Hiesinger, H., Liu, Y., McCanta, M. C., Moriarty, D. P., Norman, M. D., Runyon, K. D., Schwenger, S. P., Swindle, T. D., van der Bogert, C. H., & Wiens, R. C. (2018). Curie: Constraining Solar System Bombardment using in situ radiometric dating. 49th Lunar and Planetary Science Conference, The Woodlands, TX, Abstract #1029.

Colaprete, A., Schultz, P., Heldmann, J., Wooden, D., Shirley, M., Ennico, K., Hermalyn, B., Marshall, W., Ricco, A., Elphic, R.C., & Goldstein, D. (2010). Detection of water in the LCROSS ejecta plume. *Science*, 330, 6003, 463–468.

Connolly, J. F. (2006). Constellation program overview. NASA Presentation, https://www.nasa.gov/pdf/163092main_constellation_program_overview.pdf

Conrad, J. W., Nimmo, F., Fassett, C. I., & Kamata, S. (2018). Lunar impact history constrained by GRAIL-derived basin relaxation measurements., *Icarus*, 314, 50–63.

Correia, A. C. M. & Laskar, J. (2004). Mercury's capture into 3/2 spin-orbit resonance as a result of its chaotic dynamics. *Nature*, 429, 848–850.

Correia, A. C. M. & Laskar, J. (2009). Mercury's capture into the 3/2 spin-orbit resonance including the effect of core-mantle friction. *Icarus*, 201, 1–11.

Costes, N., Farmer, J., & George, E. (1972). Mobility performance of the Lunar Roving Vehicle: terrestrial studies – Apollo 15 results. NASA Technical Report, TR R-401, National Aeronautics and Space Administration, Washington, D.C.

Cuk, M., Gladman, B. J., & Stewart, S. T. (2010). Constraints on the source of lunar cataclysm impactors. *Icarus*, 207, 590–594.

Daubar, I. J., Atwood-Stone, C., Byrne, S., McEwen, A. S., and Russell, P. S. (2014). The morphology of small fresh craters on Mars and the Moon. *Journal of Geophysical Research*, 119, 2620–2639, <http://doi:10.1002/2014JE004671>

Denevi, B. W., Ernst, C. M., Prockter, L. M., & Robinson, M. S. (2018a). The geologic history of Mercury. Eds. by Solomon, S. C., Nittler, L. R., Anderson, B. J., Mercury: The view after MESSENGER, Cambridge University Press, University of Cambridge, Cambridge, UK., 144–175.

Denevi, B. W., Chabot, N. L., Murchie, S. L., Becker, K. J., Blewett, D. T., Domingue, D. L., Ernst, C. M., Hash, C. D., Hawkins, S. E., Keller, M. R., Laslo, N. R., Nair, H., Robinson, M. S., Seelos, F. P., Stephens, G. K., Turner, F. S., & Solomon, S. C. (2018b). Calibration, Projection, and Final Image Products of MESSENGER's Mercury Dual Imaging System. *Space Science Reviews*, 214, 2, <https://doi.org/10.1007/s11214-017-0440-y>

Denevi, B. W., Seelos, F. P., Ernst, C. M., Keller, M. R., Chabot, N. L., Murchie, S. C., Domingue, D. L., Hash, C. D., & Blewett, D. T. (2016). Final calibration and multispectral map products from the Mercury Dual Imaging System Wide-Angle Camera on MESSENGER. 47th Lunar and Planetary Science Conference, The Woodlands, TX, Abstract #1264.

Denevi, B. W., Ernst, C. M., Meyer, H. M., Robinson, M. S., Murchie, S. L., Whitten, J. L., Head, J. W., Watters, T. R., Solomon, S. C., Ostrach, L. R., Chapman, C. R., Byrne, P. K., Klimczak, C., & Peplowski, P. N. (2013a). The distribution and origin of smooth plains on Mercury. *Journal of Geophysical Research*, 118, 891–907.

Denevi, B. W., Ernst, C. M., Whitten, J. L., Head, J. W., Murchie, S. L., Watters, T. R., Byrne, P. K., Blewett, D. T., Solomon, S. C., & Fassett, C. I. (2013b). The volcanic origin of a region of intercrater plains on Mercury. 44th Lunar and Planetary Science Conference, The Woodlands, TX, Abstract #1218.

Denevi, B. W., Robinson, M. S., Solomon, S. C., Murchie, S. L., Blewett, D. T., Domingue, D. L., McCoy, T. J., Ernst, C. M., Head, J. W., Watters, T. R., & Chabot, N. L. (2009). The evolution of Mercury's crust: A global perspective from MESSENGER, *Science*, 324, 613–618, <http://doi:10.1126/science.1172226>

De Rosa, D., Bussey, B., Cahill, J. T., Lutz, T., Crawford, I. A., Hackwill, T., van Gasselt, S., Neukum, G., Witte, L., McGovern, A., Grindrod, P. M., Carpenter, J. D. (2012). Characterisation of potential landing sites for the European Space Agency's Lunar Lander project. *Planetary and Space Science*, 74, 1, 224–246, <https://doi.org/10.1016/j.pss.2012.08.002>

Djachkova, M. V., Litvak, M. L., Mitrofanov, I. G., & Sanin, A. B. (2017). Selection of Luna-25 Landing Sites in the South Polar Region of the Moon. *Solar System Research*, 51, 3, 185–195.

Dominov, E., & Mest, S. C. (2009). Geology of Antoniadi crater, South Pole-Aitken basin. 40th Lunar and Planetary Science Conference, The Woodlands, TX, Abstract #1460.

Dundas, C. M., Keszthelyi, L. P., Bray, V. J., & McEwen A. S. (2010). Role of material properties in the cratering record of young platy-ridged lava on Mars. *Geophysical Research Letters*, 37, L12203, <http://doi:10.1029/2010GL042869>

Ehresmann, M., Gabrielli, R. A., Herdrich, G., & Laufer, R. (2017). Lunar based massdriver applications. *Acta Astronautica*, 134, 189–196.

Elkins-Tanton, L.T. & Hager, H. B. (2005). Giant meteoroid impacts can cause volcanism. *Earth and Planetary Science Letters*, 239, 219–232.

Elphic, R., Eke, V., Teodoro, L., Lawrence, D., & Bussey, D. (2007). Models of the distribution and abundance of hydrogen at the lunar south pole. *Geophysical Research Letters*, 34, 13, L13204, <http://doi:10.1029/2007GL029954>

Eppler, D., Adams, B., Archer, D., Baiden, G., Brown, A., Carey, W., Cohen, B., Condit, C., Evans, C., Fortezzo, C., Garry, B., Graff, T., Gruener, J., Heldmann, J., Hodges, K., Hörz, F., Hurtado, J., Hynes, B., Isaacson, P., Juranek, C., Klaus, K., Kring, D., Lanza, N., Lederer, S., Lofgren, G., Marinova, M., May, L., Meyer, J., Ming, D., Monteleone, B., Morisset, C., Noble, S., Rampe, E., Rice, J., Schutt, J., Skinner, J., Tewksbury-Christle, C. M., Tewksbury, B. J., Vaughan, A., Yingst, A., & Young, K. (2013). Desert Research and Technology Studies (DRATS) 2010 science operations: operational approaches and lessons learned for managing science during human planetary surface missions. *Acta Astronautica*, 90, 2, 224–241.

Ernst, C. M., Denevi, B. W., & Ostrach, L. R. (2017). Updated absolute age estimates for the Tolstoj and Caloris basins, Mercury. 48th Lunar Planetary Science Conference, The Woodlands, TX., Abstract #2934.

Ernst, C. M., Denevi, B. W., Barnouin, O. S., Klimczak, C., Chabot, N. L., Head, J. W., Murchie, S. L., Neumann, G. A., Prockter, L. M., Robinson, M., Solomon, S. C., &

Watters, T. R. (2015). Stratigraphy of the Caloris basin, Mercury: Implications for volcanic history and basin impact melt. *Icarus*, 250, 413–429.

European Space Agency, (2019). ESA Strategy for Science at the Moon. p. 1–45, https://sci.esa.int/documents/34161/35992/1567260389633-ESA_Strategy_for_Science_at_the_Moon.pdf

Fa, W., Liu, T., Zhu, M.-H., & Haruyama, J. (2014). Regolith thickness over Sinus Iridum: Results from morphology and size-frequency distribution of small impact craters. *Journal of Geophysical Research*, 119, 1914–1935.

Fagan, A. L., Ennis, M. E., Pogue, J. N., Porter, S., Snape, J. F., Neal, C. R., & Kring, D. A. (2010). Science-rich mission sites within South Pole-Aitken basin. 41th Lunar and Planetary Science Conference, The Woodlands, TX., Abstract #2467.

Fassett, C. I. (2016). Analysis of impact crater populations and the geochronology of planetary surfaces in the inner solar system. *Journal of Geophysical Research*, 121, 10, 1900–1926.

Fassett, C. I., & Head, J. W. (2008). The timing of martian valley network activity: Constraints from buffered crater counting. *Icarus*, 195, 61–89. <https://doi.org/10.1016/j.icarus.2007.12.009>

Fassett, C. I., Head, J. W., Blewett, D. T., Chapman, C. R., Dickson, J. L., Murchie, S. L., Solomon, S. C., & Watters, T. R. (2009). Caloris impact basin: Exterior geomorphology, stratigraphy, morphometry, radial sculpture, and smooth plains deposits. *Earth and Planetary Science Letters*, 285, 297–308, <http://doi:10.1016/j.epsl.2009.05.022>

Fassett, C. I., Kadish, S. J., Head, J. W., Solomon, S. C., & Strom, R. G. (2011). The global population of large craters on Mercury and comparison with the Moon. *Geophysical Research Letters*, 38, L10202.

Fassett, C. I., Head, J. W., Baker, D. M. H., Zuber, M. T., Smith, D. E., Neumann, G. A., Solomon, S. C., Klimczak, C., Strom, R. G., Chapman, C. R., Prockter, L. M., Phillips, R. J., Oberst, J., & Preusker, F. (2012a). Large impact basins on Mercury: Global distribution, characteristics, and modification history from MESSENGER orbital data. *Journal of Geophysical Research*, 117, E00L08.

Fassett, C. I., Head, J. W., Kadish, S. J., Mazarico, E., Neumann, G. A., Smith, D. E., & Zuber, M. T. (2012b). Lunar impact basins: Stratigraphy, sequence and ages from superposed impact crater populations measured from Lunar Orbiter Laser Altimeter (LOLA) data. *Journal of Geophysical Research*, 117, E00H06. <https://doi.org/10.1029/2011JE003951>

Fegan, E. R., Rothery, D. A., Marchi, S., Massironi, M., Conway, S. I., & Anand, M. (2017). Late movement of basin-edge lobate scarps on Mercury. *Icarus*, 288, 226–234.

Ferrari, S., Massironi, M., Marchi, S., Byrne, P. K., Klimczak, C., Martellato, E., & Cremonese, G. (2015). Age relationships of the Rembrandt basin and Enterprise Rupes, Mercury. *Geological Society, London, Special Publications*, 401, 1, 159–172, <https://doi.org/10.1144/SP401.20>

Flahaut, J., Carpenter, J., Williams, J.-P., Anand, M., van Westrenen, W., Füre, E., Xiao, L., & Zhao, S. (2020). Regions of Interest (ROI) for future exploration missions to the lunar South Pole. *Planetary and Space Science*, <https://doi.org/10.1016/j.pss.2019.104750>

Flude, S., Halton, A. M., Kelley, S. P., Sherlock, S. C., Schwanethal, J., & Wilkinson, C. M. (2014). Observation of centimetre-scale argon diffusion in alkali feldspars: implications for $^{40}\text{Ar}/^{39}\text{Ar}$ thermochronology. *Geological Society, London, Special Publications*, 378, 1, 265–275.

French, B. M. (1998). *Traces of catastrophe: a handbook of shock-metamorphic effects in terrestrial meteorite impact structures*. Lunar and Planetary Institute, LPI Contribution No. 954., Houston, TX.

Fu, X-H., Qiao, L., Zhang, J., Ling, Z-C., & Li, B. (2020). The subsurface structure and stratigraphy of Chang'E-4 landing site: orbital evidence from small craters on the Von Karman crater floor. *Research in Astronomy and Astrophysics*, 20, 1, 8–12, <http://doi:10.1088/1674-4527/20/1/8>

Gaddis, L. R., Staid, M. I., Tyburczy, J. A., Hawke, B. R., & Petro, N. E. (2003). Compositional analyses of lunar pyroclastic deposits. *Icarus*, 161, 2, 262–280, [http://doi:10.1016/S0019-1035\(02\)00036-2](http://doi:10.1016/S0019-1035(02)00036-2)

Garrick-Bethell, I., & Zuber, M.T. (2009). Elliptical structure of the lunar South Pole-Aitken basin. *Icarus* 204, 399–408, <http://dx.doi.org/10.1016/j.icarus.2009.05.032>

Garrick-Bethell, I., Miljkovic, K., Hiesinger, H., van der Bogert, C. H., Laneuville, M., Shuster, D. L., & Korycansky, D. G. (2020). Troctolite 76535: A sample of the Moon's South Pole-Aitken basin? *Icarus*, 338, <https://doi.org/10.1016/j.icarus.2019.113430>.

Gault, D., E. (1970). Saturation and equilibrium conditions for impact cratering on the lunar surface: criteria and implications. *Radio Science*, 5, 2, 273–291.

Gault, D., E., Guest, J. E., Murray, J. B., Dzurisin, D., & Malin, M. C. (1975). Some comparisons of impact craters on Mercury and the Moon. *Journal of Geophysical Research*, 80, 2444–2460.

Gemperline, J., Hynek, B. M., Robbins, S. J., Osterloo, M. K., Mueller, K., & Thomas, R. (2017). Age estimates of geologic units around the Rembrandt basin, Mercury. 48th Lunar and Planetary Science Conference, The Woodlands, TX., Abstract #2864.

Gibson, K. E., & Jolliff, B. L. (2011). Correlation of surface units and FeO concentrations in the South Pole-Aitken basin interior. 42nd Lunar and Planetary Science Conference, The Woodlands, TX., Abstract #2326.

Gilbert, G. (1893). The moon's face. A study of the origin of its features. *Bulletin of Philosophical Society of Washington*, 12, 241–292.

Gomes, R., Levison, H. F., Tsiganis, K., & Morbidelli, A. (2005). Origin of the cataclysmic late heavy bombardment period of the terrestrial planets. *Nature*, 435, 466–469.

Green, R. O., Pieters, C., Mouroulis, P., Eastwood, M., Boardman, J., Glavich, T., Isaacson, P., Annadurai, M., Besse, S., Barr, D., Buratti, B., Cate, D., Chatterjee, A., Clark, R., Cheek, L., Combe, J., Dhingra, D., Essandoh, V., Geier, S., Goswami, J. N., Green, R., Haemmerle, V., Head, J. W., Hovland, L., Hyman, S., Klima, R., Koch, T., Kramer, G., Kumar, A. S. K., Lee, K., Lundeen, S., Malaret, E., McCord, T., McLaughlin, S., Mustard, J., Nettles, J., Petro, N., Plourde, K., Racho, C., Rodriguez, J., Runyon, C., Sellar, G., Smith, C., Sobel, H., Staid, M., Sunshine, J., Taylor, L., Thaisen, K., Tompkins, S., Tseng, H., Vane, G., Varanasi, P., White, M., & Wilson, D. (2011). The Moon Mineralogy Mapper (M3) imaging spectrometer for lunar science: instrument description, calibration, on-orbit measurements, science data calibration and on-orbit validation. *Journal of Geophysical Research*, 116, E10, <https://doi.org/10.1029/2011JE003797>

Gruener, J.E., & Joosten, B.K. (2009). NASA Constellation program office regions of interest on the Moon: a representative basis for scientific exploration, resource potential, and mission operations, Eds. by Mackwell, S. J., Lunar Reconnaissance Orbiter Science Targeting Meeting Report. Arizona State University, Tempe, AZ, p. 58.

Haber, T., Scherer, E., E., Bast, R., & Sprung, P. (2017). ¹⁷⁶Lu-¹⁷⁶Hf Isochron Dating of Strongly Cosmic Ray Exposed Samples-A case study on Apollo 14 Impact Melt Rock 14310. 48th Lunar and Planetary Science Conference, The Woodlands, TX., Abstract #2911.

Hamann, C. (2017). Projectile-target interaction and rapid, high-temperature geochemical processes in impact melts. PhD Thesis, p. 360, Freie Universität Berlin, Berlin, Germany.

Harland, D. (2008). Exploring the Moon: the Apollo Expeditions. Second ed. Praxis Publishing Ltd, Chichester, UK.

Harrison, D. A., Ambrose, R., Bluethmann, B., & Junkin, L. (2008). Next generation rover for lunar exploration. IEEE Conference Proceedings, p. 1–14, <http://doi.10.1109/AERO.2008.4526234>

Hartmann, W. K. (1964). On the Distribution of Lunar Crater Diameters. Communications of the Lunar and Planetary Laboratory, 2, 197–204.

Hartmann, W. K. (1969). Terrestrial, Lunar, and Interplanetary Rock Fragmentation. Icarus, 10, 201.

Hartmann, W. K. (1975). Lunar "cataclysm": A misconception? Icarus, 24, 181–187.

Hartmann, W. K. (1995). Planetary cratering I: Lunar highlands and tests of hypotheses on crater populations. Meteoritics, 30, 451–467.

Hartmann W. K. (2003). Megaregolith evolution and cratering cataclysm models – Lunar cataclysm as a misconception (28 years later). Meteoritics and Planetary Science, 38, 579–593.

Hartmann, W. K. (2019). History of the terminal cataclysm paradigm: Epistemology of a planetary bombardment that never (?) happened. Geosciences, 9, 7, 285, <https://doi.org/10.3390/geosciences9070285>

Hartmann, W. K., & Wood, C. A. (1971). Moon: Origin and evolution of multi-ring basins. Moon, 3, 3–78.

Hartmann, W. K., Strom, R., Weidenschilling, S., Blasius, K., Woronow, A., Dence, M., Grieve, R., Diaz, J., Chapman, C., Shoemaker, E., & Jones, K. (1981). Chronology of Planetary Volcanism by Comparative Studies of Planetary Craters. In Basaltic Volcanism on the Terrestrial Planets (Basaltic Volcanism Study Project), Pergamon Press, Elmsford, NY, USA, 1050–1127.

Haruyama, J., Matsunaga, T., Ohtake, M., Morota, T., Honda, C., Yokota, Y., Torii, M., Ogawa, Y., & the LISM Working Group (2008). Global lunar-surface mapping experiment using the Lunar Imager/Spectrometer on SELENE. Earth Planets Space, 60, 243–255.

Haruyama, J., Ohtake, M., Matsunaga, T., Morota, T., Honda, C., Yokota, Y., Abe, M., Ogawa, Y., Miyamoto, H., Iwasaki, A., Pieters, C.M., Asada, N., Demura, H., Hirata, N., Terazono, J., Sasaki, S., Saiki, K., Yamaji, A., Torii, M., & Jean-Luc, J. (2009). Long-lived volcanism on the lunar farside revealed by SELENE terrain camera. *Science*, 323, 5916, 905–908, <http://doi:10.1126/science.1163382>

Haruyama, J., Ohtake, M., Matsunaga, T., Morota, T., Honda, C., Yokota, Y., Pieters, C.M., Hara, S., Hioki, K., Saiki, K., Miyamoto, H., Iwasaki, A., Abe, M., Ogawa, Y., Takeda, H., Shirao, M., Yamaji, A., & Josset, J. L. (2008). Lack of exposed ice inside lunar south pole Shackleton crater. *Science*, 322, 5903, 938–939.

Haskin, L. A., Korotev, R. L., Rockow, K. M., & Jolliff, B. L. (1998). The case for an Imbrium origin of the Apollo Th-rich impact-melt breccias. *Meteoritics & Planetary Science*, 33, 5, 959–975.

Hawkins, S. E., Boldt, J. D., Darlington, E. H., Espiritu, R., Gold, R. E., Gotwols, B., Grey, M. P., Hash, C. D., Hayes, J. R., Jaskulek, S. E., Kardian, C. J., Keller, M. R., Malaret, E. R., Murchie, S. L., Murphy, P. K., Peacock, K., Prockter, L. M., R. Reiter, A., Robinson, M. S., Schaefer, E. D., Shelton, R. G., Sterner, R. E., Taylor, H. W., Watters, T. R., & Williams, B. D. (2007). The Mercury Dual Imaging System on the MESSENGER Spacecraft. *Space Science Reviews*, 131, 1–4, 247–338.

Head, J. W. (1974). Morphology and structure of the Taurus-Littrow Highlands (Apollo 17): Evidence for their origin and evolution. *Moon*, 9, 355–395.

Head, J. W., Fassett, C. I., Kadish, S. J., Smith, D. E., Zuber, M. T., Neumann, G. A., & Mazarico, E. (2010). Global distribution of large lunar craters: Implications for resurfacing and impactor populations. *Science*, 329, 1504–1507.

Head, J. W., Chapman, C. R., Strom, R. G., Fassett, C. I., Denevi, B. W., Blewett, D. T., Ernst, C. M., Watters, T. R., Solomon, S. C., Murchie, S. L., Prockter, L. M., Chabot, N. L., Gillis-Davis, J. J., Whitten, J. L., Goudge, T. A., Baker, D. M., Hurwitz, D. M., Ostrach, L. R., Xiao, Z, Merline, W. J., Kerber, L., Dickson, J. L., Oberst, J., Byrne, P. K., Klimczak C., & Nittler, L. R. (2011). Flood volcanism in the northern high latitudes of Mercury revealed by MESSENGER, *Science*, 333, 1853–1856, <http://doi:10.1126/science.1211997>

Head, J. W., Murchie, S. L., Prockter, L. M., Solomon, S. C., Chapman, C. R., Strom, R. G., Watters, T. R., Blewett, D. T., Gillis-Davis, J. J., Fassett, C. I., Dickson, J. L., Morgan, G. A., & Kerber, L. (2009). Volcanism on Mercury: Evidence from the first MESSENGER flyby for extrusive and explosive activity and the volcanic origin of plains. *Earth and Planetary Science Letters*, 285, 227–242.

Hiesinger, H., Jaumann, R., Neukum, G., & Head, J. W. (2000). Ages of mare basalts on the lunar nearside. *Journal of Geophysical Research*, 105, E12, 29239–29275.

Hiesinger, H., Head, J. W., Wolf, U., Jaumann, R., & Neukum, G. (2002). Lunar mare basalt flow units: thicknesses determined from crater size-frequency distributions. *Journal Geophysical Research Letters*, 29, 8, 891–894.

Hiesinger, H., Head, J. W., Wolf, U., Jaumann, R., Neukum, G. (2003). Ages and stratigraphy of mare basalts in Oceanus Procellarum, Mare Nubium, Mare Cognitum, and Mare Insularum. *Journal of Geophysical Research*, 108, E7.

Hiesinger, H., van der Bogert, C. H., Pasckert, J. H., Funcke, L., Giacomini, L., Ostrach, L. R., Robinson, M. S. (2012a). How old are young lunar craters? *Journal of Geophysical Research* ,117, E12, E00H10.

Hiesinger, H., van der Bogert, C., H., Pasckert, J., H., Schmedemann, N., Robinson, M., S., Jolliff, B., & Petro, N. (2012b). New crater size-frequency distribution measurements of the South Pole-Aitken Basin. 43rd Lunar and Planetary Science Conference, The Woodlands, TX., Abstract #2863.

Hopkins, M. D., & Mojzsis, S. J. (2015). A protracted timeline for lunar bombardment from mineral chemistry, Ti thermometry and U–Pb geochronology of Apollo 14 melt breccia zircons. *Contrib. Mineral Petrol*, 169, 30, <http://doi.10.1007/s00410-015-1123-x>

Hopkins, J., Pratt, C., Hall, S., Scott, A., Farquar, R., & Dunham, D. (2013). Proposed orbits and trajectories for human missions to the Earth-Moon L2 region. 64th International Astronautical Congress, Beijing, China.

Housen, K. R., & Holsapple, K. A. (2011). Ejecta from impact craters. *Icarus*, 211, 856–875.

Howard, A. D. (2007). Simulating the development of Martian highland landscapes through the interaction of impact cratering, fluvial erosion, and variable hydrologic forcing. *Geomorphology*, 91, Issues 3–4, 332–363.

Huang, J., Xiao, Z., Flahaut, J., Martinot, M., Head, J., Xiao, X., Xie, M., & Xiao, L. (2018). Geological characteristics of Von Kármán crater, northwestern South Pole-Aitken Basin: Chang'E-4 landing site region. *Journal of Geophysical Research*, 123, 7, 1684–1700, <https://doi.org/10.1029/2018JE005577>.

Hufenbach, B., Laurini, K.C., Satoh, N., Lange, C., Martinez, R., Hill, J., Landgraf, M., Bergamasco, A. (2015). International missions to lunar vicinity and surface-near- term

mission scenario of the global space exploration roadmap. 66th International Astronomical Congress, Jerusalem, Israel.

Humm, D. C., Tschimmel, M., Brylow, S. M., Mahanti, P., Tran, T. N., Braden, S. E., Wiseman, S., Danton, J., Eliason, E. M., & Robinson, M. S. (2016). Flight Calibration of the LROC Narrow Angle Camera. *Space Science Reviews*, 200, 431–473.

Hurwitz, D. M., & Kring, D. A. (2013). Composition and structure of the South Pole-Aitken basin impact melt sheet. 41th Lunar and Planetary Science Conference, The Woodlands, TX. Abstract #2224.

Hurwitz, D. M., Kring, D. A. (2014). Differentiation of the South Pole-Aitken basin impact melt sheet: implications for lunar exploration. *Journal of Geophysical Research*, 119, 1110–1133.

Hurwitz, D. M., Kring, D. A. (2015). Potential sample sites for South Pole-Aitken basin impact melt within the Schrödinger basin. *Earth and Planetary Science Letters*, 427, 31–36.

Hynek, B. M., Robbins, S. J., Mueller, K., Gemperline, J., Osterloo, M. K., & Thomas, R. (2016). Unlocking Mercury's geological history with detailed mapping of Rembrandt basin: Year 2. Annual Planetary Geologic Mappers Meeting, Flagstaff, AZ, Abstract #7023.

International Space Exploration Coordination Group (2013). The global exploration roadmap. National Aeronautics and Space Administration. https://www.nasa.gov/sites/default/files/files/GER-2013_Small.pdf

International Space Exploration Coordination Group (2018). The global exploration roadmap. National Aeronautics and Space Administration. https://www.nasa.gov/sites/default/files/atoms/files/ger_2018_small_mobile.pdf

Iqbal, W., Hiesinger, H., & van der Bogert, C. H. (2019a). Geological mapping and chronology of lunar landing sites: Apollo 11. *Icarus*, 333, 528–547.

Iqbal, W., Hiesinger, H., & van der Bogert, C. H. (2019b). New geological maps and crater size-frequency distribution measurements of the Apollo 17 landing site. 50th Lunar and Planetary Science Conference, The Woodlands, TX, Abstract #1005.

Iqbal, W., Hiesinger, H., & van der Bogert, C. H. (2018). Reinvestigating the crater size-frequency distribution of the Apollo 12 landing site. 49th Lunar and Planetary Science Conference, The Woodlands, TX. Abstract #1002.

Ivanov, B. A. (2001). Mars/Moon Cratering Rate Ratio Estimates. *Space Science Reviews*, 96, 87–104.

Ivanov, B. A. (2008). Size-frequency distribution of asteroids and impact craters: estimates of impact rate. Eds. by V.V. Adushkin and I.V. Nemchinov, *Catastrophic Events Caused by Cosmic Objects*, Springer, 91–116.

Ivanov, B. A., Neukum, G., Bottke, W. F., & Hartmann, W. K. (2002). The Comparison of Size-Frequency Distributions of Impact Craters and Asteroids and the Planetary Cratering Rate. *Asteroids*, 3, 89–101.

Ivanov, M. A., Abdrakhimov, A. M., Basilevsky, A. T., Demidov, N. E., Guseva, E. N., Head, J. W., Hiesinger, H., Kohanov, A. A., and Krasilnikov, S. S. (2017). Geological characterization of the three high-priority landing sites for the Luna-Glob mission. *Planetary and Space Science*, 1–17, <http://dx.doi.org/10.1016/j.pss.2017.08.004>

Ivanov, M., Hiesinger, H., Orgel, C., Pasckert, J., van der Bogert, C., & Head, J. W. (2018). Geology of the northern portion of the SPA basin on the Moon: Evidence for compositional stratification of the ancient lunar crust. 49th Lunar and Planetary Science Conference 49, The Woodlands, TX., Abstract #1138.

Ivanov, M. A., Hiesinger, H., van der Bogert, C. H., Orgel, C., Pasckert, J. H., and Head, J. W. (2018). Geologic history of the northern portion of the South Pole-Aitken basin on the Moon. *Journal of Geophysical Research*, 123, 2585–2612. <https://doi.org/10.1029/2018JE005590>

Jaumann, R., Hiesinger, H., Anand, M., Crawford, I., Wagner, R., Sohl, F., Jolliff, B., Scholten, F., Knapmeyer, M., Hoffmann, H., Hussmann, H., Grott, M., Hempel, S., Köhler, U., Krohn, K., Schmitz, N., Carpenter, J., Wiczorek, M., Spohn, T., Robinson, M., & Oberst, J. (2012). Geology, geochemistry, and geophysics of the Moon: status of current understanding. *Planetary and Space Sciences*, 74, 1, 15–41.

Jawin, E. R., Valencia, S. N., Watkins, R. N., Crowell, J. M., Neal, C. R., & Schmidt, G. (2019). Lunar science for landed missions workshop findings report. *Earth and Space Science*, 6, 2–40. <https://doi.org/10.1029/2018EA000490>

Jia, Y., Zou, Y., Ping, J., Xue, C., Yan, J., and Ning, Y. (2018). The scientific objectives and payloads of Chang'E-4 mission. *Planetary and Space science* 162, 207–215, <https://doi.org/10.1016/j.pss.2018.02.011>

Jolliff, B. L., Alkalai, L., Pieters, C. M., Head, J. W., Papanastassiou, D. A., & Bierhaus, E. B. (2010). Sampling the South Pole-Aitken basin: Objectives and site selection criteria. 41th Lunar and Planetary Science Conference, The Woodlands, TX., Abstract #2450.

Jolliff, B. L., Gillis, J. J., Haskin, L. A., Korotev, R. L., & Wieczorek, M. A. (2000). Major lunar crustal terranes: surface expressions crust-mantle origins. *Journal of Geophysical Research*, 105, E2, 4197–4216.

Jolliff, B. L., Haskin, L. A., Korotev, R. L., Papike, J. J., Shearer, C. K., Pieters, C. M., & Cohen, B. (2003). Scientific expectations from a sample of regolith and rock fragments from the interior of the lunar South Pole-Aitken basin. 34th Lunar and Planetary Science Conference, The Woodlands, TX., Abstract # 1989.

Jolliff, B. L., Shearer, C. K., Papanastassiou, D. A., & Liu, Y. (2017). Why do we need samples from the Moon's South Pole-Aitken basin and what would we do with them? 48th Lunar and Planetary Science Conference, The Woodlands, TX., Abstract #1300.

Jones, A. (2020). Chang'e 4 Celebrates a Year on the Farside of the Moon. *Sky & Telescope*, January 5., <https://www.skyandtelescope.com/astronomy-news/change-4-celebrates-year-on-the-farside/>

Jourdan, F., Mark, D. F., & Verati, C. (2014). Advances in ⁴⁰Ar/³⁹Ar dating: from archaeology to planetary sciences – introduction. *Geological Society, London, Special Publications*, 378, 1,1–8.

Kamata, S., Sugita, S., Abe, Y., Ishihara, Y., Harada, Y., Morota, T., Namiki, N., Iwata, T., Hanada, H., Araki, H., Matsumoto, K., Tajika, E., Kuramoto, K., & Nimmo, F. (2015). The relative timing of Lunar Magma Ocean solidification and the Late Heavy Bombardment inferred from highly degraded impact basin structures. *Icarus*, 250, 492–503.

Karachevtseva, I., Oberst, J., Scholten, F., Konopikhin, A., Shingareva, K., Cherepanova, E., Guskova, E., Haase, I., Peters, O., Plescia, J., Robinson, M. (2013). Cartography of the Lunokhod-1 landing site and traverse from LRO image and stereo topographic data. *Planetary and Space Science*, 85,175–187.

Karachevtseva, I., Kozlova, N. A., Kokhanov, A. A., Zubarev, A. E., Nadezhdina, I. E., Patratiy, V. D., Konopikhin, A. A., Basilevsky, A. T., Abdrakhimov, A. M., Oberst, J., Haase, I., Jolliff, B. L., Plescia, J. B., & Robinson, M. S. (2017). Cartography of the Luna-21 landing site and Lunokhod-2 traverse area based on Lunar Reconnaissance Orbiter Camera images and surface archive TV-panoramas. *Icarus*, 283, 104–121.

Kato, M., Sasaki, S., & Takizawa, Y. (2010). The Kaguya mission overview. *Space Science Reviews*, 154, 1–4, 3–19, <https://doi.org/10.1007/s11214-010-9678-3>

Klima, R. L., Pieters, C. M., Boardman, J. W., Green, R. O., Head, J. W. III., Isaacson, P. J., Mustard, J. F., Nettles, J. W., Petro, N. E., Staid, M. I., Sunshine, J. M., Taylor, L. A., Tompkins, S. (2011). New insights into lunar petrology: Distribution and

composition of prominent low - Ca pyroxene exposures as observed by the Moon Mineralogy Mapper (M3). *Journal of Geophysical Research*, 116, E00G06, <http://doi:10.1029/2010JE003719>

Kneissl, T., van Gasselt, S., & Neukum, G. (2011). Map-projection-independent crater size-frequency determination in GIS environments – New software tool for ArcGIS. *Planetary and Space Science*, 59, 1243–1254. <https://doi.org/10.1016/j.pss.2010.03.015>

Kneissl, T., Michael, G. G., & Schmedemann, N. (2016). Treatment of non-sparse cratering in planetary surface dating. *Icarus*, 277, 187–195. <https://doi.org/10.1016/j.icarus.2016.05.015>

Kneissl, T., Michael, G. G., Platz, T., & Walter, S. H. G. (2015). Age determination of linear surface features using Buffered Crater Counting approach – Case studies of the Sirenum and Fortuna Fossae graben systems on Mars. *Icarus*, 250, 384–394.

Korotev, R. (2000). The great lunar hot spot and the composition and origin of the Apollo mafic (LKFM) impact-melt breccias. *Journal of Geophysical Research*, 105, E2, 4307–4345.

König, B. (1977). Investigations of primary and secondary impact structures on the moon and laboratory experiments to study the ejecta of secondary particles. Ruprecht Karl Universität, SCITRAN, Inc., p. 88.

Kramer, G. Y., Kring, D. A., Nahm, A. L., & Pieters, C. M. (2013). Spectral and photogeologic mapping of Schrödinger basin and implications for post-South Pole-Aitken impact deep subsurface stratigraphy. *Icarus*, 233, 131–148.

Kreslavsky, M. A., Head, J. W., Neumann, G. A., Zuber, M. T., & Smith, D. E. (2014). Kilometer-scale topographic roughness of Mercury: Correlation with geologic features and units, *Geophysical Research Letters*, 41, 8245–8251. <http://doi:10.1002/2014GL062162>

Kring, D. (2007). Lunar Exploration Initiative: lunar EVA sample mass.

Kring, D.A. (2011). Lunar surface systems study: Malapert massif, unpublished manuscript.

Kring, D.A. (2014). Exploring the Schrödinger and South Pole-Aitken basins on the lunar farside. 40th COSPAR Scientific Assembly, 40.

Kring, D. (2017). The lunar electric rover (aka space exploration vehicle) as a geological tool. In: Fifth European Lunar Symposium. p. 125.

Kring, D. A., & Cohen, B. A. (2002). Cataclysmic bombardment throughout the inner Solar System 3.9 – 4.0 Ga. *J. Geophys. Res. Planets*, 107,(E2), 4–10.

Kring, D. A., & Durda, D. D. (2012). A Global Lunar Landing Site Study to Provide the Scientific Context for Exploration of the Moon. Lunar and Planetary Institute, LPI Contribution Nr. 1694, Houston, TX., p. 688.

Kring, D. A., Kramer, G. Y., & Potter, R. W. K. (2013). Interpreting the depth of origin of the Schrödinger peak ring and implications for other impact basins. 5th Large Meteorite Impacts and Planetary Evolution, LPI Contribution Nr. 1737, p. 3069.

Kring, D. A., Kramer, G. Y., Bussey, D. B. J., & Hurley, D. M. (2014). Prominent volcanic source of volatiles in the south polar region of the Moon. Annual Meeting of the Lunar Exploration Analysis Group, 1820.

Kring, D., Bleacher, J., Garry, W., Love, S., & Young, K. (2017). The utility of a small pressurized rover with suit ports for lunar exploration: a geologist's perspective. NASA Exploration Science Forum.

Kring, D. A., Kramer, G. Y., Collins, G. S., Potter, R. W. K., & Chandnani, M. (2016). Peak-ring structure and kinematics from a multi-disciplinary study of the Schrödinger impact basin. *Nature Communications*, 7, 13161.

Landgraf, M., Carpenter, J., & Sawada, H. (2015). HERACLES concept – an international lunar exploration architecture study. Lunar Exploration Analysis Group.

Lawrence, D., Elphic, R., Feldman, W., Prettyman, T., Gasnault, O., & Maurice, S. (2003). Small-area thorium features on the lunar surface. *Journal of Geophysical Research*, 108, E9.

Lawrence, D., Puetter, R., Elphic, R., Feldman, W., Hagerty, J., Prettyman, T., & Spudis, P. (2007). Global spatial deconvolution of Lunar Prospector Th abundances. *Geophysical Research Letters*, 34, L03201.

Lawrence, D. J., Feldman, W. C., Barraclough, B. L., Binder, A. B., Elphic, R.C., Maurice, S., & Thomsen, D. R. (1998). Global elemental maps of the Moon: the Lunar Prospector gamma-ray spectrometer. *Science*, 281, 5382, 1484–1489.

Lawrence, D. J., Feldman, W. C., Elphic, R. C., Little, R. C., Prettyman, T. H., Maurice, S., Lucey, P. G., & Binder, A. B. (2002). Iron abundances on the lunar surface as

measured by the Lunar Prospector gamma-ray and neutron spectrometers. *Journal of Geophysical Research*, 107, E12, 1–26.

Le Feuvre, M., & Wieczorek, M.A. (2008). Nonuniform cratering of the terrestrial planets. *Icarus*, 197, 291–306. <http://dx.doi.org/10.1016/j.icarus.2008.04.011>

Le Feuvre, M., & Wieczorek, M. A. (2011). Nonuniform cratering of the Moon and a revised crater chronology of the inner Solar System. *Icarus*, 214, 1–20.

Lemelin, M., Blair, D., Roberts, C., Runyon, K., Nowka, D., & Kring, D. A. (2014). High-priority lunar landing sites for in situ and sample return studies of polar volatiles. *Planetary and Space Science*, 101, 149–161.

Lemelin, M., Lucey, P. G., Gaddis, L. R., Hare, T., & Ohtake, M. (2016). Global map products from the Kaguya Multiband Imager at 512 ppd: Minerals, FeO, and OMAT. 47th Lunar and Planetary Science Conference, The Woodlands, TX, Abstract #2994.

Liu, T., Michael, G., Engelmann, J., Wünnemann, K., & Oberst, J. (2019). Regolith mixing by impacts: Lateral diffusion of basin melt. *Icarus*, 321, 691–704. <https://doi.org/10.1016/j.icarus.2018.12.026>

Lockheed Martin (2016). Orbital coverage for the South Pole-Aitken basin center.

Lucey, P. G., Taylor, G. J., Hawke, B. R., & Spudis, P. D. (1998a). FeO and TiO concentrations in the South Pole-Aitken basin: implications for mantle composition and basin formation. *Journal of Geophysical Research*, 103, 3701–3708.

Lucey, P. G., Blewett, D. T., & Hawke, R. (1998b). Mapping the FeO and TiO₂ content of the lunar surface with multispectral imagery. *Journal of Geophysical Research*, 103, E2, 3679–3699.

Lucey, P. G., Blewett, D. T., & Jolliff, B. L. (2000). Lunar iron and titanium abundance algorithms based on final processing of Clementine ultraviolet-visible images. *Journal of Geophysical Research*, 105, 20,297–20,306.

Lunar Exploration Analysis Group (2016). The Lunar Exploration Roadmap: Exploring the Moon in the 21st Century: Themes, Goals, Objectives, Investigations, and Priorities. Version 1.3, <https://www.lpi.usra.edu/leag/roadmap/>

Lunar Exploration Analysis Group (2017). Advancing Science of the Moon: Report of the Specific Action Team. 7–8 August 2017, Houston, TX., <https://www.lpi.usra.edu/leag/reports/ASM-SAT-Report-final.pdf>

Lunar Exploration Science Working Group (1995). Lunar surface exploration strategy – Final report. Tech. rep.

Mahaffy, P. R., Webster, C. R., Cabane, M., Conrad, P. G., Coll, P., Atreya, S. K....& Mumm, E. (2012). The Sample Analysis at Mars investigation and instrument suite. *Space Science Reviews*, 170, 1, 401–478.

Mahanti, P., Humm, D. C., Robinson, M. S., Boyd, A. K., Stelling, R., Sato, H., Denevi, B. W., Braden, S. E., Bowman-Cisneros, E., Brylow, S. M., & Tschimmel, M. (2016). Inflight Calibration of the Lunar Reconnaissance Orbiter Camera Wide Angle Camera. *Space Science Reviews*, 200, 393–430.

Mandt, K. E., Greathouse, T. K., Retherford, K. D., Gladstone, G. R., Jordan, A. P., Lemelin, M., Koeber, S. D., Bowman-Cisneros, E., Patterson, G. W., Robinson, M., Lucey, P. G., Hendrix, A. R., Hurley, D., Stickle, A. M., & Pryor, W. (2016). LRO-lamp detection of geologically young craters within lunar permanently shaded regions. *Icarus*, 273, 114–120.

Manske, L., Marchi, S., & Wünnemann, K. (2019). Production and provenience of impact-generated melt by large scale collisions on Mars., 50th Lunar and Planetary Science Conference, The Woodlands, TX., Abstract #2753.

Marchi, S., Bottke, W. F., Kring, D. A., & Morbidelli, A. (2012). The onset of the lunar cataclysm as recorded in its ancient crater populations. *Earth and Planetary Science Letters*, 325–326, 27–38.

Marchi, S., Mottola, S., Cremonese, G., Massironi, M., & Martellato, E. (2009). A new chronology for the Moon and Mercury. *The Astronomical Society*, 137, 4936–4948. <https://doi.org/10.1088/0004-6256/137/6/4936>

Marchi, S., Chapman, C. R., Fassett, C. I., Head, J. W., Bottke, W. F., & Strom, R. G. (2013). Global resurfacing of Mercury 4.0–4.1 billion years ago by heavy bombardment and volcanism. *Nature*, 499, 59–61.

Marchi, S., Massironi, M., Cremonese, G., Martellato, E., Giacomini, L., & Prockter, L. (2011). The effects of the target material properties and layering on the crater chronology: The case of Raditladi and Rachmaninoff basins on Mercury. *Planetary and Space Science*, 59, 1968–1980.

Massachusetts Institute of Technology (2016). Percentage Earth visibility map. http://imbrium.mit.edu/EXTRAS/ILLUMINATION/RELEASE_2014/IMG.

Mayor, M., & Queloz, D. (1995). A Jupiter-mass companion to a star-type star. *Nature*, 378, 355–359.

Mazanek, D. D., Troutman, P. A., Culbert, C. J., Leonard, M. J., & Spexarth, G. R. (2009). Surface buildup scenarios and outpost architectures for Lunar Exploration. IEEE Aerospace Conference, 1–23.

Mazarico, E., Neumann, G., Smith, D., Zuber, M., & Torrence, M. (2011). Illumination conditions of the lunar polar regions using LOLA topography. *Icarus*, 211, 2, 1066–1081.

McDougall, I. & Harrison, T.M. (1999). *Geochronology and Thermochronology by the $^{40}\text{Ar}/^{39}\text{Ar}$ Method*. Oxford University Press, Second Edition, New York, USA, p. 269.

Melosh, H. J. (1989). *Impact cratering: a geologic process*. Oxford University Press, New York, USA.

Meyer, J., Elkins-Tanton, L., & Wisdom, J. (2010). Coupled thermal–orbital evolution of the early Moon. *Icarus*, 208, 1–10. <http://dx.doi.org/10.1016/j.icarus.2010.01.029>

Meyer, H. M., Denevi, B. W., Boyd, A. K., & Robinson, M. S. (2016). The distribution and origin of lunar light plains around Orientale basin. *Icarus*, 273, 135–145.

Meyer, H. M. (2018). *The Formation and Degradation of Planetary Surfaces: Impact Features and Explosive Volcanic Landforms on the Moon and Mars*. Ph.D. dissertation, Arizona State University, AZ.

Michael, G. G. (2013). Planetary surface dating from crater size-frequency distribution measurements: Multiple resurfacing episodes and differential isochron fitting. *Icarus*, 226, 885–890.

Michael, G. G., & Neukum, G. (2010). Planetary surface dating from crater size-frequency distribution measurements: Partial resurfacing events and statistical age uncertainty. *Earth and Planetary Science Letters*, 294, 223–229.

Michael, G. G., Basilevsky, A., & Neukum, G. (2018). On the history of the early meteoritic bombardment of the Moon: Was there a terminal lunar cataclysm? *Icarus*, 302, 80–103.

Michael, G. G., Kneissl, T., & Neesemann, A. (2016). Planetary surface dating from crater size-frequency distribution measurements: Poisson timing analysis. *Icarus*, 277, 279–285.

Miljković, K. Wieczorek, M. A., Collins, G. S., Laneuville, M., Neumann, G. A., Melosh, H. J., Solomon, S. C., Phillips, R. J., Smith, D. E., & Zuber, M. T. (2013). Asymmetric

distribution of lunar impact basins caused by variations in target properties. *Science*, 342, 724–726.

Moratto, Z. M., Broxton, M. J., Beyer, R. A., Lundy, M., & Husmann, K. (2010). Ames Stereo Pipeline, NASA's open source automated stereogrammetry software. 41th Lunar and Planetary Science Conference, The Woodlands, TX., Abstract #2364.

Morbidelli, A., Levison, H. F., Tsiganis, K., & Gomes, R. (2005). Chaotic capture of Jupiter's Trojan asteroids in the early Solar System. *Nature*, 435, 462–465.

Morbidelli, A., Marchi, S., Bottke, W. F., & Kring, D. A. (2012). A sawtooth-like timeline for the first billion years of lunar bombardment. *Earth and Planetary Science Letters*, 355–356, 144–151.

Morbidelli, A., Brasser, R., Gomes, R., Levison, H. F., & Tsiganis, K. (2010). 2010. Evidence from the Asteroid Belt for a Violent Past Evolution of Jupiter's Orbit. *The Astronomical Journal*, 140, 1391–1401.

Morbidelli, A., Nesvorny, D., Laurenz, V., Marchi, S., Rubie, D. C., Elkins-Tanton, L., Wieczorek, M., & Jacobson, S. (2018). The timeline of the lunar bombardment: Revisited. *Icarus*, 305, 262–276.

Moriarty, D. P., & Pieters, C. M. (2015). The nature and origin of Mafic Mound in the South Pole-Aitken Basin. *Geophysical Research Letters*, 42, 19, 7907–7915.

Moriarty, D. P., & Pieters, C. M. (2016). Impact melt and magmatic processes in central South Pole-Aitken basin. 47th Lunar and Planetary Science Conference, The Woodlands, TX., Abstract #1735.

Moriarty, D. P., & Pieters, C. M. (2018). The character of South Pole-Aitken basin: patterns of surface and sub-surface composition. *Journal of Geophysical Research*, 123, 3, 729–747, <https://doi.org/10.1002/2017JE005364>

Morrison D. A., & Bussy D. B. J. (2007). The Apollo and Korolev basins and the stratigraphy of the lunar crust. 28th Lunar and Planetary Science Conference, The Woodlands, TX., Abstract #1501.

Nakamura, R., Matsunaga, T., Ogawa, Y., Yamamoto, S., Hiroi, T., Saiki, K., Hirata, N., Arai, T., Kitazato, K., Takeda, H., Sugihara, T., Kodama, S., Ohtake, M., Haruyama, J., & Yokota, Y. (2009). Ultramafic impact melt sheet beneath the South Pole-Aitken basin on the Moon. *Geophysical Research Letters*, 36, 22.

National Research Council (2007). The scientific context for exploration of the Moon: final report. The National Academies Press, Washington, D.C., p. 108.

National Research Council (2011). Vision and voyages in the planetary science at the decade. The National Academies Press, Washington, D.C., p. 398.

Neukum, G. (1971). Untersuchungen über Einschlagskrater auf dem Mond. Thesis, University of Heidelberg.

Neukum, G. (1977). Lunar cratering. Philosophical Transactions of the Royal Society of London, Series A, Mathematical and Physical Sciences, 285, 267–272.

Neukum, G. (1983). Meteoritenbombardement und datierung planetarer oberflaechen. Habilitation Thesis, Ludwig-Maximilians Universität München, Fakultät für Geowissenschaften, München, Germany, p. 186.

Neukum, G., & Ivanov, B. A. (1994). Crater size distributions and impact probabilities on Earth from lunar, terrestrial planet, and asteroid cratering data. Eds. by Gehrels, T., Matthews, M. S., Schumann, A. M., Hazards Due to Comets and Asteroids, 359–416, University of Arizona Press, Tucson, AZ.

Neukum, G. & Koenig, B. (1976). Dating of individual lunar craters. 7th Lunar Science Conference, The Woodlands, TX, Proceedings, Volume 3. New York, Pergamon Press, Inc., p. 2867-2881. (A77-34651 15-91)

Neukum, G. & Wise, D. U. (1976). Mars: A standard crater curve and possible new time scale. Science, 194, 1381–1387.

Neukum, G., Ivanov, B. A., & Hartmann, W. K. (2001a). Cratering Records in the Inner Solar System in Relation to the Lunar Reference System. Space and Science Reviews, 96, 55–86.

Neukum, G., König, B., & Arkani-Hamed, J. (1975). A Study of Lunar Impact Crater Size Distributions. The Moon, 12, 201–229.

Neukum, G., Oberst, J., Hoffmann, H., Wagner, R., & Ivanov, B. A. (2001b). Geologic evolution and cratering history of Mercury. Planetary and Space Science, 49, 1507–1521.

Neumann, G. A., Zuber, M. T., Wieczorek, M. A., Head, J. W., Baker, D. M., Solomon, S. C., Smith, D. E., Lemoine, F. G., Mazarico, E., Sabaka, T. J., Goossens, S. J., Melosh, H. J., Phillips, R. J., Asmar, S. W., Konopliv, A. S., Williams, J. G., Sori, M. M., Soderblom, J. M., Miljković, K., Andrews-Hanna, J. C., Nimmo, F., & Kiefer, W. S. (2015). Lunar impact basins revealed by Gravity Recovery and Interior Laboratory measurements. Science Advances, 1, e1500852.

Norman, M. D., & Nemchin, A., A. (2014). A 4.2 billion year old impact basin on the Moon: U--Pb dating of zirconolite and apatite in lunar melt rock 67955. *Earth and Planetary Science Letters*, 388, 387–398.

Norman, M. D., Duncan, R. A., & Huard, J. J. (2006). Identifying impact events within the lunar cataclysm from ^{40}Ar - ^{39}Ar ages and compositions of Apollo 16 impact melt rocks. *Geochimica et Cosmochimica Acta*, 70, 6032–6049.

Norman, M. D., Duncan, R. A., & Huard, J. J. (2010). Imbrium provenance for the Apollo 16 Descartes terrain: Argon ages and geochemistry of lunar breccias 67016 and 67455. *Geochimica et Cosmochimica Acta*, 74, 763–783.

Noyelles, B., Frouard, J., Makarov, V. V., & Efroimsky, M. (2014). Spin-orbit evolution of Mercury revisited. *Icarus*, 241, 26–44.

Oberbeck, V. R., & Quaide, W. L. (1968). Genetic implications of Lunar regolith thickness variations. *Icarus*, 9, 1, 446–465.

Oberbeck, V. R., Quaide, W. L., Arvidson, R. E., & Aggarwall, H. R. (1977). Comparative studies of lunar, Martian, and Mercurian craters and plains. *Journal of Geophysical Research*, 82, 1687–1698.

Oberst, J., Christou, A., Suggs, R., Moser, D., Daubar, I. J., McEwen, A. S., Burchell, M., Kawamura, T., Hiesinger, H., Wünnemann, K., Wagner, R., & Robinson, M. S. (2012). The present-day flux of large meteoroids on the lunar surface—a synthesis of models and observational techniques. *Planetary and Space Science* 74, 179–193.

O'Brien, D. P., & Greenberg, R. (2003). Steady-state size distributions for collisional populations: analytical solution with size-dependent strength. *Icarus*, 164, 334–345.

Öhman, T., & Kring, D.A. (2012). Photogeologic analysis of impact melt-rich lithologies in Kepler crater that could be sampled by future missions. *Journal of Geophysical Research*, 117, E12.

Ohtake, M., Uemoto, K., Yokota, Y., Morota, T., Yamamoto, S., Nakamura, R., Haruyama, J., Iwata, T., Matsunaga, T., & Ishihara, I. (2014). Geologic structure generated by large-impact basin formation observed at the South Pole-Aitken basin on the Moon. *Geophysical Research Letters*, 41, 2738–2745.

Ohtake, M., Pieters, C. M., Isaacson, P., Besse, S., Yokota, Y., Matsunaga, T., Boardman, J., Yamamoto, S., Haruyama, J., Staid, M., Mall, U., & Green, R. O. (2013). One Moon, Many Measurements 3: Spectral reflectance. *Icarus*, 226, 364–374, <http://dx.doi.org/10.1016/j.icarus.2013.05.010>

Öpik, E. J. (1960). The lunar surface as an impact counter. *Monthly Notices of the Royal Astronomical Society*, 120, 404–411.

Orgel, C., Fassett, C. I., Michael, G., Riedel, C., van der Bogert, C. H., & Hiesinger, H. (2020). Re-examination of the population, stratigraphy, and sequence of mercurian basins: Implications for Mercury's early impact history and comparison with the Moon. *Journal of Geophysical Research*, Accepted manuscript on 1. April 2020, DOI: [10.1029/2019JE006212](https://doi.org/10.1029/2019JE006212).

Orgel, C., Michael, G. G., Fassett, C. I., Van der Bogert, C. H., Riedel, C., Kneissl, T., & Hiesinger, H. (2018). Ancient bombardment of the inner solar system - Reinvestigation of the 'fingerprints' of different impactor populations on the lunar surface. *Journal of Geophysical Research*, 123, 3, 748–762. <https://doi.org/10.1002/2017JE005451>

Orgel, C., Ivanov, M. A., Hiesinger, H., Prissang, R., Michael, G., van der Bogert, C. H., Pasckert, J. H., & Walter, S. H. G. Characterization of high-priority landing sites for robotic exploration missions in the Apollo basin, Moon. Manuscript in preparation to *Planetary Science Journal*.

Orgel, C., Allender, E. J., Almeida, N. V., Cook, J., Ende, J. J., Kamps, O., Mazrouei, S., Slezak, T. J., Soini, A. J., & Kring, D. A. (2017). Landing site assessment for Phase-2 of eDSH-enabled Lunar missions being examined as an ISECG's GER mission scenario. 5th European Lunar Symposium, Münster, Germany, 167–168.

Osinski, G. R., & Pierazzo, E. (2012). Impact cratering: processes and products. Eds. by Osinski, G. R. and Pierazzo, E. *Impact cratering: processes and products*. Wiley-Blackwell, p. 330, ISBN: 978-1-405-19829-5.

Ostrach, L. R., Robinson, M. S., & Denevi, B. W. (2012). Distribution of impact melt on Mercury and the Moon. 43th Lunar and Planetary Science Conference, The Woodlands, TX., Abstract #1113.

Ostrach, L. R., Robinson, M. S., Whitten, J. L., Fassett, C. I., Strom, R. G., Head, J. W., & Solomon, S. C. (2015). Extent, age, and resurfacing history of the northern smooth plains on Mercury from MESSENGER observations. *Icarus*, 250, 602–622.

O'Sullivan, K., Kohout, T., Thaisen, K., & Kring, D. A. (2011). Calibrating several key lunar stratigraphic units representing 4 b.y. of lunar history within Schrödinger basin. *Recent Advances and Current Research Issues in Lunar Stratigraphy*. Geological Society of America Special Paper, 477, 117–127.

Padovan, S., Wieczorek, M. A., Margot, J-L., Tosi, N., & Solomon, S. C. (2015). Thickness of the crust of Mercury from geoid-to-topography ratios. *Geophysical Research Letters*, 42, 1029–1038.

Paige, D. A., Siegler, M. A., Zhang, J. A., Hayne, P. O., Foote, E. J., Bennett, K. A., Vasavada, A. R., Greenhagen, B. T., Schofield, J. T., McCleese, D. J., Foote, M. C., DeJong, E., Bills, B. G., Hartford, W., Murray, B. C., Allen, C. C., Snook, K., Soderblom, L. A., Calcutt, S., Taylor, F. W., Bowles, N. E., Bandfield, J. L., Elphic, R., Ghent, R., Glotch, T. D., Wyatt, M. B., & Lucey, P. G. (2010). Diviner lunar radiometer observations of cold traps in the Moon's south polar region. *Science*, 330, 6003, 479–482.

Pasckert, J. H., Hiesinger, H., & van der Bogert, C. H. (2018). Lunar farside volcanism in and around the South Pole-Aitken basin. *Icarus*, 299, 538–562.

Petro, N. E., & Jolliff, B. L. (2011). Basin and crater ejecta contributions to the South Pole-Aitken basin (SPA) regolith; positive implications for robotic surface samples. *Journal of Geophysical Research*, 109, E6.

Petro, N. E., & Pieters, C. M. (2004). Surviving the heavy bombardment: ancient material at the surface of South Pole-Aitken basin. *Journal of Geophysical Research*, 109, E6.

Pierazzo, E., Vickery, A. M., & Melosh, H. J. (1997). A Reevaluation of Impact Melt Production. *Icarus*, 127, 408–423.

Pieters, C. M., Head, J. W., Gaddis, L., Jolliff, B., & Duke, M. (2001). Rock types of South Pole-Aitken basin and extent of basaltic volcanism. *Journal of Geophysical Research*, 106, E11, 28001–28022.

Pieters, C. M., Boardman, J., Buratti, B., Chatterjee, A., Clark, R., Glavich, T., Green, R., Head, J. W. III, Isaacson, P., Malaret, E., McCord, T., Mustard, J., Petro, N., Runyon, C., Staid, M., Sunshine, J., Taylor, L., Tompkins, S., Varanasi, P., & White, M. (2009). The Moon Mineralogy Mapper (M3) on Chandrayaan-1. *Current Science*, 96, 4, 500–505.

Pike, R. J. (1980). Control of crater morphology by gravity and target type: Mars, Earth, Moon. 11th Lunar and Planetary Science Conference, 2159–2189.

Pike, R. J. (1988). Geomorphology of impact craters on Mercury. Eds by Vilas, F., Chapman, C. R., Matthews, M. S., Mercury. University of Arizona Press, Tucson, AZ, 165–273.

Potter, R. W. K., Head, J. W., Guo, D., Liu, J., & Xiao, L. (2018). The Apollo peak-ring impact basin: Insights into the structure and evolution of the South Pole–Aitken basin. *Icarus*, 306, 139–149.

Potts, N. J., Gullikson, A. L., Curran, N. M., Dhaliwal, J. K., Leader, M. K., Rege, R. N., & Kring, D. A. (2015). Robotic traverse and sample return strategies for a lunar farside mission to the Schrödinger basin. *Advances in Space Research*, 55, 1241–1254.

Povilaitis, R. Z., Robinson, M., S., van der Bogert, C., H., Hiesinger, H., Meyer, H., M., & Ostrach, L., R. (2017). Crater density differences: Exploring regional resurfacing, secondary crater populations, and crater saturation equilibrium on the moon. *Planetary and Space Science*, <https://doi.org/10.1016/j.pss.2017.05.006>

Platz, T., Michael, G., Tanaka, K. L., Skinner, J. A., & Fortezzo, C. M. (2013). Crater-based dating of geological units on Mars: Methods and application for the new global geological map. *Icarus*, 225, 1, 806–827, <http://doi:10.1016/j.icarus.2013.04.021>

Prieur, N. C., Rolf, T., Wünnemann, K., & Werner, S. C. (2018). Formation of simple impact craters in layered targets: Implications for lunar crater morphology and regolith thickness. *Journal of Geophysical Research*, 123, <https://doi.org/10.1029/2017JE005463>

Prockter, L. M., Ernst, C. M., Denevi, B. W., Chapman, C. R., Head, J. W., Fassett, C. I., Merline, W. J., Solomon, S. C., Watters, T. R., Strom, R. G., Cremonese, G., Marchi, S., & Massironi, M. (2010). Evidence for young volcanism on Mercury from the third MESSENGER flyby. *Science*, 329, 668–671.

Qiao, L., Zhu, P., Fang, G., Xiao, Z., Zou, Y., Zhao, J., Zhao, N., Yuan, Y., Qiao, L., Zhang, X., Zhang, H., Wang, J., Huang, J., Huang, Q., He, Q., Zhou, B., Ji, Y., Zhang, Q., Shen, S., Li, Y., & Gao, Y. (2015). A young multilayered terrane of the northern Mare Imbrium revealed by Chang'E-3 mission. *Science*, 347, 6227, 1226–1229.

Qingyun, D., Fei, L., Jianguo, Y., Zhiyong, X., & Rodriguez, J. A. P. (2018). Buried Impact Features on Mercury as Revealed by Gravity Data. *Journal of Geophysical Research*, 123, 11, 3005–3019.

Quaide, W. L., & Oberbeck, V. R. (1968). Thickness determinations of the lunar surface layer from lunar impact craters. *Journal of Geophysical Research*, 73, 16, 5247–5270. <https://doi.org/10.1029/JB073i016p05247>

Riedel, C., Michael, G. G., & Kneissl, T. (2017). Crater counting on heavily cratered surfaces: Implementing non-sparseness correction in an ArcGIS independent tool for

planetary surface dating. 3rd Planetary Data Workshop 2017, LPI Contribution 1986, Abstract #7017.

Riedel C., Michael, G., Kneissl, T., Orgel, C., Hiesinger, H. & van der Bogert, C. H. (2018). A New Tool to Account for Crater Obliteration Effects in Crater Size-Frequency Distribution Measurements. *Earth and Space Science*, 5, 258–267. <https://doi.org/10.1002/2018EA000383>

Robbins, S. J. (2014). New crater calibrations for the lunar crater-age chronology. *Earth and Planetary Science Letters*, 403, 188–198.

Robinson, M. S., Murchie, S. L., Blewett, D. T., Domingue, D. L., Hawkins, S. E., Head, J. W., Holsclaw, G. M., McClintock, W. E., McCoy, T. J., McNutt, R. L., Prockter, L. M., Solomon, S. C., & Watters, R. T. (2008). Reflectance and color variations on Mercury: Regolith processes and compositional heterogeneity. *Science*, 321, 66–69.

Robinson, M. S., Brylow, S. M., Tschimmel, M., Humm, D., Lawrence, S. J., Thomas, P. C., Denevi, B. W., Bowman-Cisneros, E., Zerr, J., Ravine, M. A., Caplinger, M. A., Ghaemi, F. T., Schaffner, J. A., Malin, M. C., Mahanti, P., Bartels, A., Anderson, J., Tran, T. N., Eliason, E. M., McEwen, A. S., Turtle, E., Jolliff, B. L., & Hiesinger, H. (2010). Lunar Reconnaissance Orbiter Camera (LROC) Instrument Overview. *Space Science Reviews*, 150, 81–124.

Roberts, J. H. & Barnouin, O. S. (2012). The effect of the Caloris impact on the mantle dynamics and volcanism on Mercury. *Journal of Geophysical Research*, 117, E02007.

Runyon, K., Blair, D. M., Lemelin, M., Nowka, D., Roberts, C. E., Paige, D. A., Spudis, P., & Kring, D. A. (2012). Volatiles at the lunar south pole: a case study for a mission to Amundsen. 43rd Lunar and Planetary Science, The Woodlands, TX., Abstract # 1619.

Ryder G. (1990). Lunar samples, lunar accretion and the early bombardment of the Moon. *Earth and Space Science News*, 71, 10, 313–323.

Ryder G. (2002). Mass flux in the ancient Earth–Moon system and benign implications for the origin of life on Earth. *Journal of Geophysical Research*, 107, E4, 5022, <http://doi:10.1029/2001JE001583>

Sanin, A. B., Mitrofanov, I. G., Litvak, M. L., Malakhov, A., Boynton, W. V., Chin, G., Droege, G., Evans, L. G., Garvin, J., Golovin, D. V., Harshman, K., McClanahan, T. P., Mokrousov, M. I., Mazarico, E., Milikh, G., Neumann, G., Sagdeev, R., Smith, D. E., Starr, R. D., & Zuber, M. T. (2012). Testing lunar permanently shadowed regions for water ice: LEND results from LRO. *Journal of Geophysical Research*, 117, E12.

Schmidt, R. M., & Housen, K. R. (1987). Some recent advances in the scaling of impact and explosion cratering. *International Journal of Impact Engineering*, 5, 543–560.

Schmitt, H., H., Petro, N., E., Wells, R., A., Robinson, M., S., Weiss, B., P., & Mercer, C. M. (2017). Revisiting the field geology of Taurus-Littrow. *Icarus*, 298, 2–33.

Senthil Kumar, P., Keerthi, V., Senthil Kumar, A., Mustard, J., Gopala Krishna, B., Amitabh, Ostrach, L. R., Kring, D. A., Kiran Kumar, A. S., & Goswami, J. N. (2013). Gullies and landslides on the moon: evidence for dry-granular flows. *Journal of Geophysical Research*, 118, 2, 206–223.

Senthil Kumar, P., Sruthi, U., Krishna, N., Lakshmi, K.J.P., Menon, R., Amitabh, , Gopala Krishna, B., Kring, D. A., Head, J. W., Goswami, J. N., & Kiran Kumar, A. S. (2016). Recent shallow moonquake and impact-triggered boulder falls on the Moon: new insights from the Schrödinger basin. *Journal of Geophysical Research*, 121, 2, 147–179.

Siegler, M. A., Bills, B. G., & Paige, D. A. (2013). Orbital eccentricity driven temperature variation at Mercury's poles. *Journal of Geophysical Research*, 118, 930–937.

Shearer, C., Neal, C., Borg, L., Jolliff, B., Papanastassiou, D., Treiman, A., Floss, C., Rutherford, M., Norman, M., & Farquhar, J. (2007). Analysis of lunar sample mass capability for the lunar exploration architecture. CAPTEM Analysis Document, https://www.lpi.usra.edu/lunar/strategies/captem_sample_return.pdf

Shearer, C. K., Hess, P. C., Wieczorek, M. A., Pritchard, M. E., Parmentier, E. M., Borg, L. E., Longhi, J., Elkins-Tanton, L. T., Neal, C. R., Antonenko, I., Canup, R. M., Halliday, A. N., Grove, T. L., Hager, B. H., Lee, D-C., & Wiechert, U. (2006). Thermal and magmatic evolution of the Moon. *Reviews in Mineralogy and Geochemistry*, 60, 1, 365–518, <https://doi.org/10.2138/rmg.2006.60.4>

Shoemaker, E., M. (1965). Preliminary analysis of the fine structure of the lunar surface in Mare Cognitum. *International Astronomical Union Colloquium*, 5, 23–77.

Shoemaker, E. M. (1977). Astronomically Observable Crater-forming Projectiles. Eds by D. J. Roddy, R. O. Pepin, and R. B. Merrill, *Impact and Explosion Cratering*, Pergamon Press, New York, 639–656.

Shoemaker, E. M., & Hackmann, R. J. (1962). Stratigraphic basis for a lunar time scale, in the Moon. Eds. by Z. Kopal & Z. K. Mikhailov, *IAU Symposium*, vol. 14, 289–300, Academic Press, London and New York.

Shoemaker, E., Robinson, M., & Eliason, E. (1994). The south pole region of the Moon as seen by Clementine. *Science*, 266, 5192, 1851–1854.

Smith, D. E., Zuber, M. T., Jackson, G. B., Cavanaugh, J. F., Neumann, G. A., Riris H. ...& Zagwodzki, T. W. (2010). The Lunar Orbiter Laser Altimeter investigation on the Lunar Reconnaissance Orbiter Mission. *Space Science Reviews*, 150, 209–241.

Smith, D. E., Zuber, M. T., Neumann, G. A., Lemoine, F. G., Mazarico, E., Torrence, M. H., McGarry, J. F., Rowlands, D. D., Head, J. W., Duxbury, T. H., Aharonson, O., Lucey, P. G., Robinson, M. S., Barnouin, O. S., Cavanaugh, J. F., Sun, X., Liiva, P., Mao, D., Smith, J. C., & Bartels, A. E. (2010). Initial observations from the Lunar Orbiter Laser Altimeter (LOLA). *Geophysical Research Letters*, 37, 18, <https://doi.org/10.1029/2010GL043751>

Smith, D. E., Zuber, M. T., Neumann, G. A., Mazarico, E., Lemoine, F. G., Head, J. W....& Mcclanahan, T. (2017). Summary of the results from the lunar orbiter laser altimeter after seven years in lunar orbit. *Icarus*, 283, 70–91.

Snape, J., F., Nemchin, A., A., Grange, M., L., Bellucci, J., J., Thiessen, F., Whitehouse, M., J. (2016). Phosphate ages in Apollo 14 breccias: Resolving multiple impact events with high precision U-Pb SIMS analyses. *Geochimica et Cosmochimica Acta*, 174, 13–29.

Spudis, P. D., & Guest, J. E. (1988). Stratigraphy and geologic history of Mercury. Eds. by F. Vilas, C. R. Chapman, and M. S. Matthews, Mercury, 118–164, Univ. of Arizona Press, Tucson, AZ.

Spudis, P. D., Wilhelms, D., E., Robinson, M., S. (2011). The Sculptured Hills of the Taurus Highlands: Implications for the relative age of Serenitatis basin chronologies and the cratering history of the Moon. *Journal of Geophysical Research*, 116, E00H03.

Spudis, P. D., Bussey, B., Plescia, J., Josset, J. L., & Beau-Vivre, S. (2008). Geology of Shackleton crater and the South Pole of the Moon. *Geophysical Research Letters*, 35, 14.

Sruthi, U., & Kumar, P. S. (2014). Volcanism on farside of the Moon: new evidence from Antoniadi in South Pole-Aitken basin. *Icarus*, 242, 249–268.

Steenstra, E. S., Martin, D. J., McDonald, F. E., Paisarnsombat, S., Venturino, C., O'Hara, S., Calzada-Diaz, A., Bottoms, S., Leader, M. K., Klaus, K. K., & van Westrenen, W. (2016). Analyses of robotic traverses and sample sites in the Schrödinger basin for the (HERACLES) human-assisted sample return mission concept. *Advances in Space Research*, 58, 1050–1065.

Stöffler, D. & Grieve, R. A. F. (2007). Impactites. Eds. by Fettes, D. and Desmons, J., *Metamorphic Rocks: A Classification and Glossary of Terms, Recommendations of the International Union of Geological Sciences*. Cambridge University Press, Cambridge, UK, 82–92, 111–125, and 126–242.

Stöffler, D., & Ryder, G. (2001). Stratigraphy and isotope ages of lunar geologic units: Chronological standard for the inner solar system. *Space Science Reviews*, 96, 9–54.

Stöffler, D., Ryder, G., Ivanov, B., A., Artemieva, N., A., Cintala, M., J., & Grieve, R., A., F. (2006). Cratering history and Lunar chronology. *Reviews in Mineralogy and Geochemistry*, 60, 519–596.

Stöffler, D., Bischoff, A., Borchardt, R., Burghelle, A., Deutsch, A., Jessberger, E., K., Ostertag, R., Palme, H., Spettel, B., Reimold, U., W., Wacker, K., & Winke, H. (1985). Composition and evolution of the lunar crust in the Descartes Highlands, Apollo 16. *Journal of Geophysical Research*, 90, S02, C449–C506.

Stuart-Alexander, D. (1978). Geological map of the central far side of the Moon. United States Geological Service Map, I-1047.

Stuart-Alexander, D. E., & Howard, K. A. (1970). Geologic map of the central far side of the Moon. United States Geological Service Map, I-1047.

Strom, R. G. (1977). Origin and relative age of lunar and mercurian intercrater plains. *Physics of Earth and Planetary Interiors*, 15, 156–172.

Strom, R. G., & Neukum, G. (1988). The cratering record on Mercury and the origin of impacting objects. in *Mercury*, 336–373, University of Arizona Press, Tucson, AZ.

Strom, R. G., Trask, N. J., & Guest, H. E. (1975). Tectonism and volcanism on Mercury. *Journal of Geophysical Research*, 80, 2478–2507.

Strom, R. G., Malhotra, R., Ito, T., Yoshida, F., & Kring, D. A. (2005). The origin of planetary impactors in the inner Solar System. *Science*, 309, 1847–1850.

Strom, R. G., Malhotra, R., Xiao, Z.-Y., Ito, T., Yoshida, F., & Ostrach, J. R. (2015). The inner solar system cratering record and the evolution of impactor populations. *Research in Astronomy and Astrophysics*, 15, 3, 407–434.

Strom, R., Banks, M. E., Chapman, C. R., Fassett, C. I., Forde, J. A., Head, J. W., Merline, W. J., Prockter, L. M., & Solomon, S. C. (2011). Mercury crater statistics from MESSENGER flybys: Implications for stratigraphy and resurfacing history. *Planetary and Space Science*, 59, 1960–1967.

Swindle, T., D., Spudis, P., D., Taylor, G., J., Korotev, R., L., Nichols, R., H., Jr., & Olinger, C., T. (1991). Searching for Crisium basin ejecta: Chemistry and ages of Luna 20 impact melts. 21th Lunar and Planetary Science Conference, Houston, TX, Proceedings 167–181.

Tanaka K. L. (1982). A new time-saving crater-count technique, with application to narrow features. NASA Technical Memorandum, TM-85127, 123–125.

Tera, F., Papanastassiou, D. A., & Wasserburg, G. J. (1974). Isotopic evidence for a terminal lunar cataclysm. *Earth and Planetary Science Letters*, 22, 1–21.

The Vision for Space Exploration (2004). NASA Headquarters, Washington, D.C., NP-200401-334-HQ,
https://www.nasa.gov/pdf/55583main_vision_space_exploration2.pdf

Thiessen, F., Hiesinger, H., van der Bogert, C. H., Pasckert, J.H., & Robinson, M.S. (2012). Surface Ages and Mineralogy of Lunar Light Plains in the South-Pole Aitken Basin. 43rd Lunar and Planetary Science Conference, The Woodlands, TX, Abstract #2060.

Thomas, R. J., Rothery, D. A., Conway, S. J., & Anand, M. (2014). Long-lived explosive volcanism on Mercury. *Geophysical Research Letters*, 41, 6084–6092,
<http://doi:10.1002/2014GL061224>

Tosi, N., Čadek, O., Běhouňková, M., Káňová, M., Plesa, A.-C., Grott, M., & Wiczorek, M. A. (2015). Mercury's low-degree geoid and topography controlled by insolation-driven elastic deformation. *Geophysical Research Letters*, 42, 18, 7327–7335. <https://doi.org/10.1002/2015GL065314>

Trang, D., Gillis-Davis, J., Williams, K., Bussey, D.B.J., Spudis, P.D., Carter, L.M., Neish, C.D., Thompson, B., & Patterson, W. (2010). Using Mini-RF to investigate the anomalous UVVIS spectrum in the Apollo and Plato region. 41th Lunar and Planetary Science Conference, The Woodlands, TX, Abstract #2652.

Trask, N. J., & Guest, J. E. (1975). Preliminary geologic terrain map of Mercury. *Journal of Geophysical Research*, 80, 2461–2477,
<http://doi:10.1029/JB080i017p02461>

Tsiganis, K., Gomes, R., Morbidelli, A., & Levison, H. F. (2005). Origin of the orbital architecture of the giant planets of the Solar System. *Nature*, 435, 459–461.

Vago, J. L., Westall, F., Pasteur Instrument Teams, Landing Site Selection Working Group, Coates, A. J., Jaumann, R., Korablev, O...& the ExoMars Project Team

(2017). Habitability on early Mars and the search for biosignatures with the ExoMars Rover. *Astrobiology*, 17, 6–7, 471–510.

van der Bogert, C. H., Hiesinger, H., & Spudis, P. (2017). The age of the Crisium impact basin. *New Views of the Moon 2*, Münster, Germany, LPI Contribution Nr. 1988, Abstract #6009.

van der Bogert, C. H., Hiesinger, H., Spudis, P., Runyon, K. D., & Denevi, B. W. (2018). The age of the Crisium impact basin. 49th Lunar and Planetary Science Conference, The Woodlands, TX, Abstract #1028.

van der Bogert, C. H., Michael, G., Kneissl, T., Hiesinger, H., & Pasckert, J. H. (2015). Effects of count area size on absolute model ages derived from random crater size-frequency distributions. 46th Lunar and Planetary Science Conference, The Woodlands, TX, Abstract #1742.

van der Bogert, C. H., Hiesinger, H., Dundas, C. M., Krüger, T., McEwen, A. S., Zanetti, M., & Robinson, M. S. (2017). Origin of discrepancies between crater size-frequency distributions of coeval lunar geologic units via target property contrasts. *Icarus*, 298, 49–63, <http://doi:10.1016/j.icarus.2016.11.040>

Vander Kaaden, K. E., & McCubbin, F. M. (2015). Exotic crust formation on Mercury: Consequences of shallow, FeO-poor mantle. *Journal of Geophysical Research*, 120, 195–209, <http://doi:10.1002/2014JE004733>

Vasavada, A. R., Paige, D. A., & Wood, S. E. (1999). Near-surface temperatures on Mercury and the Moon and the stability of polar ice deposits. *Icarus*, 141, 179–193.

Vaughan, W. M., & Head, J. W. (2014). Impact melt differentiation in the South Pole-Aitken basin: some observations and speculations. *Planetary and Space Science*, 91, 101–106.

Wang, Q., & Liu, J. (2016). A Chang'e-4 mission concept and vision of future Chinese lunar exploration activities. *Acta Astronautica*, 127, 678–683.

Wartho, J.-A., Kelley, S. P., & Elphick, S. C. (2014). Ar diffusion and solubility measurements in plagioclases using the ultra-violet laser depth-profiling technique. Geological Society, London, Special Publications, 378, 137–154.

Watson, K., Murray, B. C., & Brown, H. (1961). The behavior of volatiles on the lunar surface. *Journal of Geophysical Research*, 66, 9, 3033–3045.

Watters, T. R., Head, J. W., Solomon, S. C., Robinson, M. S., Chapman, C. R., Denevi, Fassett, C. I., Murchie, S. L., & Strom, R. G. (2009). Evolution of the Rembrandt impact basin on Mercury, *Science*, 324, 618–621.

Weider, S. Z., Nittler, L. R., Starr, R. D., Crapster-Pregont, E. J., Peplowski, P. N., Denevi, B. W., Head, J. W., Byrne, P. K., Hauck, S. A., Ebel, D. S., & Solomon, S. C. (2015). Evidence for geochemical terranes on Mercury: Global mapping of major elements with MESSENGER's X-Ray Spectrometer. *Earth and Planetary Science Letters*, 416, 109–120.

Werner, S. C. (2014). Moon, Mars, Mercury: Basin formation ages and implications for the maximum surface age and the migration of gaseous planets. *Earth and Planetary Science Letters*, 400, 54–65.

Werner, S. C., & Ivanov, B. A. (2015). Exogenic Dynamics, Cratering, and Surface Ages. Eds. by Schubert, G., *Treatise on Geophysics (Second Edition)*, 10, 327–365. <http://dx.doi.org/10.1016/B978-0-444-53802-4.00170-6>

Whitley, R., Landgraf, M., Sato, N., Picard, M., Goodliff, K., Stephenson, K., Narita, S., Gonthier, Y., Cowley, A., Hosseini, S., & Schonenborg, R. (2017). Global Exploration Roadmap derived concept for human exploration of the Moon. Global Space Exploration Conference, Beijing, China.

Whitley, R., & Martinez, R. (2016). Options for staging orbits in cislunar space. *IEEE Aerospace Conference*. 1–9.

Whitten, J. L., & Head, J. W. (2015). Rembrandt impact basin: Distinguishing between volcanic and impact-produced plains on Mercury. *Icarus*, 258, 350–365.

Whitten, J. L., Head, J. W., Denevi, B. W., & Solomon, S. C. (2014). Inter crater plains on Mercury: Insights into unit definition, characterization, and origin from MESSENGER datasets. *Icarus*, 241, 97–113.

Wichman R. W., & Schultz P. H. (1989). Sequence and mechanisms of deformation around the Hellas and Isidis impact basins on Mars. *Journal of Geophysical Research*, 94, 17333–17357.

Wieczorek, M. A., & Phillips, R. J. (2000). The "Procellarum KREEP Terrane": Implications for mare volcanism and lunar evolution. *Journal of Geophysical Research*, 105, E8, 20, 417–20,430. <https://doi.org/10.1029/1999JE001092>

Wieczorek, M. A., Correia, A. C. M., Le Feuvre, M., Laskar, J., & Rambaux, N. (2012). Mercury's spin-orbit resonance explained by initial retrograde and subsequent synchronous rotation. *Nature Geosciences*, 5, 18–21.

Wieczorek, M. A., Neumann, G. A., Nimmo, F., Kiefer, W. S., Taylor, G. J., Melosh, H. J., Phillips, R. J., Solomon, S. C., Andrews-Hanna, J. C., Asmar, S. W., Konopliv, A. S., Lemoine, F. G., Smith, D. E., Watkins, M. M., Williams, J. G., & Zuber, M. T. (2013). The crust of the Moon as seen by GRAIL. *Science*, 339, 671–675.

Williams, J.-P., Ruiz, J., Rosenburg, M. A., Aharonson, O., & R. J. Phillips (2011). Insolation driven variations of Mercury's lithospheric strength. *Journal of Geophysical Research*, 116, E01008, <https://doi.org/10.1029/2010JE003655>

Wilhelms, D. E. (1976). Mercurian volcanism questioned. *Icarus*, 28, 551–558.

Wilhelms, D. E. (1987). The geologic history of the Moon. USGS Special Paper 1348.

Wilhelms, D. E., & McCauley, J. F. (1971). Geologic map of the near side of the Moon. U.S. Geological Survey. Map, I-703.

Wilhelms, D. E. (1979). Relative ages of lunar basins. Report of Planetary Geology Programme. 1978–1979, NASA TM 80339, 135–137.

Wilhelms, D. E., Howard, K. A., & Wilshire, H. G. (1979). Geologic map of the south side of the Moon. No. I-1162.

Woronow, A. (1977). Crater saturation and equilibrium: a Monte Carlo simulation. *Journal of Geophysical Research*, 82, 17, 2447–2456.

Wu, B., Li, F., Ye, L., Qiao, S., Huang, J., Wu, X., & Zhang, H. (2014). Topographic modeling and analysis of the landing site of Chang'E-3 on the Moon. *Earth and Planetary Science Letters*, 405, 257–273.

Wu, W., Li, C., Zuo, W., Zhang, H., Liu, J., Wen, W., Su, Y., Ren, X., Yan, J., Yu, D., Dong, G., Wang, C., Sun, Z., Liu, E., Yang, J., & Ouyang, Z. (2019). Lunar farside to be explored by Chang'e-4. *Nature Geoscience*, 12, 4, 222–223, <https://doi.org/10.1038/s41561-019-0341-7>

Wünnemann, K., Zhu, M.-H., & Stöffler, D. (2016). Impacts into quartz sand: crater formation, shock metamorphism, and ejecta distribution in laboratory experiments and numerical models. *Meteoritics & Planetary Science*, 51, 1762–1794.

Xiao, Z., & Werner, S. C. (2015). Size-frequency distribution of crater populations in equilibrium on the Moon. *Journal of Geophysical Research*, 120, 20, 2277–2292.

Xiao, L., Zhu, P., Fang, G., Xiao, Z., Zou, Y., Zhao, J., Zhao, N., Yuan, Y., Qiao, L., Zhang, X., Zhang, H., Wang, J., Huang, J., Huang, Q., He, Q., Zhou, B., Ji, Y., Zhang,

Q., Shen, S., Li, Y., & Gao, Y. (2015). A young multilayered terrane of the northern Mare Imbrium revealed by Chang'E-3 mission. *Science*, 347, 6227, 1226–1229.

Yamamoto, S., Nakamura, R., Matsunaga, T., Ogawa, Y., Ishihara, Y., Morota, T., Hirata, N., Ohtake, M., Hiroi, T., Yokota, Y., & Haruyama, J. (2012). Olivine-rich exposures in the South Pole-Aitken basin. *Icarus*, 218, 331–344.

Yingst, A., & Head, J. W. (1999). Geology of mare deposits in South-Pole Aitken basin as seen by Clementine UVVIS data. *Journal Geophysical Research*, 104, E8, 18957–18979, <https://doi.org/10.1029/1999JE900016>

Young, J. (1940). A Statistical Investigation of Diameter and Distribution of Lunar Craters. *J. Brit. Astron. Assoc.*, 50, 309–326.

Zakamska, N. L., & Tremaine, S. (2004). Excitation and propagation of eccentricity disturbances in planetary systems. *The Astronomical Journal*, 128, 869–877.

Zellner, N. E. B. (2017). Cataclysm No More: New Views on the Timing and Delivery of Lunar Impactors. *Astrobiology*, 47, 3, 261–280, <https://doi.org/10.1007/s11084-017-9536-3>

Zhang, J. A., & Paige, D. A. (2009). Cold-trapped organic compounds at the poles of the Moon and Mercury: implications for origins. *Geophysical Research Letters*, 36, 16, L16203, <http://doi:10.1029/2009GL038614>

Zhang, J. A., & Paige, D. A. (2010). Correction to cold-trapped organic compounds at the poles of the Moon and Mercury: implications for origins. *Geophysical Research Letters*, 37, 3, <https://doi.org/10.1029/2009GL041806>

Zuber, M. T., Smith, D. E., Watkins, M. M., Asmar, S. W., Konopliv, A. S., Lemoine, F. G., Melosh, H. J., Neumann, G. A., Phillips, R. J., Solomon, S. C., & Wieczorek, M. A. (2013). Gravity field of the Moon from the Gravity Recovery and Interior Laboratory (GRAIL) mission. *Science*, 339, 6120, 668–671.

Eidesstattliche Erklärung

Hiermit erkläre ich, dass ich die vorliegende Dissertation mit dem Thema

“Early Bombardment History of the Inner Solar System and Links to Future Human and Robotic Exploration Missions to the Moon”

selbstständig verfasst und angefertigt habe und keine anderen als die angegebenen Quellen und Hilfsmittel verwendet habe. Geistiges Eigentum anderer Autoren wurde als solches gekennzeichnet.

Des Weiteren versichere ich, dass ich an keiner anderen Stelle ein Prüfungsverfahren beantragt bzw. die Dissertation in dieser oder anderer Form an keiner anderen Fakultät als Dissertation vorgelegt habe.

Ort, Datum

Unterschrift

CURRICULUM VITAE

Csilla Orgel

EDUCATION

2016 – 2020 Ph.D. Geological Sciences, Freie Universität Berlin, Berlin, Germany

2015 – 2016 M.Sc. Geological Sciences, Freie Universität Berlin, Berlin, Germany

2007 – 2011 B.Sc. Earth Sciences, Eötvös Loránd University, Budapest, Hungary

PROFESSIONAL EMPLOYEMENT AND INTERNSHIPS

2019 Research Fellow on Planetary Surface Exploration
European Space Agency/ESTEC,
Noordwijk, The Netherlands

2018 Visiting Scholar
NASA Marshall Space Flight Center
Huntsville, AL

2017 Visiting Scholar
Westfälische Wilhelms-Universität
Münster, Germany

2016 – 2019 Research Assistant/Student Representative, SFB/TRR-170 Project
Planetary Sciences and Remote Sensing Group, Freie Universität Berlin
Berlin, Germany

2016 CLSE 2016 Exploration Science Summer Intern
Lunar and Planetary Institute
Houston, TX

2014 – 2015 M.Sc. Intern, Erasmus Training Program Scholarship
Deutsches Zentrum für Luft und Raumfahrt (DLR)
Berlin, Germany

2014 – 2016 M.Sc. Intern
Planetary Sciences and Remote Sensing Group, Freie Universität Berlin
Berlin, Germany

2010 – 2015 Volunteer, Analog-Astronaut Trainer, Geologist
Austrian Space Forum, PolAres Project

Innsbruck, Austria

2008 – 2011 B.Sc. Intern/Student Representative
Department of Physical and Applied Geology, Eötvös Loránd University
Budapest, Hungary

2007 – 2008 Volunteer
Hungarian Academy of Sciences, Piskèstetö Observatory

AWARDS

- 2014 Student Travel Grant (DLR)
Alpbach Summer School
Alpbach, Austria
- 2014 Erasmus Training Program Scholarship (5 months)
Deutsches Zentrum für Luft-und Raumfahrt (DLR)
Berlin, Germany
- 2013 Honor of the Association of Hungarian Women in Science
Category: Space Sciences
- 2013 Erasmus Scholarship (2013 Summer Semester)
Freie Universität Berlin
Berlin, Germany
- 2012 Student Travel Grant (European Space Agency, ESA)
International Astronautical Congress
Naples, Italy
- 2011 1st Prize in the National University Science Student Conference
Nyiregyhaza, Hungary
- 2009 1st Prize in the Regional University Student Conference
Budapest, Hungary
- 2004 – 2007 Numerous High School Awards from the Hungarian Astronomical
Association and the Hungarian Astronautical Society

PEER-REVIEWED PAPERS

18. Riedel, C., Minton, D. A., Michael, G., **Orgel, C.**, van der Bogert, C. H., & Hiesinger, H. (2020). Degradation of Small Simple and Large Complex Lunar Craters: Not a Simple Scale Dependence. *Journal of Geophysical Research*, <https://doi.org/10.1029/2019JE006273>
17. **Orgel, C.**, Fassett, C. I., Michael, G., Riedel, C., van der Bogert, C. H., & Hiesinger, H. (2020). Re-examination of the population, stratigraphy, and sequence of mercurian basins: Implications for Mercury's early impact history and comparison with the Moon. *Journal of Geophysical Research*, 125, e2019JE006212, <https://doi.org/10.1029/2019JE006212>
16. Poulet, F., Gross, C., Horgan, B., Loizeau, D., Bishop, J. L., Carter, J., & **Orgel, C.** (2020). Mawrth Vallis, Mars: a fascinating place for in situ exploration. *Astrobiology*, 20, 2, <http://doi:10.1089/ast.2019.2074>
15. Séjourné, A., Costard, F., Swirad, Z. M., Łosiak, A., Bouley, S., Smith, I., Balme, M. R., **Orgel, C.**, Ramsdale, J. D., Hauber, E., Conway, S. J., van Gasselt, S., Reiss, D., Johnsson, A., Gallagher, C., Skinner, J. A., Kereszturi, A., & Platz T. (2019). Mapping the northern plains of Mars: using morphotype and distribution of ice-related landforms to understand multiple ice-rich deposits in Utopia Planitia. *Journal of Geophysical Research*, 124, 2, 483–503, <http://doi:10.1029/2018JE005665>
14. **Orgel, C.**, Hauber, E., van Gasselt, S., Reiss, D., Johnsson, A., Ramsdale, J. D., Smith, I., Swirad, Z. M., Wilson, J. T., Séjourné, A., Balme, M. R., Conway, S. J., Costard, F., Eke, V. R., Gallagher, C., Kereszturi, A., Łosiak, A., Massey, R. J., Platz, T., Skinner, J. A., & Teodoro, L. F. A. (2019). Gridmapping the Northern Plains of Mars: A New Overview of Recent Water- and Ice-Related Landforms in Acidalia Planitia. *Journal of Geophysical Research*, 124, 2, 454–482, <http://doi:10.1029/2018JE005664>
13. Ramsdale, J. D., Balme, M. R., Gallagher, C., Conway, S. J., Smith, I., Hauber, E., **Orgel, C.**, Séjourné, A., Costard, F., Eke, V. R., van Gasselt, S., Johnsson, A., Kereszturi, A., Łosiak, A., Massey, R. J., Platz, T., Reiss, D., Skinner, J. A., Swirad, Z. M., Teodoros, L. F. A., & Wilson, J. T. (2019). Gridmapping the northern plains of Mars: Geomorphological, Radar and Water-Equivalent Hydrogen results from Arcadia Planitia suggest possible fluvial and volcanic systems overlain by a ubiquitous and heavily degraded ice-rich latitude-dependent mantle. *Journal of Geophysical Research*, 124, 2, 504–527, <http://doi:10.1029/2018JE005663>
12. Ivanov, M. A., Hiesinger, H., van der Bogert, C. H., **Orgel, C.**, Paskert, J. H., Head, J. W. 2018: Geologic history of the northern portion of the South Pole-Aitken basin on the Moon. *Journal of Geophysical Research*, 123, 10, 2585–2612, <https://doi.org/10.1029/2018JE005590>

11. Allender, E. J., **Orgel, C.**, Almeida, N. V., Cook, J., Ende, J. J., Kamps, O., Mazrouei, S., Slezak, T. J., Soini, A.-J., & Kring, D. A. (2018). Traverses for the ISECG-GER Design Reference Mission for Humans on the Lunar Surface. *Advances in Space Research*, 63, 1, 692–727, <https://doi.org/10.1016/j.asr.2018.08.032>
10. De Toffoli, B., Pozzobon, R., Mazzarini, F., **Orgel, C.**, Massironi, M., Giacomini, L., Mangold, N., & Cremonese, G. (2018). Estimate of depths of source fluids related to mound fields on Mars. *Planetary and Space Science*, 164, 164–173, <https://doi.org/10.1016/j.pss.2018.07.005>
09. Riedel, C., Michael, G., Kneissl, T., **Orgel, C.**, Hiesinger, H., & van der Bogert, C. H. (2018). A New Tool to Account for Crater Obliteration Effects in Crater Size-Frequency Distribution Measurements. *Earth and Space Science*, 5, 258–267, <https://doi.org/10.1002/2018EA000383>
08. **Orgel, C.**, Michael, G., Fassett, C. I., van der Bogert, C. H., Riedel, C., Kneissl, T., & Hiesinger, H. (2018). Ancient bombardment of the inner Solar System – Reinvestigation of the “fingerprints” of different impactor populations on the lunar surface. *Journal of Geophysical Research*, 123, 3, 748–762, <http://doi.org/10.1002/2017JE005451>
07. Ramsdale, J. D., Balme, M. R., Conway, S. J., Gallagher, C., van Gasselt, S., Hauber, E., **Orgel, C.**, Sejourne, A., Skinner, J. A., Jr., Costard, F., Johnsson, A., Losiak, A., Reiss, D., Swirad, Z., Kereszturi, A., Smith, I., & Platz, T. (2017). Grid-based mapping: a method for rapidly determining the spatial distributions of small features over very large areas. *Planetary and Space Science*, 140, 49–61. <https://doi.org/10.1016/j.pss.2017.04.002>
06. Cross, M., Battler, M., Maiwald, V., van’t Woud, H., Ono, A., Schlacht, I., L., **Orgel, C.**, Foing, B., & Mclsaac, K. (2016). Operational Lessons Learnt from the 2013 ILEWG EuroMoonMars-B Analogue Campaign for Future Habitat Operations on Moon and Mars. *Acta Futura*, 10, 61–73, <https://zenodo.org/record/202179#.XhSbOfIKq2w>
05. Losiak, A., Gołębiewska, I., **Orgel, C.**, Moser, L., MacArthur, J., Boyd, A., Hettrich, S., Wittek, S., Jones, N., & Groemer, G. (2014). Remote Science Support during MARS2013: testing a map-based system of data processing and utilization for the future long-duration planetary missions. *Astrobiology*, 14, 5, 417–430, <http://doi:10.1089/ast.2013.1071>
04. Groemer, G. E., Soucek, A., Frischauf, N., Stumptner, W., Ragonig, C., Sams, S., Bartenstein, T., Haeuplik-Meusburger, S., Petrova, P., Evetts, S., Sivenesan C., & the **MARS2013 Team** (2014). The MARS2013 Mars Analog Mission. *Astrobiology*, 14, 5, 360–376, <https://doi.org/10.1089/ast.2013.1062>

03. Groemer, G. E., Foresta, L., Turetschek, T., & the **MARS2013 Team** (2014). A case for using ground-based thermal inertia measurements to detect Martian caves. *Astrobiology*, 14, 5, 431–437, <https://doi.org/10.1089/ast.2013.1063>
02. Groemer, G. E., Sattler, B., Weisleitner, K., Hunger, L., Kohstall, C., Frisch, A., Jozefowicz, M., Meszynski, S., Storrie-Lombardi, M., & the **MARS2013 Team** (2014). Field trial of a Dual-Wavelength Fluorescent Emission (L.I.F.E) instrument and the Magma White rover during the MARS2013 Mars Analog Mission. *Astrobiology*, 14, 5, 391–405, <https://doi.org/10.1089/ast.2013.1081>
01. **Orgel, C.**, Kereszturi, A., Váczi, T., Groemer, G., & Sattler, B. (2014). Scientific Results and Lessons Learned from an Integrated Crewed Mars Exploration Simulation at the Rio Tinto Mars Analogue Site. *Acta Astronautica*, 94, 2, 736–748, <http://doi:10.1016/j.actaastro.2013.09.014>

ABSTRACTS

Altogether 52 abstracts submitted to various international conferences, e.g. LPSC, EGU, IAC, EPSC, ELS, and Planetary Cryosphere Workshop.

Appendices

Part V presents the Appendices published along with the peer-reviewed publications and related to specific chapters. Due to the extensive nature of the Appendices, they can be found electronically on the attached CD to this thesis.

Appendix A gives Supplementary Information to Chapter 5

CD directory\Csilla_Orgel_PhD\APPENDIX\APPENDIX_A

Appendix B gives Supplementary Information to Chapter 6

CD directory\Csilla_Orgel_PhD\APPENDIX\APPENDIX_B

Appendix C gives Supplementary Information to Chapter 7

CD directory\Csilla_Orgel_PhD\APPENDIX\APPENDIX_C

Appendix D gives Supplementary Information to Chapter 8

CD directory\Csilla_Orgel_PhD\APPENDIX\APPENDIX_D